Microanalysis of sulphide rims: desulphurisation, late-stage oxidation, and possible effects on PGE formation in chromite seams of the Rum layered intrusion, Scotland.

Kimberley Pentland

Degree of Master of Science (Research)

University of Glasgow

College of Science and Engineering

ABSTRACT

A sample derived from the chromite seam of the Unit 7-8 boundary of the Rum layered intrusion (Scotland) was studied to investigate enriched rims within base-metal sulphides (BMS). Two separate data sets were derived from the sample. The exposure data set calibrated and optimised SEM-EDS acquisition and addressed fundamental questions regarding 'what makes good quality data' for effective machine learning (ML), and highlighted the effectiveness of ML for micro-analysis. Analysis techniques involved Poisson noise scaling, factor analysis (FA), and hierarchical density-based clustering algorithm (HDBSCAN). Results indicated that the optimum number of average counts per pixel lies ~ 1200. The mineralogical data set addressed elemental changes across the BMS and explored their origins, aiding understanding of magmatic formation and corroborating a proposed secondary process to account for features observed (rims, oxides, platinum group minerals/metals). Analysis techniques involved SEM-imaging, SEM-EDS data, TEM-imaging, EELS analysis, ML algorithms (FA, HDBCAN), and stoichiometry calculations. Results displayed that the main change occurring within the enriched rims is that of sulphur loss, with mineral formulae displaying a change from Cu-S rich chalcopyrite to Cu-enriched S-poor chalcocite/digenite, accompanied by spatially complementary magnetite. These results indicated that the intrusive suite underwent a period of sulphur-degassing post emplacement, under low-temperature, low fluid-rock, oxidative conditions. Spatial observations regarding PGM grains within sulphide-silicate mineral boundaries with high proximity to Fe-oxides additionally indicated that the proposed processes of alteration could be a catalyst for PGM formation.

AWKNOWLEDGEMENTS

Firstly, I would like to express my appreciation to my supervisor Dr Joshua Franz Einsle, who's guidance and support during this master's has been invaluable. His belief, confidence, and most of all, his patience, even during more challenging times, I am deeply grateful for. I am also greatly thankful to my secondary supervisor Dr Iain Neill for all his support and feedback during this project. I am extremely grateful to my peer, and friend, Matthew Divers. His tolerance, help, generosity, and comradeship during this process has been priceless. Thank you for always being in my corner. I would like to extend thanks to Dr Brian O'Driscoll for access and permission to the sample of Unit 7-8. Lastly, I would like to extend thanks to all university staff and students who aided me in anyway and made me feel welcome.

Thank you to my friends. Ciara, thank you for your support, I am glad we shared this experience together, and I am so deeply proud of you. To Nathan, Lisa, Emma, Liv, and Izzy, thank you for your encouragement and support. Thank you for making me feel seen and heard. Additionally, thanks to my friends from home, Lauren, Kyle, and Dane, for keeping me grounded. To all my colleagues at Travelodge, thank you for your flexibility and consideration.

I am also deeply grateful to my family. The last two and a half years have been challenging for all of us, and I miss you all more now than ever before. To my parents, I would like to extend my deepest gratitude for your continuous love and support. To my brother, Luke, I am grateful for our bond, your humour, and your genuineness. To Hannah, you are unbelievably strong, brave, and ambitious, you put grown men to shame. To Alex, I know if you were here, you would have something funny to say about my 'boring' degree, I miss you. To my grandparents, and all my family, your strength and perseverance in the face of the unimaginable is deeply admirable.

Lastly, to my dear Sophs, I am endlessly appreciative of you, thank you.

TABLE OF CONTENTS

LIST OF FIGURES

LIST OF TABLES

AUTHORS DECLARATION

I declare that, except where explicit reference is made to the contribution of other authors, that this thesis is the result of my own and does not include work submitted for any other degree at any institution

Kimberley Pentland

CHAPTER 1: INTRODUCTION

1.1 Layered Intrusions

Layered intrusions are regarded as the crystalised remnants of mafic-ultramafic magma chambers and have been recorded as a distinct category of igneous rock body by Wager and co-workers since the 1930's. They have been intensely examined due to the preservation of important igneous properties and processes which occur during the evolution of the chamber such as (i) fractional crystallisation, (ii) crystal growth and nucleation, (iii) elemental composition (both major and trace), (iv) formation of platinum group elements (Pt, Pd, Cr), and (v) liquid immiscibly (Scoates & Wall, 2015; Latypov et al., 2024). Layered intrusions occur throughout geological history, ranging from the Hadean and Archean era, for example the Nuasahi intrusion in India which dates back to 3123 Ma, to the Cenozoic, such as the east Greenland intrusions of Kruuse Fjord and Skaergaard which date to 55-45 Ma (O'Driscoll & VanTongeren, 2017; Smith & Maier, 2021). A comprehensive study conducted by Smith and Maier in 2021 compiled data, including ages, of 565 layered intrusions across the globe. Of the intrusions investigated, 11.0% formed in the Archaean, 25.2% in the Proterozoic, and 41.0% in the Phanerozoic (with the remaining 22.8% being "unconstrained"). Regardless of occurring across all periods of geological time, layered intrusions remain a rarity within the geological record.

Globally, layered intrusions have been found on every continent across Earth (Fig. 1.1), with the bulk of terrestrial intrusions occurring within Archaean cratons such as Kaapvaal (Bushveld, Uitkimst, Stella, Trompsburg *etc.*), Zimbabwe (Great Dyke), and Montana (Stillwater), as well as within or proximal to the dilated margins of cratonic blocks, for example, the Brasilia Belt intrusions of the Amazonia craton (Cana Brava, Niquelandia, Barro Alto) and the Halls Creek Orogen intrusions of the Kimberley craton (Hart, Savannah, Planton). Interestingly, there are very few layered intrusions which are not connected to the Archaean cratons within their peripheries (Smith & Maier, 2021). Stratigraphically speaking, most of the known and exploited layered intrusions have been emplaced within the upper crust (Bushveld Complex, Muskox Intrusion, and the Paleoproterozoic Fennoscandian Intrusions) (Kerans, 1983; Buick et al., 2001; Lauri et al., 2012; Latypov et al., 2024). Few mid-crustal layered intrusions have been reported, and there are even fewer lower crustal on record (Hasvik Intrusion, Mordor

Complex, and the intrusions of Halls Creek Orogen) (Tegner et al., 1999; Le Vaillant et al., 2020; Holwell & Blanks, 2021; Latypov et al., 2024). The lack of records regarding mid-lower crustal layered intrusions is believed to be due to uplift, erosion and exposure. However, modern geophysical investigation methods and drilling programs are aiming to characterise unexposed layered intrusions and develop knowledge around layered intrusions at depth (Latypov et al., 2024).

It has been hypothesised that layered intrusions are not restricted to Earth and may occur on the Moon and Mars. Whole rock compositions collected by the Mars Spirit rover in the Columbia Hills region of the Gusev crater have been suggested to be indicative of a layered intrusion containing harzburgites, olivine norites, apatite bearing leucocratic norites and gabbronorites (Francis, 2011). These discoveries have implications on both our understanding of magmatic systems within extraterrestrial conditions and may eventually have impacts on mineral resource considerations and exploitation (Francis, 2011; O'Driscoll & VanTongeren, 2017; Smith & Maier, 2021).

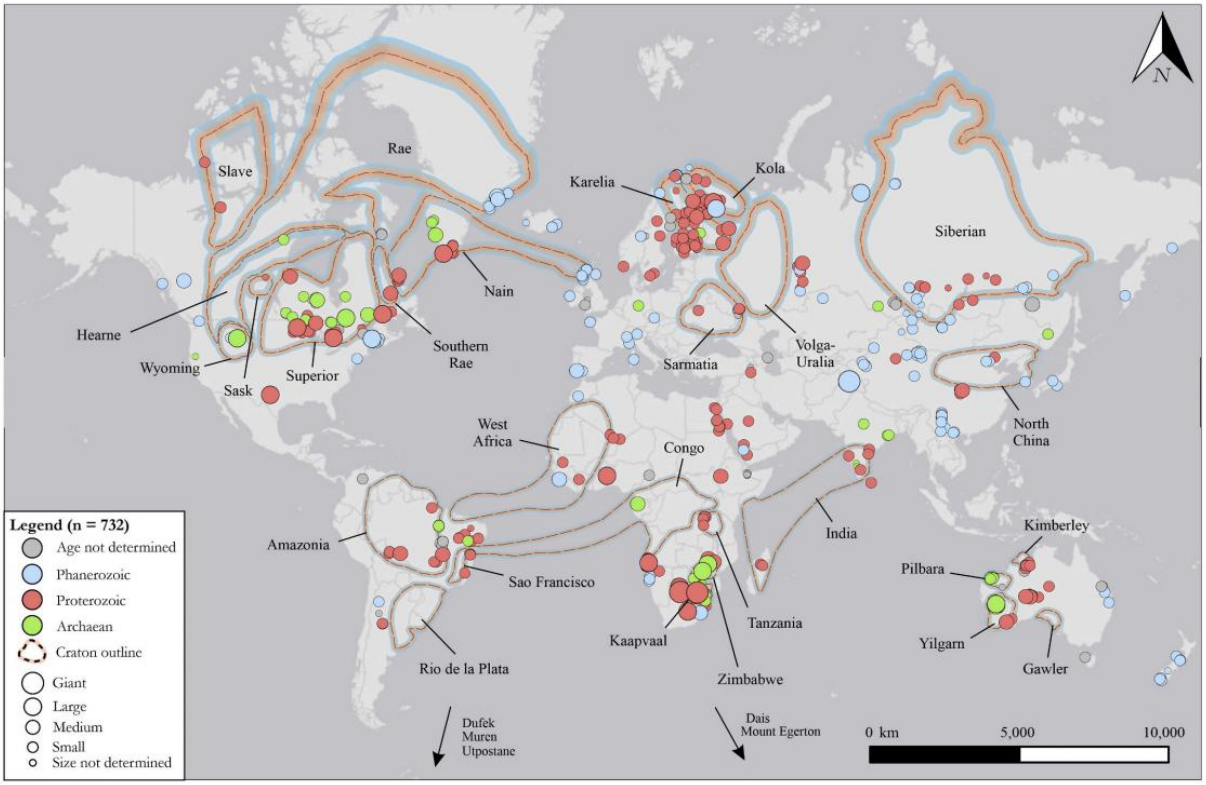

Fig. 1.1.1: Global distribution of layered intrusions regarding their age and size. Sizes are defined as follows; Giant > 10,000 km^2 , large > 1,000 km^2 , medium > 100 km^2 , and small < 100 km^2. (Smith and Maier., 2021)

Layered mafic-ultramafic intrusions (LMI) typically form under anorogenic tectonic settings during periods of intense magmatic activity (O'Driscoll & Gonzalez-Jimenez., 2016). The ages and locations of many layered intrusions are seen to line up with the amalgamation and dismemberment of supercontinents, periods in which tectonic conditions generate the mass magmatic activity required to form large igneous provinces (LIP) with which layered intrusions are associated. During times of supercontinent amalgamation intense magmatic activity can be triggered by (i) slab roll-back and lithospheric extension, (ii) trans-tensional rift zones created by oblique collision, and (iii) sub-continental lithospheric mantle (SCLM) delamination as a consequence to subduction. During periods of supercontinent separation, layered intrusion formation can be temporally linked to subsequent mantle plume activity. Few layered intrusions are seen to have formed during periods of supercontinent stability (O'Driscoll & Gonzalez-Jimenez, 2016; O'Driscoll & VanTongeren, 2017; Smith & Maier, 2021).

The size and morphology of layered intrusions vary extensively across the globe, however, for a significant proportion of LMI the original physical characteristics have been altered by post-magmatic processes such as erosion, subsidence and tectonism, with those older in age particularly affected. For example, the Stillwater intrusion of Montana (United States) is regarded as a tectonic remnant of a Bushveld-style layered intrusion which is missing 2-3km of the upper section. Subsequently, post-magmatic processes can make determining the original shape and size of intrusions arduous and affect the efficiency of layered intrusion categorisation (Smith & Maier, 2021; Latypov et al., 2024).

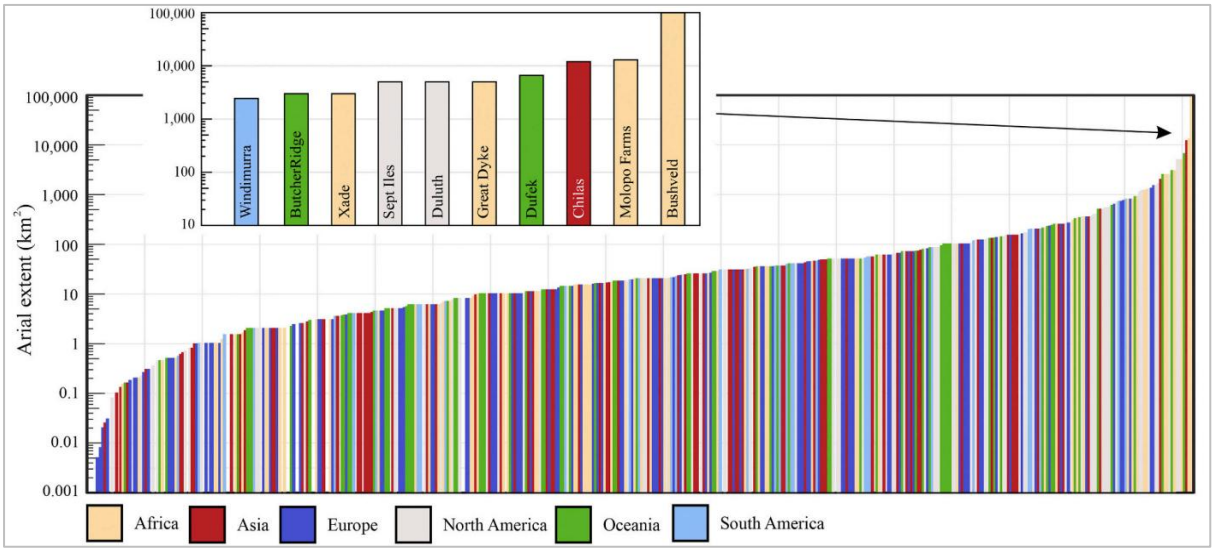

Fig. 1.1.2: Size distribution of layered intrusions (n =480) colour co-ordinated based on continent of origin, with an enlarged plot showing the 10 largest layered intrusions. (Smith and Maier., 2021).

Data from the 565 layered intrusions analysed by Smith and Maier (2021) found that the average surface area of a layered intrusion is around 444 km^2. The scope of surface area values is substantial ranging from 'Giant' intrusions of more than 10,000 km^2 in size (Bushveld Complex ≥100,000 km^2) to 'Small' intrusions less than 1 km^2 (Fig. 1.2). Stratigraphic thickness is also highly variable, with intrusions ranging from extremes of 12 km to as little as a few 10s of meters. For layered intrusions there appears to be no obvious dependence between thickness and length in comparison to other types of intrusive bodies. It has been hypothesized that layered intrusions have a thickness threshold of around 10km, equivalent to 30/40% thickness of the continental crust (Fig. 1.3) (Cruden et al., 2018). Progression from small layered intrusions to large layered intrusions is seen to observe a lengthening dominated growth regime, by which their length/thickness (L/T) ratio increases with increasing volume (Cruden et al., 2018; Smith & Maier, 2021).

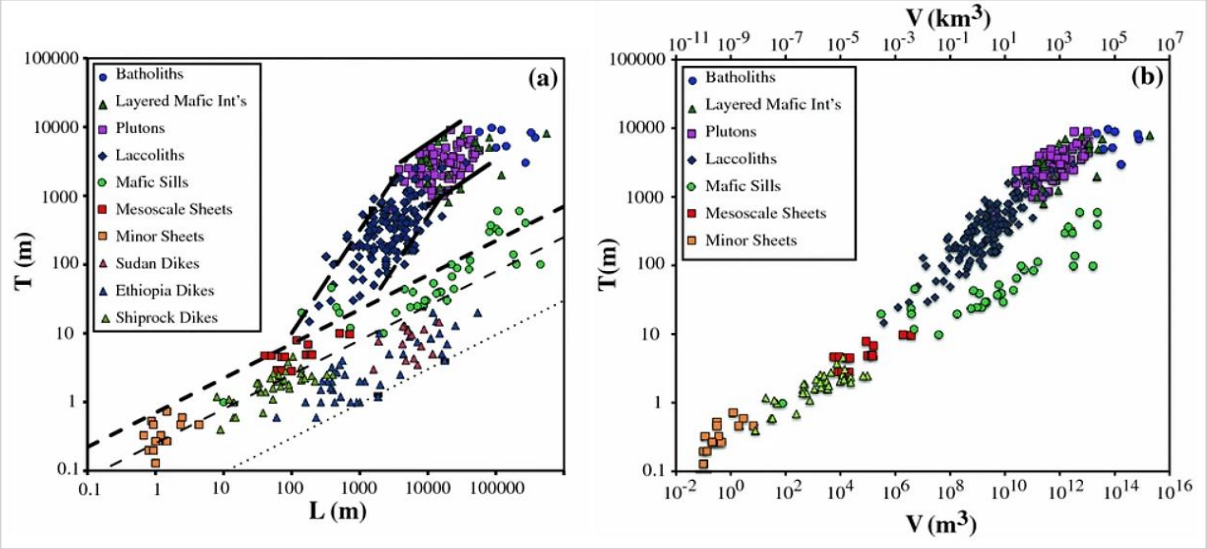

Fig. 1.1.3: a) log Thickness (T) plotted against log Length (L), Layered intrusions seen to be capped at 10km. b) log Thickness (T) plotted against Volume (V) plots. The solid and dashed lines are bounding curves for different classifications of intrusions. (Cruden et al., 2018).

Traditionally layered intrusion morphology was divided into the classes 'chonoliths' and 'lopolithic'. In recent years the applicability of these terms, particularly 'lopolithic', has been questioned. Cawthorn and Miller (2018) alternatively proposed terms funnel-, wedge-, and sheet-shaped (aka tubular) to be more in character with the intrusions geometries outlined by geophysical data. Similarly, recent research by Latypov et al (2024) has separated layered intrusion morphology into five classes (i) Funnel-shaped (V-shaped), (ii) Sheet-shaped (tabular), (iii) U-shaped, (iv) Chonolithic (tubular), and (v) Blade-shaped (Fig. 1.4). Evidence suggests the morphology of layered intrusions is partially controlled by tectonic conditions/movement. Anisotropy of magmatic susceptibility and electron back scatter

diffraction data of several large layered igneous complexes expose evidence for central unit subsidence which is believed to be somewhat responsible for gravitational phase sorting of cumulus minerals and consequent layering (Maier et al., 2013; Vukmanovic et al., 2019; Bolle et al., 2021; Latypov et al; 2014). Similarly, Bladed-shaped layered intrusions (also referred to as bladed dykes) such as Savannah of Australia are believed to have formed as a result of both horizontal and vertical propagation conditions commonly observed in shield volcano environments (Barnes et al., 2016; Barnes & Mungall, 2018; Latypov et al., 2024).

Layers within intrusions are repeated cyclic units of sheet like cumulates grading from unevolved to evolved compositions. These vary based on differences in (i) mineralogy (monomineralic, leucocratic, subversion to alteration or weathering), (ii) grain size and shape (planer, convolute, lenticular, seams, *etc.*), and (iii) chemical composition of the minerals. This means individual layers can be accurately characterised by differences in their lithology and composition (modal, graded, or cryptic), contacts (sharp, irregular, wavy, convolute, gradational or unconformable), regularity (cyclic, rhythmic or comb), and continuity (continuous, discontinuous, truncated or intermittent) (Namur et al., 2015; Smith & Maier, 2021; Latypov et al., 2024).

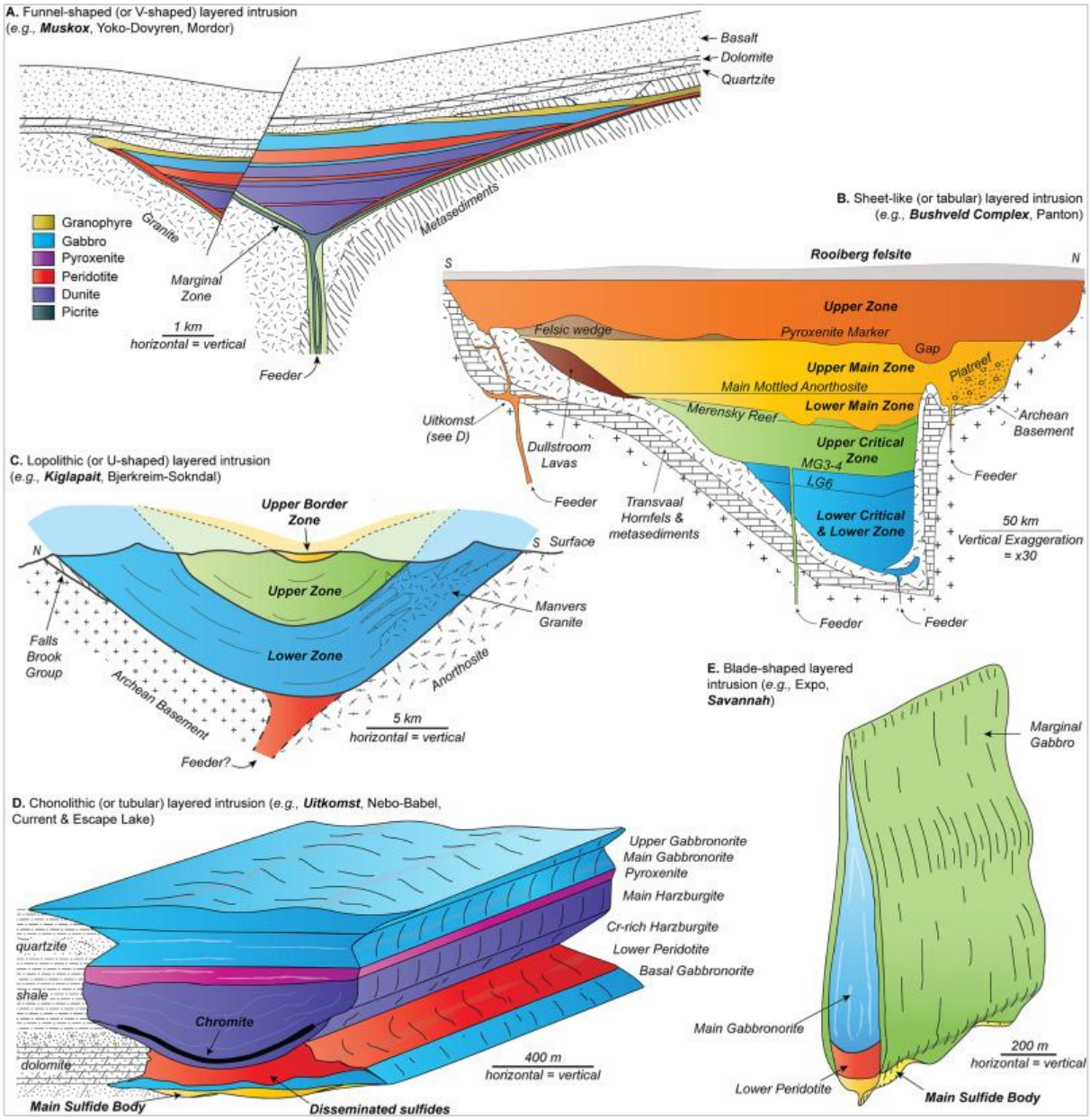

Fig. 1.1.4: Illustrated examples of geomorphological classes of layered intrusions. (A) Funnel-shaped (or V-shaped) intrusion, illustrated by the Muskox Intrusion (modified from Irvine and Smith, 1967). (B) Sheet-shaped (tabular) intrusion, illustrated by the Bushveld Complex (modified from Kruger, 2005). (C) 'Lopolithic' (U-shaped) intrusion, illustrated by the Kiglapait intrusion (Morse, 1969; Fourny et al., 2019). (D) Chonolithic (tubular) intrusion, illustrated by the Uitkomst intrusion (modified from Maier et al., 2018b). (E) Bladed-shaped intrusion, illustrated by the Savannah intrusion (modified from Barnes et al., 2016a). (Latypov et al., 2024.)

Magmatic chambers of layered intrusions can either be described as 'open systems' or 'closed systems'. 'Open system' describes crustal magma chambers which were periodically partially drained and replenished from the basaltic source, with 'closed systems' being isolated from new magma and drainage (Cawthorn, 1996). The type of system can effect which mechanisms of crystallisation is dominant within the chamber. The Skaergaard Intrusion in southeast

Greenland is a textbook example of a closed intrusion. In closed intrusions, due to the prevalence of crystallisation in the lower portion of the bulk magma alongside the build-up of crystals derivative from the roof and the walls pulled within convection currents, or, the collapse of volatile mush zones, the main location of crystal accretion is the floor of the magma chamber. The formation of an insulating blanket of mush on the chamber floor together with the production of latent heat as the interstitial liquid crystallises amplifies the initial asymmetry of cooling, and prohibits the undercooling required for in-situ nucleation of crystals from the bulk magma at the floor. Therefore, primocryst formation via heterogeneous nucleation can only occur at the magma-mush interface on the chamber floor immediately after magma emplacement. It is suggested that these effects are only apparent when around 100m of the floor blanket has been formed, with microstructural evidence suggesting that only the lowest tens of metres of the floor cumulate sequence formed on the floor of the Skaergaard intrusion (Morse, 1988; Holness et al., 2020; Latypov et al., 2024). Crystallisation behaviour in open systems which are intermittently replenished by batches of super-heated magma is different as the arrival of hot magma into a pre-existing body triggers abundant nucleation and crystal growth. Incoming primitive magma which is denser than the pre-existing evolved magma within the chamber will cause convection within the chamber and eventually accumulate on the floor of the chamber, leading to growth and nucleation at the available magma-mush interface. Open systems tend to be more common, examples include Bushveld and the Rum layered intrusion (Latypov et al., 2024).

Most models for layered intrusion formation are deeply rooted in fractional crystallisation and gravity accumulation theories by which metals and minerals separate out from the melt as conditions within the magma chamber change and settle at the base of the melt due to gravity to produce layers of crystalised material, a theory which went unchallenged into the 1970's (Latypov et al., 2024). Although well versed, the discovery and subsequent analysis of hundreds of layered intrusions over the last five decades has prompted researchers to believe that layering cannot be explained by gravitational settling alone (Smith & Maier, 2021). Generally, theorised formation processes can be divided into dynamic (syn-emplacement, convection-related, mechanical, and late-stage mush-related) and non-dynamic processes (fluctuations in intensive parameters) (Namur et al., 2015). Several theories regarding formation processes have been suggested, with theories differing across intrusions. For example, Spandler et al, 2005, have proposed that layers and seams within The Stillwater Complex form due to pressure changes and roof rock assimilation whereas theories proposed

for Bushveld, South Africa, revolve around a three-step process combining stratified magma columns, crystal slurries and cumulative assimilation (Hepworth et al., 2018). It is argued that fractional crystallisation may not be the singular origin of layers within the Rum layered intrusion, and particularly not the origin of the chromite seams separating/within the mafic layers. The in-situ model suggests that the chromite and sulphide droplets grow directly at the crystal-liquid interface and continuously extract PGM and noble metals from the fresh magma routinely delivered by convection within the chamber (Latypov et al., 2013). Current in-situ theories suggest that this magma replenishment was provided by sills within the intrusion (Hepworth et al., 2018). These different theories regarding layered intrusion formation, and consequent seam formation, is still a topic of debate today.

1.2 Platinum group metals

Platinum group metals (PGMs) were first discovered in the late 1700's by Lewis (1753, 1757), and the early 1800's by Tennent (1804) and Wollaston (1805). PGMs are iron (Fe), copper (Cu) and cobalt (Co) alongside the six transition metals found in the d-block of the periodic table of elements (Groups 8, 9 & 10, as well as periods 5 & 6). These metals are ruthenium (Ru), rhodium (Rh), palladium (Pd), osmium (Os), iridium (Ir) and platinum (Pt), which can further be divided into two sections; light PGMs (Ru, Rh & Pd) and heavy PGMs (Os, Ir & Pt), respective to their atomic weight (Puchtel, 2018; Hughes et al., 2021).

These transition minerals are among the rarest in the Earth's upper continental crust with concentrations ranging from highs of 0.52 ppb for Pd to lows of 0.022 ppb for Ir. The PGM transition metals have melting points higher than Fe (1665 K), ranging from lows of 1828 K for Pd to highs of 3306 K for Os. Rh, Ir, Pd, and Pt elemental form is cubic in symmetry (fcc) whereas Os and Ru are hexagonal in shape (hpc). Geochemically, in magmatic systems PGMs are highly chalcophile (sulphur loving) in behaviour, as well as partially siderophile (iron loving). This is the consequence of both settings within the magmatic chamber and the chemical structure of the PGMs. Firstly, terrestrial magmatic chambers tend to be oxidised to a degree at which native Fe formation is not as stable. Secondly, PGMs exist in multiple valence states ($0 \leq 8$) and thus have bonding activities ruled by their overlapping d-orbitals. These d-orbitals consist of unpaired electrons which can form metal-metal bonds, (for example with other PGMs) or covalent bonds with minerals which are electron acceptors (for example with S). Despite differences in elemental form and symmetry, PGMs can occur in solid form together, with chalcogenides (e.g., S, Te), siderophiles (Fe) and other semi-metals (e.g., As, Sb) (O'Driscoll & González-Jiménez, 2015; Puchtel, 2018; Hughes et al., 2021)

PGMs are regarded as an incredibly important resource as they have multiple applications and uses, often described as catalyst (refining crude oil, production of fine/commodity chemicals *etc.*) and non-catalyst uses (industrial: electrical and machine uses, healthcare, jewellery *etc.*) (Hughes et al., 2021). Demand for these metals is high across these industries due to their resistance to corrosion and oxidation, high melting points, electrical conductivity and catalytic activity. PGMs are also a vital resource in the advancement of green technology (green

hydrogen, fuel cells *etc.*), which is vital to reduce carbon emissions and reach global and national development goals (Koek et al., 2010; Li et al., 2023).

Current research shows that global demand for PGMs is increasing, with certain studies projecting demands to grow exponentially, with estimates of climbs of up to 240-fold by 2050, causing a demand of 51,400 tons (Rasmussen et al., 2019). This growth in demand is particularly important to note due to the abundance of PGMs which are among some of the rarest minerals within the earth's crust (Puchtel, 2018). Furthermore, PGM distribution is highly concentrated with 30% of global reserves containing 97% of global PGMs. The vast majority of PGMs are supplied by the Bushveld layered intrusion, South Africa, with PGM reserves totalling to 63,000 tonnes, followed by Russia's Noril'sk-Talnakh field and modest but recognisable contributions from Zimbabwe, USA, and Canada (Li et al., 2023; Hughes et al., 2021). This mineral distribution has made countries across the globe highly dependent on these nations, particularly South Africa and Russia, which are both currently unstable due to Russia's ongoing invasion of Ukraine as well as potential technological, infrastructural, and social problems in South Africa, with recent mine strikes and associated violence causing concerns within certain regions. This instability surrounding the lead two producers has caused concerns for many nations over resource security outside of potential supply vs demand issues (Mudd et al., 2018).

Due to their current essential uses both in more general industries (jewellery, automotive, agriculture) and within the growing green industry, the current and the projected increase of demand, and the strains on the international supply chain stated above, PGMs have been defined as 'critical elements'.

1.3 PGMs within layered intrusions and their relationship with sulphides

Platinum group mineral deposits occur within layered intrusions in a multitude of spatial forms. Due to the nature of their chemical structure discussed briefly earlier in this chapter, platinum group metals are chalcophile elements which are commonly hosted by base metal sulphides (BMS) such as pentlandite, chalcopyrite, pyrite and/or platinum group minerals as well as being heavily associated with chromite. Developing knowledge regarding PGMs hosts and their occurrence within layered various intrusions has a direct and positive influence on resource management (Mina & Anenburg, 2024).

The most common and most studied type of PGM deposits within layered intrusions are known as 'Reef-style' deposits, the most notable example being the Merensky reefs of the Bushveld Complex. Other PGM deposit types include massive seams, contact type ore, and placer (Zientek, 2012; Smith & Maier, 2021).

Reef-type mineralisation occurs within a variety of rock types such as peridotites (Bird River Belt), pyroxenites (The Great Dyke), chromitites, gabbro's (Skaergaard), magnetite's and anorthosites (Penikat). The reefs tend to be located in the lower and central portions of layered intrusions. Occurring along or within the base of the intrusion (Platreef), several meters above the base of the intrusion (Merensky Reef, Bushveld), or at the base of cyclic units within the layered intrusion (Merensky Reef, Bushveld). Reef-type deposits are given their name due to their spatial distribution as they occupy narrow stratiform horizons, occurring in layers which extend laterally commonly for several kilometres across the layered intrusion (Maier, 2005; Godel, 2015). The Rum layered suite can be classified as a reef-type deposit, with PGMs contained within thin chromite seams, typically between 2-3mm in width (however, in some locations extend to a cm in width), which extend laterally for hundreds of km (Hepworth et al., 2020; Kaufmann et al., 2020). As well as chromite, these seams are abundant in base metal sulphides (BMS)(Kaufmann et al., 2020).

As previously discussed in section 1.3, there a multitude of theories surrounding the formation of layering and chromite sulphide rich seams in intrusive suites, like the uppers vs downers theories discussed in O'Driscoll et al., (2010) and Hepworth et al., (2018). Processes that are

more widely accepted are the basics involving sulphide and chromite formation, which have important links to PGM mineralisation. These include processes like magma mixing, magmatic-flow, sulphide saturation, segregation, and accumulation (Latypov et al., 2024; Smith & Maier, 2021).

In the majority of layered intrusions PGM occur between the contact of BMS and silicates, the contact of BMS and oxides, or within a BMS itself. Other recorded instances include PGM within BMS inclusions within chromite and olivine grains (Ballhaus & Sylvester, 2000; Godel et al., 2007). This is consistent for the Rum layered suite. Of PGMs within the chromite seam, more than 71% of them are associated with BMS (Power et al., 2000).

In regard to chromites, consistent with fractional crystallisation, chromite mineralisation occurs first at higher temperatures. Chromite formation involves changes in chemical and/or physical conditions within the magmatic chamber which cause the magma to become super-saturated in chromite, as well as eliminate other phases from the liquidus. This therefore causes chromite to crystallise, commonly in mono-mineralise layers. These changes in chemical/physical contents can be via magma mixing, changes in oxygen, changes in pressure, or assimilation of country rock (Latypov et al., 2017; Mondal & Mathez, 2007). Due to high temperature mineralisation, some minor sulphide droplets enriched in PGMs become entrapped within chromite minerals (González-Jiménez et al., 2025). Regarding sulphides, mineralisation occurs when intra-magmatic chambers reach a sulphide saturation point, which leads to the exsolution of sulphide minerals at mass. This can occur by similar methods to chromite mineralisation, via magma mixing, crustal assimilation, or pressure changes. When this limit is reached the sulphur minerals segregate from the magma, and due to their density, sink and accumulate (Barnes et al., 2016; Chistyakova et al., 2019; Michaud et al., 2019; O'Driscoll et al., 2025). This typically occurs between 1000ºC and 1400ºC (Ruan et al., 2020). This immiscible sulphide liquid then 'scavenges' from the surrounding melt minerals with high affinity, such as PGMs (O'Driscoll et al., 2025).

Reef-style layered deposits of chromite, sulphur and PGM are therefore a consequence of a number of complex conditions occurring within the magmatic chamber.

1.4 Base metal sulphides

Due to their occurrence in layered intrusions, sulphide formation is widely researched regarding their impact on magmatic chamber conditions, layering and PGM formation, as well as evidence they provide via textures and isotope data regarding processes at play within the magma chamber like magma mixing, crustal assimilation *etc.* (O'Driscoll et al 2025). Base metal sulphides (BMS) are typically magmatic in origin. Mafic pulses of magma involved in the formation of layered intrusions are typically low in sulphur, therefore for sulphur mineralisation to occur, and consequently, high amounts of localised PGM formation to occur, an important trigger must be met. This is commonly referred to as the sulphide saturation level or sulphide immiscibility level, by in which a sulphide rich melt separates from the main magma body. It is well regarded that the main trigger for sulphide immiscibility is crustal contamination, particularly from high sulphur containing units such as shales/evaporites (Barnes et al., 2016; Michaud et al., 2019; She et al., 2025). Base metal sulphides of the Rum layered intrusion, including those located within the chromite seam, are all characterised by $\delta^{34}S$ isotopes of ranges of around 10%. Samples analysed contain isotopically light end members, with values ranging from -5% - +5% of those located within the chromite rich seam. Applicable contaminants occur at both ends of this range, for example, Triassic calcrete with $\delta^{34}S$ values of +5.6‰, and Jurassic calcareous sediment with $\delta^{34}S$ values of − 18.6‰. These results indicate that crustal sulphur derived from assimilation of Jurassic sedimentary rocks, in combination with magmatic sulphur, aided triggering the sulphur saturation point within the Rum intrusion system (O'Driscoll et al., 2025). Once an immiscible sulphide liquid forms, highly chalcophile elements concentrate into the sulphide liquid in proportion to their respective partition coefficients. PGMs, Ni, and Cu are all highly chalcophile, with partition coefficients between silicate liquids and such ranging from hundreds in regard to Ni and Cu, to thousands and tens of thousands in regard to PGMs (Zientek., 2012). Sulphur segregation often occurs at high temperatures ranging from 1000º- 1400º. The precise temperature varies due to the composition of the magma, proportion of sulphur present and proportion of oxygen present (Evans et al., 2008; Fonseca et al., 2009; Ruan et al., 2020).

Due to the immiscible nature of sulphide liquid, sulphide droplets form. Although chromite mineralisation occurs prior at high temperatures between 1200-1400ºC, dense sulphide droplets commonly become entrapped within the chromite seam. Sulphides can crystallise as inclusions

within the chromite grains, or interstitially in the spaces between chromite grains and surrounding olivine and plagioclase (Foose and Nicholson., 1990; González-Jiménez et al., 2025). Early experimental evidence proposed that as an immiscible sulphide liquid cools it fractionates into a monosulphide solution (MSS) and a residual sulphide melt (SM) (Naldrett & Duke, 1980; Naldrett, 2004). The MSS is iron-rich, leaving Ni, Cu, Pt and Pd to partition between the MSS and SM (Ballhaus et al. 2001; Mungall et al. 2005). Ni partition is dependent on the metal/S ratio and temperature, therefore, Ni may partition alongside the MSS while S, Pt, and Pd remain in the SM (Mungall., 2007). Experimental data shows that around 850ºC the SM crystallises into an intermediate solid solution (ISS) (Craig & Kullerud, 1969).

Work produced by Helmy et al., (2021) builds upon this plethora of older work to monitor sulphide textural evolution down-temperature and confine compositional variations at different temperatures by using a stepped experimental approach and a starting mix of $(Fe,Ni,Cu)_{1.01}$ S, similar to natural Bushveld ores (Helmy et al., 2021).

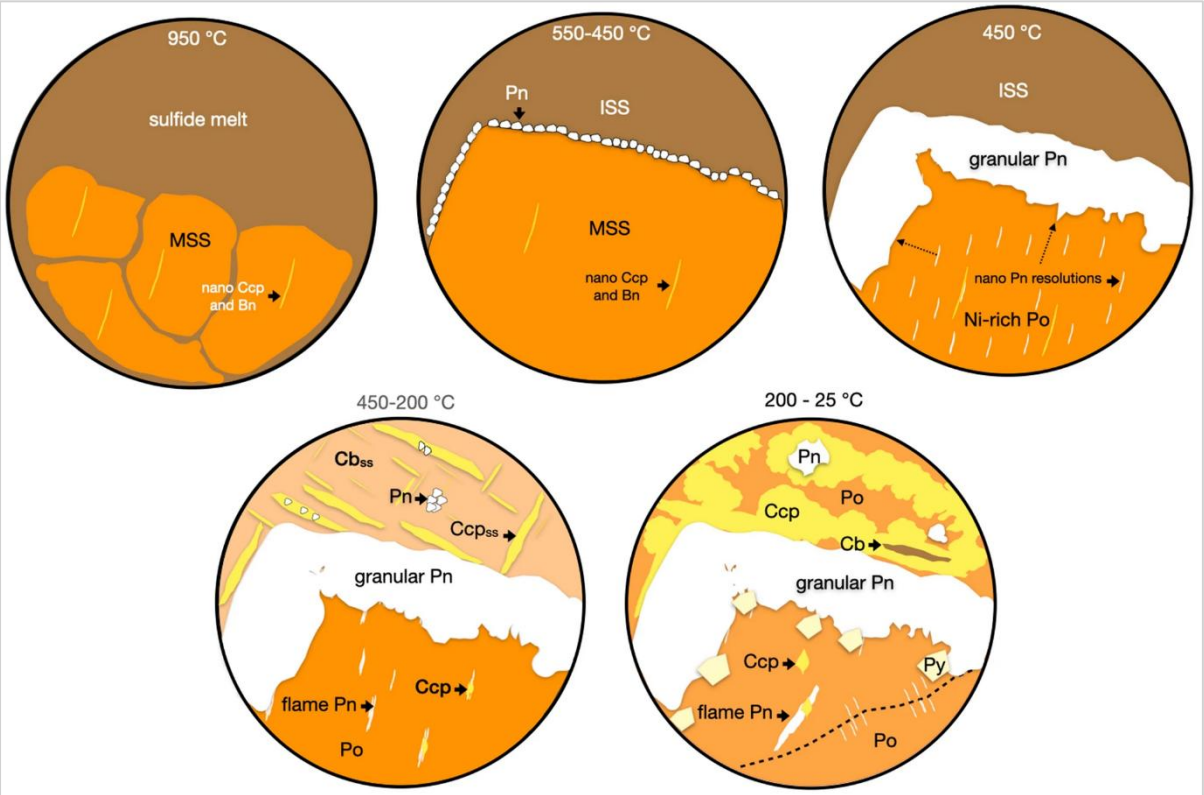

Figure 1.4.1: Conceptual diagram presenting the key processes involved in sulphide mineralisation at different temperatures provided by experimental models from Helmy et al., (2021).

Results produced were consistent with previous equilibrium studies. MSS is the first phase to form at 950ºC and persist until 450ºC. However, transition from SM to ISS is seen to be between 750ºC – 650ºC, around 100º-200ºC lower than previous experiments. This solidus may shift to lower temperatures in the presence of magnetite, semimetals, and volatiles (Craig & Kullerud 1969; Mungall 2007; Helmy et al., 2021). Pentlandite is observed to nucleate at expense of the MSS when the ratio of Ni:Fe approaches 2:1 and temperatures drop below 500ºC. Nucleation occurs from the front of the MSS and remains fastest above 400ºC. Formation can also occur from the ISS at around 200ºC, with textural observations indicating that pentlandite formation occurs after chalcopyrite. Pyrrhotite, which is Ni rich, is produced from subsolidous reactions between the MSS and ISS at around 450ºC. However, pyrrhotite within layered intrusions is commonly Ni-poor (Helmy et al., 2021). Ni-poor pyrrhotite primarily forms from the MSS above 450ºC, with additional pyrrhotite produced by decomposition of the ISS. Nano chalcopyrite lamellae can be hosted within the MSS, crystalline at 950ºC. Chalcopyrite grains however crystalise from the SM and ISS due to its Cu rich composition (in comparison to Fe/Ni rich MSS), beginning at 450ºC (Figure 6.2.1) (Helmy et al., 2021).

1.5 Importance of Rum

The importance of layered intrusions and their contents (e.g. PGMs, sulphides, and chromites) regarding academic, economic, and technological advantages has already been discussed in section 1.1 and 1.2. The importance of Rum specifically, as a layered intrusive deposit, is grounded in that of academic theory, rather than extraction and economics. The Ilse of Rum is under environmental protection, classified as a National Nature Reserve (NNR) (NatureScot, 2025). But due to its age and size, Rum acts as an extremely effective analogue site for other larger more economically viable deposits around the world (Mathez & Kinzler, 2017; O'Driscoll & VanTongeren, 2017).

Layered mafic-ultramafic intrusions have occupied a central importance in the field of igneous petrology for more than a century. There are many layered intrusion deposits located around the globe, but sites of the highest advantage to the petrology field are exposed 'exceptional' deposits, of which there are comparatively few. Among these listed sites is the Bushveld Complex and the Rum layered suite (O'Driscoll & VanTongeren, 2017). Bushveld is one of the

main sites Rum is commonly referred as an analogue to, with comparisons being made between the two dating back to the 1950's (Brown, 1956; Mathez & Kinzler, 2017).

The Rum layered suites acts as an effective analogue for more than one reason. Physically, in regard to age and structure, Rum is younger (60.5 Ma) and therefore less deformed than its Bushveld counterpart (2.5 Ga) (Bell & Williamson., 2024; Emuleus & Troll., 2005; Latypov et al., 2022). Rum's smaller size is also an advantage, measuring 30km^2 in comparison to Bushvelds total of around 600,000km^3 (Latypov et al., 2022; O'Driscoll et al., 2007). Furthermore, Rum's emplacement is shallow in comparison to that of Bushveld (Mathez & Kinzler, 2017). These factors combined increase both exposure and accessibility to observe layering, boundaries, sills, and other features present within the Rum layered suite.

In terms of petrology, there are a variable number of similarities between Rum and Bushveld. Earlier work noted that layering of Rum is rhythmic rather than cyclic, similarly too, and hence leading to comparisons with the Bushveld complex (Brown, 1956). Both Rum and Bushvelds chromite seams are significantly enriched in PGMs, typically the reef-style deposit (extending laterally for several km in Rum to several thousand km in Bushveld), and most importantly, PGM mineralisation in parts of the Rum layered suite are similar to that of the Merensky Reef and UG2 deposits of the Bushveld intrusion (Kaufmann et al., 2020; Mathez & Kinzler, 2017). Specifically, the occurrence of Cr-spinel seams at unconformable boundaries between anorthosite and mafic cumulate (as is the Unit 7-8 sample investigated within this project) (Kaufmann et al., 2020; O'Driscoll et al., 2009; Power et al., 2000).

Combined, these physical and petrological conditions make Rum a reliable analogue site for the Bushveld intrusion. Previous work regarding formation processes (in-situ vs ex-situ), fractional crystallisation, magma replenishment, and metasomatism draw direct comparisons between the Rum suite and the Bushveld complex, developing knowledge and understanding across the sites (Hepworth et al., 2020; Kaufmann et al., 2020; Latypov et al., 2022; Mathez & Kinzler, 2017). Thus, in this project, developing knowledge on sulphide mineralisation and features within the chromite seam of the unit 7-8 boundary, the possible effects of sulphur degassing or post-deposition alteration, and how these processes may effect PGM enrichment, could potentially be applicable to similar chromite horizons within the Bushveld complex, as well as many other intrusions across the globe.

1.6 Project objectives

The core objectives of this project are to utilise multiple microscopy methods such as the Scanning Electron Microscope (SEM), Focused Ion Beam (FIB), and the Transmission Electron Microscope (TEM), as well as machine learning algorithms to investigate the geochemistry and structure of the observable rims and heterogeneous sections within sulphides, as well as related platinum grain minerals of the chromite seams within the Rum layered intrusion. Developing our understanding of these enriched rims could aid in understanding sulphide mineralisation and post-emplacement alteration. Geochemical and structural micro-analysis can indicate the temperature conditions that may be at play, in conjunction with other processes such as sulphur degassing, late-stage oxidation, and aqueous alteration, as well as recognise sulphide formation/alterations impact on platinum group element enrichment.

Secondary objectives within this project are in regard to how conditions during data collection can affect the quality of the data produced, more specifically, how changing exposure conditions and increasing the number of average counts per pixel can affect the quality data produced. Investigations into what the optimum number of average counts per pixel is, and at what point does increasing the average counts (and conversely, data collection time) become futile.

CHAPTER 2: REGIONAL GEOLOGY

2.1 Geology of Scotland

Scotland is renowned globally for its geological and geomorphological diversity, comprising igneous, sedimentary, and metamorphic rocks, some of which date back to the Archaean (Figure 2.1.1) (Gordon & Stone, 2021; Smith et al., 2024).

During Scotland's history it has typically been associated with the margin of the Laurentian landmass, which is today represented by much of modern-day Greenland and Canada. Scotland preserves evidence of processes including rifting, subduction, continental collision, and mountain building in the form of sedimentary basins, volcanic centres and belts of deformed rock (Stone et al., 2012; Gordan & Stone, 2021; Smith et al., 2024). Scotland is presently divided into five major tectonostratigraphic terranes which are bound by major fault structures which were typically active in some form during the Palaeozoic Grampian and Caledonian orogenic episodes, reflecting opening and closure of the Iapetus Ocean (Fig. 2.1.2) (Stone et al., 2012).

In the Cenozoic Era, Scotland underwent its most recent period of magmatic activity and upheaval. During the early Palaeocene, the North Atlantic region, including the west and south of Scotland, was subject to intense magmatic activity including explosive volcanism, lava flows, hypabyssal intrusions, central igneous complexes, and linear dyke swarms. (Bell & Williamson., 2024). Magmatic activity was partly a consequence of continental breakup and opening of the North Atlantic Ocean, augmented by the effect of an upwelling mantle plume (Larsen et al., 2015; Saunders., 2015). Decompression melting of the upper mantle occurred as the proto-Icelandic plume impacted the base of the lithosphere. Accompanying lithospheric thinning led to the development of rift basins off the west coast of Scotland, which in turn enabled batches of magma to ascend upwards through the crust. Together, magmatic activities are referred to as forming the North Atlantic Igneous Province (NAIP) (Hole & Natland, 2020; Millett et al., 2024; Bell & Williamson, 2024).

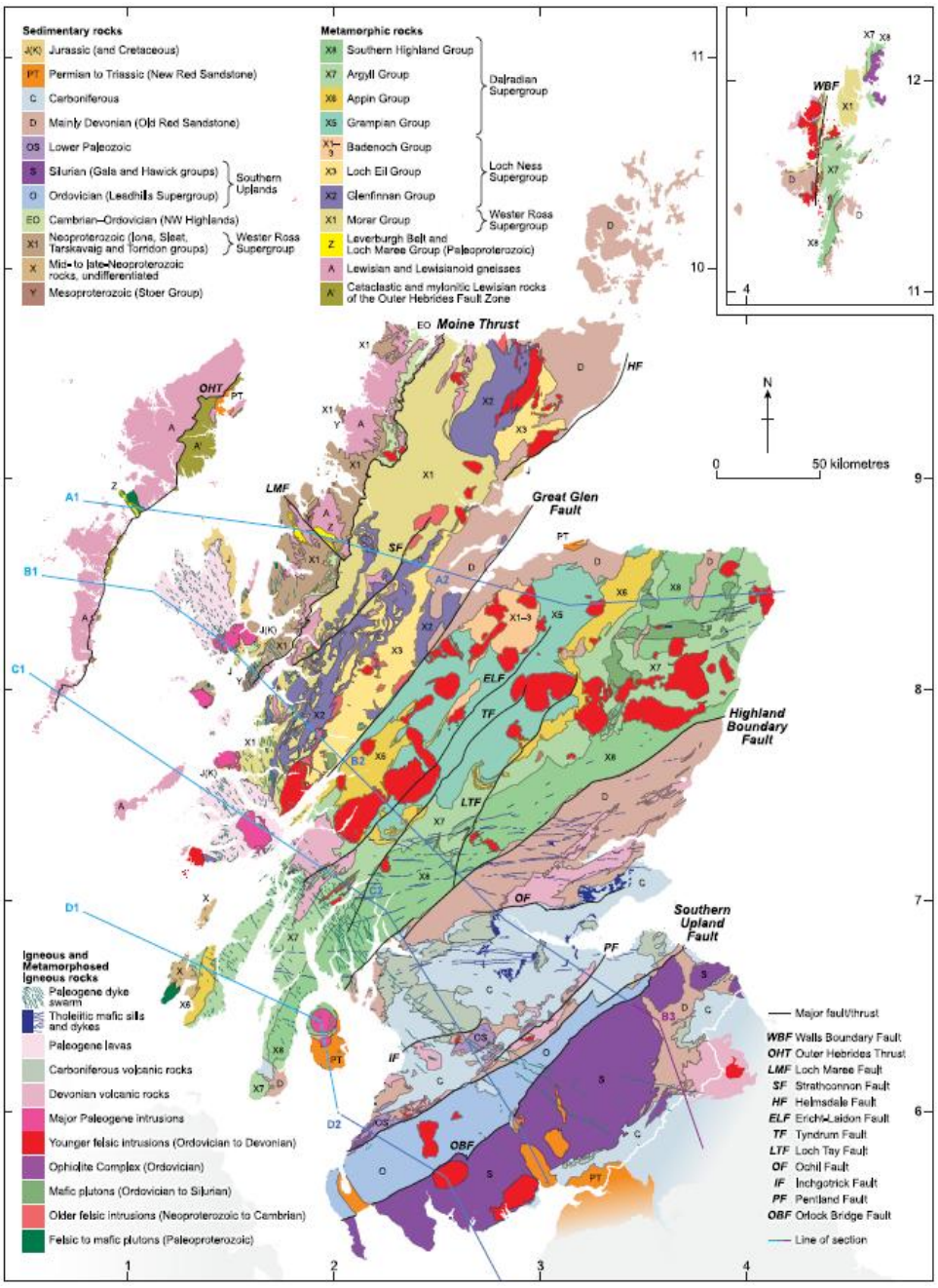

Figure 2.1.1: Geological map of Scotland, showing major rock groups and there corresponding position of formation in geological time, as well as many major fault lines (Smith et al., 2024) .

The NAIP is one of the most extensively studied, and, one of the most expansive Large Igneous Provinces (LIPs) on Earth, spanning an estimated area of 1.3×10^6 km^2, from Baffin Island of Greenland, to Mid/East Ulster of Northern Ireland, to the west coast of Norway (Figure 2.1.2) (Eldholm & Grue, 1994; Saunders et al., 1997; Millett et al., 2024). Activity within the NAIP has commonly been divided into two phases of volcanism. An initial phase which started around 61Ma, prior to break up, composed of primarily continent basaltic volcanism, and a

following phase, which was significantly much more voluminous, associated more so with the opening of the NE Atlantic Ocean around 4 Ma later (Saunders., 2015; Wilkinson et al., 2017).

For reference, the British section of the NAIP has commonly been referred to as British Palaeocene Igneous Province (BPIP) or the Tertiary Igneous Province (TIP) (Emeleus & Bell, 2005; Jerram et al., 2009; Judd, 1889). As many of the magmatic deposits associated with the NAIP in Scotland are located within islands and adjacent shoreland of the Inner Hebrides, such as the Isles of Skye, Rum, Mull and so on, the term Hebridean Igneous Province (HIP) has also been coined (Figure 3.1.3 b)) (Bell & Williamson, 2024).

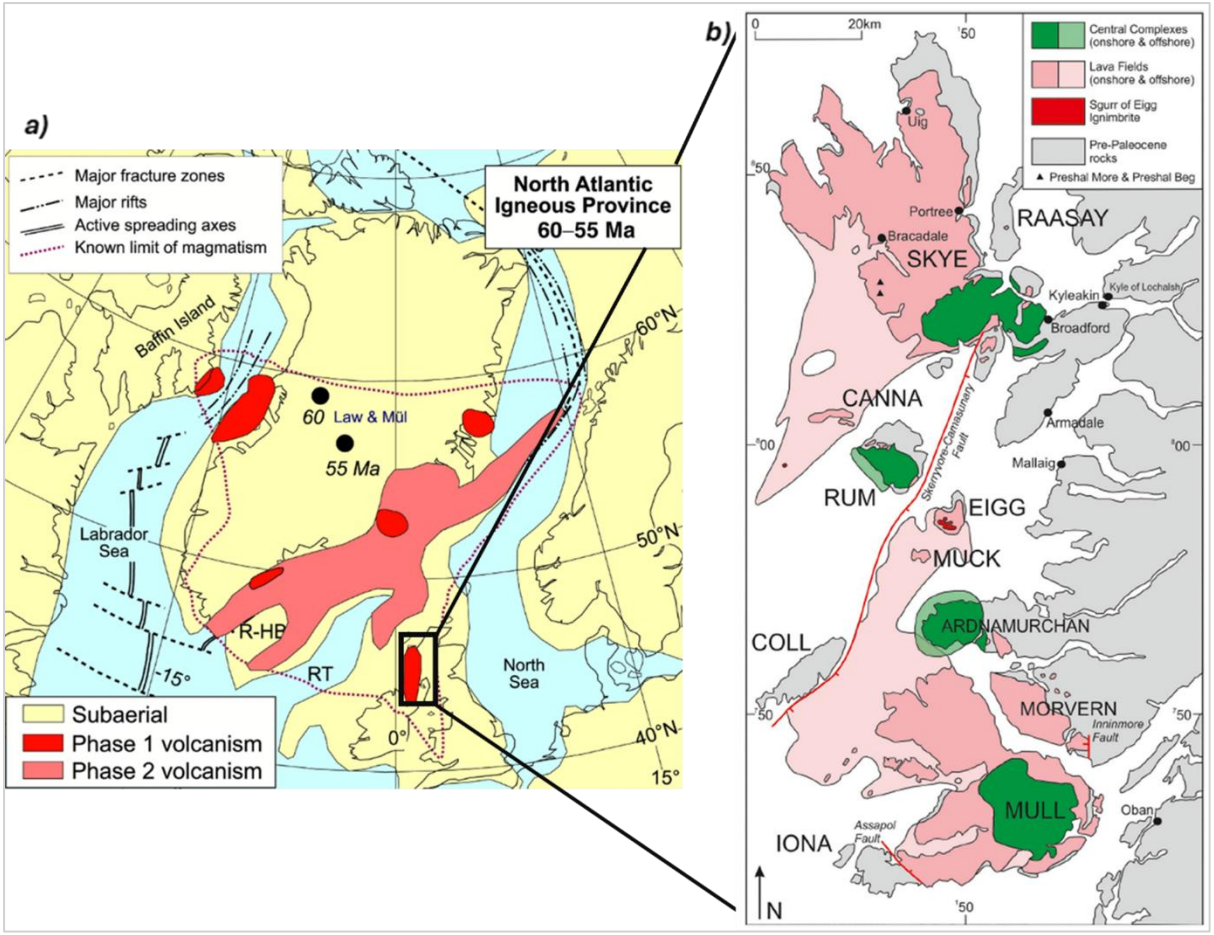

Table 2.1.2: a) Map displaying phase 1 and phase 2 of volcanism within the NAIP. b) Close of map of the boxed section in map a), depicting the onshore and offshore extent of lava fields (red) and igneous complexes (green) within the HIP. (Saunders., 2015; Bell & Williamson., 2024; modified from Emeleus & Bell., 2005).

The HIP consists of two distinct forms of igneous deposits; i) lava fields; ii) central complexes. Lava field deposits are by far the more laterally extensive of the two deposits, shown on Figure 2.1.2 *b*,) extending both onshore and offshore, particularly dominant on the Isle of Mull and

the Isle of Skye. Central Igneous Complexes are not as laterally extensive, however, are volumetrically dominant. These deposits are primarily onshore on the islands of Mull, Skye and Rum (Saunders, 2015; Bell & Williamson, 2024).

Lava fields of the HIP formed due to intense volcanic activity facilitated by fissure systems. However, their deposition was also, in part, constrained geographically by pre-existing Mesozoic rift basin structures (Brown et al., 2009; Bell & Williamson, 2024). The fields themselves contain thick (several hundreds of meters) sequences of subaerial flood basalts, occasionally interbedded with pyroclastic (including ignimbrite) units (Brown et al., 2009). Central igneous complexes of the HIP formed within basement highs, by and large where they were traversed by NE-SW-trending faults presumed to be Caledonian (i.e. Silurian to Early Devonian) in age. This is the case for the Rum Igneous complex which is close to the Skerryvore-Camasunary fault (Bell & Williamson, 2024; Upton et al., 2023).

Intrusive magmatic suites of the HIP contain exposures often termed ‘world class’, displaying a variety of magmatic processes (Jerram et al., 2009). Central igneous complexes have been the focus of research over the last number of decades, providing major contributions on igneous petrology (Baily et al., 1924; Brown & Bell, 2007; Williamson & Bell, 2012; Bell & Williamson, 2024; Phillips et al., 2013) and petrogenesis including mantle source characteristics, crustal interaction, and magma evolution processes (Dickin, 1981; Dickin & Exley, 1980; Kent & Fitton, 2000; Kerr, 1995; Kerr et al., 1999), all of which assist our understanding of large igneous provinces both locally and worldwide (Chambers & Fitton, 2000).

2.2 Geology of the Isle of Rum

The Isle of Rum is the largest of a collection of Isles named “The Small Isles” within the Inner Hebrides of Scotland. The island occupies a ridge of Precambrian rock of the Hebridean Terrane, between the Mesozoic basins of the Sea of the Hebrides and the Inner Hebrides (Figure 2.1.1) (Emeleus et al., 1996; Emeleus & Bell, 2005; Emeleus & Troll, 2014; Upton et al., 2023). This island is noted for near-total exposure of a Palaeogene layered intrusion which has drawn favourable comparison to global type examples including Skaergaard in Greenland and Bushveld in South Africa (Emeleus, 1997; O’Driscoll & VanTongeren, 2017).

The oldest unit on the island is the Lewisian gneiss formation, which only outcrops on the surface within the central intrusion in proximity to the Main Ring Fault (MRF). This gneiss is unconformably overlain by the late-Proterozoic Torridon group of sandstones and shales, which dominate the geology of the north/north-east of the island. Toward the northwest corner of the island, on Monadh Dubh north of Glen Shellesder, Triassic age sandstone deposits can be found. The last of the pre-Palaeocene rock units are thin slivers of lower-Jurassic sedimentary units preserved in arciform pieces of the MRF (Upton et al., 2023). All of these units pre-date the Rum Igneous complex, which is the main concern of this project.

The Rum Igneous Complex is one of the earlier complexes formed in the HIP, with isotopic dating placing various unit emplacement between 61 – 59 Ma (Figure 2.2.1). Igneous emplacement on Rum initiated with onshore extrusions of lava and ignimbrites, followed by a mass intrusive complex, which crops both onshore and offshore (Bell & Williamson, 2024). Units of the Rum Igneous Complex were emplaced during Palaeocene into previously discussed pre-Palaeocene rock units, as well as more recently deposited volcanic rock from the Eigg lava field, dated between 60.65 ± 0.07 and 60.45 ± 0.07 by Ar/Ar dating (Chambers et al., 2005; Troll et al., 2008; Emeleus & Troll, 2014).

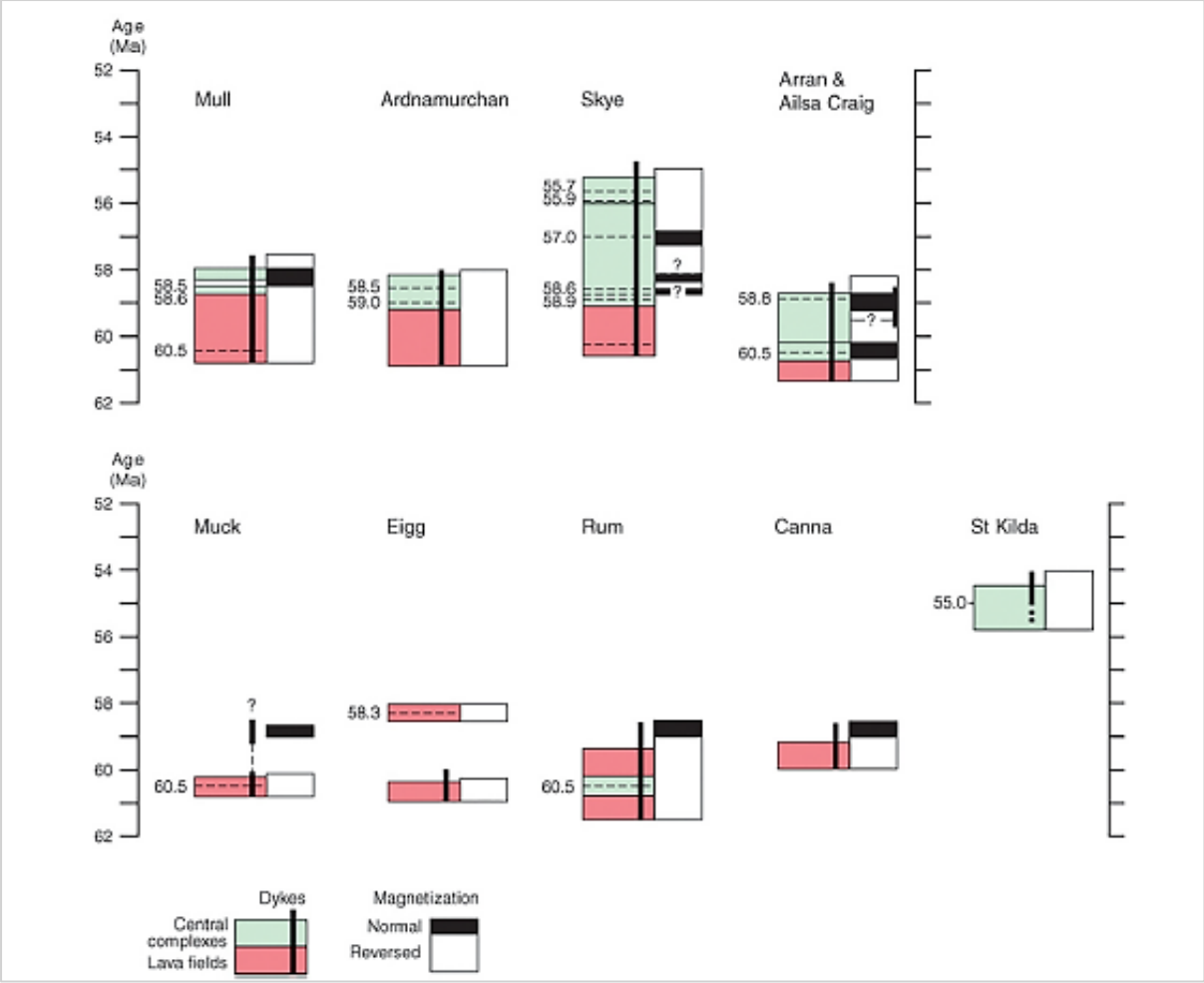

Table 2.2.1: Figure summarising the evolution of intrusive and extrusive units within the BPIP, based on radiometric dating of the units using either Ar/Ar or U/Pb dating. Rum is seen to be one of the earlier complex formations (Emuleus and Troll., 2005; Bell & Williamson., 2024).

Formation (and subsequent decay) of the Rum Igneous Complex is divided into three stages; Stage 1, fault system formation and avalanches, dominated by silicate magmatism (granites, ignimbrites, felsites, *etc*.); Stage 2, dominated by mafic/ultra-mafic magmatism (gabbro's, troctolites, peridotite units) and minor intrusive body emplacement; Stage 3, dominated by erosion and deposition (Emeleus & Troll, 2014; Bell & Williamson, 2024; Upton et al., 2023). Stages will be discussed in depth, however, a summary of events is presented in Table 2.3.1.

Table 2.2.1: Table summarises the sequence of events within each stage of the Rum Igneous Complex's formation. Events are listed in chronological order (from youngest to oldest). NMZ = North Marginal Zone, SMZ = South Marginal Zone. Table modified (Emeleus & Troll, 2014; Upton et al., 2023).

Stage 1	• System of ring faults develop > Period of massive uplift > Collapse of caldera units > Formation of avalanche deposits. • Minor discordant intrusive units of silicate composition intrude – dykes formed of porphyritic rhyodacite, tuff and breccias – *Rhyodacite dated by Ar/Ar dating 60.33 ± 0.21 Ma (Troll & Nicoll., 2008).* • Major granitic bodies intrude – micro-porphyritic Western Granite – *Ar/Ar dating 60.01 ± 0.45Ma (Chambers et al., 2005).* • Minor granitic bodies intrude – Papadil and Long Loch.	
Stage 2	• Change in magma from felsic (stage 1) to mafic/ultra-mafic. • NE/SW trending dykes of the Muck Swarm intruded in the NMZ and SMZ. • N/S trending dykes and basaltic cone sheets intruded int the NMZ and SMZ. • Intrusion of the Eastern Layered and Western layered intrusions (peridotites), quickly followed by Intrusion of the Central intrusion (peridotite) - *Rum Central Intrusive suite dated by U/Pb dating to be 60.53 ± 0.04 Ma (Hamilton et al., 1998).* • Emplacement of gabbro and peridotite plugs.	Central uplift accompanying these stages
Stage 3	• High intensity period of erosion > deep valley development > mass removal of rock > accumulation within deep valleys. • Eruption of basaltic lavas from the Canna Lava Formation (Skye Lava Group) – *Dated by Ar/Ar dating 59.98 ± 0.24 Ma (Chambers et al., 2005).*	Often, deposition of these units occurred at the same time, forming interbedded breccia-basalts.

The first event to occur in Stage 1 is the formation of the Main Ring Fault (MRF), which in turn forms both the North Marginal Zone (NMZ) and South Marginal Zone (SMZ). Faulting lead to uplift of up to 2 km, as well as tilting, doming, and deformation of the Torridon Group sandstones/shales and Lewisian Gneiss (Emeleus & Troll, 2014). As doming progressed, substantial quantities of the Torridon sandstone separated from the dome and slid gravitationally down low-angle faults. Further subsidence of the block to the interior of the MRF produced a caldera structure. Un-bedded mega-breccias formed after caldera wall collapse lead to an avalanche of debris on the caldera floor (Troll et al., 2000; Emeleus & Troll, 2011; Emeleus & Troll, 2014). Finer grained sandstone deposits also formed due to an intra-caldera fluvial-lacustrine system. Uplift and subsidence within the MRF was accompanied by

the felsic magmatism. Early felsic magmatism was dominated by the emplacement of minor intrusive bodies of porphyritic rhyodacite (ignimbrites), and crystal-vitric tuffs into the recently developed Caldera units, into the breccias. Dating of plagioclase phenocrysts within rhyodacite deposits by Ar/Ar has provided an age of 60.33 ± 0.21 Ma (Troll et al., 2008; Troll et al., 2011; Emeleus & Troll, 2014). Geochemical and isotopic analysis of Sr and Nd support that rhyodacite intrusive units were derived from partial melting (>70%) of the Lewisian gneiss, with no contamination from Moinian metasedimentary rocks (characterised by highly radiogenic isotopic values of Sr and Pb) (Figure 2.2.2) (Geldmacher et al., 2002; Meyer et al., 2009; Emeleus & Troll, 2014). The intrusive masses of porphyritic rhyodacite located in Coire Dubh and Dibidil also contain rounded fragments of basaltic material, indicating an interaction occurring between silicic and mafic magmas, and backing the idea consistent across the LIP of magma mixing being a significant process (Bell, 1983; Emeleus & Troll, 2014; Upton et al., 2023).

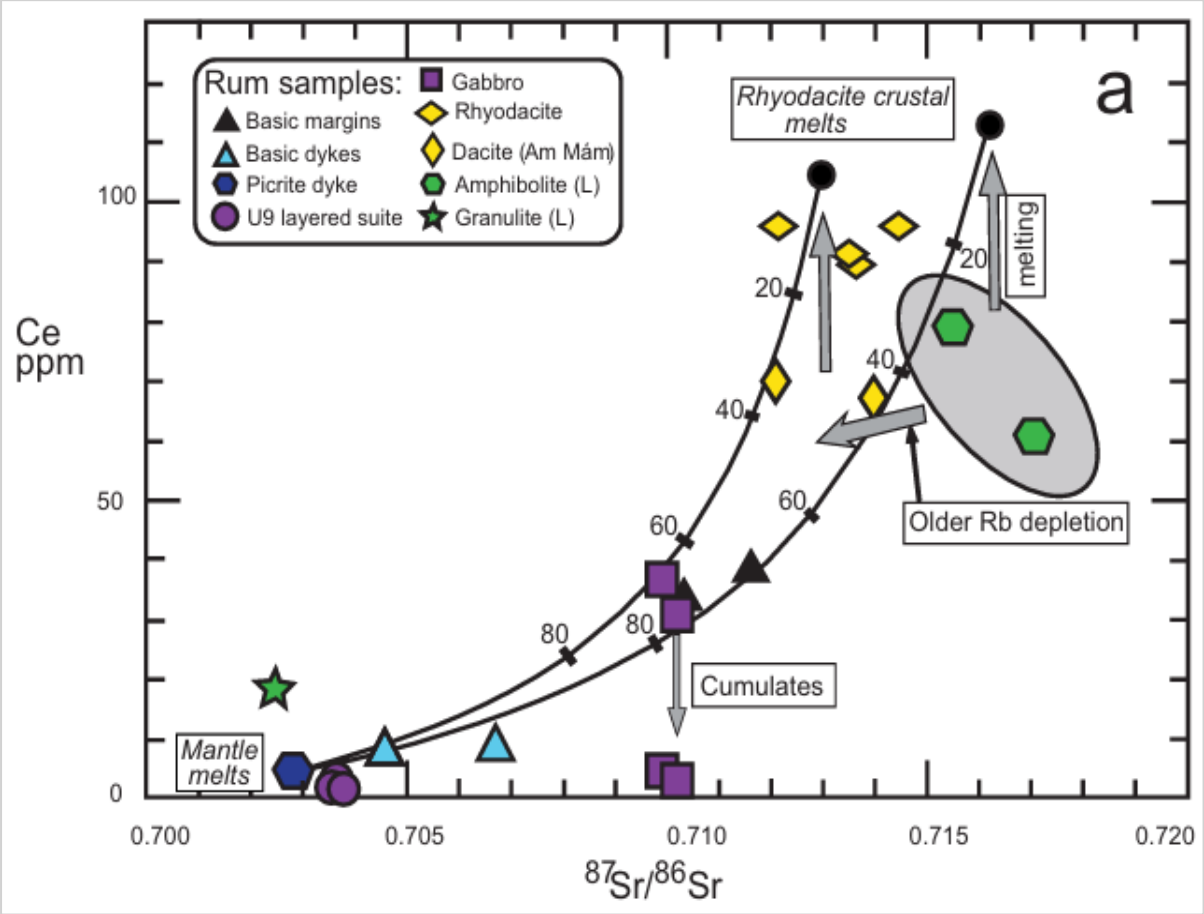

Figure 2.2.2: Sr^{87}/Sr^{86} vs.Ce (ppm) plot for representative Rum samples. As Ce is an incompatible element which is enriched in crustal rocks, increasing Ce alongside Sr/Sr is indicative of strong crustal influences on parent melts. Decreasing Ce and Sr/Sr is therefore indicative of strong mantle influences on parent melts (Meyer et al., 2009; Emeleus & Troll., 2014).

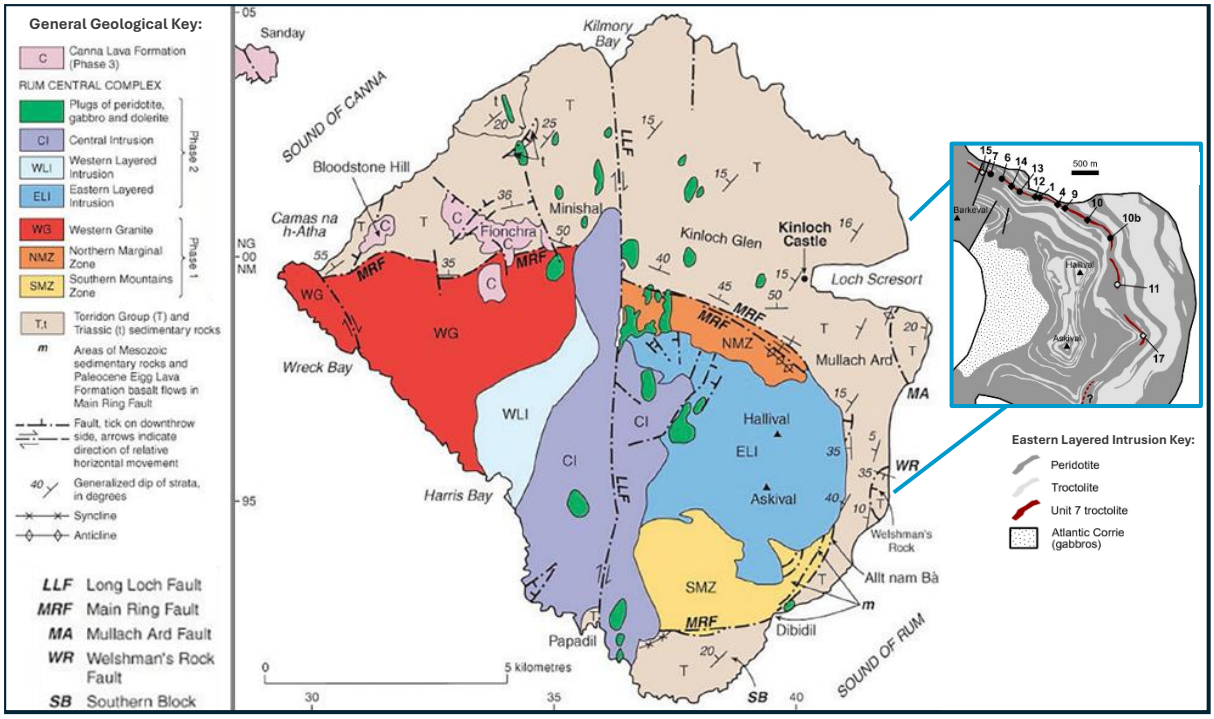

Figure 2.2.3: Geological map and key of the Isle of Rum, highlighting the different units and the stage (coined 'Phase') in which they formed. To the right of the figure there is a smaller map of the ELI complex, displaying the cyclic layering and highlighting Unit 7, which is highly relevant to this project. Figure modified (Emeleus & Troll., 2014; Kaufmann et al., 2020).

The Am Mam Breccias of the NMZ consist of a multitude of blocks; pre-paleocene gneiss and sandstone, as well as blocks and mega-blocks of mafic material such as gabbro and feldspathic peridotite, all contained within a diorite matrix. The observation of mafic material within these minor silicic intrusive bodies is highly significant as it provides evidence that mafic and ultra-mafic rocks had begun to form at this stage but did not dominate within the Rum Igneous Complex until stage 2 (Upton et al., 2023). The micro-porphyritic Western Granite, as well as related smaller granitic bodies located in Papadil (South Rum) and Long Loch (Central Rum), post-date the porphyritic rhyodacite deposits but are similar in composition (Emeleus & Troll, 2014; Bell & Williamson, 2024; Upton et al., 2023). Ar/Ar dating of the major western granitic complex has revealed an age of 60.01 ± 0.45 Ma (Chambers et al., 2005). Therefore, the majority of silicic units formed in stage 1, and are of crustal origin, with isotope signatures mirroring the underlaying Lewisian Gneiss (Emeleus & Troll, 2014; Troll et al., 2020; Bell & Williamson, 2024; Upton et al., 2023).

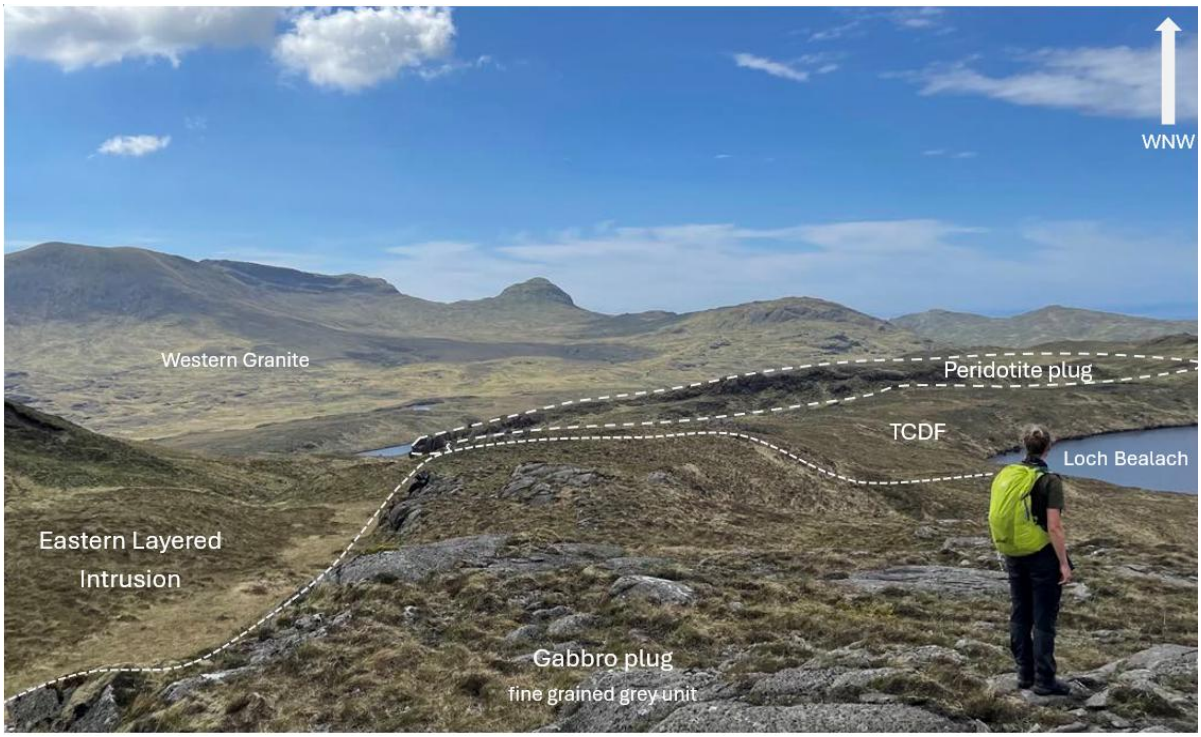

Figure 2.2.4: Photographs taken during excursion 1 15/05/2024. Full fieldwork file available in supplementary material. Annotated to show the changing lithologies as excursion transverses westwards toward Primoch lochs. Topography consists of later stage 2 gabbro and peridotite plugs, with stage 1 major western granitic complex in the distance. (CTDF = Fiachanis Gritty Sandstone).

Stage 2 of formation of the Rum Igneous Complex commenced with a change in magmatic conditions from silicic dominated to mafic dominated. The first units emplaced following this change are a series of minor intrusive bodies, a mass of dykes of the Muck Swarm, which trend NW-SE, along with NNE/N trending dykes and cone sheets of basaltic composition. These minor intrusive units particularly dominate the NMZ and SMZ of the Rum Igneous Complex (Emeleus & Troll, 2014; Bell & Williamson, 2024; Upton et al., 2023). The volumetrically dominant mafic intrusion emplaced during stage 2 is the Ultrabasic Intrusive Complex (UIC), dated by U/Pb methods to be 60.53 ± 0.04 Ma (Hamilton et al., 1998). The UIC can be separated into three sections; the Eastern Layered Intrusion (ELI), Western Layered Intrusion (WLI), and the Central Intrusion (CI) (Figure 2.2.2). Intrusions within the UIC are composed of olivine rich mafic rock units, such as felspathic peridotite, bytownite gabbro and troctolite, however, lithological structure and textural features do differ between the intrusive units (Emeleus & Troll, 2014; Bell & Williamson, 2024; Upton et al., 2023).

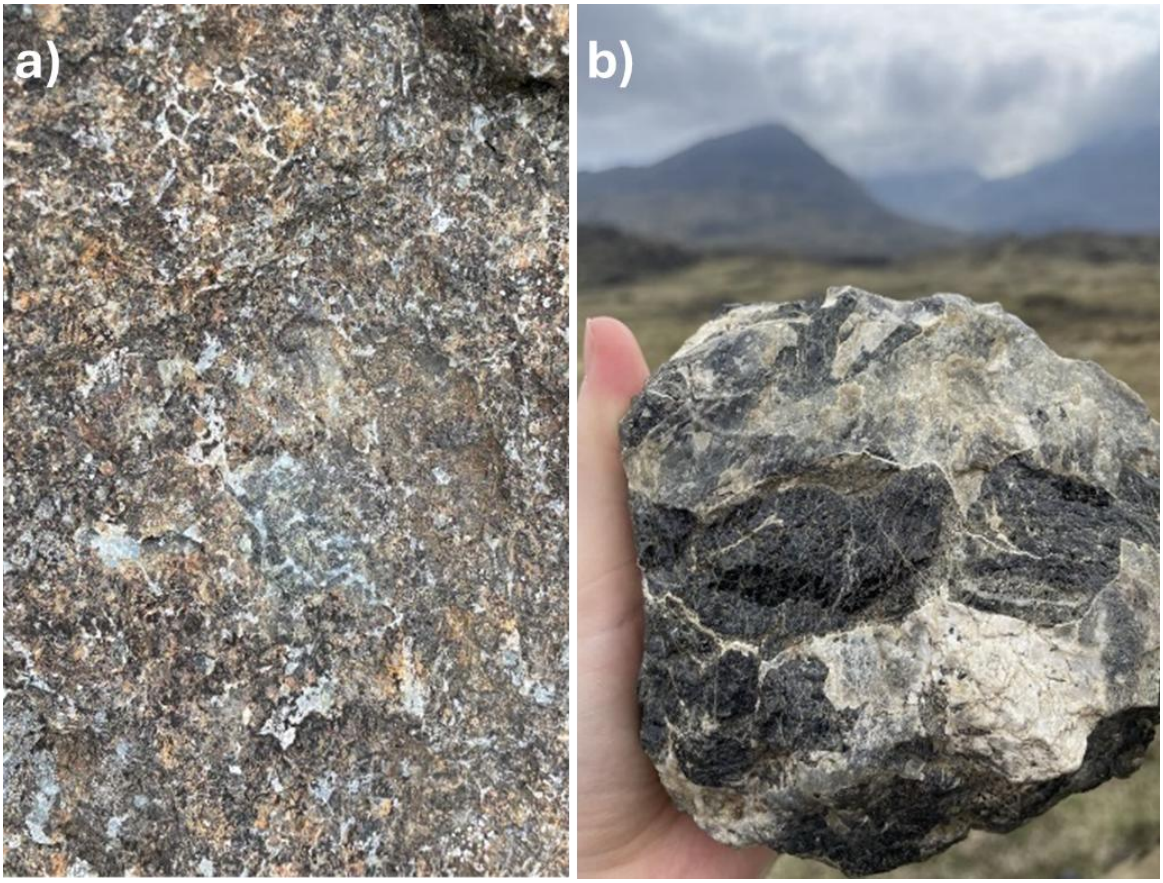

Figure 2.2.5: Photographs taken during excursion 2 16/05/2024. Full fieldwork file available in supplementary material. **a)** Planar view of harrisitic texture. **b)** Rock fragment of Western Layered Intrusion displaying extreme harrisitic texture.

The ELI and WLI were fully formed prior to the completion of formation of the CI, which is largest intrusive body of the UIC. The ELI, containing the peaks of Hallival and Askival, is formed of 16 rhythmic units (also known as doublets) creating mass layering extending to at least 700m thick (Bell & Williamson, 2024). Layering is typically modal, based on differing mineralogical compositions producing distinct macro-units of peridotite (olivine rich) and troctolite (mostly olivine and plagioclase feldspar), with minor areas of anorthosite (upwards of 90% plagioclase feldspar) material common within troctolite along unit boundaries (Bell & Williamson, 2024; Upton et al., 2023). Within some units layering can be distinguished by textural features present. Layers of peridotite tend to form dark layers which are easily weathered, contrasting to the lighter grey, resistant troctolites and gabbro's (Figure 2.2.6 a, Figure 4.1.5) (Emeleus & Troll, 2014; Bell & Williamson, 2024; Upton et al., 2023).

Commonly, chromite spinel seams can be observed within the ELI, frequently along unit boundaries. The sample used in this project was obtained from the boundary between units 7-

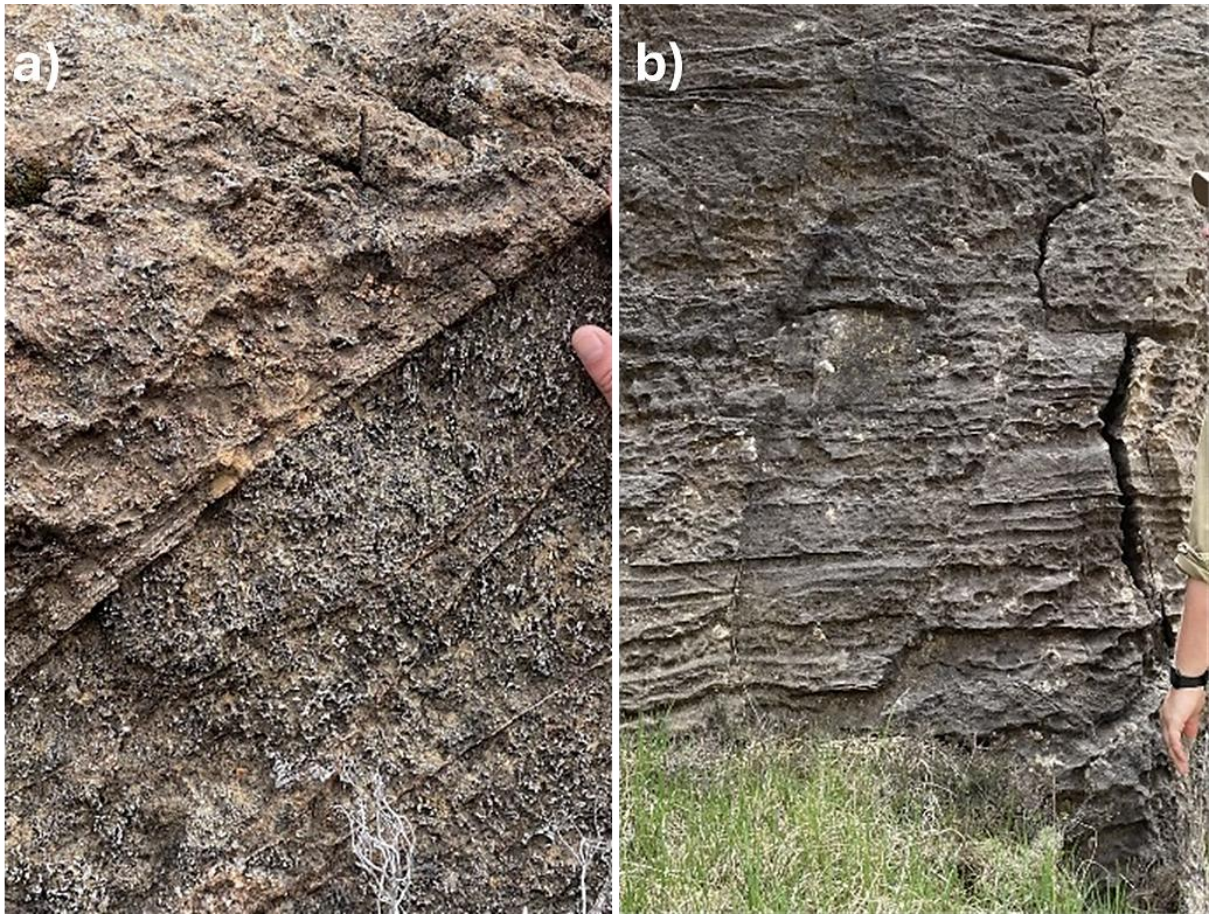

Figure 2.2.6: Photographs taken during excursion 2 16/05/2024. Full fieldwork file available in supplementary material. **a)** Layering within Western Layered Intrusion, two distinct units. **b)** Layering within peridotite of the Western Layered Intrusion.

8. The WLI of the UIC comprises of a series of layered bytownite gabbro, overlain by units of peridotite (Figure 4.1.4). Overall, the WLI is believed to extend for a minimum of 600m, similar to the depth of the ELI. (Emeleus & Troll, 2014; Bell & Williamson, 2024; Upton et al., 2023). A unique texture can be observed within the WLI, known as 'Harrisitic'. Harrisite refers to the rocks containing large, long, elongated olivine crystals which have typically formed perpendicular to the stratification of the rock, first observed, recorded, and coined by Alfred Harker in 1908 (Figure 2.2.5) (Brown, 1956). Harrisitic texture is likely a consequence of short periods of tranquillity within olivine-rich, crystal-poor, Mg-high magma, with skeletal olivine crystals growing within a short period of time, perhaps days or less (Emeleus & Troll, 2020; Upton et al., 2023).

Both the ELI and WLI intrusion formed at relatively the same time in stage 2. Their emplacement is believed to be the result of lateral extension of successive sheet-like injections

Figure 2.2.7: Photographs taken during excursion 2 16/05/2024. Full fieldwork file available in supplementary material. **a)** Photograph of triangle shaped chunk of layered troctolite and peridotite overlain by troctolite within the central intrusion. **b)** Photograph of wavy ductile deformation within the central intrusion.

of mafic/ultra-mafic magma from the CI supplied by feeders along the graben like structure of the Long Loch Fault (an open system), underneath the cover of earlier uplifted rocks (Bell & Williamson., 2024; Upton et al., 2023). As discussed in the introduction, many models have been proposed in regards to layered intrusion formation, and this remains with ELI/WLI mineralisation (such as fractional crystallisation/crystal settling & sorting/in-situ reactions, combined with post-deposition deformation reactions/pore-infilling crystallisation) (Emeleus & Bell, 2005; Emeleus & Troll, 2014; Troll et al., 2020). Recent opinions regard that formation was most likely achieved by a multi-step method including aspects of fractional crystallisation and gravitational settling, as well as the modern in-situ model (Bell & Williamson, 2024; Upton et al., 2023).

The CI is the youngest and largest of the UIC, composed of a complex assemblage of mega-blocks of layered troctolite (1500m x 400m x 30m), massive peridotite, and peridotite breccia. Dips of layering within individual troctolite blocks is seen to be consistent, however, other blocks have different dip values, suggesting that during formation there was high amounts of disruption, rotation, and slumping (Figure 2.2.7 *a)*). This ductile behaviour present during formation is also displayed by many wave-like features within the CI unit (Figure 2.2.7 *b)*). There are several generations of intrusive breccias present within the CI, up to 400m wide and trending N-S. These breccias are attributed to periods of subsidence within the magma chamber

linked to extensional events affecting the LLF. The geochemistry of rocks within the UIC suggest that residual batches of basaltic magma were vented, leading to the formation of basaltic volcano (Emeleus & Troll, 2014; Troll et al., 2020; Bell & Williamson, 2024; Upton et al., 2023).

Stage 3 is dominated by erosion and sedimentary/igneous deposition, as aggregational volcanic activity related to the formation of the Rum Igneous Complex ceases. Erosion was vigorous, developing deep valleys, which then filled with eroded clasts from the freshly formed Igneous Complex's, deposited by north-flowing rivers. These deposits become interbedded and layered with lavas of the Skye Lava Field which tended to pond against the flanks of the volcano, observed particularly in the NW of the island (Emeleus & Troll, 2014; Bell & Williamson, 2024).

Dates produced from Ar/Ar and U/Pb methods indicate igneous activity lasted ~800,000 years or less (Troll et al., 2008). It is important to note that Ar/Ar dating has a tendency to produce younger results than U/Pb, typically yielding results which are 1% younger (Renne et al., 1998). When taking account for minor age discrepancies, activity at the Rum igneous centre could have taken ~500,000 years or less (Troll et al., 2008). These ages, combined with physical observations, reiterate that stages 1 and 2 of formation were effectively coeval, and were immediately followed by stage 3 (Emeleus & Troll, 2011). Post-dating these stages, the long loch fault is seen to undergo significant right-lateral movement, and the island is subjected to mass erosion due to repeated extension and retreat of ice sheets during the Pleistocene (Emeleus & Troll, 2014; Bell & Williamson, 2024; Upton et al., 2023).

The Isle of Rum is of particular interest to this project due to the well exposed layering within the UIC, particularly the ELI, and the well-preserved chromite seams within this layering, containing sulphides and associated PGMs (Power et al., 2000; O'Driscoll & González-Jiménez, 2015; O'Driscoll et al., 2025). Uncovering the geochemical structure within the highlighted rims of the sulphide material could aid in interpretations regarding the origin of these sulphides (magmatic/hydrothermal), their relationship to PGM enrichment, and overall queries regarding the process which lead to the formation of layers within the complex at large (Power et al., 2000; O'Driscoll et al., 2025).

CHAPTER 3: METHODS

3.1 Fieldwork

A 4-day long fieldwork trip was taken to observe field relations, identify and locate the units of layered intrusion, and understand the larger tectonic system in which the Rum layered intrusion formed. Fieldwork was conducted from 14th – 17th of May 2024. The majority of excursions were based or partially based of routes from 'A geological excursion guide to Rum: the Palaeocene igneous rocks of the Isle of Rum, Inner Hebrides' by Henry Emeleus and V.R Troll. The excursion on the 15th included aspects of "Excursion 2: The Northern Marginal Zone" observing contact boundaries, dykes and the main ring fault, then transversing west wards past Loch Gainmhich towards Primoch Lochs observing plugs of gabbro within main ring fault and the unconformable relationship between gritty sandstone and gneiss. The excursion on the 16th included aspects within "Excursion 4A: The Central Intrusion" observing harrisitic textures within peridotite and bytownite troctolite. The last excursion on the 17th consisted of aspects of "Excursion 3: Hallival and Askival", with the primary aim to locate the different units within the Eastern Layered intrusion and record layering, chromite seams and any other features within the units which relate to the primary aim of the project.

3.2 Optical Microscope

The thin section used in this project was provided by Dr Brian O'Driscoll to the author and when produced was done so in line with the University of Glasgow standard procedures. The sample is derived from the Unit 7-8 boundary of the Eastern Layered Intrusion within the Rum igneous complex (NM 39043, 97391). Optical petrography using both transmitted and reflected light was conducted on the unit 7-8 Rum sample at a variety of magnifications. Equipment used is the Zeiss Axio Imager M2 using Zen software. Optical microscope work enabled the identification of sulphide hot spots within the seam and made identification and analysis of sulphides of interest in the scanning electron microscope (SEM) easier. The aim was to locate areas which were most likely to provide sulphides that reached the investigation criteria set to reflect the core aims of this project.

3.3 Scanning Electron Microscope

The Scanning Electron Microscope (SEM) is one of the most commonly used instruments in regards to microanalysis across disciplines, particularly over the last decade as multiple progressions in software development have notably increased the ability of studying solid matter. Pairing the SEM's back scatter electron imaging (BSE) with directed steering of the electron beam for energy dispersive X-ray spectroscopy (EDS) provides chemical analysis of a subject carried out at 1um resolution, with modern SEM units equipped with EDS detectors able of detecting and identifying elements from Be to U, and characterising elements 1 – 2um depth within the sample surface (Schulz et al., 2020; Kostryzhev & Murphy, 2024). SEM-EDS is particularly useful over other SEM analytical techniques due to several reasons; i) simplicity of the instrumentation; ii) minimal sample preparation; iii) high spatial resolution; iv) high analysis speeds; v) automation providing the ability to analyse large sample areas within one loading cycle (Kostryzhev & Murphy, 2024). Combined, these features provide the qualities necessary to analyse micro-element relationships in the rims of the sulphides chosen in this project, and develop our understanding of them.

In this project image sampling and geochemical mapping was conducted on the unit 7-8 Rum thin section which was coated with ~20 nm carbon. Data was collected using a Zeiss Sigma variable pressure field-emission-gun scanning electron microscope (VP-FEGSEM) equipped with an Oxford Instruments Ultim Max 170 mm^2 energy dispersive X-ray spectroscopy (EDS) detector based in the Geo-analytical Electron Microscopy and Spectroscopy (GEMS) facility at the University of Glasgow. Backscattered electron (BSE) imaging, secondary electron (SE) imaging and Energy-dispersive X-ray spectroscopy (EDS) were all collected from the unit 7-8 sample using an accelerating voltage of 20 kV, working distance of 8.0 mm and an aperture of 60 µm. Two sub-sets of SEM data collected from this sample were used in this project.

The first data set was collected prior by Dr Joshua Franz Einsle and consisted of data of the same sulphide mineral taken under 9 different exposure settings (Table 3.3.1), with exposure changing with each set in order to determine the extent of which increasing exposure settings, particularly increasing the average number of counts, effects the quality of the EDS data produced. To clarify, 'exposure' within this project refers to increasing the electron beams dose to the sample area in order to achieve more total counts. This requires altering the dwell time

(us) or electron dose per pixel, which in turn increases collection time (Table 3.1.1). This data set will be referred to as the exposure data set. EDS mapping data was acquired and later processed using Oxford Instruments Aztec 6.0 software.

The second data set consisted of sulphide minerals of interest which had met the following criteria to qualify for EDS analysis in regards to the aims of this project; contained enhanced rims along the edge of the sulphide mineral, hosted more than one sulphide phase within one sulphide mineral grain, and/or was a sulphide mineral grain containing a platinum group metal grain. This data set will be referred to as the mineralogical data set. EDS mapping data was acquired and later processed using Oxford Instruments Aztec 6.0 software. Analysis produced isolated element maps of each element chosen during analysis, which, after fine tuning in oxford instruments, can be layered to create a layered element map. EDS data in both of these of these are useful for observing basic interactions between elements within mineral grains.

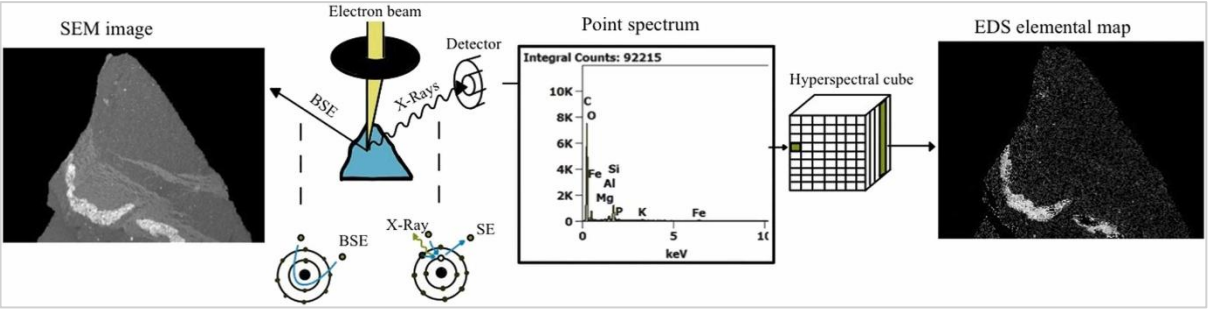

Figure 3.3.1: Figure displaying the acquisition of BSE and EDS images (Duma et al., 2022).

Table 3.3.1: Table of the various exposure settings and other relevant information in regards to the data collection process of each respective test of the exposure data set.

test	experiment N*	magnification	WD (mm)	aperture	Energy kV	resolution x	resolution y	frames	process time (ms)	dwell (us)	dose per pixel	frame time (s)	total time (s)	total map time (min) (1.d.p)	channels	HFW (um)	Pixel size (um) (2.d.p)	live time(s)	live time (m) (2.d.p)	total counts	cts/pixel (average counts) (2.d.p)
1	1	500	8	60	20	512	437	5	3	200	1000	40	200	3.3	2048	582	1.14	197	3.28	13832974	70.36
2	x	500	8	60	20	512	437	15	5	600	9000	112	1680	28	2048	582	1.14	1769	29.48	124272843	632.08
3	3	500	8	60	20	1024	768	15	3	800	12000	158	2370	39.5	2048	582	0.57	9437	157.28	659667344	838.81
4	x	500	8	60	20	1024	768	60	5	100	6000	20	1200	20	2048	582	0.57	4719	78.65	330436467	420.17
5	2	500	8	120	20	512	437	5	3	200	1000	40	200	3.3	2048	582	1.14	197	3.28	36438207	185.33
6	5	500	8	120	20	512	437	15	5	600	9000	112	1680	28	2048	582	1.14	1769	29.48	328281279	1669.72
7	x	500	8	120	20	1024	768	15	3	800	12000	158	2370	39.5	2048	582	0.57	9437	157.28	1754069702	2230.41
8	4	500	8	120	20	1024	768	60	5	100	6000	20	1200	20	2048	582	0.57	4719	78.65	882513361	1122.17
9	6	500	8	120	20	1024	768	30	3	600	18000	112	3360	56	2048	582	1.14	14156	235.93	2638063880	3354.47

3.4 Focused Ion Beam

Focused Ion Beam (FIB) microscopes have become powerful tools in microanalysis. Interaction between the Ga+/electron beam, extracted from the gun, and the targeted material can offer a range of functions such as imaging, milling, and deposition, leading to a variety of analysis techniques. Similar to a SEM the FIB incident beam can produce high resolution SE images. Images produced tend to have a higher signal/noise ratio and an enhanced contrast of the targeted samples surface. Further uses of the FIB imaging include ion imaging namely secondary ion mass spectrometry (SIMS), electron backscatter diffraction (EBSD), and cathodoluminescence (CL) integration. Milling and deposition tools can be used to generate samples for further nanoscale analysis of targeted material either in the Transmission Electron Microscope (TEM) or for Atom Probe Tomography (APT). Lastly, duel beam FIB systems can be used for 3D tomography, here the incident beam can be used for serial milling of the sample while simultaneous SEM imaging of cross sectional images can be collected and later segmented and visualised using the appropriate software (e.g., Avizo). These methods can prove vital for geochemical microanalysis of a large variety of geological material (Lui et al., 2020).

In this project the FIB was specifically used to produce Transmission Electron Microscope (TEM) lamella for nanoscale analysis. Sample preparation was conducted using a Thermoscientifc Helios 660 Plasma FIB fitted with a Xenon Plasma Focused Ion Beam Gun within the plasma column and a Elstar Schottky Field Emission Gun within the electron column. As well as equipped with multiple element detectors. The lamella was produced by the following methodology; (i) sample loading, (ii) E-beam platinum protective layer deposition, (iii) ion beam platinum protective layer deposition, (iv) milling, (v) U-cuts, (vi) lift out, and lastly (vii) mounting on grid post using the ‘flag pole’ method. A detailed manual regarding this general methodology named ‘TEM Sample Manual Preparation Procedures’ can be found on the Yale University webpage (Yale West Campus Materials Characterization Core, 2023).

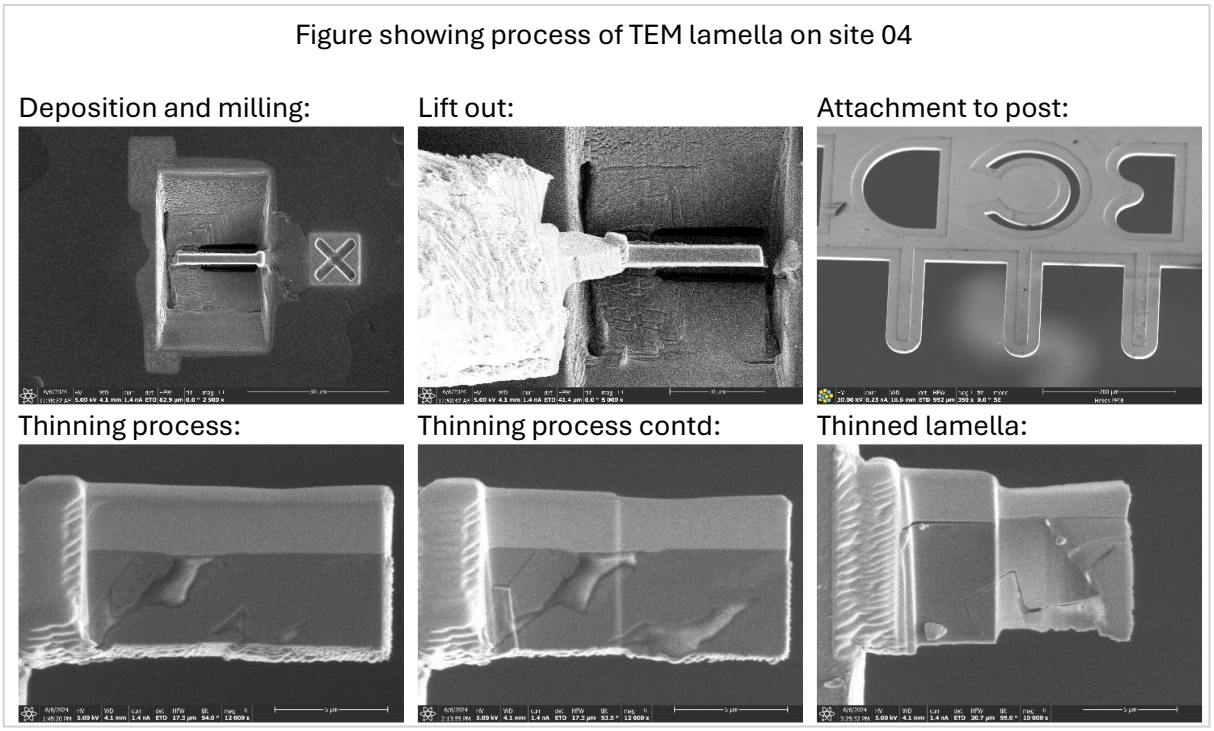

Figure 3.4.1: Figure showing the methodology of TEM lamella preparation used within this project (method adapted from Yale West Campus Materials Characterization Core, 2023).

Figure above displays how the previously described methodology was adapted and carried out within this project (Yale West Campus Materials Characterization Core, 2023). Due to complications with natural cracks causing lamella to shatter or break off during training on 2/3 practice samples, caution was taken during the thinning process of site 04 lamella, thinning only the stable right hand side (which contained the area of interest) to required thickness (<100 nm).

Site 04 from the experimental data set was chosen to produce a TEM lamella sample from for a variety of reasons; the presence of a rim of interest; the presence of three separate sulphide phases within one mineral grain; the reduced number of cracks within sulphide grains; and lastly, due to elemental changes being present over a small distance. Two lamella were produced from this site.

3.5 Transmission Electron Microscope

Transmission Electron Microscopy (TEM) can provide microstructural, crystallographic, compositional, and electronic information from a micrometre to sub-nanometre scale across selected sections of the prepared sample. Despite the advantages of this technique regarding the wide variety of information which can be acquired as well as the element of scale, the TEM is not as widely used as other microscopes within the geoscience field due to perceptions of the TEM requiring difficult and time consuming sample preparation as well as certain methods requiring extensive knowledge of electron-beam interactions to produce an accurate interpretation of the data produced. However, due to developments in the automation of the process of thin sample preparation, TEM lamella analysis has become more accessible and hopefully will become more prevalent in geological microanalysis (Lee, 2010).

In this project, two TEM lamellae from site 04 of the experimental data set were prepared using the methodology previously explained in section 3.4. TEM lamella 1 was analysed in the TEM-MAGTEM of the Kevlin Nano-Characterisation Suite. Data collected from lamella 1 includes High-Angle Angular Dark Field (HAADF) imaging and Electron Energy Loss Spectrometry (EELS).

EELS data acquisition methods differed across the locations investigated in the TEM. Acquisition of EELS data from location 1 utilised Spectral Gatan Fitting (Digital Micrograph) software, a model based fitting approach to quantify elemental intensity where the spectral background and edge intensity are treated as a single model (EELS.info, 2025; Gatan, 2025). Aligning with EELS Atlas (2025) intensity guide, element edges identified include Fe L_3-edge 708eV, O K-edge 532 eV, and M_1-edge Cu 123eV (EELS Altas, 2025; Thompson & Vaughan, 2009; Williams, 2001). Location 2 utilised a simpler integration method, and manual sulphur quantification. Element edges included a range of the major Fe L-edges, from L_2-edge 721 eV to L_3-edge 708 eV, and the major Cu $L_{2,3}$-edges, from L_2-edge 951 eV to L_3-edge 931 eV, as well as standard major S K-edge of 2472 eV (EELS Atlas, 2025). Similarity, location 3 did not utilise an automated simple background, and utilised a method similar to location 2, using L2,3-edge Fe and Cu, and standard K-edge S values (EELS Atlas, 2025).

3.6 Machine Learning Techniques

Evaluation of the SEM-EDS data sets discussed within the previous chapter was conducted using a variety of Machine Learning (ML) analysis techniques. ML analysis is becoming an increasingly utilised tool regarding microanalysis across scientific disciplines, including geology. ML methods are particularly useful regarding geological microanalysis as they can efficiently discover, categorise, and occasionally describe structural patterns within geochemical data sets (Yuyang He et al., 2022) Furthermore, as data sets have become increasingly denser and complex overtime, many ML techniques have developed to aide analysis of these 'high-dimensional' data packs. This is achieved by applying algorithms that classify the data, pull-out latent (hidden) variables that explain the data set to a higher degree of accuracy, or, by identifying and segmenting data which have similar properties and act in similar ways into groups. This reduces the overall quantity of data whist maintaining, or improving the quality of the data set (Wilkinson et al., 2019). There are a large variety of ML tasks well established within the data-discovery field which aide high-dimensional data analysis in this way such as dimensional reduction, classification, regression and cluster analysis (Petrelli, 2024). This is particularly useful for this project as the SEM-EDS data acquired in both the exposure data set and the mineralogical data set is high dimensional due to the imaging axis data provided by the SEM unit and the 2048 energy channels provided by the EDS detector, creating multi-dimensional data packs occupying measurements from 512(x) × 347(y) × 2048(e) (Test 1) to 1024(x) × 768 (y) × 2048 (e) (Test 9) which in turn contain a high volume of arrays (Figure 3.6.1). Among previously stated ML tasks, unsupervised learning algorithms such as dimensional reduction and clustering have proven to be extremely valuable for decoding and understanding the geochemical and textural record stored within igneous and metamorphic rocks respectively, and prove particularly useful to enhance visualisation of mineral data collected (Petrelli, 2024). Observation of minor elements and structures within thin sections proves to be complex due typically being located in minor assemblies, dimensional reduction and clustering algorithms enhance the signal-noise ratio, providing us with a way of distinguishing these structures from the data set and extracting their specific spectra (Khudhur, et al., 2024). These properties make dimensional reduction and clustering algorithms highly appropriate analysis techniques in regards to the context of this project with dimensional reduction and clustering tasks conducted on the EDS-SEM data sets collected reducing the quantity of the highly-dimensional data whilst maintaining its integrity,

and, enabling patterns within the data relating to the geochemistry of the rims and multi-phase features of interest in the sulphides to be discovered and subsequently categorised, aiding the verification of and building upon geochemical data already provided by EDS element maps.

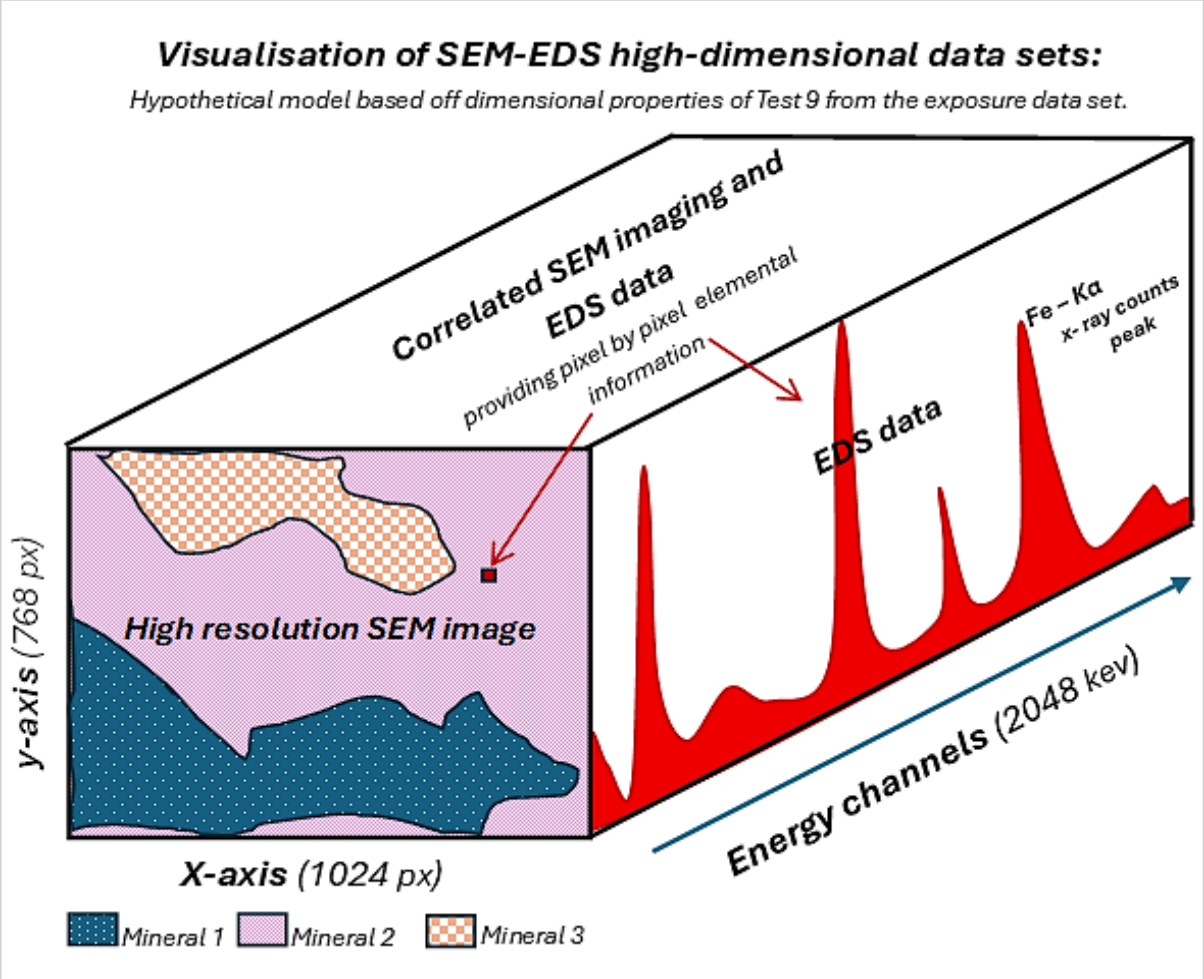

Figure 3.6.1: Visualisation of EDS-SEM multi-dimensional data, based on dimensional values of Test 9 from exposure data set. Model is hypothetical and purely for demonstrational purposes.

A multi-step ML workflow using unsupervised learning algorithms was used to analyse the data set's collected, derived from previous micro-analysis projects; '*Tracking subsurface active weathering processes in serpentinite'* (Tominaga et al., 2021), and, '*Interrogation of ecotoxic elements distribution in slag and precipitated calcite through a machine learning-based approach aided by mass spectrometry*' (Khudhur et al., 2024). The methodology used is as follows; (i) data exportation, (ii) data calibration, (iii) data decomposition, (iv) clustering, and (v) Bruker analysis and stoichiometry calculations. ML processing was conducted within Jupyter Lab using python and facilitated by utilising the following libraries; Hyperspy, NumPy , scikit-learn, Matplotlib, and pandas.

Firstly, SEM-EDS data was exported using the Oxford Instruments AZtex software. Secondly, this data was then calibrated and normalised by performing Poisson Noise Scaling. This step is integral when processing spectroscopic data. Due to the sheer size of multivariate data sets, the large volume of data, and the large volume of noise within this data, can have a negative impact on ML algorithms ability to segregate important chemical information. Spectroscopic analytical techniques, such as SEM-EDS, which relies on counting x-rays in order to form spectra information, are seen to contain noise that typically follows a Poisson trend, with noise produced due to independent, random electron arrivals (Keenan & Kotula, 2004; Hasinoff, 2016). This infers that the uncertainty within a given data point is not a constant value, but rather, the uncertainty within a data point increases with the number of counts that are presented by that point (Keenan & Kotula., 2004). In other words, the probability of a certain event and/or number of events occurring within a certain time frame is dependent on the average rate of those events occurring, independent and uncorrelated to events that occurred previously (Joy., 2008). In the case of EDS-SEM analysis, electrons may be expected to arrive at a constant rate of r electrons per a specific duration of time, however, as electrons function independently of each other, they cannot be expected to arrive at regular intervals. Within a specific duration of time (t), the number of electrons that are expected to arrive is equal to $N = rt$, however, due to the uncorrelated nature of electron arrivals, it is highly unlikely that the number that actually arrived to be equal to rt, hence the basis of Poisson noise distribution (Woan., n.d.). Therefore, in lower-dimensional data packs with less counts, Poisson noise is common and can be highly noticeable. Common multi-dimensional analytical tools (PCA,FA *etc.*) assume that data packs follow a Gaussian noise distribution, which contrasts Poisson by assuming the magnitude of uncertainty is constant, the noise level is therfore assumed to be constant and occur independently of the individual size of a specific data point (In EDS-SEM, noise is levelled across the image)(Keenan & Kotula, 2004; Hasinoff, 2016). Increasing data counts would eventually produce Gaussian distribution, however, due to operating costs, time constraints, multiple desired sites of analysis, and concerns over sample damage it is difficult to obtain this type of data (Thompson, 2001; Keenan & Kotula, 2004., Ozawa, 2023). Therefore, to increase effectiveness of these ML algorithms on spectroscopic data, regardless of counts, Poisson Noise Scaling can be applied prior to analysis to account for this assumption. Scaling involves weighting the data accordingly, essentially 'evening the playing field' by making uncertainties within the data set more consistent (Keenan & Kotula, 2004). In non-scaled data sets, small, spectroscopic features may be combined with noise during ML analysis tasks, therefore Poisson noise normalisation of data not only decreases noise and increases the image quality,

but will in turn enhance the results produced by analytical ML techniques (Keenan & Kotula, 2004). This is an essential step for this project to ensure that the small features, such as the sulphide rims, are effectively pulled out from the data sets collected in this project. Thirdly, decomposition of data is conducted. This process is commonly conducted within high dimensional data packs to reduce the dimensions within the data whilst maintaining the maximum amount of variability and therefor integrity, as well as having an further effect on noise reduction. Initially, data decomposition was executed on the exposure data set by using Factor Analysis (FA) and Principal Component Analysis (PCA) respectively.

Stated by Joliffe and Morgan, "Despite their different formulations and objectives, it can be informative to look at the results of both techniques on the same data set. Each technique gives different insights into the data structure, with PCA concentrating on explaining the diagonal elements, and factor analysis the off-diagonal elements, of the covariance matrix" (Joliffe & Morgan, 1992). To expand, PCA converts a set of patterns of a number of variables into a set of values that are linearly uncorrelated, labelled principle components, in which the optimal amount of chemical information is captured in the smallest number of principal components (Keenan & Kotula., 2004; Wilkinson et al., 2019). Geometrically, PCA works by performing orthogonal rotations. First, the direction in the data's dimensional space in which the location of the data is most effectively described is found, once found, this vector is determined the first principal component. Once determined, the second direction (orthogonal to that of the first) which best describes the data that is not included within principle component 1, is determined and subsequently named principle component 2. This process then repeats accounting for the remaining data (Jolliffe, 2002; Keenan & Kotula, 2004; Wilkinson et al., 2019). FA differs from PCA as instead of distinguishing uncorrelated variables, FA focuses on identifying latent factors within the data set and highlights the underlaying structure which explains how said factors are related. Similar to PCA, after determining the first factor, a rotation is performed within the data's dimensional space when determining the following factors. Unlike PCA, rotation can either be orthogonal (when un-related), or oblique (when related) (Abdi, 2003; Suhr, 2005). In this workflow, the rotation used in both decomposition method is varimax rotation (an orthogonal rotation). In short, varimax rotation is used to improve the results produced by PCA and FA by maximising the variance of the squared loadings within each factor. Each factor/component produced contains a small number of large loadings and a large number of small loadings. Varimax then searches for a rotation that works to maximise the variation of loadings within the factors/components, therefore in a given factor, a specific

variable pulled out will load more strongly, and other variables will reduced. This benefits results by increasing the clarity of the factors, simplifying the structure within the data, and, increasing the distinction between factors (Abdi, 2003; Dilbeck, 2017; Jin et al., 2020). Combined, these benefits aid the ease of interpretation of results produced by these algorithms. The differences of results produced from these methods on the exposure data set was important to deciding which method was more applicable to this project, which was determined to be FA.

Lastly, clustering was performed on the decomposed data set using a Hierarchical Density Based clustering of Applications with Noise (HDBSCAN) algorithm. This specific algorithm was developed by Campello, Moulavi, Sander and McInnes, expanding on previous density-based clustering techniques to enable the clustering algorithm to determine clusters of varying densities. HDBSCAN achieves this by taking the data points within a data space and ranking them based on their density, before removing unstable clusters which have a low life-span and density within the ranking, effectively ruling them as 'noise' (McInnes et al., 2016). This clustering allows for Semantic Segmentation of the mineral to occur via the production of these 'clusters'.

'Clusters' and their corresponding data can then be exported and later characterised using the Bruker ESPRIT spectrum and ESPRIT Quant tools, which produces reports of each individual cluster detailing the respective weight percentages of present elements by evaluating the clusters respective spectra. These results can then be used to identify the minerals of each cluster by correlating elemental weight percentages and mineral chemical formula, and subsequently produce accurate mineral maps. This is achieved by utilizing Stoichiometry calculation methods outlined in 'An introduction to the Rock-Forming Minerals' (Deer et al., 2013).

CHAPTER 4: EXPOSURE DATA SET: CALIBRATION & TRAINING

4.1 Results

The exposure data set contains 9 different files all of which taken at different parameters which lead to different degrees of exposure (Table 4.1.1). Of the 9 tests, 6 where chosen for further analysis to demonstrate the affects exposure has on data. Selection of which tests to analyse was primarily based on the average counts per pixel, with the 6 tests chosen occupying a range of average counts from 70.36 (2.d.p) to 3354.47 (2.d.p).

Table 4.1.1: Table showing the average counts of the 9 different data sets and highlighting the sets which have been chooses for further processing and analysis.

Raw data title	Data chosen for analysis	Experiment title	Average counts (2.d.p)
test_1.rpl	x	1	70.36
test_2.rpl		NA	632.08
test_3.rpl	x	3	838.81
test_4.rpl		NA	420.17
test_5.rpl	x	2	185.33
test_6.rpl	x	5	1669.72
test_7.rpl		NA	2230.41
test_8.rpl	x	4	1122.17
test_9.rpl	x	6	3354.47

As shown on table 4.1.1 above, the 6 data sets chosen for analysis and comparison are reasonably evenly spaced in regards to the average number of counts in order to provide an effective comparison to which at what point additional counts become fairly redundant at improving the quality of data.

As discussed in the methodology chapter, EDS data was processed by the following sequence; (i) data exportation, (ii) data calibration, (iii) data decomposition, and (iv) clustering. Raw data was exported using Oxford Instruments in the form of .raw and .rpl files. These files where then calibrated within Jupyter lab using hyperspy.

Table 4.1.2: Table showing acquisition settings of each chosen set of the exposure data set.

Experiment	Raw data title	Average counts (2.d.p)	Process time (1-6)	Dwell time (us)	Dose per pixel	Live mins (2.d.p)	FA	Number of Clusters
1	test_1	70.35	3	200	1000	3.28	5	5
2	test_5	185.33	3	200	1000	3.28	5	7
3	test_3	838.81	3	800	1200	157.28	5	10
4	test_8	1122.17	5	100	6000	78.65	6	11
5	test_6	1669.72	5	600	9000	29.48	6	8
6	test_9	3354.47	3	600	18000	235.93	6	14

Post calibration three separate stages of data decomposition occur. The first being noise reduction and decomposition by Poisson noise scaling. The results of this process and its effects on noise can be seen in figure 4.1.1.

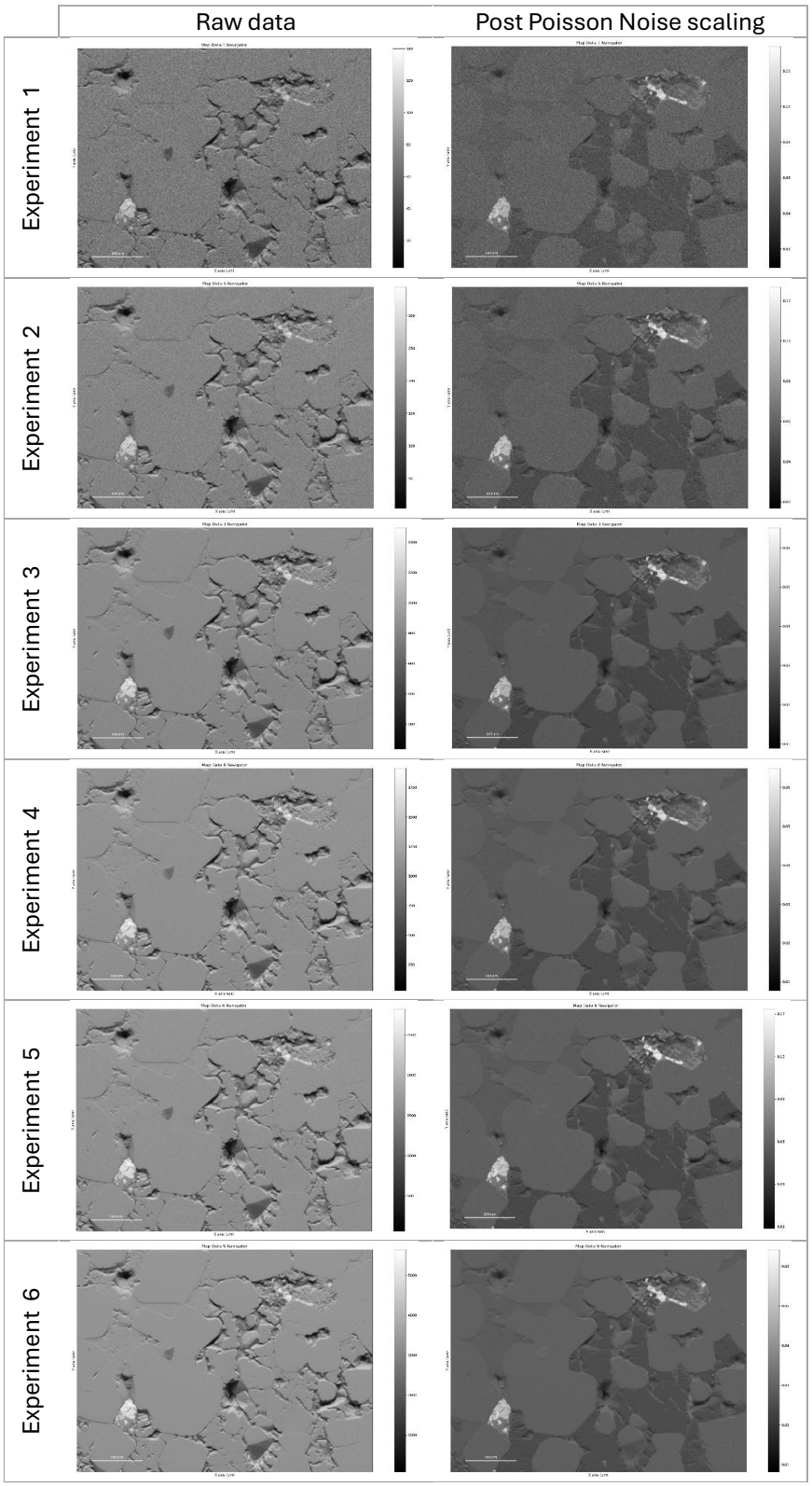

Figure 4.1.1: Comparison of the quality of each data set (with the average counts increasing along the ordinate axis) pre and post decomposition by Poisson noise scaling.

Poisson noise scaling is seen to be effective on all of the data sets regardless of counts, with image quality increasing alongside an increasing average number of counts. Noise decreases most significantly between experiment 2 and 3, whereas overall image quality, such as image definition, sharpness, depth etc., increases most significantly between experiment 3 to 4, and 4 to 5. There is an increase in image quality between image quality between experiment 5 and 6, however, not of a proportion comparable to that of the jump between 3 to 4, and 4 to 5.

The second and third stage of data decomposition involves Factor Analysis (FA). Initially FA is ran on an over-estimated number of factors, in this project this is 20 factors, in order to heuristically determine the optimal amount using scree plots, factor heat maps, and scores/loading plots. Once the optimal amount of factors has been determined, FA can then be performed using this optimal number as the third and final stage of data decomposition.

The decomposition scree plots of each of the 6 tests chosen for further analysis within the exposure data set have been combined into one scree plot (Figure 4.1.2). Decomposition scree plots visualise the variation within the data set by plotting the percentage of explained variance (y-axis) against the number of factors (x-axis). Seen here, the relationship between the degree of exposure during data collection and the number of significant factors is positive, by which as the average counts of a data set increase, as does the number of optimal factors. Observed below, explained variance for all experiments is nearly identical up until factor 5. Low count experiments 1 and 2 are seen to plateau significantly earlier than experiments 3, 4, 5, and 6. Explained variance in these latter experiments remain close, separating slightly post factor 6, then again at factor 11. The most significant difference in explained variance per factor occurs between experiment 2 and experiment 3.

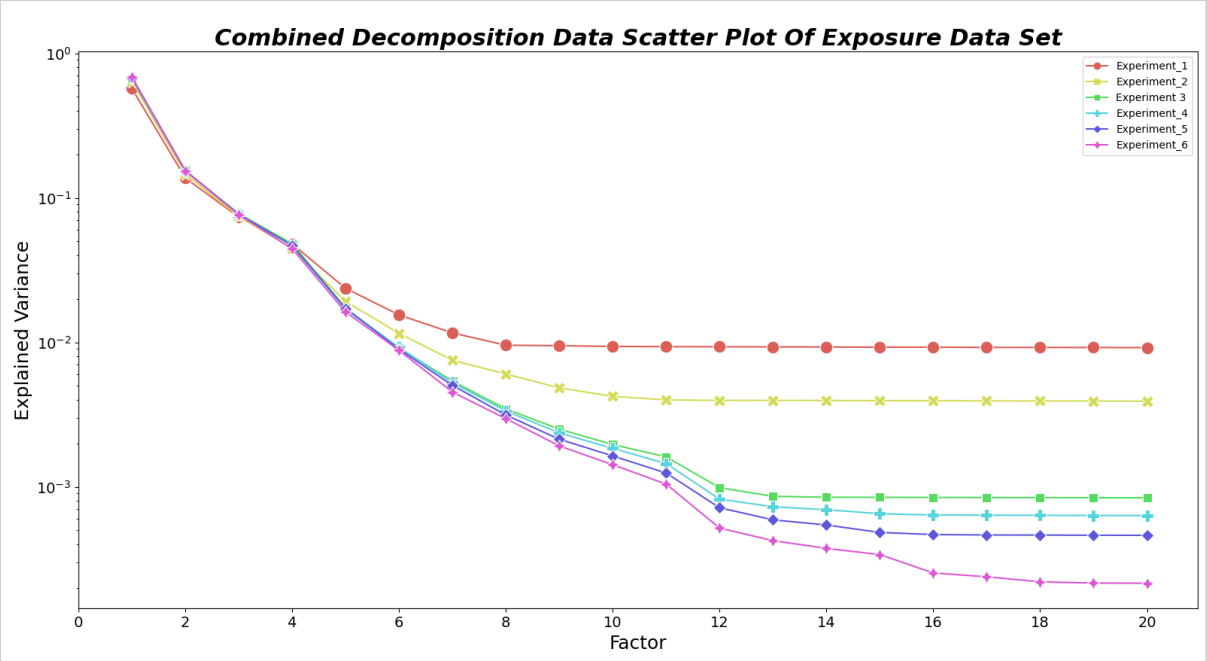

Figure 4.1.2: Figure combining decomposition scatter plots of the 6 different experiments chosen from the exposure data set. Decomposition scatter plots were combined in python using matplotlib and seaborn. Data is plotted on a logarithmic scale.

This relationship can be further demonstrated by the evaluation of the heat maps of each factor of each respective data set which have been combined into one figure (Figure 4.1.3) for ease of comparison. Within this figure three major and one minor jump in quality of the data produced by FA within the first 14 components can be observed (in regards to noise present and definition). The first jump is observed between experiment 1 and experiment 2 as the noise within the first 10 factors is reduced, particularly within the initial 6 factors. The next jump is seen between experiment 2 and experiment 3 as there is a significant reduction of noise within the first 11 factors, as well as an increase in definition and quality of the heat maps produced. The third jump in quality is observed between experiment 3 and experiment 4 as there is a notable increase in definition and quality within the first 11 factors, as a significant reduction in noise across factors 12-14. The last jump is observed between experiment 4 and experiment 6, though this jump is negligible, with noise reduction and definition increase within the last three data sets being less intense than the three jumps observed prior.

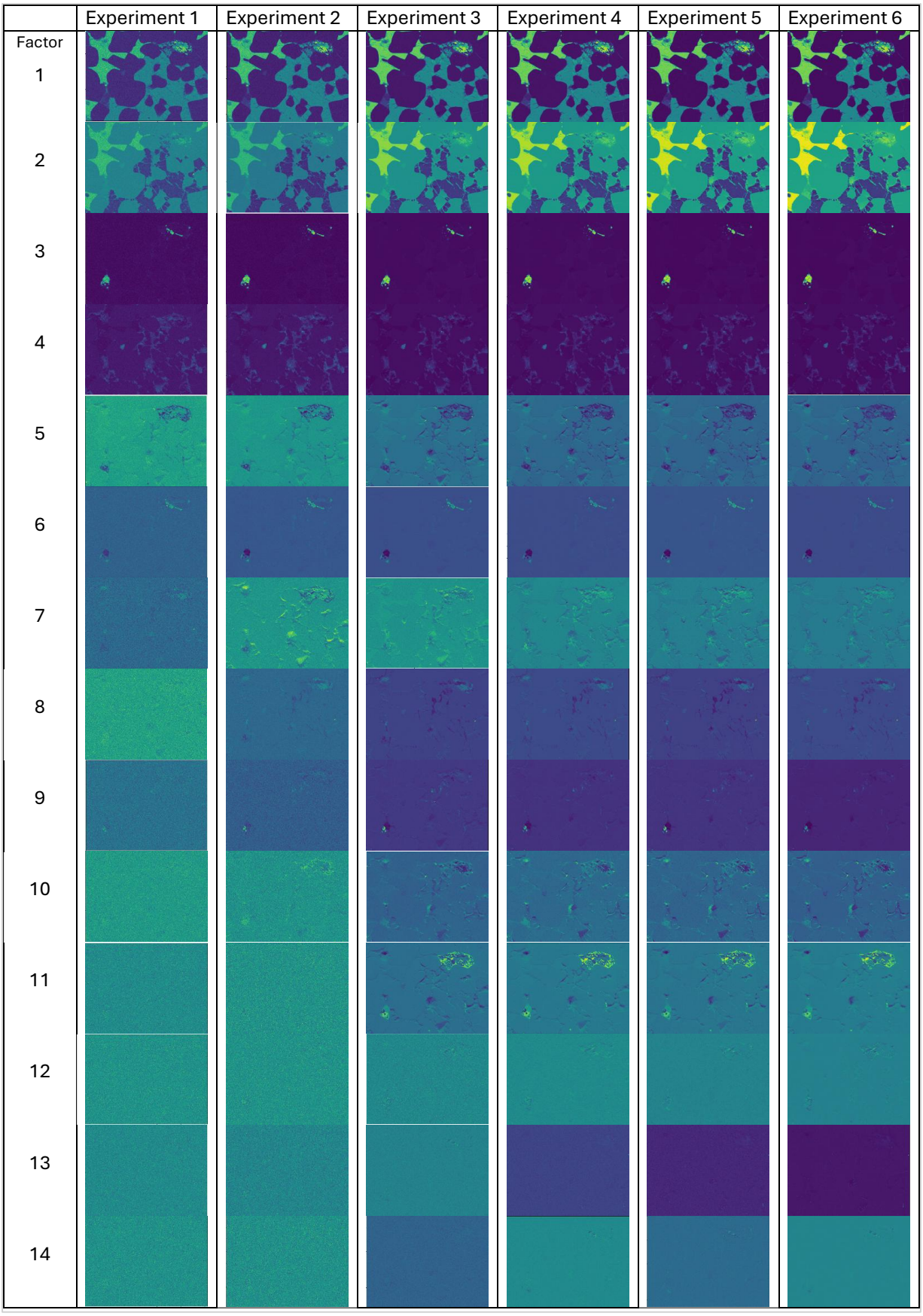

Figure 4.1.3: Comparison of heat maps of each factor of each respective data set chosen for analysis from the exposure data set.

Using the decomposition scree plots and heat maps produced from the previous stage, the optimal number of factors in which the variance within the data set is effectively explained can be determined. The final step of the machine learning analysis process is clustering using HDBSCAN, performed on the each data set which was previously reduced to the optimal number of factors (Table 4.1.3).

Table 4.1.3: Table of the optimal number of factors for each data set as well as the number of clusters produced from HDBSCAN on each respective data set.

Experiment	Raw data title	Average counts	Optimal number of Factors	Number of Clusters produced
1	test_1	70.358144	5	5
2	test_5	185.334305	5	7
3	test_3	838.810404	5	10
4	test_8	1122.173768	6	11
5	test_6	1669.72493	6	8
6	test_9	3354.47169	6	14

Generally speaking, the relationship between average number of counts and the number of clusters produced using HDBSCAN is positive. The only experiment that does not follow this trend is experiment 5.

Segmentation of each of these data sets can be seen in the cluster images below (Figure 4.1.4 & 4.1.5). Observed here is the positive relationship between average counts, and segmentation within the mineral, particularly well displayed by segmentation within the sulphide mineral in the top left. Jumps observed in segmentation mirror that of jumps observed in the optimal number of factors, The first jump in segmentation occurs between experiment 1 and experiment 2, paired with an intense decrease in noise and increase in image quality. This jump is followed by experiment 2 to experiment 3, in which segmentation, noise reduction, and image quality increases more significantly than prior. Segmentation observed within the latter 3 experiments is highly similar, particularly between experiment 4 and experiment 6.

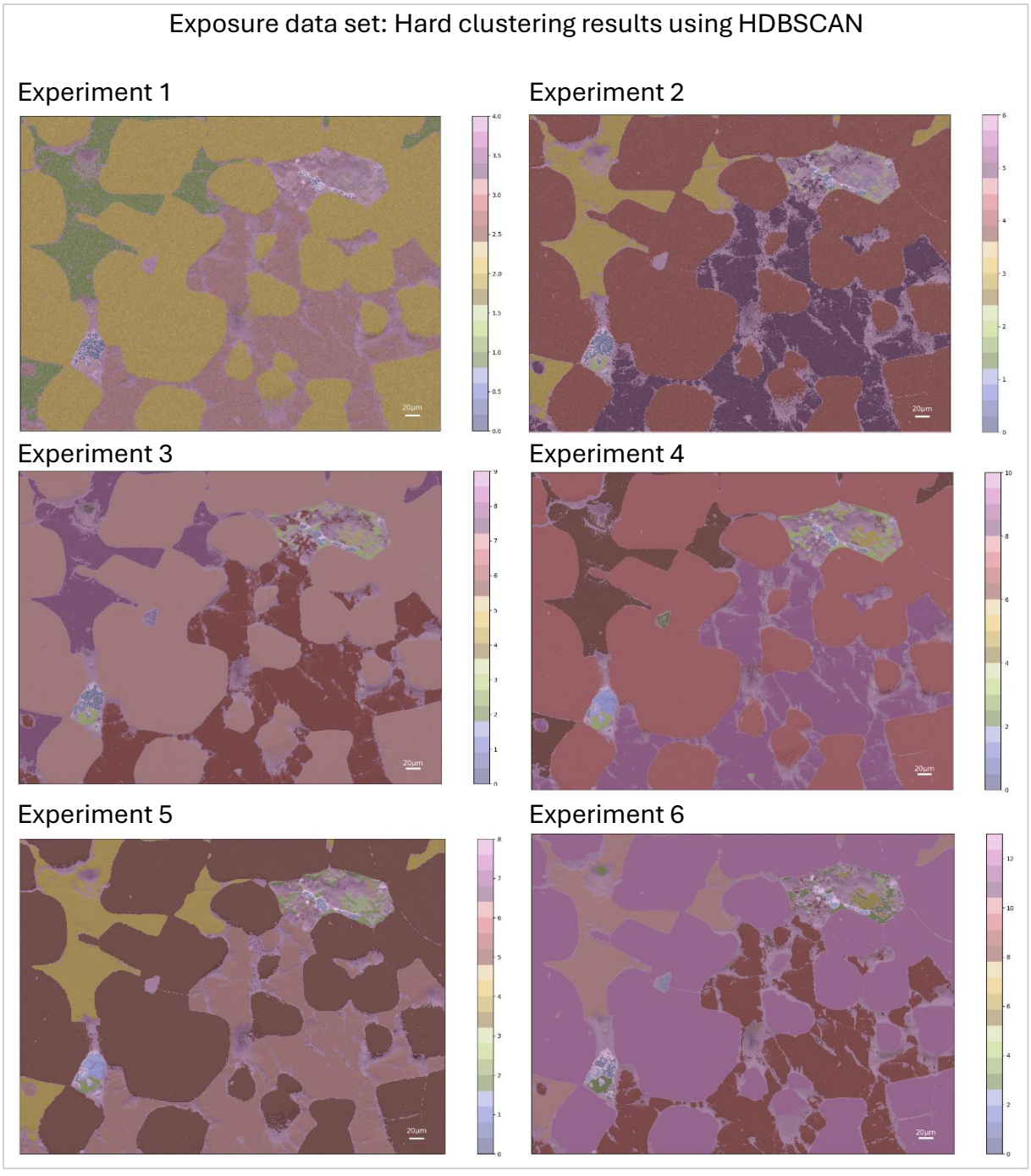

Figure 4.1.4: Figure showing the hard clustering results on the chosen experiments from the exposure data set. Clustering was performed using HDBSCAN. The decomposition settings (number of optimal factors) and the number of clusters produced for each experiment can be seen in table 4.1.2.

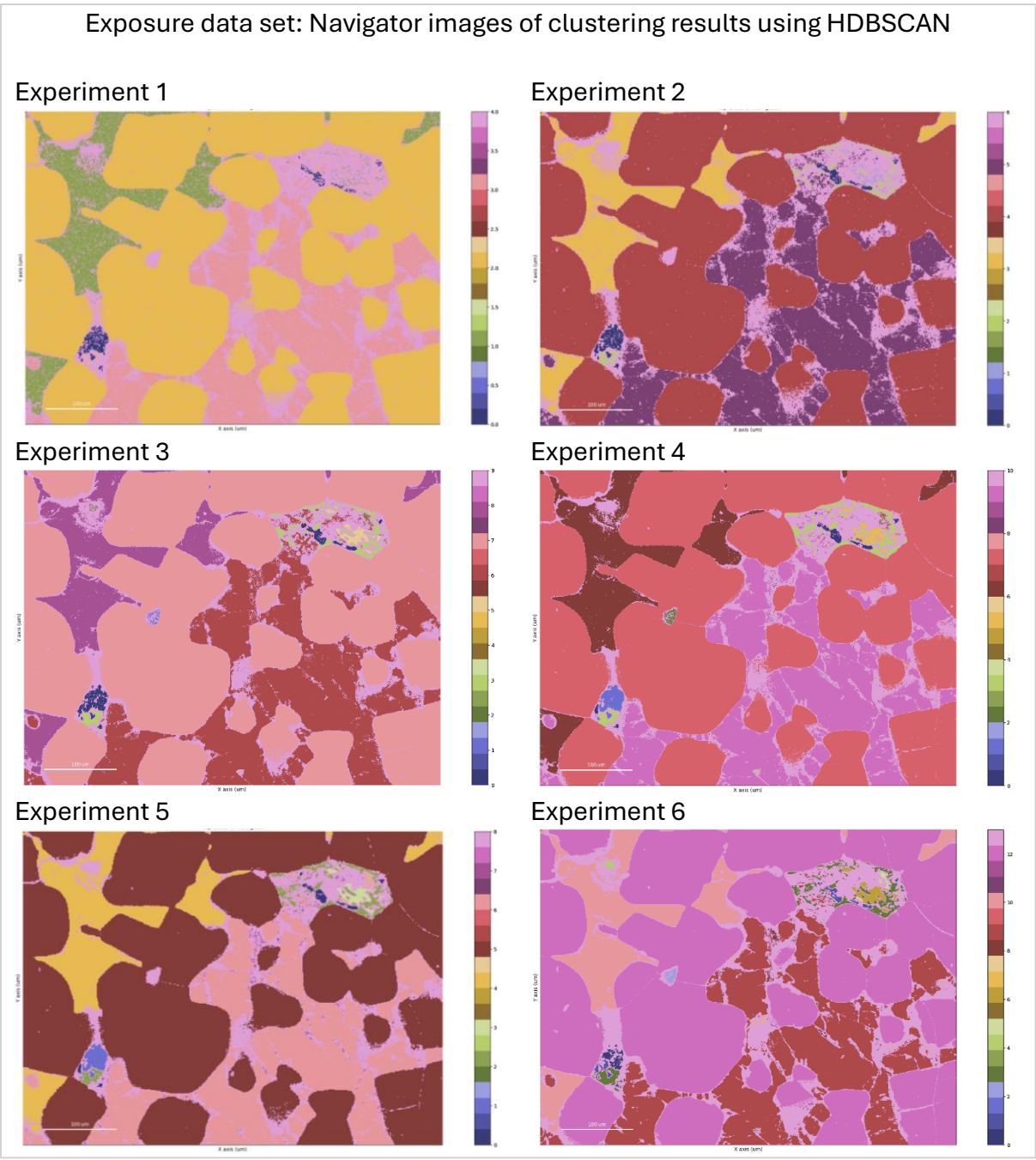

Figure 4.1.5: Figure showing the navigator images of the clustering results on the chosen experiments from the exposure data set. Clustering was performed using HDBSCAN The decomposition settings (number of optimal factors) and the number of clusters produced for each experiment can be seen in table 4.1.2.

Bruker analysis of the clusters produced from the first three experimental data sets, each containing <1000 average counts per pixel, effectively displays the intense increase in data quality produced by increasing the average counts per pixel.

Experiment 1 pulls out the bare basics of the mineralogical boundaries in the area of interest, producing 4 mineralogical clusters. Very little segmentation of the sulphide mineral in the top left corner can be seen (Figure 4.1.6, Table 4.1.4). Experiment 2 builds upon this base, producing 2 more mineralogical clusters which are able to pull out some more minor segmentation (Figure 4.1.7, Table 4.1.9). The largest jump is seen between experiment 2 and 3. In experiment 3, the sulphide mineral is far better segmented containing 4 different mineral clusters, all producing appropriate mineral formulae, and providing a more detailed understanding of the sulphide mineral (Figure 4.1.8, Table 4.1.6).

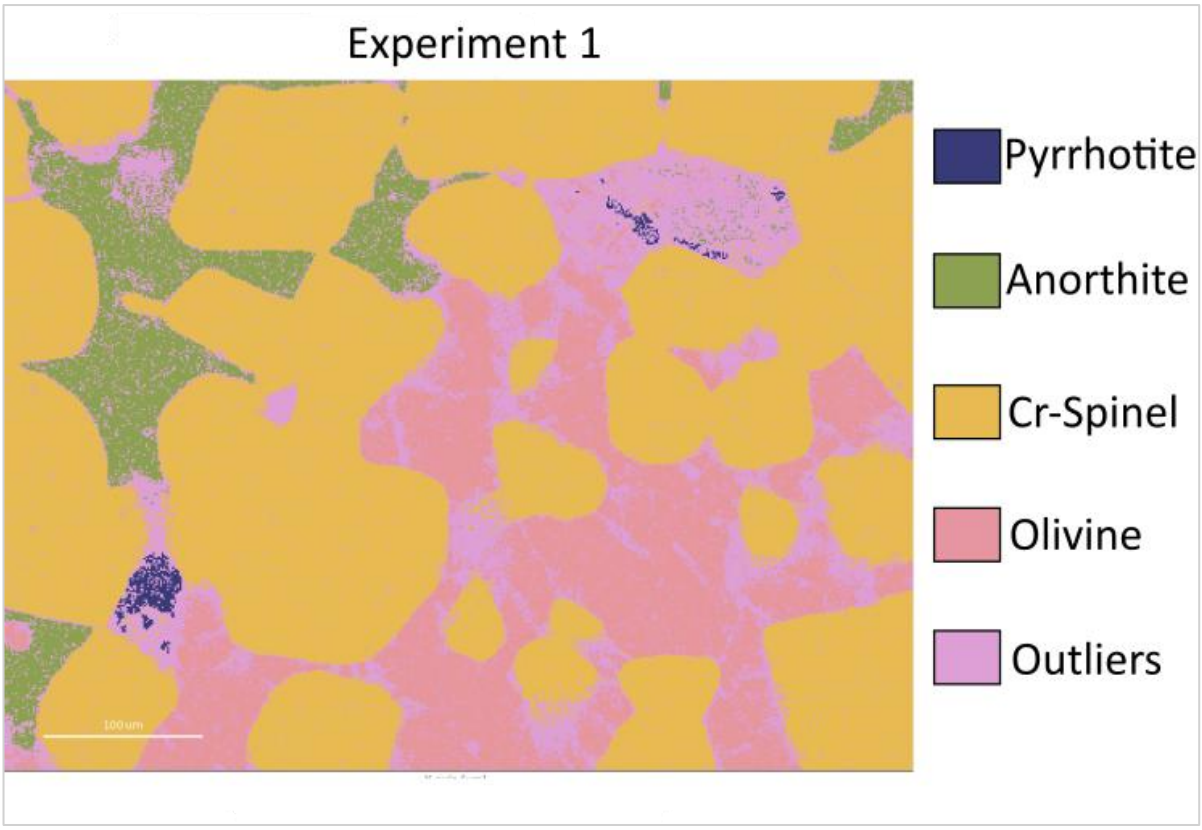

Figure 4.1.6: Figure of HDBSCAN clustering of experiment 1. Clusters and their respective mineralogy calculated using Bruker analysis.

Table 4.1.4: Calculated mineralogy of the clusters of experiment 1

Experiment 1		
	Mineralogy	Calculated formula
Cluster 1	Pyrrhotite	$Fe_{0.85}\ S_{0.95}$
Cluster 2	Anorthite	$(Na_{0.08}, Ca_{0.92})\ \Sigma 1.0\ Si_{1.95}\ Al_{1.99}\ O_8$
Cluster 3	Cr-spinel	$(Mg_{0.54}, Fe^{2+}_{0.21}, Ti^{4+}_{0.02})(Al_{1.06}, Cr_{0.57}, Fe^{3+}_{0.49}, Fe^{2+}_{0.04})O_4$
Cluster 4	Olivine	$(Mg_{1.88}, Fe_{0.24})\Sigma 2.12\ Si_{0.89}\ O_4$
Cluster 5	Outliers	/

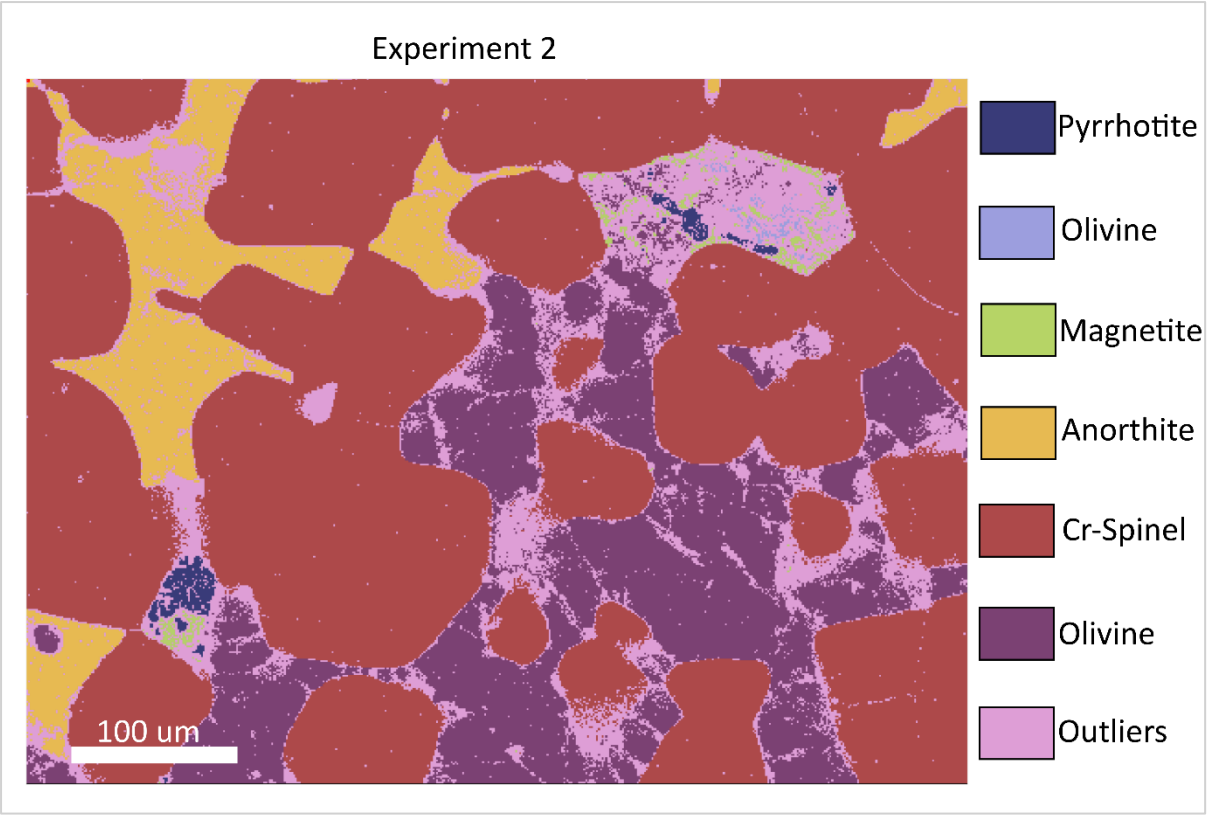

Figure 4.1.7: Figure of HDBSCAN clustering of experiment 2. Clusters and their respective mineralogy calculated using Bruker analysis.

Table 4.1.5: Calculated mineralogy of the clusters of experiment 2

Experiment 2		
	Mineralogy	Calculated formula
Cluster 1	Pyrrhotite	$Fe_{0.94}\ S_{0.81}$
Cluster 2	Olivine	$(Mg_{0.43}, Fe_{0.10}, Ca_{1.63})\ \Sigma 2.16\ Si_{0.82}\ O_4$
Cluster 3	Magnetite	$Fe^{2+}_{0.82}\ Fe^{3+}_{1.64}\ O_4$
Cluster 4	Anorthite	$Ca_{1.02}\ (Al_{1.98}, Si_{1.94}, O_8)$
Cluster 5	Cr-spinel	$(Mg_{0.55}, Fe^{2+}_{0.19}, Ti^{4+}_{0.02})(Al_{1.07}, Cr_{0.58}\ Fe^{3+}_{0.46})O_4$
Cluster 6	Olivine	$(Mg_{1.90}, Fe_{0.26})\Sigma 2.16\ Si_{0.87}\ O_4$
Cluster 7	Outliers	/

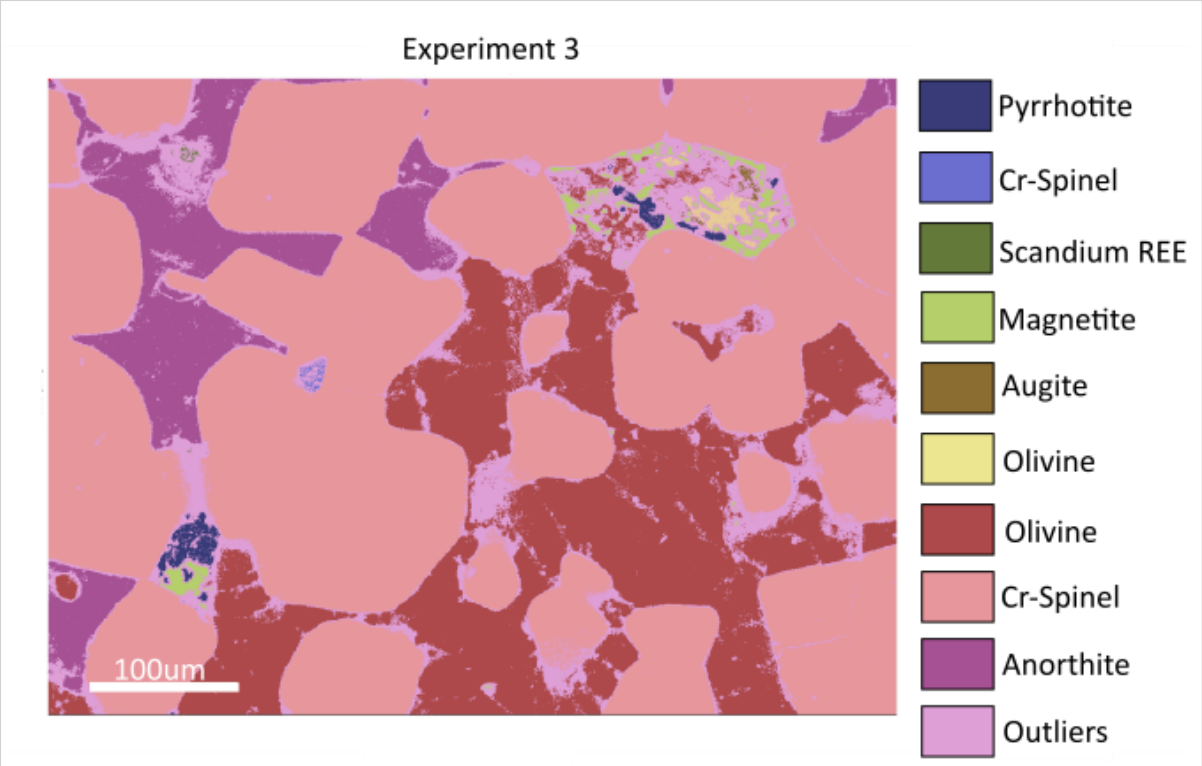

Figure 4.1.8: Figure of HDBSCAN clustering of experiment 3. Clusters and their respective mineralogy calculated using Bruker analysis.

Table 4.1.6: Calculated mineralogy of the clusters of experiment 3

Experiment 3		
	Mineralogy	Calculated formula
Cluster 1	Pyrrhotite	$Fe_{0.76}\ S_{0.95}$
Cluster 2	Cr-spinel	$(Fe_{0.68},Mg_{0.54})\ \Sigma 1.22(Cr_{0.55},\ Al_{1.16})\ \Sigma 1.71\ O_4$
Cluster 3	Scandium REE*	Likely incorrect reading
Cluster 4	Magnetite	$Fe^{2+}_{0.83}\ Fe^{3+}_{1.66}\ O_4$
Cluster 5	Augite	$(Ca_{0.60},\ Mg_{1.04},\ Fe_{0.26},\ Ti_{0.04})\ \Sigma 1.94\ (Si_{1.50},\ Al_{0.62})\ \Sigma 2.12\ O_6$
Cluster 6	Olivine	$(Mg_{0.44},\ Fe_{0.10,}\ Ca_{1.60})\Sigma 2.14\ Si_{0.83}\ O_4$
Cluster 7	Olivine	$(Mg_{1.86},\ Fe_{0.26})\Sigma 2.12\ Si_{0.92}\ O_4$
Cluster 8	Cr-spinel	$(Mg_{0.32},\ Fe^{2+}_{1.78},\ Ti^{4+}_{0.01})(Al_{1.06},\ Cr_{0.57}\ Fe^{3+}_{0.49,}\ Fe^{2+}_{0.04})O_4$
Cluster 9	Anorthite	$Ca_{1.0}\ (Al_{2.00},\ Si_{1.94},\ O_8)$
Cluster 10	Outliers	/

Brucker analysis of the clusters produced from the later three experiments <1000 average counts per pixel display how the segmentation above this number of average counts is effective at pulling out both the base mineralogy and more minor features within the chosen area (Figures 4.1.9,4.1.10,4.1.11).

The more basic mineralogy of larger mineral areas such as Cr-spinel, anorthite, and olivine remains the same as the previous three experiments. Increasing data counts does however allow for differentiation of additional smaller variations in this base, such as an Enstatite-Ferrosilite series, reflected in all three of the <1000 counts per pixel experiments, as well as segmentation of more than one Cr-spinel cluster in experiments 4 and 6. Demonstrating the advantage of achieving data packs of <1000 counts per pixel.

Additionally, experiments over 1000 average counts per pixel are able to segment the different sulphide phases within the sulphide mineral. In the earlier experiments 1-3, the sulphide mineral was only categorised as pyrrhotite, whereas in the latter three exposure sets the sulphide mineral is segmented into pyrrhotite and chalcopyrite.

In all three latter experiments the mineral in the top left is divided into 5 clusters, with mirroring mineralogy, despite the fact that experiment 6 is double the average counts of experiment 4 (Figure 4.1.9, 4.1.11, Table 4.1.7, 4.1.9,). Indicating that increase in mineral segmentation and data quality is not exponential and eventually plateaus.

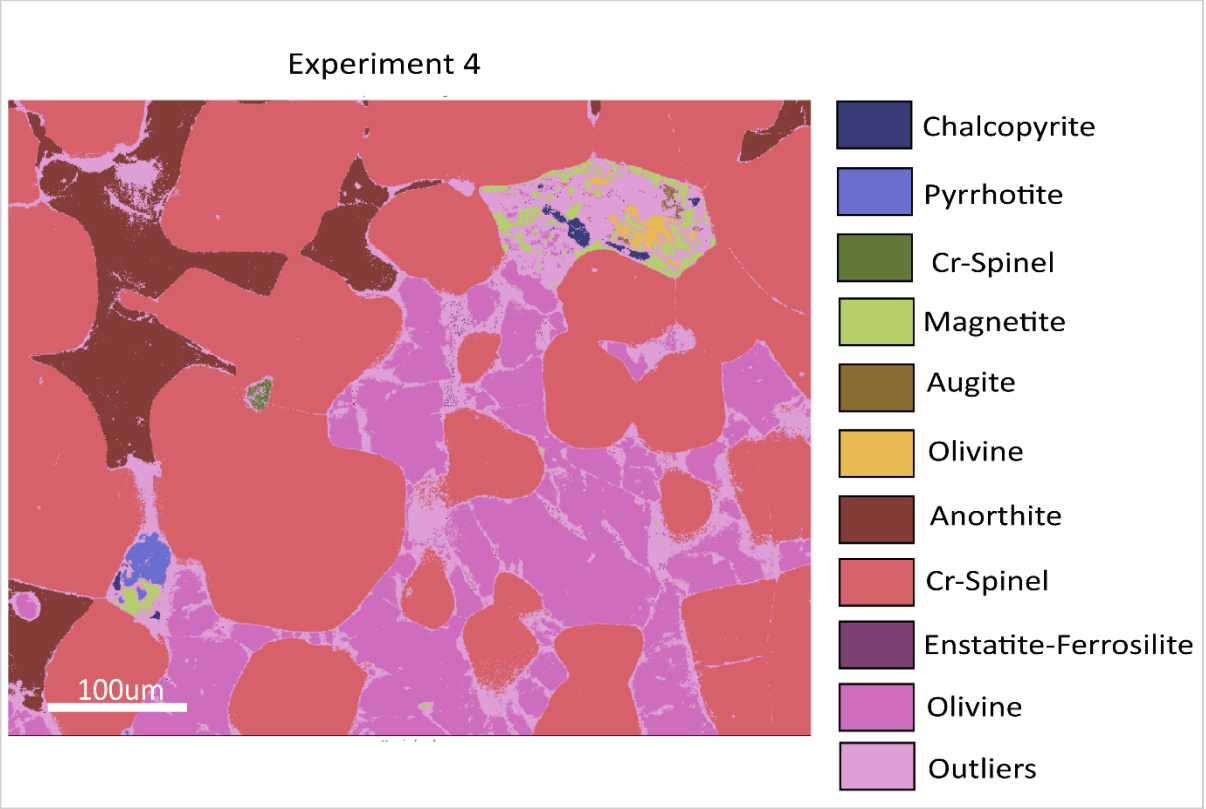

Figure 4.1.9: Figure of HDBSCAN clustering of experiment 4. Clusters and their respective mineralogy calculated using Bruker analysis.

Table 4.1.7: Calculated mineralogy of the clusters of experiment 2

Experiment 4		
	Mineralogy	Calculated formula
Cluster 1	Chalcopyrite	$Cu_{0.74}\,Fe_{0.67}\,S_{1.72}$
Cluster 2	Pyrrhotite	$Fe_{1.02}\,S_{0.96}$
Cluster 3	Cr-spinel	$(Fe_{0.70},Mg_{0.54})_{\Sigma 1.24}(Cr_{0.58}, Al_{1.13})_{\Sigma 1.71}\,O_4$
Cluster 4	Magnetite	$Fe^{2+}_{0.82}\,Fe^{3+}_{1.64}\,O_4$
Cluster 5	Augite	$(Ca_{0.58}, Mg_{1.03}, Fe_{0.24}, Ti_{0.03})_{\Sigma 1.88}\,(Si_{1.43}, Al_{0.62})_{\Sigma 2.05}\,O_6$
Cluster 6	Olivine	$(Mg_{0.44}, Fe_{0.10,}\,Ca_{1.61})_{\Sigma 2.15}\,Si_{0.83}\,O_4$
Cluster 7	Anorthite	$Ca_{1.0}\,(Al_{2.00}, Si_{1.94}, O_8)$
Cluster 8	Cr-spinel	$(Mg_{0.52}, Fe^{2+}_{0.32}, Ti^{4+}_{0.01})(Al_{1.02}, Cr_{0.57}\,Fe^{3+}_{0.47,}\,Fe^{2+}_{0.03})O_4$
Cluster 9	Enstatite-Ferrosilite	$(Mg_{0.61}, Fe_{0.24})_{\Sigma 0.85}\,Si_{0.96}\,O_4$
Cluster 10	Olivine	$(Mg_{1.99}, Fe_{0.25})_{\Sigma 2.24}\,Si_{0.88}\,O_4$
Cluster 11	Outliers	/

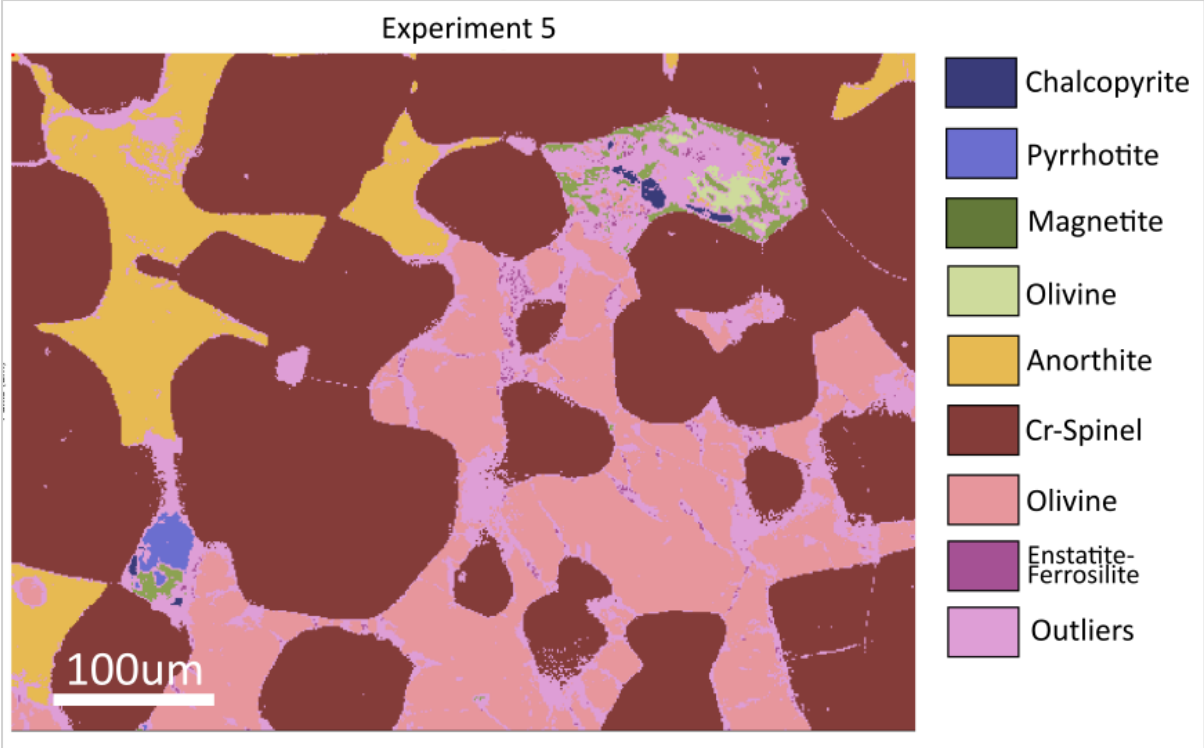

Figure 4.1.10: Figure of HDBSCAN clustering of experiment 5. Clusters and their respective mineralogy calculated using Bruker analysis.

Table 4.1.8: Calculated mineralogy of the clusters of experiment 5

Experiment 5		
	Mineralogy	Calculated formula
Cluster 1	Chalcopyrite	$Cu_{0.59}\,Fe_{0.57}\,S_{0.95}$
Cluster 2	Pyrrhotite	$Fe_{1.13}\,S_{0.92}$
Cluster 3	Magnetite	$Fe^{2+}_{0.81}\,Fe^{3+}_{1.62}\,O_4$
Cluster 4	Olivine	$(Mg_{0.41}, Fe_{0.10}, Ca_{1.71})_{\Sigma 2.22}\,Si_{0.80}\,O_4$
Cluster 5	Anorthite	$Ca_{0.64}\,(Al_{2.74}, Si_{1.62}, O_8)$
Cluster 6	Cr-spinel	$(Mg_{0.51}, Fe^{2+}_{0.32}, Ti^{4+}_{0.02})(Al_{1.02}, Cr_{0.57}\,Fe^{3+}_{0.49}, Fe^{2+}_{0.04})O_4$
Cluster 7	Olivine	$(Mg_{1.96}, Fe_{0.27})_{\Sigma 2.23}\,Si_{0.89}\,O_4$
Cluster 8	Enstatite-Ferrosilite	$(Mg_{0.61}, Fe_{0.24})_{\Sigma 0.85}\,Si_{0.96}\,O_4$
Cluster 9	Outliers	/

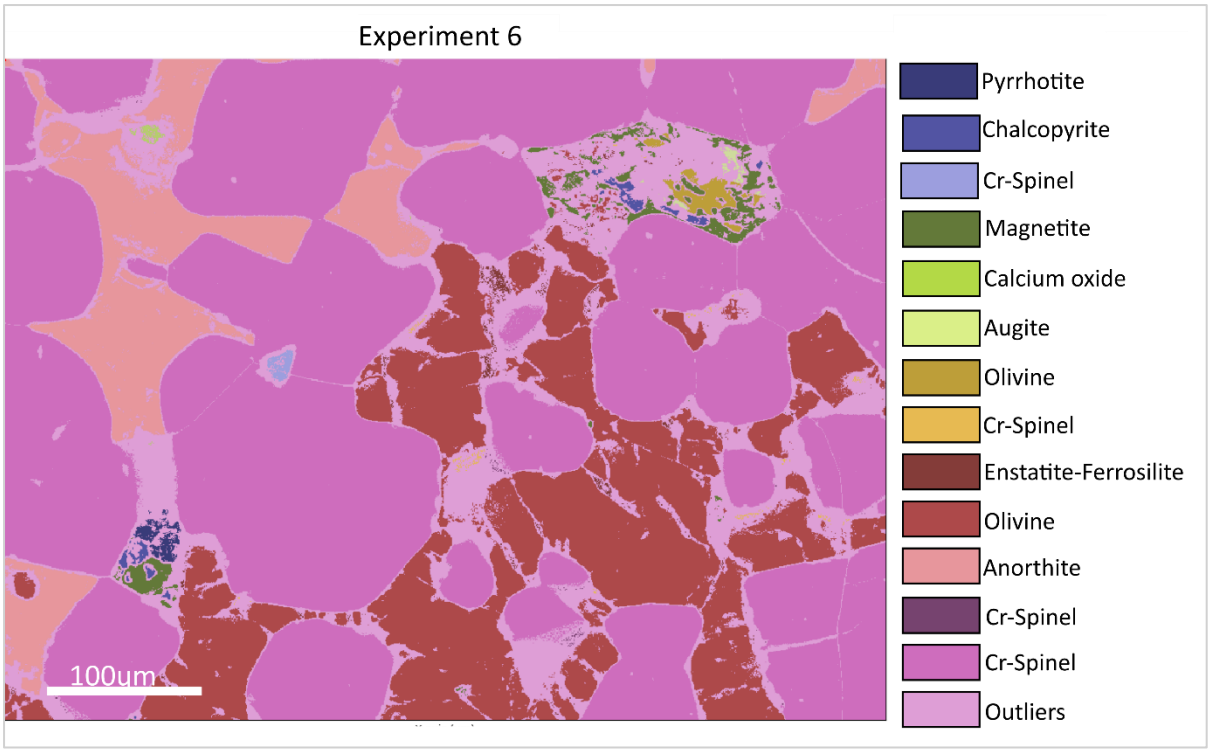

Figure 4.1.11: Figure of HDBSCAN clustering of experiment 6. Clusters and their respective mineralogy calculated using Bruker analysis.

Table 4.1.9: Calculated mineralogy of the clusters of experiment 6

Experiment 6		
	Mineralogy	Calculated formula
Cluster 1	Pyrrhotite	$Fe_{1.13}\ S_{0.96}$
Cluster 2	Chalcopyrite	$Cu_{0.91}\ Fe_{1.24}\ S_{2.00}$
Cluster 3	Cr-spinel	$(Fe_{0.73},Mg_{0.51})_{\Sigma 1.29}(Cr_{0.59}, Al_{1.20})_{\Sigma 1.79}\ O_4$
Cluster 4	Magnetite	$Fe^{2+}_{0.85}\ Fe^{3+}_{1.70}\ O_4$
Cluster 5	Calcium oxide	/
Cluster 6	Augite	$(Mg_{1.01}, Fe_{0.22}, Ca_{1.20})_{\Sigma 2.43}\ (Si_{1.33}, Al_{0.60})_{\Sigma 21.93}\ O_6$
Cluster 7	Olivine	$(Mg_{0.44}, Fe_{0.90,}\ Ca_{1.60})_{\Sigma 2.13}\ Si_{0.83}\ O_4$
Cluster 8	Cr-spinel	$(Mg_{0.46}, Fe^{2+}_{0.34}, Ti^{4+}_{0.03})(Al_{1.23}, Cr_{0.57}\ Fe^{3+}_{0.79,}\ Fe^{2+}_{0.06})O_4$
Cluster 9	Enstatite-Ferrosilite	$(Mg_{0.53}, Fe_{0.31})_{\Sigma 0.84}\ Si_{0.97}\ O_4$
Cluster 10	Olivine	$(Mg_{1.97}, Fe_{0.25})_{\Sigma 2.22}\ Si_{0.89}\ O_4$
Cluster 11	Anorthite	$Ca_{1.02}\ (Al_{1.98}, Si_{1.95}, O_8)$
Cluster 12	Cr-spinel	$(Mg_{0.47}, Fe^{2+}_{0.23}, Ti^{4+}_{0.02})(Al_{0.95}, Cr_{0.63}\ Fe^{3+}_{0.53,}\ Fe^{2+}_{0.04})O_4$
Cluster 13	Cr-spinel	$(Mg_{0.65}, Fe^{2+}_{0.22}, Ti^{4+}_{0.01})(Al_{0.82}, Cr_{0.40}\ Fe^{3+}_{0.48,}\ Fe^{2+}_{0.02})O_4$
Cluster 14	Outliers	/

To summarise, there is a positive correlation between average number of counts per pixel and image quality, optimal numbers of factor produced, and mineral segmentation produced by clustering. The major observable jumps in quality are consistently observed between experiment 2 and 3, 3 and 4, with a more minor increase noted between 4 and 6. It can therefore be noted that increasing the number of average counts per pixel will increase data image and ML result quality, but that this increase is not exponential and eventually plateaus.

CHAPTER 5: MINERALOGICAL DATA SET; FIELDWORK OBSERVATIONS, SEM, MACHINE LEARNING AND TEM RESULTS

5.1 Fieldwork observations

As discussed in the methods chapter, excursions taken during fieldwork were loosely based off routes from "A geological excursion guide to Rum: the Palaeocene igneous rocks of the Isle of Rum, Inner Hebrides" (Emeleus & Troll, 2008). Three separate excursions were undertaken on this trip, enabling observations of units across the suite to be made, and providing context to understanding the geological history of the intrusion itself. However, of these excursions, the last excursion is the most relevant to this project and detailed below.

5.1.1 17/05/2024

Fieldwork here was influenced by "Excursion 3: Hallival and Askival". This excursion involved observations regarding the Eastern Layered Intrusion, the unit in which the thin section sample worked from in this project is derived from (Figure 5.1.1). Observations regarding layering, different units, chromite seams, and geospatial relationships to other lithologies within the area are all relevant to the project.

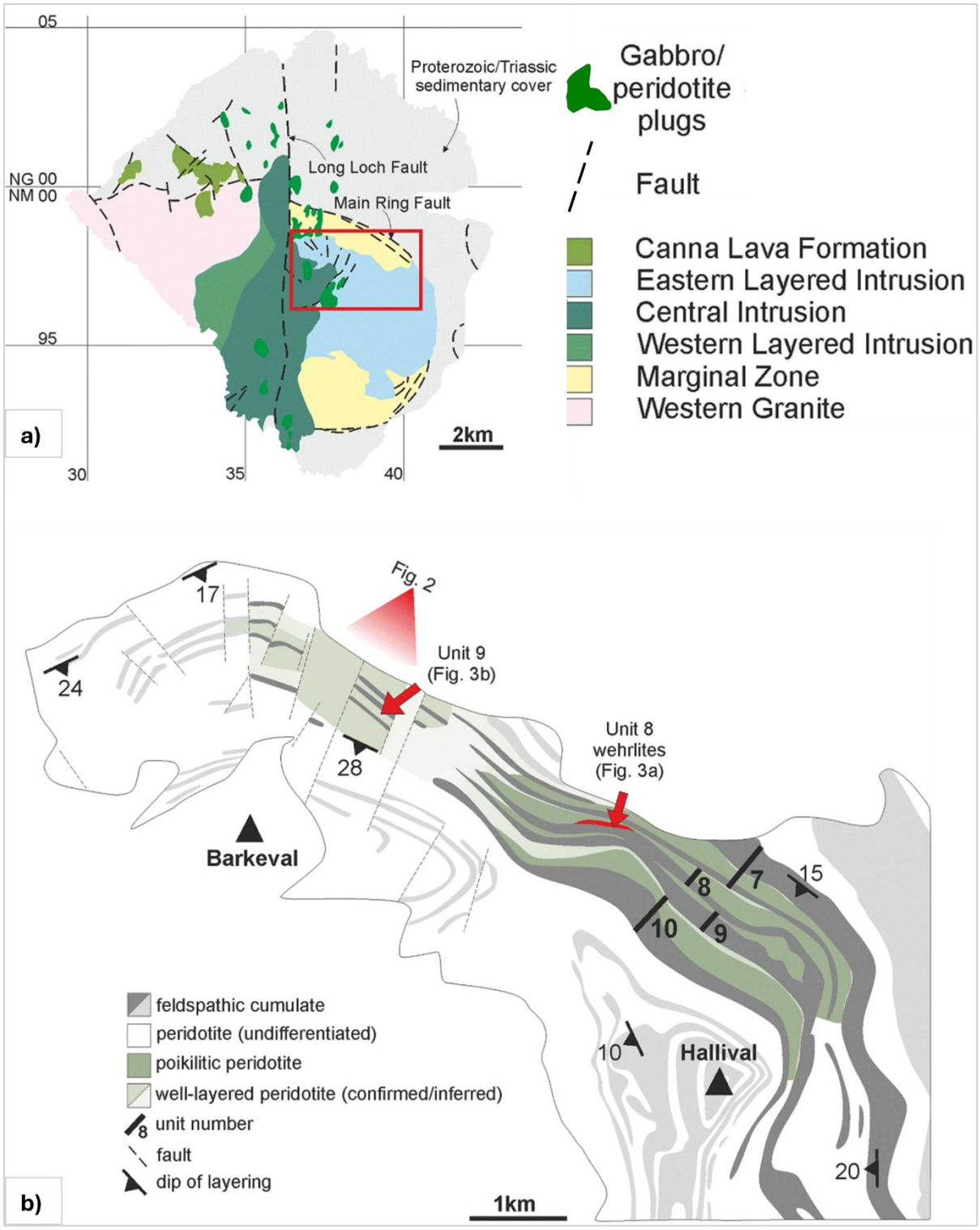

Figure 5.1.1: a) Simplified geological map of the Isle of Rum, b) Geological map of the ELI with simplified geological map of the different units. Altered from Hepworth et al., 2020.

This excursion began by transversing to Coire Dubh, before moving south/south-eastwards across the Coire Dubh breccia. Whist heading toward the eastern layered intrusion, interpretations regarding the lithologies bordering the ELI can be made by observing the topography of the area.

The ELI is bordered on the eastern side by a coarse grained marginal gabbro, which transitions into an intrusion breccia of micro granodiorite containing chunks and blocks of course grained gabbro (Figure 5.1.2). Baked margins can allegedly be observed within chunks of the Coire Dubh Breccia, however these proved difficult to locate.

Figure 5.1.2: Annotated photograph of the Eastern Layered Intrusion and the bordering units to the east.

Within the ELI there are three rock units to be aware of; troctolite (almost entirely plagioclase and olivine), peridotite (olivine rich, ultramafic), and anorthosite (predominantly plagioclase feldspar). Prior studies of the Rum layered intrusion classify troctolite (commonly referred to as 'allivalite') to contain 50-80% cumulus plagioclase, 20-50% cumulus olivine, >5% inter-cumulus clinopyroxene and >1% Cr-spinel (Holness and Winpenny, 2008). Peridotite mineralogy is defined by olivine dominance, varying from 50-80% in Rum's plug deposits, and 60-70% within the layered suite deposits (Hepworth et al., 2017; Hepworth et al., 2020; Holness et al., 2012). The olivine crystals of the layered units are typically coarse, with skeletal olivine harrisitic grains being common (Hepworth et al., 2020). Inter-cumulus peridotite phases are composed of plagioclase (10-25%), clinopyroxene (>10%), and Cr-spinel (1-1.3%) (Hepworth et al., 2017; Hepworth et al., 2020). Lastly, anorthosite can be classified as containing 90-100% plagioclase feldspar, with the minor occurrence of mafic minerals between 0-10% (BGS, 2025; Mindat.org, 2025).

The spatial relationship between the three across the unit boundaries of the ELI can become quite complex, making differentiation difficult. Foliage cover and weathering also contribute to these difficulties. Distinguishing these rock groups relies on textural observations corresponding to their known mineralogy. Generally speaking, troctolite can be distinguished by its light brown hue. Peridotite is more variable, but mostly appears a darker brown/red, coarser grained with large Fe-rich olivine crystals (sometimes displaying harrisitic like texture) which give it its red hue. Lastly, anorthosite, which is composed of predominantly plagioclase feldspar appears a light grey/white (Emeleus & Troll, 2008).

Moving south to the base of the layered intrusion, layering within the eastern unit is reflected within the topography of the area (Figure 5.1.3 *a, b,*). Moving upwards, outcrops of the ELI can be observed, some with partial layering, others showing the relationship between anorthosite-troctolite and peridotite crags and scarps (Figure 5.1.3 *c,*).

Figure 5.1.3: a) The marginal gabbro and ELI boundary. **b)** Photograph taken at the base of the ELI highlighting the observable units and the Halival summit. **c)** Exposed outcrop of ELI showing peridotite and anorthosite-troctolite relationship.

Continuing S/SE to an elevation of 400m an outcrop of the unit 7-8 boundary can be located. Here, the anorthosite-troctolite of the top of unit 7 interacts with a thin layer of peridotite of the base of unit 8. These units are separated by a chromite seam, ranging from 1mm-3mm in thickness. Atop the uppermost section of unit 7, small 'outliers' of peridotite (unit 8) can be observed within the anorthosite rich unit, with these 'outliers' being consistently separated from the peridotite by chromite seams (Figure 5.1.4). Continuing uphill, further units of the ELI can be observed. Displaying layering, auto-lithic chunks, coarse grained sections, and occasionally chromite seams (but not as pronounced as in the lower unit 7-8 boundary). Figure 5.1.5 displays some of these features.

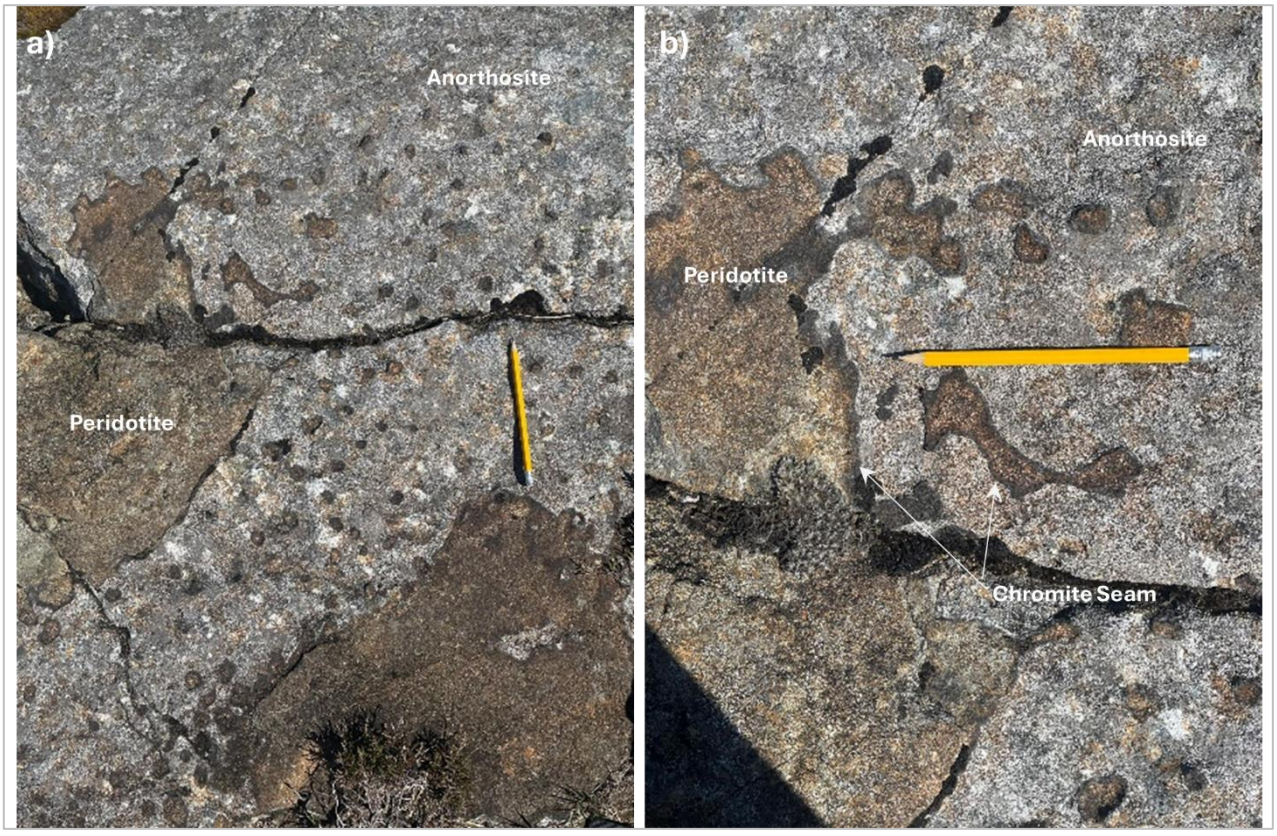

Figure 5.1.4: a) Planar view of unit 7-8 outcrop. **b)** Close up image highlighting relationship between anorthosite and peridotite, separated by chromite seam.

Due to time constraints, this was the extent to which this excursion was explored. However, the goal to observe the unit 7-8 boundary from which the thin section this project utilises was achieved within this field-day.

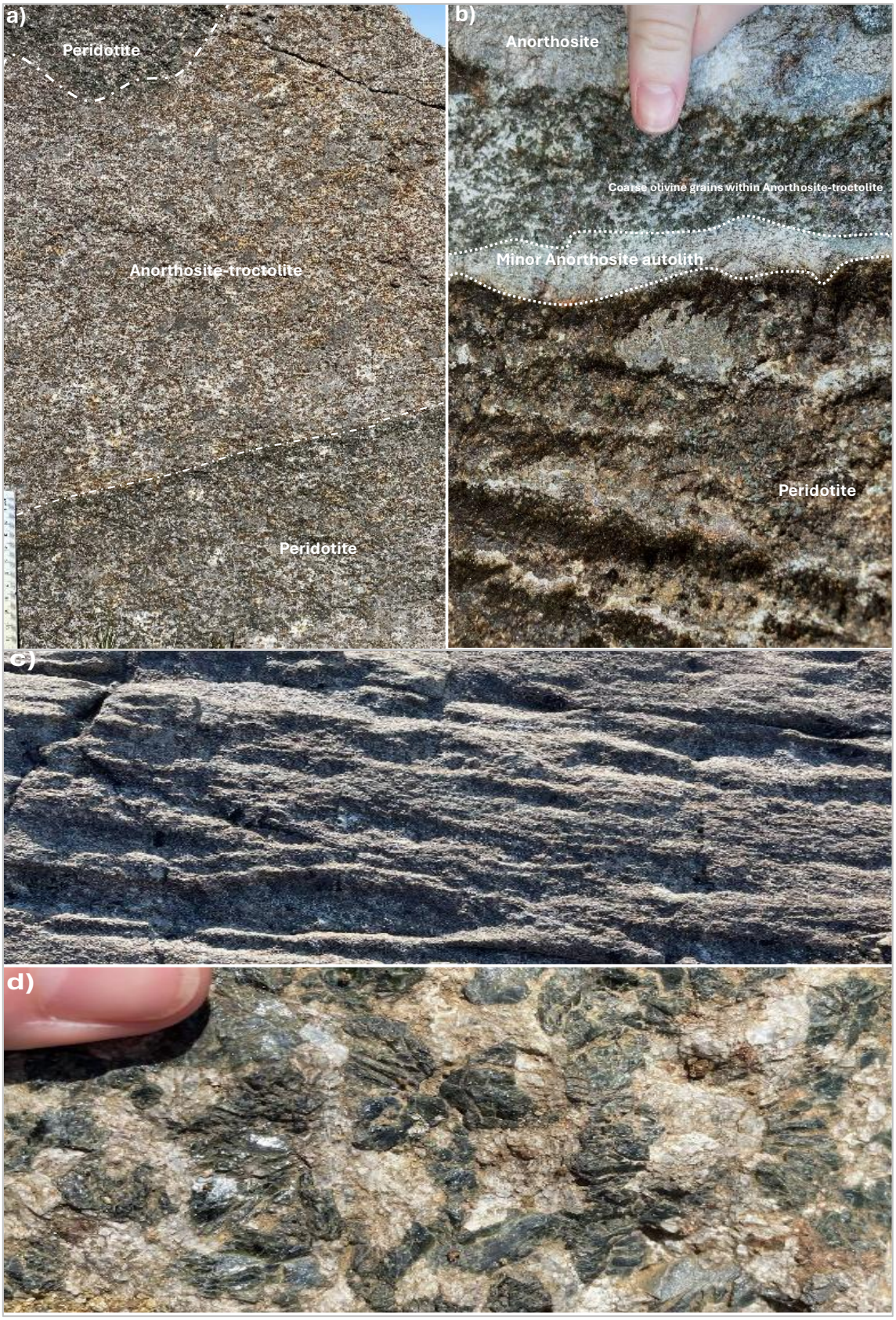

Figure 5.1.5: a) Alternating layering of peridotite and anorthosite/troctolite within ELI. **b)** Close up image of a minor anorthosite auto-lith and coarse olivine within ELI. **c)** Layering within coarse section of peridotite. **d)** Close up image of coarse olivine grains within a rock fragment from the ELI.

5.2 Optical microscope observations

The core aim of optical microscopy work was to identify hotspots of sulphides/PGMs along the chromite seam of the unit 7-8 sample as well as familiarise oneself with mineralogy of the seam and surrounding units before taking the sample to the SEM.

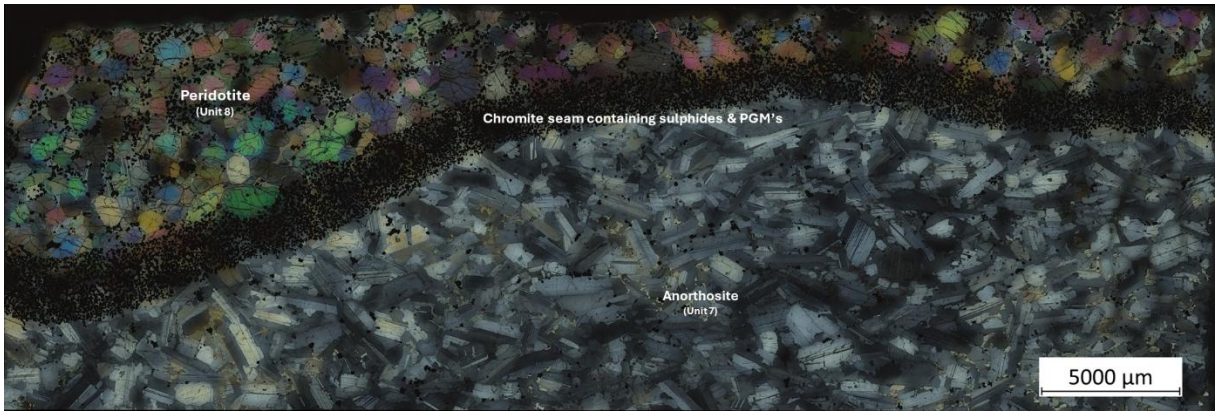

Figure 5.2.1: Optical Stich Image of the chromite seam along the unit 7-8 boundary taken using Zeiss Axio Imager M2M (cross polarised light).

Shown in Figure 5.2.1 is an Optical Stich image of the unit 7-8 boundary taken under Cross Polarised Light (XPL). Observing the sample under XPL allows identification of mineralogy to be straightforward as minerals typically have higher relief. Anorthosite is primarily composed of plagioclase feldspar, easily identified under XPL. Plagioclase feldspar is anisotropic, with interference colours ranging from first order grey to white. The most distinctive property of the plagioclase feldspar observed is the polysynthetic twinning (Deer, Howie, and Zussman, 2013, pp. 292-309). Under transmitted XPL the chromite seam and associated minerals sulphides and PGMs are easily distinguishable, appearing black due to their isotropic qualities. However, this makes it impractical to distinguish sulphide/PGM hotspots under XPL. Lastly, peridotite, is predominantly composed of olivine. Olivine is anisotropic, with interference colours ranging from second to third order. Sulphide and chromite minerals are seen to be more common and extend further into the peridotite in comparison to that of the anorthosite.

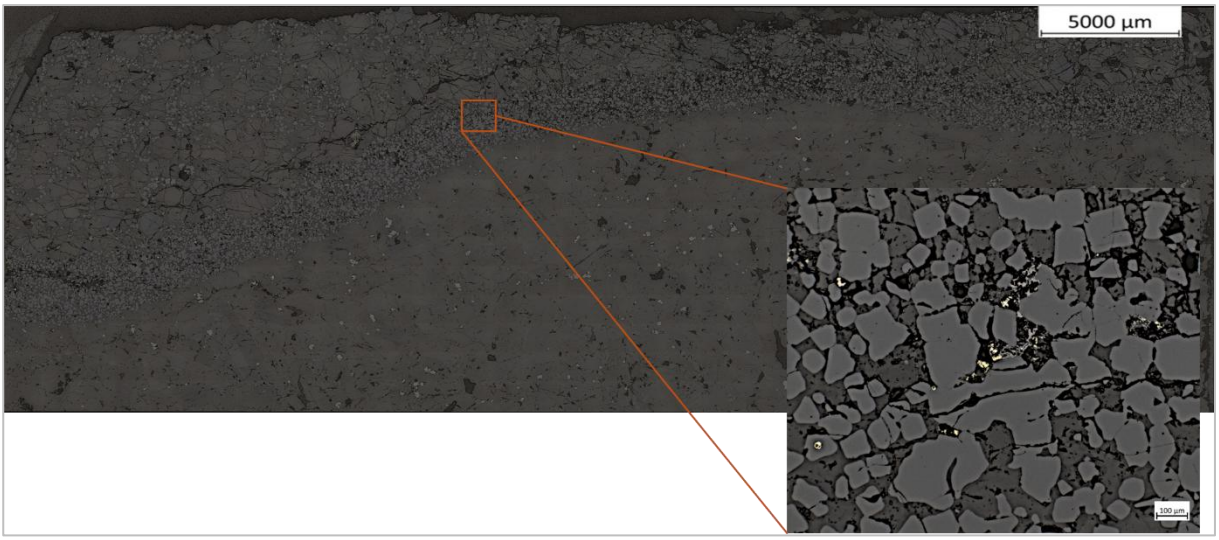

Figure 5.2.2: Optical Stich Image of the chromite seam along the unit 7-8 boundary taken using Zeiss Axio Imager M2M (plane polarised light). Image on the right shows sulphide minerals within the chromite seam.

Under reflected plane polarised light (PPL) the chromite seam is harder to distinguish from the surrounding anorthosite and peridotite, due to plagioclase feldspar and olivine having low relief (Figure 5.2.2). However, sulphide minerals can be easily identified under these conditions. Generally speaking, chalcopyrite appears yellow, pentlandite cream, and pyrite can show up black/yellow (Deer, Howie, and Zussman, 2013, pp. 432-440). During observation, it was noted that the left side and middle of the chromite seam had higher sulphide density than that of the right side, which aided planning further investigation of the sulphide minerals in the SEM.

5.3 SEM element mapping

The sample was taken to the SEM to further analyse sulphide minerals. Rims within the sulphides were previously noted by Matt Divers and Dr Joshua Franz Einsle within the team at Glasgow university.

Focusing on the left hand side and middle of the seam, due to the knowledge gained during observation under the optical microscope, lead to the identification of whole host of sulphide minerals, with upwards of 15 being imaged, some of which can be seen in Figure 5.3.1.

Sulphides had to meet at least one of three criteria points discussed in section 3.3 of the methodology chapter to qualify for EDS analysis. To refresh, briefly put, these are; (i) sulphide minerals containing enhanced rims along the edge, (ii) sulphide minerals containing more than one sulphide phase, (iii) sulphide mineral with a PGM located within/or in proximity to the mineral.

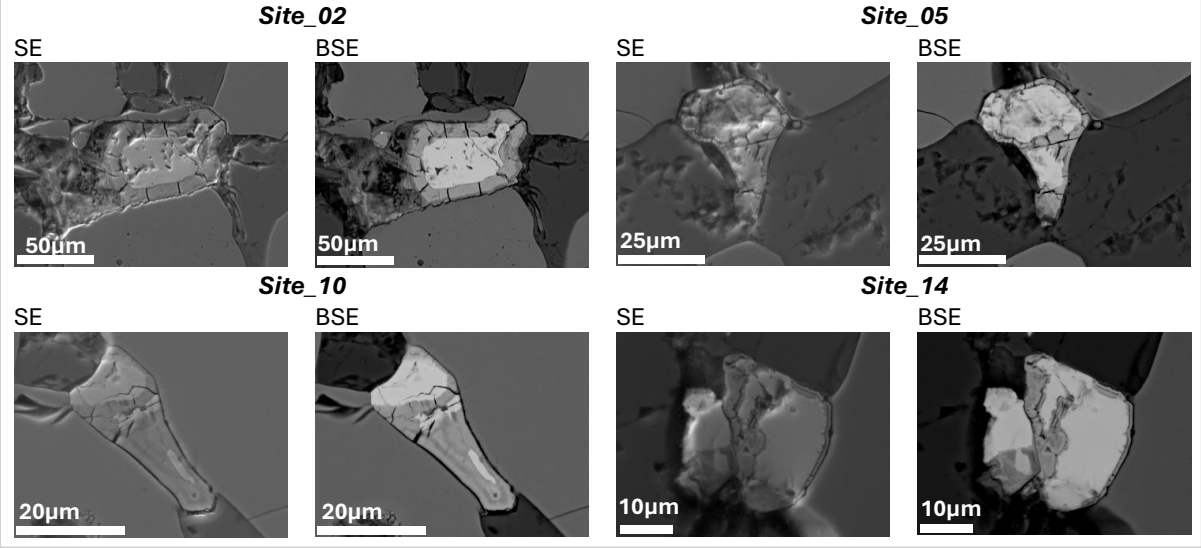

Figure 5.3.1: Figure displaying a collection of secondary electron (SE) and backscatter electron (BSE) images of sulphide minerals, within the unit 7-8 chromite seam, with rim/hotspot features. Taken in the SEM.

Out of the fifteen sulphides imaged within the SEM, four were chosen for further analysis in accordance with the criteria above. These sites, and their location in the chromite seam can be seen in Figure 5.3.2. EDS-SEM analysis of these sites produced element maps of each individual element present during analysis, which, after processing in Oxford Instruments software, can be layered to create layered element maps, which provide a good initial understanding of the geochemistry of each mineral (Figure 5.3.3).

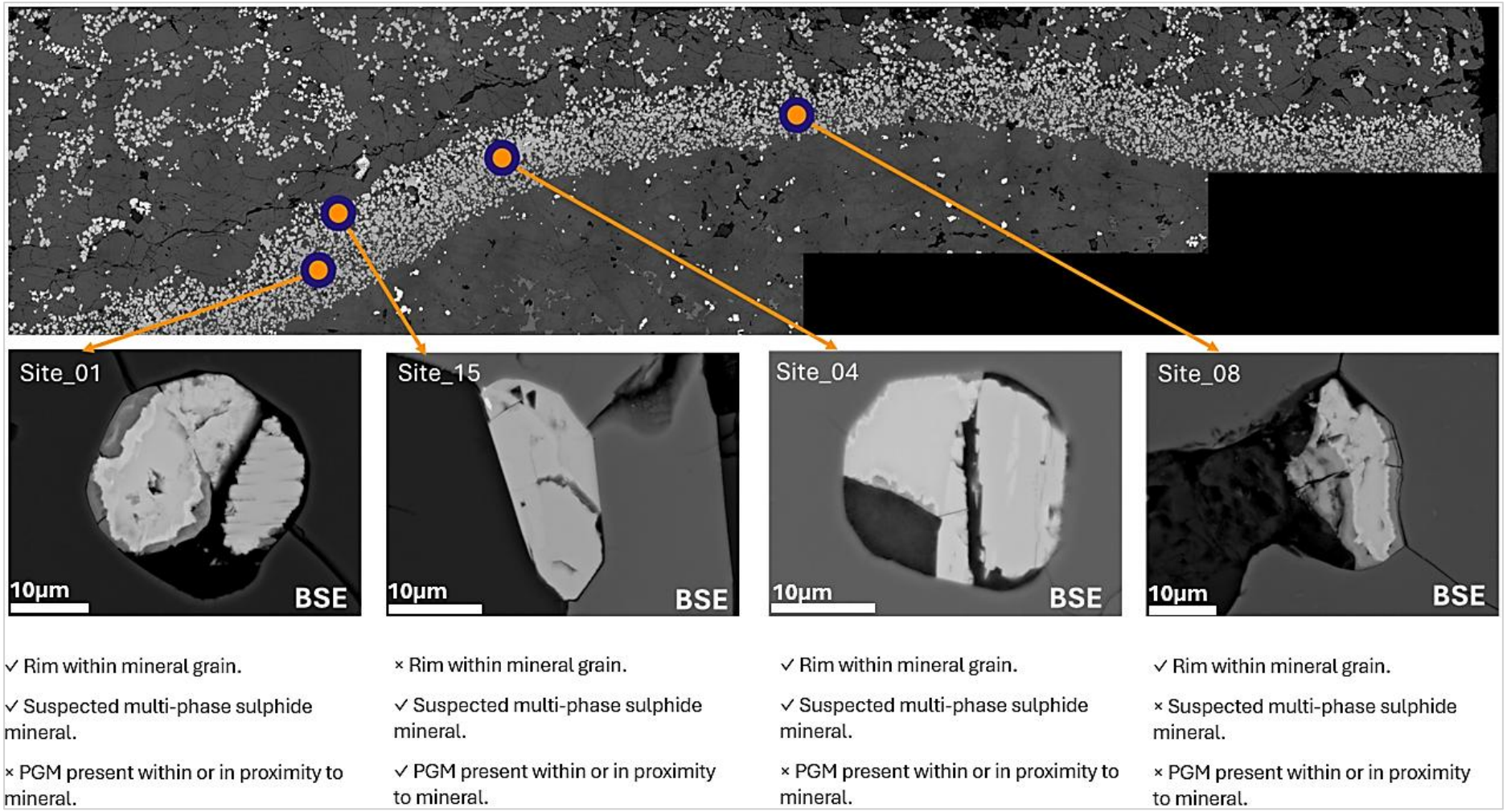

Figure 5.3.2: BSE images of the thin section taken in the SEM stitched together. Below are the BSE images of the four sites chosen for EDS analysis. The location of each site is annotated on the stitched image of the thin section. Below each site is the criteria met for EDS analysis.

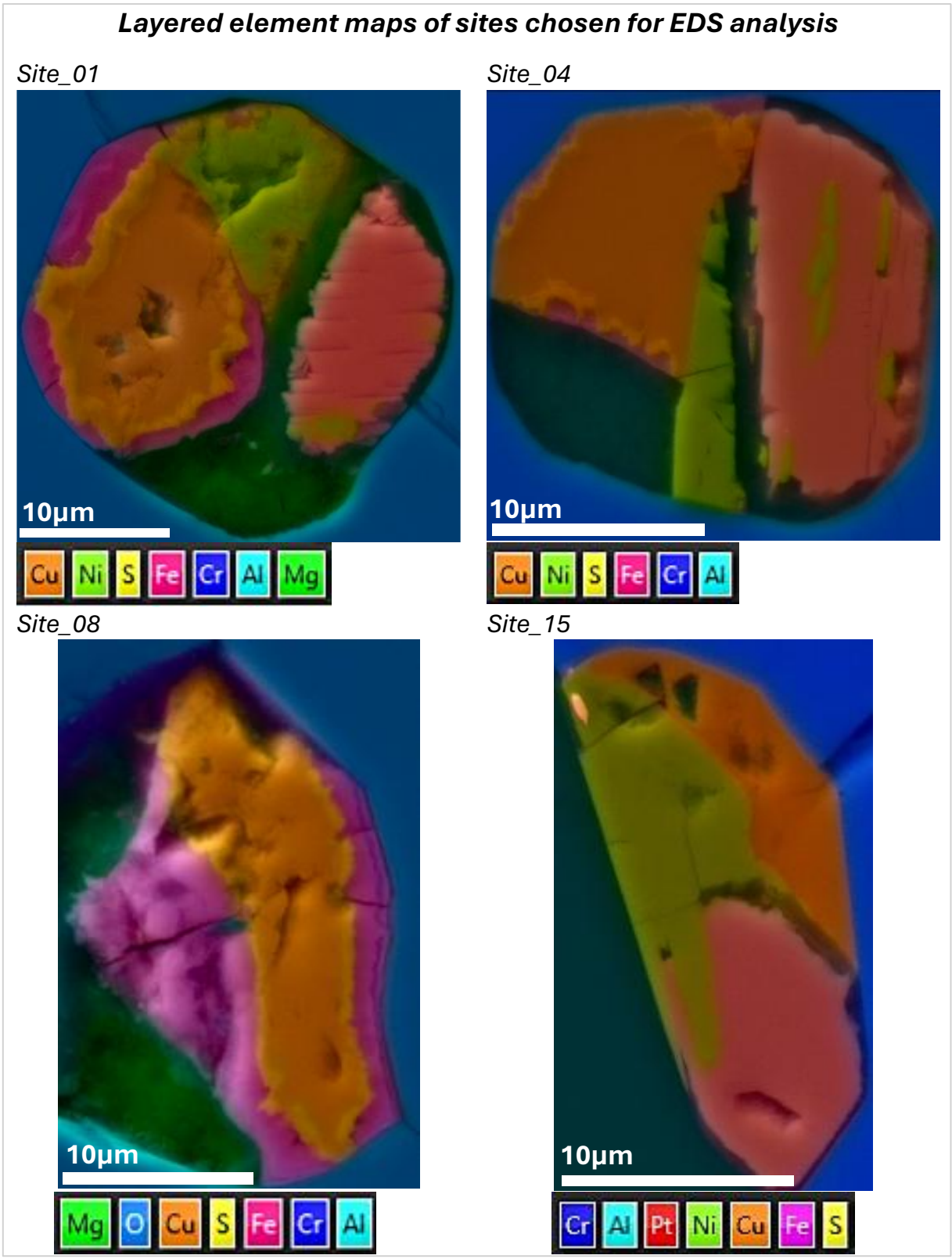

Figure 5.3.3: Displays the layered EDS element maps of each of the sites chosen for further analysis. Images were produced in Oxford Instruments, processing was required to create a colour key which displays elemental changes cohesively and additionally remains consistent.

Layered EDS maps are acceptable for looking at the general element distribution within minerals, but due to the variety of elements present the colours and mixes provided by Oxford Instruments can make results hard to read and interpret, having an impact on the quality of results. They also lack quantitative ability, with no precise intensities or mineral formulae, which in contrast can be provided by ML.

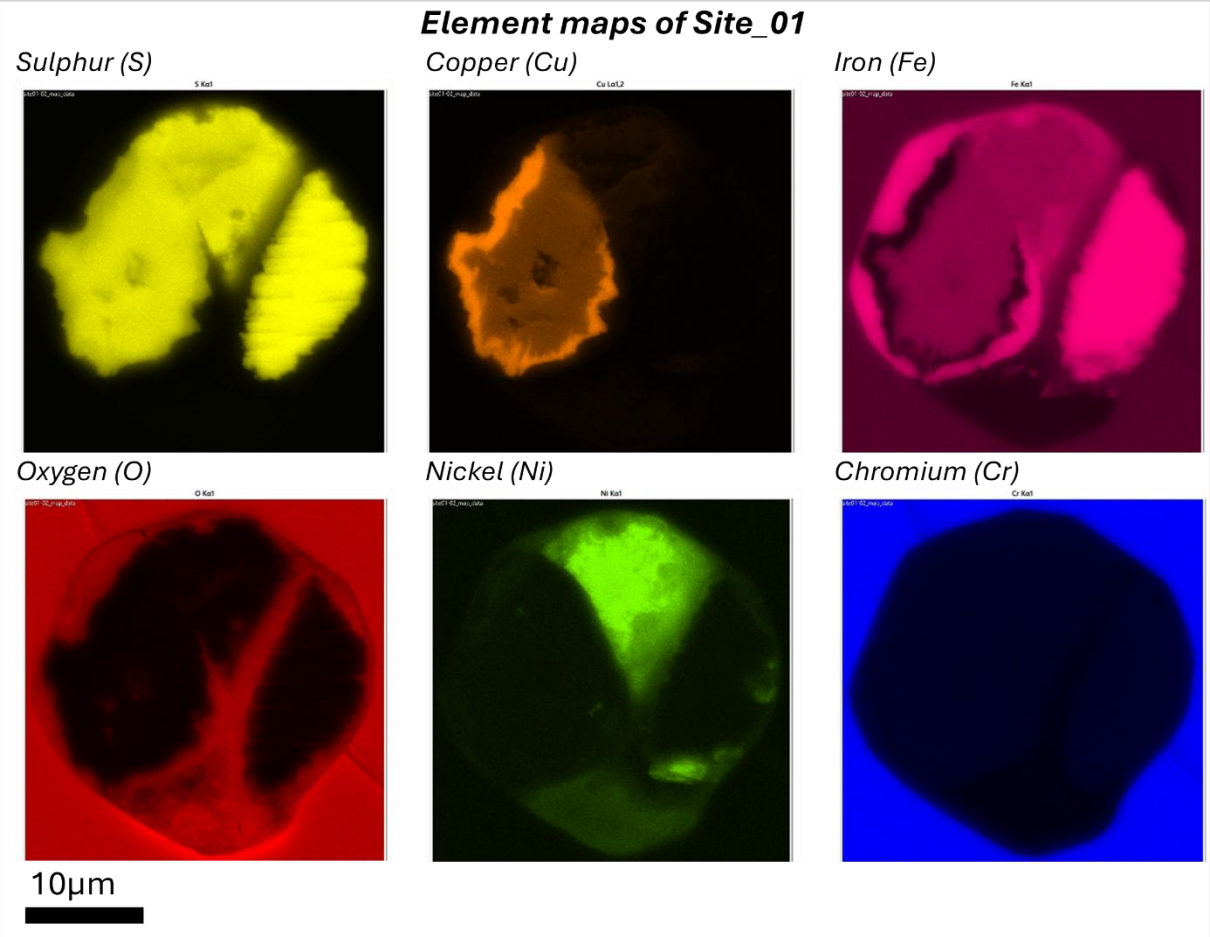

Figure 5.3.4: Figure displaying the individual element maps of site 01. Processed using Oxford Elements v6.

Site 01, was chosen for both its rims and suspected multi-phase properties. Observed in Figure 5.3.4, the rims of the mineral are seen to be depleted in iron, somewhat depleted in sulphur, and enriched in copper. The width of this enriched rim is somewhat consistent, with a thickness ranging from 1.2 – 2.6µm. In contrast, surrounding these rims, iron is enriched together with oxygen (e.g. iron oxide). Three separate sulphide phases are observed, containing copper and iron, iron and nickel, and iron respectively. A small fan like feature of Ni measuring around

3um in length can be observed within the Fe phase on the right. The sulphide grain itself is an inclusion, completely enclosed by chromite/chrome-spinel.

Site 04, chosen for EDS analysis by the same rationale as site 01, produced element maps which affirmed conclusions drawn from site 01. Rims within site 04 are also enriched in copper, depleted in iron, and slightly depleted in sulphur. Although, rims are thinner within this site between 0.2 – 1.4 um in width. Furthermore, site 04 is also a multiphase sulphide mineral, with the left section comprising of copper and iron, the lower middle of iron and nickel, and the right consisting of iron. Contrastingly to site 01, site 04 includes needle like features of Ni within the Fe mineral phase to the right, ranging from 0.3 – 8.1um in length. Similarity to site 01, site 04 is an inclusion, surrounded and bound by chromite/chrome spinel.

Site 08 meets only one of the criteria points; the presence of a rim within the mineral grain. Element maps produced from site 08 align with and re-affirm prior conclusions made about elemental properties of the rims. Rims are again seen to be enriched in copper and depleted in iron and sulphur, then bordered by an enriched zone of iron and oxygen. The rims are most consistent in width within this site, measuring around 1.6um in thickness. Site 08 is not an inclusion and is bounded by two different minerals.

Site 15 is the only site chosen for EDS analysis containing a PGM within the grain. Similar to the other multi-phased grains analysed, there are three distinct sulphide phases; top left composed of sulphur, nickel and minor iron, top right of sulphur, copper and minor iron, and the lower section of the grain consisting of sulphur and iron. The PGM present is a platinum grain located in the top left of the mineral, measuring at least 2um in length. Unlike site 01 and site 04, site 15 is not an inclusion as it is not bounded solely by chromite.

5.4 Machine learning analysis of sulphide minerals and platinum grains

To briefly refresh, the machine learning methodology used is as follows; (i) data exportation, (ii) data calibration, (iii) data decomposition, (iv) clustering, (vi) Bruker analysis and stoichiometry calculations.

(ii) data calibration

The data sets of each site were calibrated by performing Poisson noise scaling. Notably, prior to calibration, the data sets are still quite noisy despite the high number of average counts. Below are a collection of figures displaying the four sites before and after performing Poisson noise scaling.

There is an notable decrease in noise and increase in quality of the data sets after performing Poisson noise scaling, which applies to both the image quality within the navigator as well as the elemental spectra of each pixel. The results of this process also improve the resolution and definition of sulphide rims in site 01, site 04 and site 08 (Figure 5.4.1, 5.4.2, 5.4.3), as well as distinctions between sulphide phases in site 01, site 05 and site 15 (Figure 5.4.1, 5.4.3, 5.4.4).

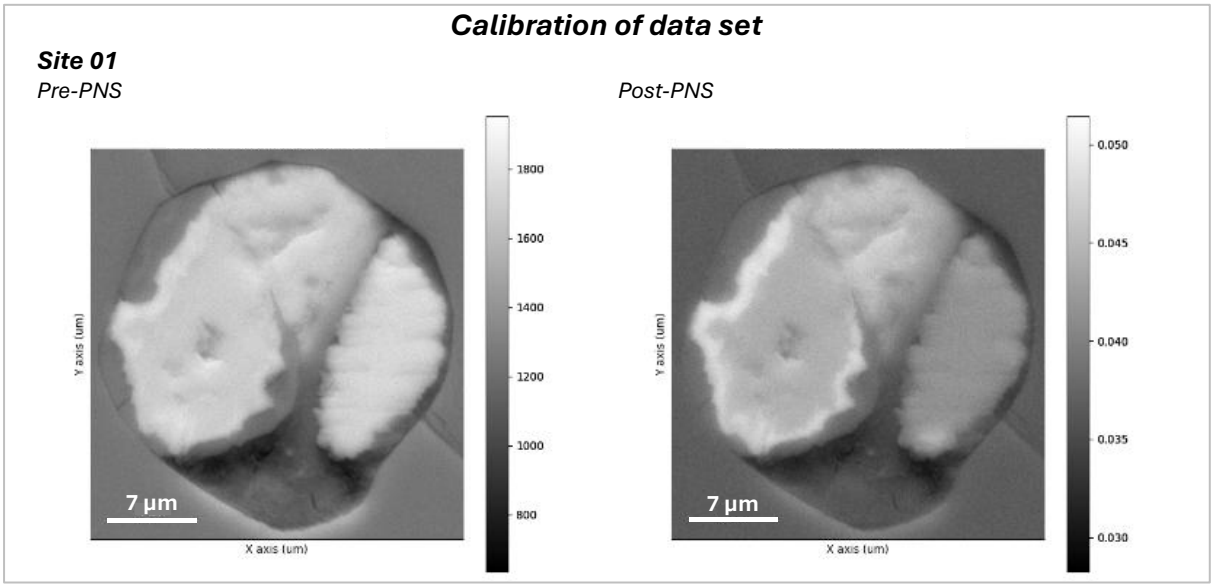

Figure 5.4.1: Poisson noise scaling results on site 01

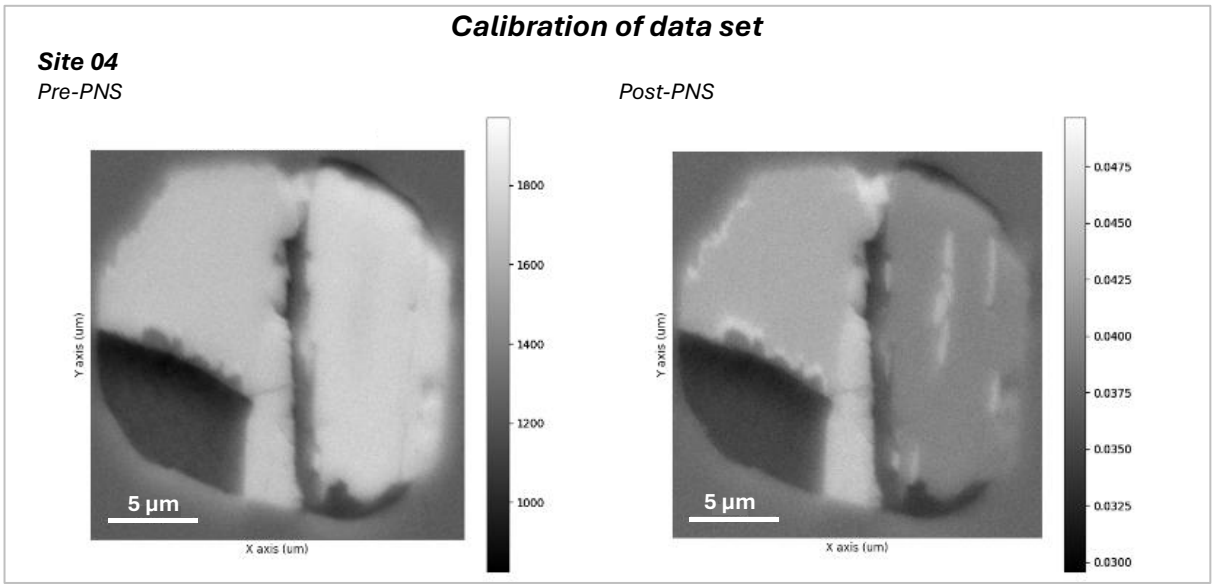

Figure 5.4.2: Poisson noise scaling results on site 04

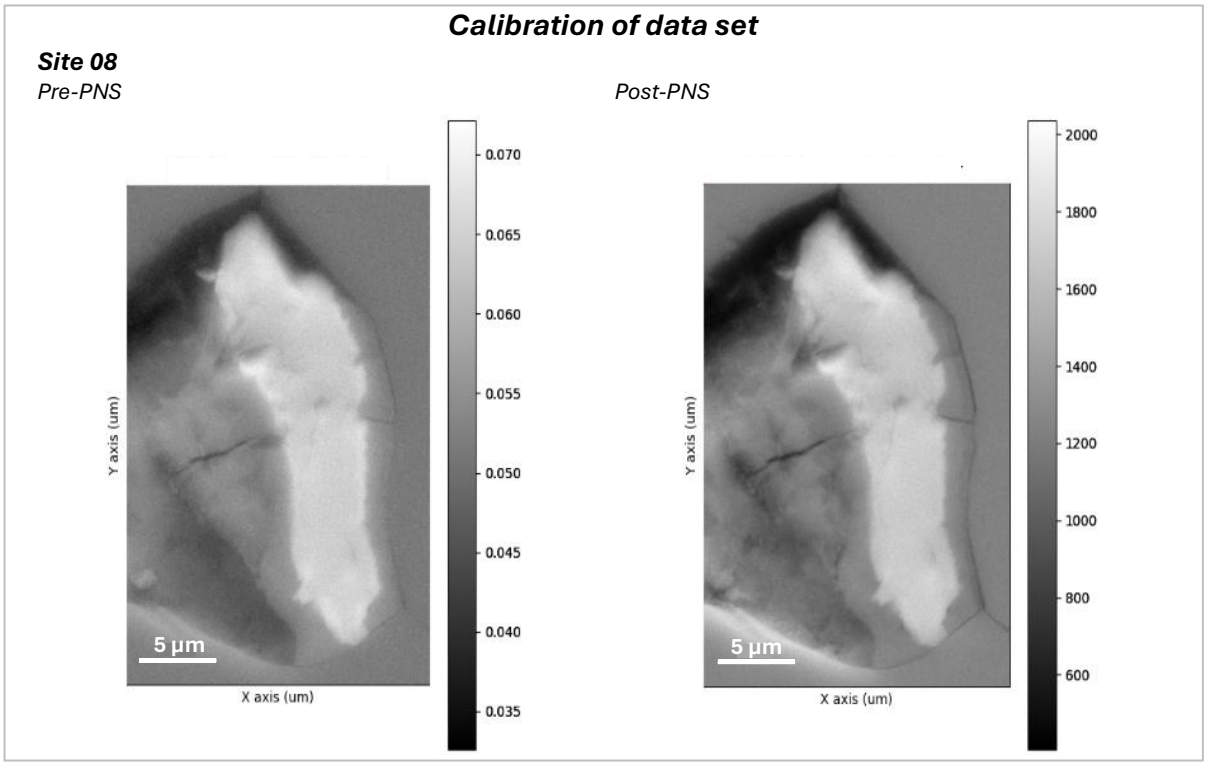

Figure 5.4.3: Poisson noise scaling results on site 08

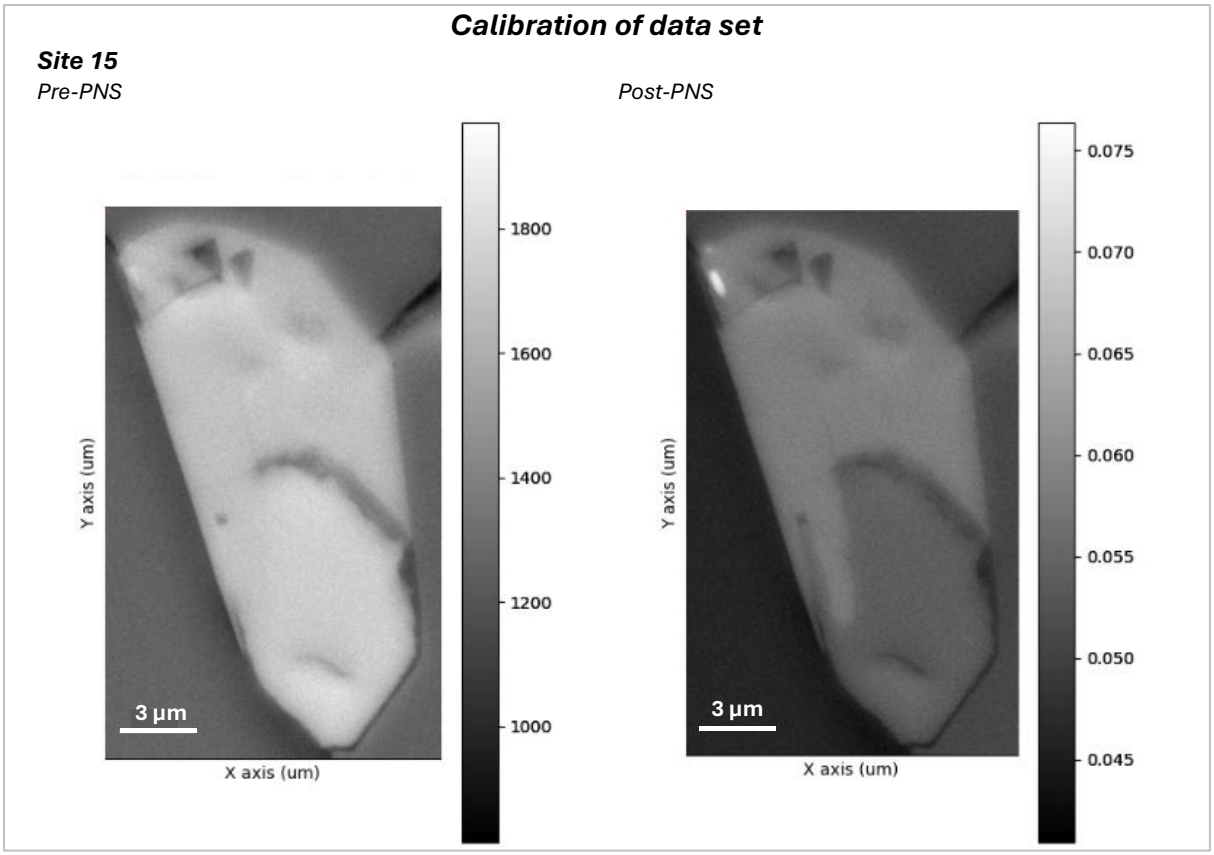

Figure 5.4.4: Poisson noise scaling results on site 15

(iii) data decomposition

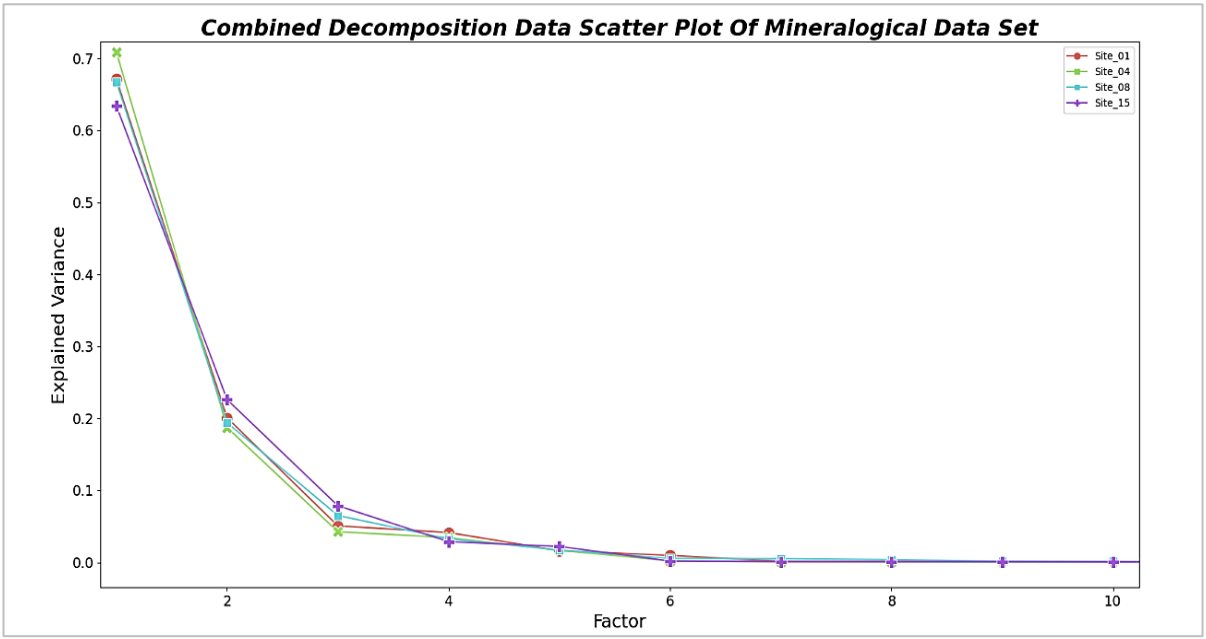

Figure 5.4.5: Combined decomposition scatter plot of the mineralogical data set. Created in jupyter lab using python, and libraries hyperspy, matplotlib, panda's and seaborn.

Data sets were dimensionally reduced using Factor Analysis (FA). First, the sets were ran with 20 factors, producing heat maps and decomposition plots. Analysis of the non-logarithmic decomposition plot (Figure 5.4.5) shows that the optimal factor of which the most variance is explained sits at 6 factors. Plotting the scatter plot logarithmically echoes this, but lets us observe relationships within the first 10 factors more accurately. The most significant increase in explained variance for sites 04, 08 and 15 is observed between factors 5 and 6 (Figure 5.4.6).

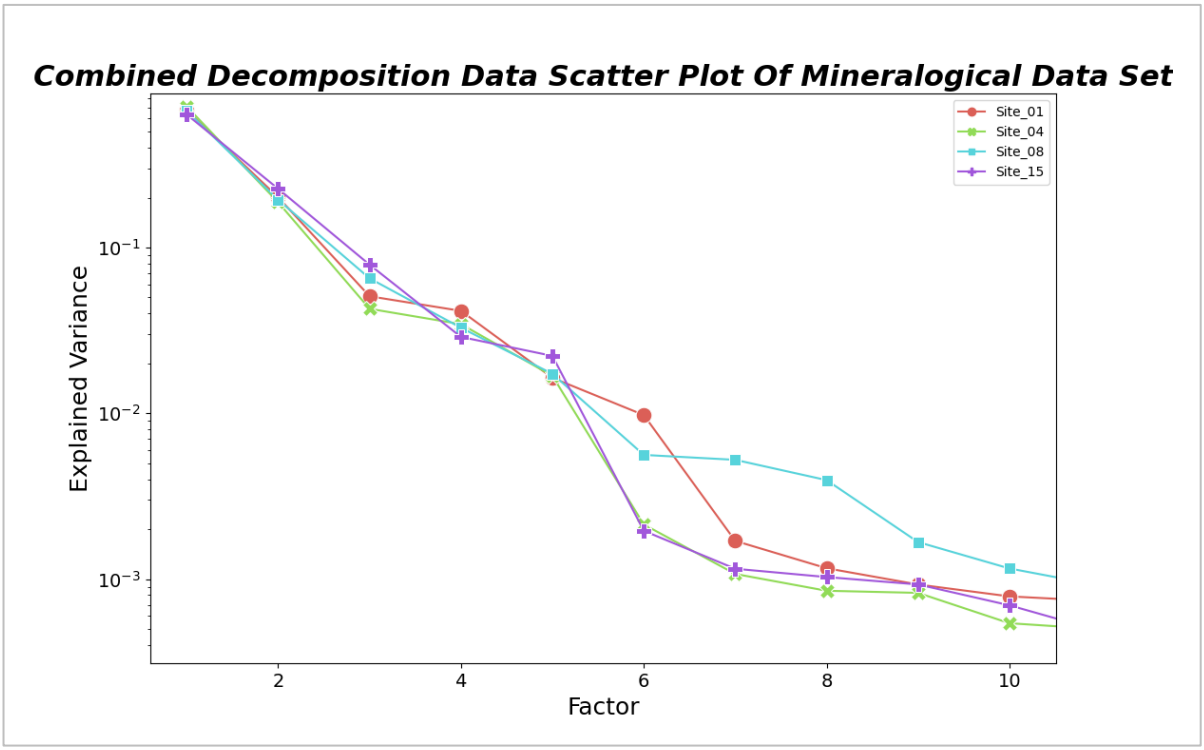

Figure 5.4.6: Combined decomposition scatter plot of the mineralogical data set plotted logarithmically. Created in jupyter lab using python, and libraries hyperspy, matplotlib, panda's and seaborn.

Table 5.4.1: Table of the determined number of optimal factors for each data set.

Data set	Average number of counts (2.d.p)	Optimal number of factors	Percentage variance explained in optimal number of factors (2.d.p)	Number of clusters produced
Site_01	1510.59	6	98.01% (0.980104)	10
Site_04	1601.50	6	98.97% (0.989706)	9
Site_08	1375.14	6	98.20% (0.982065)	9
Site_15	1577.82	7	99.34% (0.993382)	9

Analysis of factor heat maps (listed in appendix B) in combination with the decomposition scree plots (Figure 5.4.6) aided determination of the final optimal number of factors for each data set. Heat maps displayed changes in noise from factor to factor visually, helping confine which factors actually provided lower-noise higher-quality information and reducing noise pollution of data set. Figures displaying factor heat maps and corresponding spectra, scores, and loadings of the data sets ran with these optimal number of factors can be seen in the appendix B . The optimal number of factors, the percentage variance explained in each set by the optimal number of factors, and the clusters produced from each set is listed in Table 5.4.1.

(iv) cluster analysis

HDBSCAN, a clustering program was applied to the data sets dimensionally reduced by the determined number of optimal factors above. Hard clustering images of the sites are shown in figure 5.4.7,5.4.9,5.4.11, and 5.4.13. Note that python classification begins at 0, therefore in colour bars cluster 0 = cluster 1, *etc.*

Clustering of site 01 produced 10 clusters overall (Figure 5.4.7). Clustering was highly effective, producing clusters that detected the multiple sulphide phases, the rim of interest within the mineral, and the zone surrounding this rim (Cluster 4 and 2) (Figure 5.4.8).

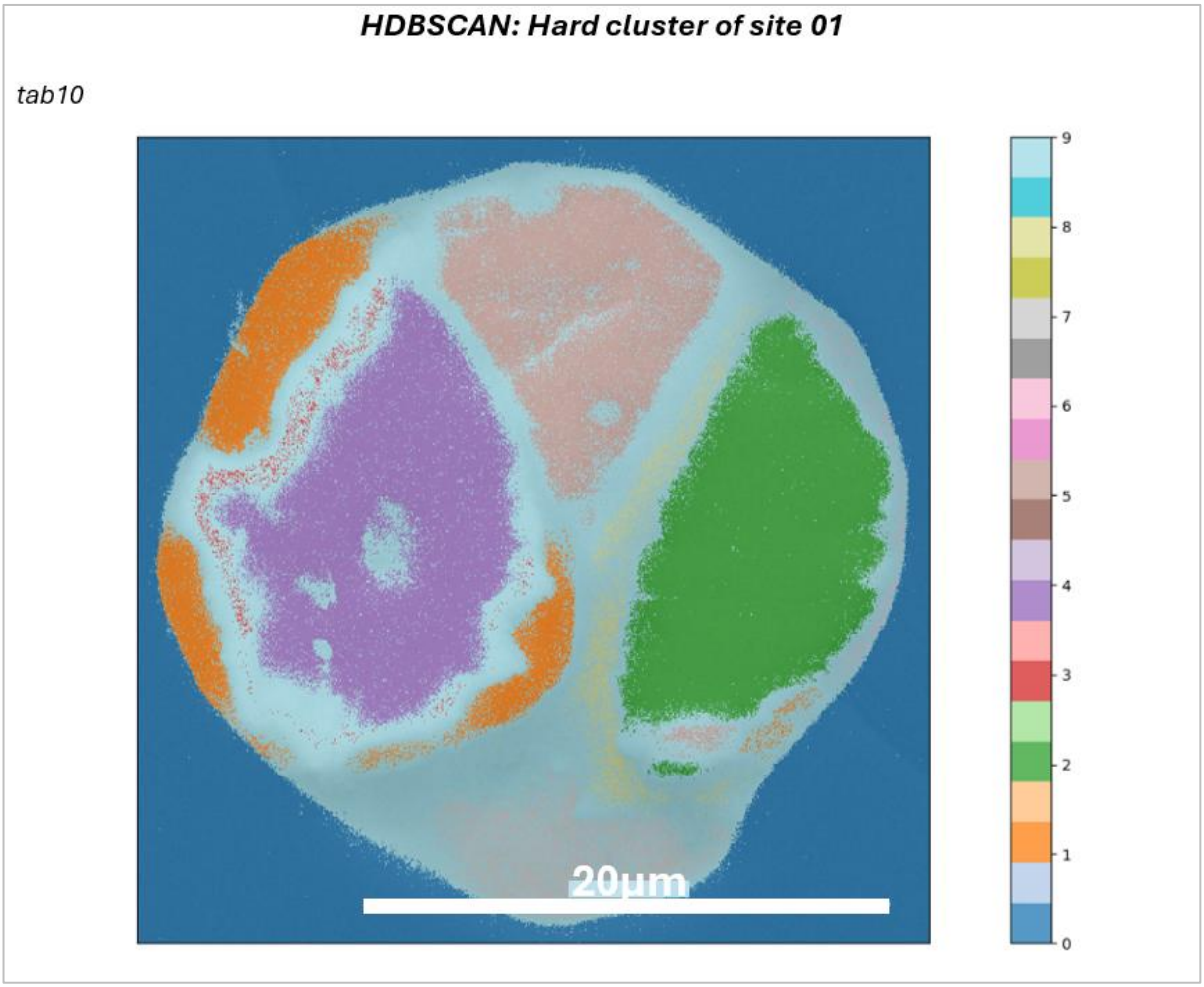

Figure 5.4.7: HDBSCAN hard clustering results of site 01. The enriched rim of interest is pulled out by the red cluster (4). Tab10 colour scheme used.

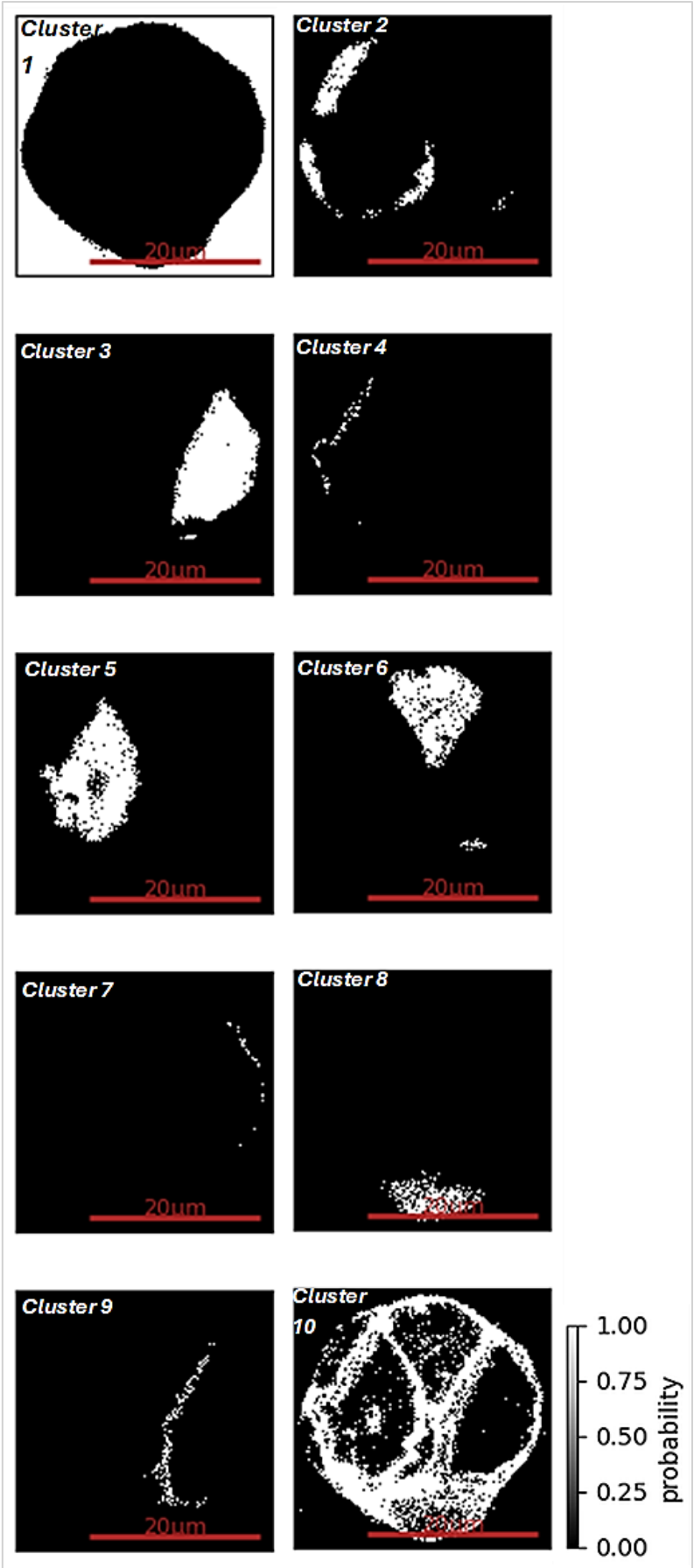

Figure 5.4.8: Images of the 10 clusters produced from HDBSCAN - site 01.

Using corresponding pixel/spectra data, and spectra signal plots produced from each cluster (appendix B), allows for preliminary observations about element composition of clusters to be made (applicable to all sites). In site 01, clusters 3, 5, and 6 present three separate phases within the grain boundary. Pixel/spectra data and spectra signal plots of cluster confirms that clusters 3, 5, and 6 are sulphide mineral phases with varying amounts of copper (cluster 5), iron (cluster 3) and nickel (cluster 6). Cluster 4 picks out the rim of interest within the sulphide mineral, and cluster 2 the zone surrounding this rim. Signal plots of cluster 4 display three main elements of composition; sulphur, copper and iron. Direct comparison to the signal plots of cluster 5, the sulphide mineral phase in which the rim is contained, displays a high reduction in iron and a significant increase in sulphur. Cluster 2 signal maps display enrichment in oxygen and iron and intense depletion in both sulphur and copper. Corresponding to interpretations derived from EDS element maps. Interestingly, there is another rim like structure highlighted cluster 7, shown in signal plots to be enriched in iron and oxygen.

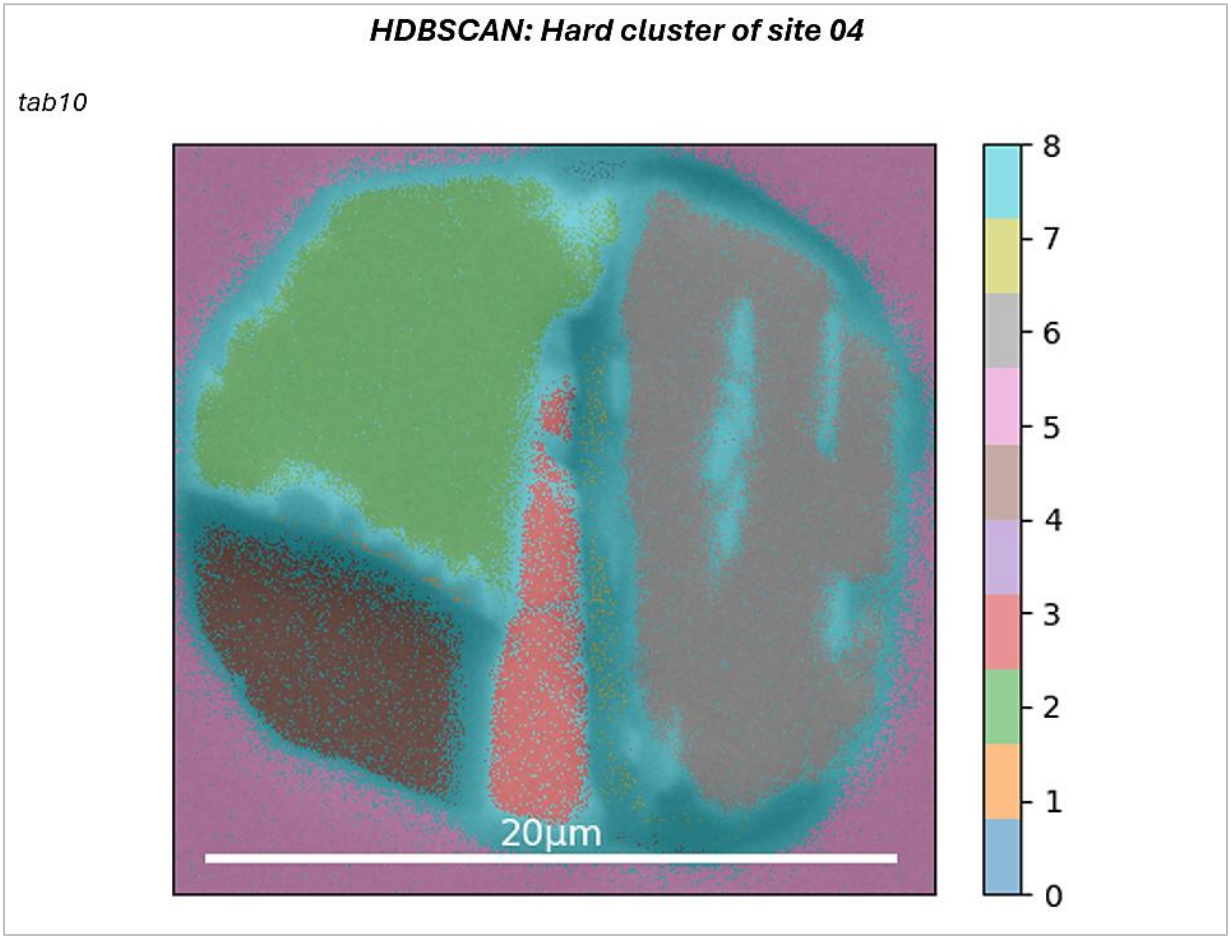

Figure 5.4.9: HDBSCAN hard clustering results of site 04. Tab10 colour scheme used.

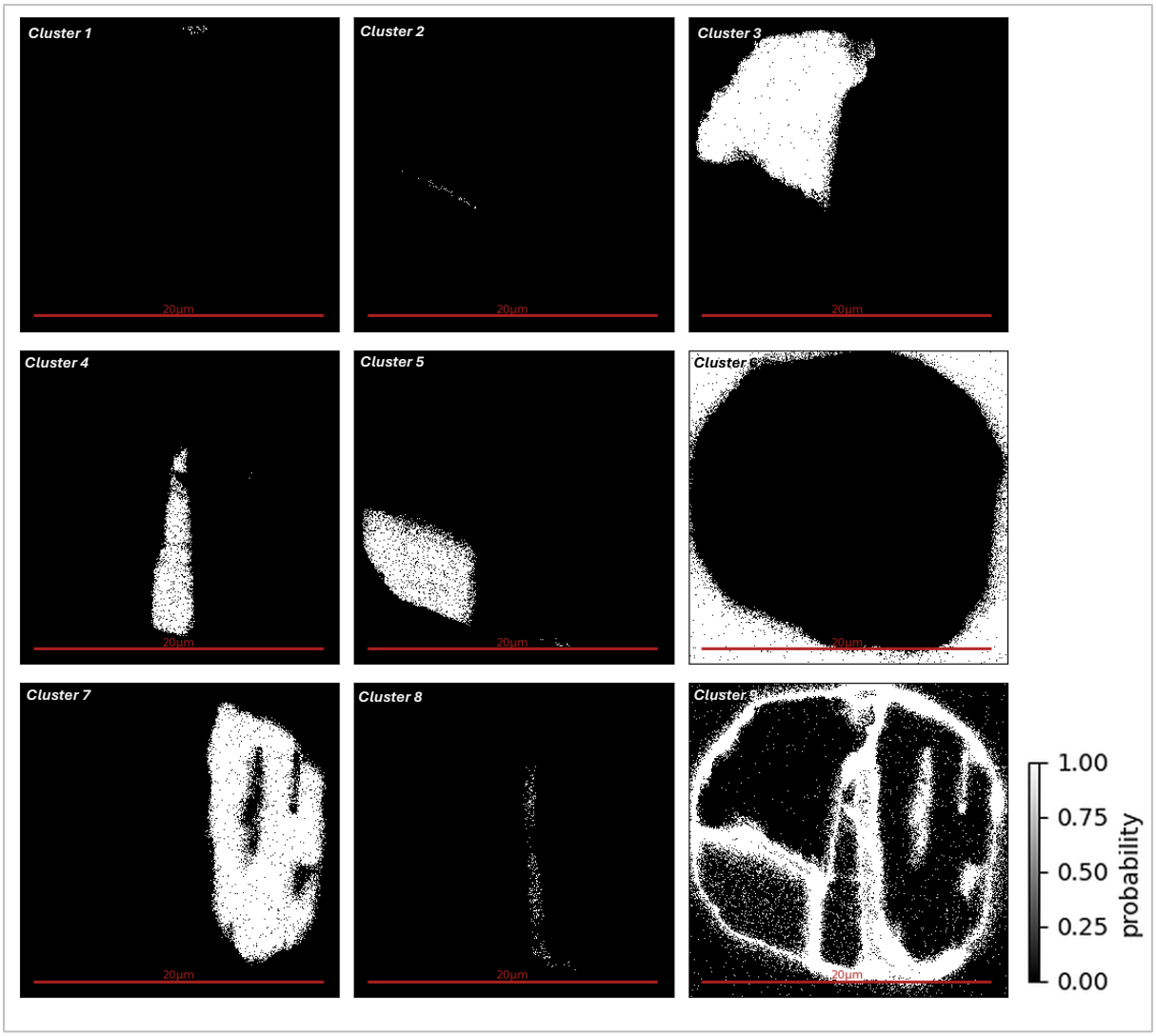

Figure 5.4.10: Images of the 9 clusters produced from HDBSCAN - site 04.

Clustering of site 04 led to less segmentation than site 01, producing 9 clusters (Figure 5.4.9, 5.4.10). Unfortunately, the rim was not pulled out within this data set, however, a section of the zone surrounding the rim was (cluster 1 & 2), shown in signal plots to be enriched in iron and oxygen, similar to cluster 2 of site 01. Similar to site 01, three sulphide phases are also distinguished through clustering, cluster 3 (sulphur rich), 4 (nickel rich), and 7 & 8 (iron rich). Cluster 6 underlines that the sulphide grain is an inclusion within a boundary enriched in aluminium, chromium, magnesium, oxygen and iron.

Site 08 also produced 9 clusters (Figure 5.4.11, 5.4.12). Similar to site 04 above, HDBSCAN struggles to segment the rim from the rest of the minerals material – likely due to its size. Cluster 2 and cluster 3 are well segmented, representing a sulphide/copper grain, and a oxidised iron zone adjacent to the rim of interest. Other clusters produced highlight the complexity of the mineralogy surrounding the sulphide grain, as it is not an inclusion purely surrounded by chromite as in site 01 and site 04. Bordering the grain is; cluster 7, predominantly composed of chromium, magnesium and iron; cluster 4, predominantly aluminium, silica and calcium; cluster 5, oxygen, magnesium, silica and aluminium; and cluster 6, composed of oxygen, aluminium, silica and iron.

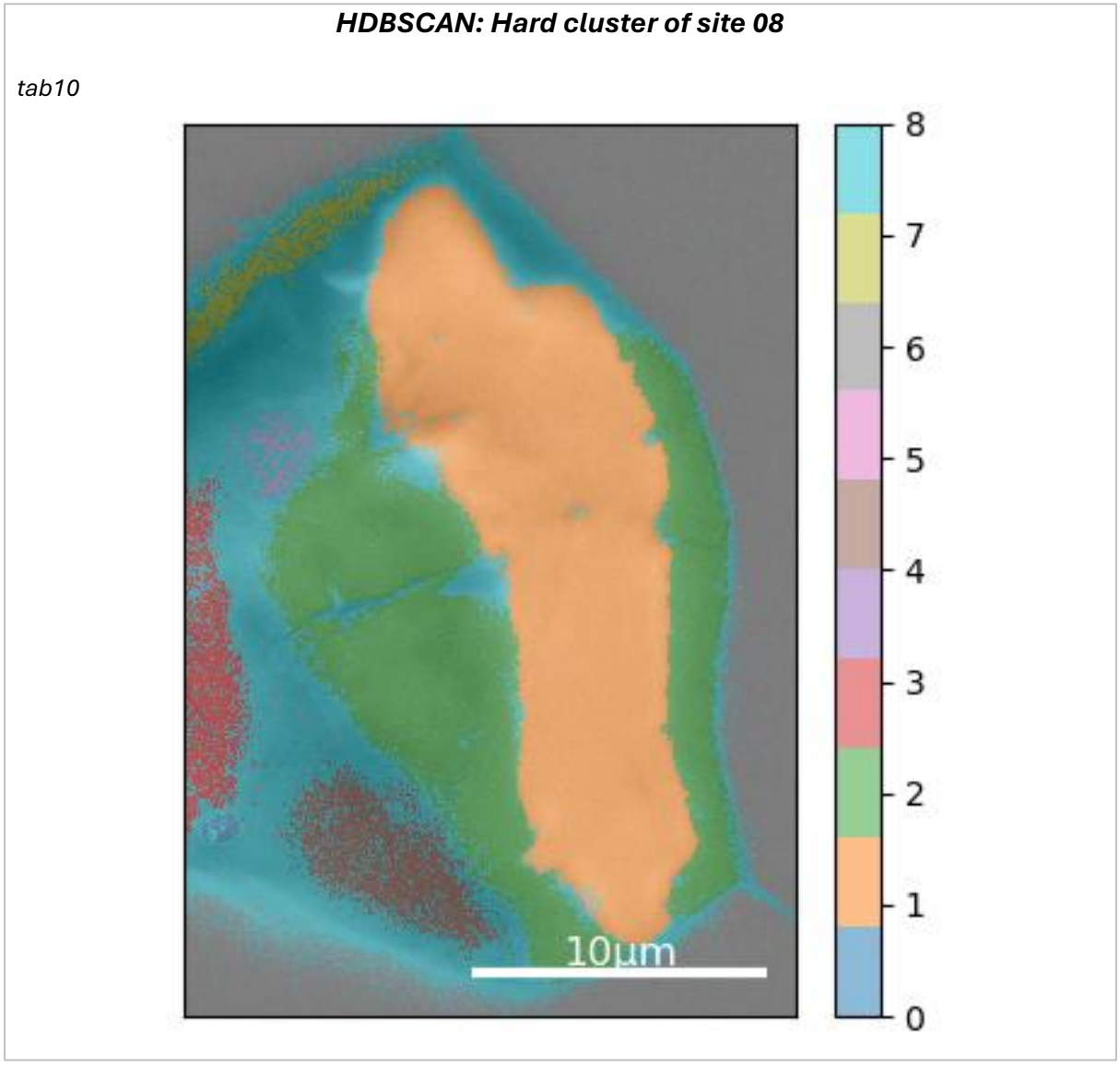

Figure 5.4.11: HDBSCAN hard clustering results of site 08. Tab10 colour scheme used.

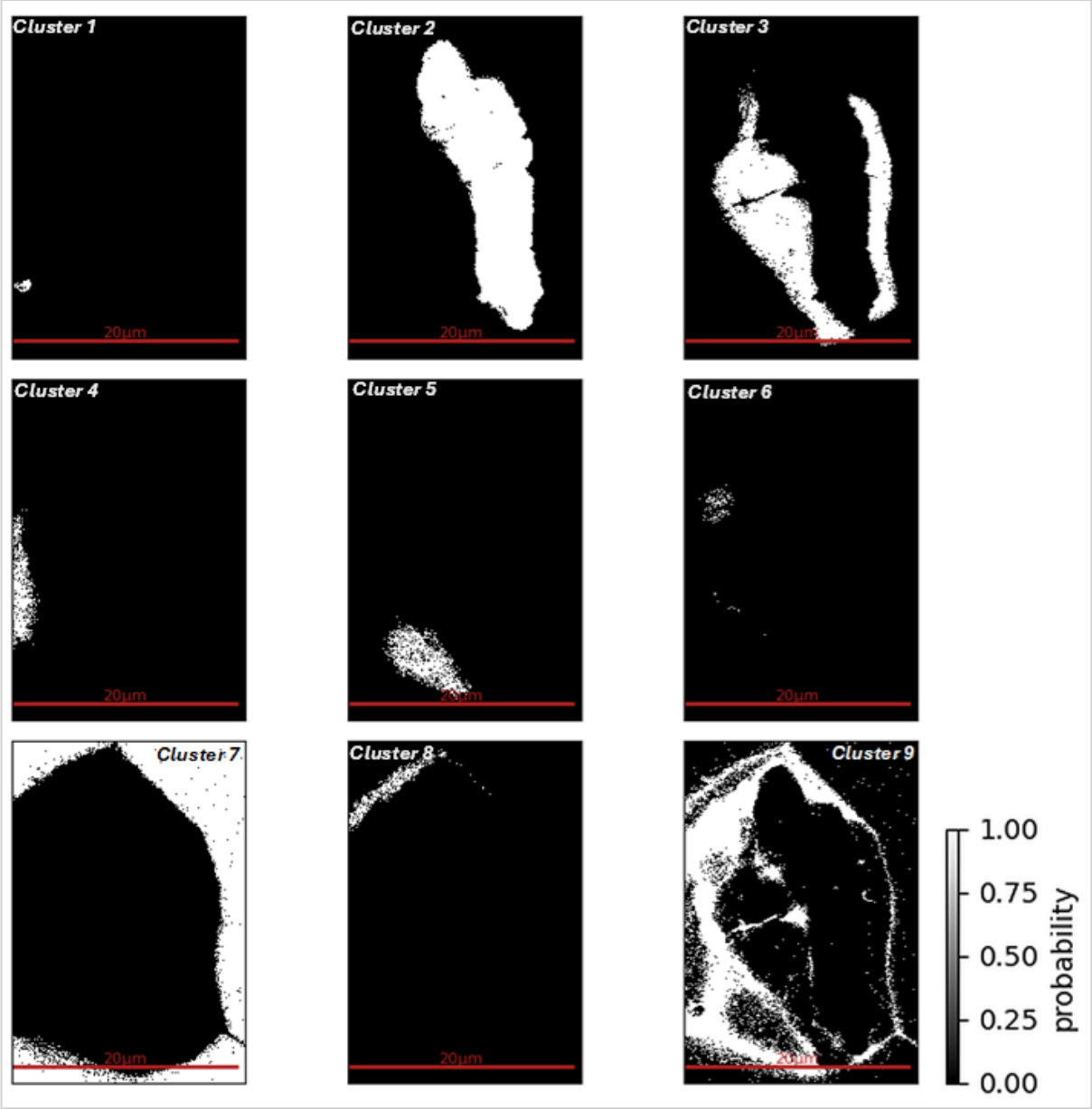

Figure 5.4.12: Images of the 9 clusters produced from HDBSCAN - Site 08.

HDBSCAN of site 15 produced nine clusters, (Figure 5.4.13, 5.4.14). Segmentation is well pronounced. The phases of the sulphide minerals are picked out by cluster 4 (iron and nickel), 8 (iron rich), 5 and 6 (iron and copper). Similar to site 08, the sulphide grain is not an inclusion, which is bordered by cluster 3, composed of aluminium, silica, oxygen and calcium, and cluster 7, composed of oxygen, aluminium, chromium and iron. Cluster 2 is an isolated area of sulphur, calcium, copper, and iron. Lastly, cluster 1 clearly defines the platinum grain present within the sulphide mineral grain.

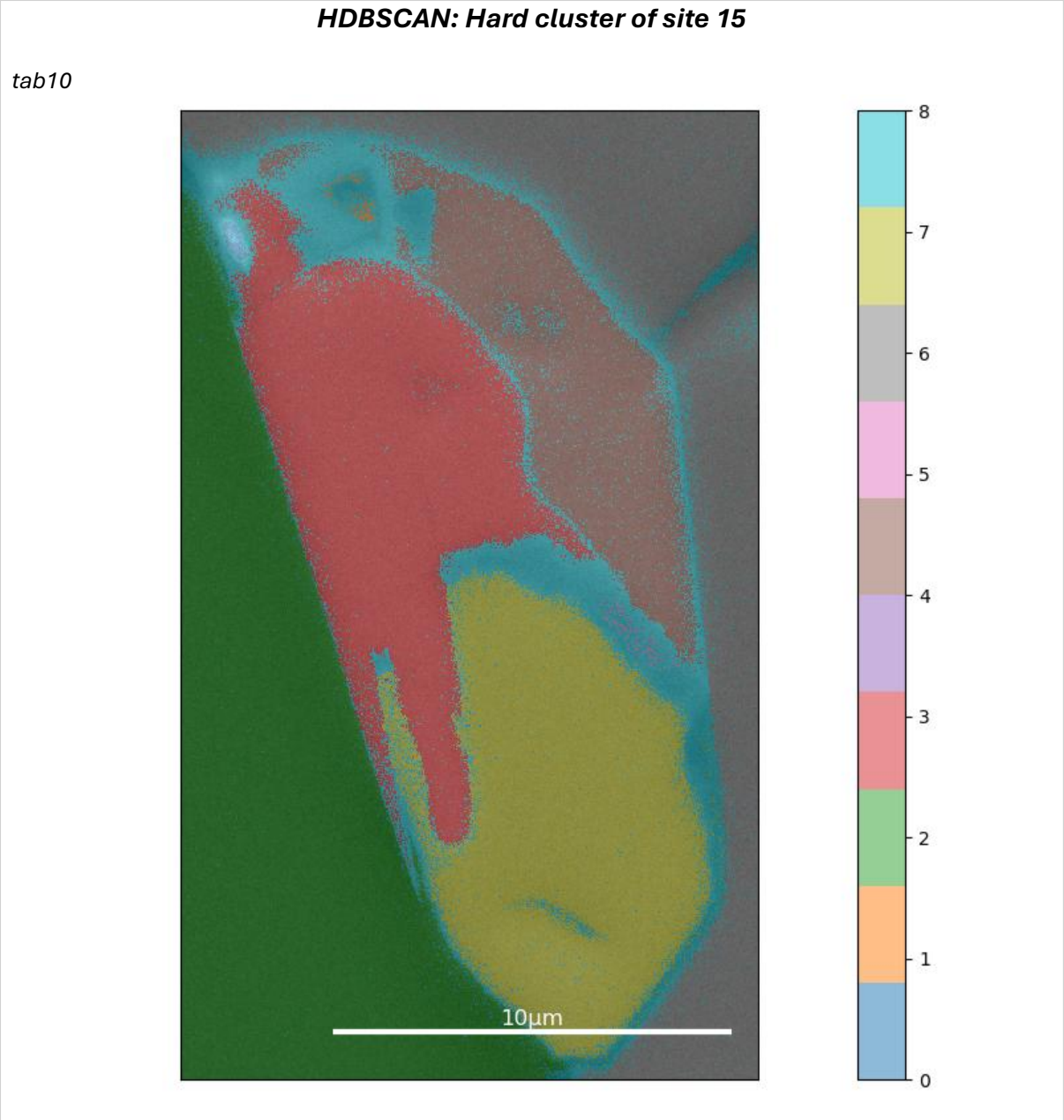

Figure 5.4.13: HDBSCAN hard clustering results of site 15. Tab10 colour scheme used.

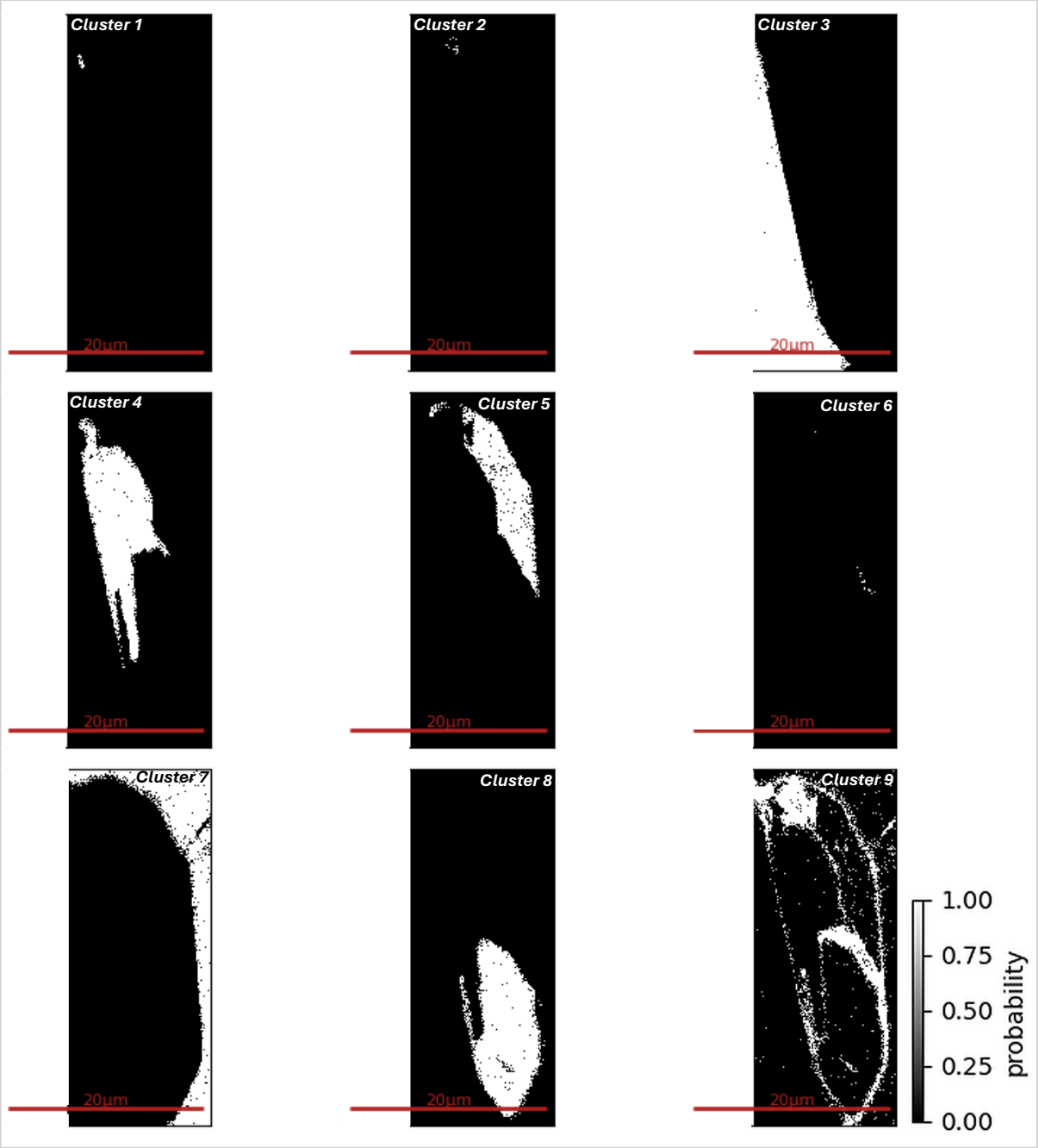

Figure 5.4.14: Images of the 9 clusters produced from HDBSCAN - Site 15.

Overall, the elemental information provided by cluster images, pixel/spectra data, and cluster spectra signal plots, aligns with the results previously produced by EDS element maps, and segments elemental differences within the sites of interest to a higher degree of definition than that of the EDS mapping produced from Oxford Instruments.

(vi) Bruker analysis & Stoichiometry calculations.

Bruker analysis produced spreadsheets containing elemental information regarding each individual cluster. Both PBZAF and Phi-Rho-Z were used in Bruker. These results can be found in the supplementary material. Numbers produced by both PBZAF and Phi-Rho-Z were averaged and used to produce the mineral formula of each cluster using the stoichiometry calculation method from 'The Rock-Forming Minerals' (Deer, Howie and Zussman, 2013). Mineralogical formulae and other information relevant for stoichiometry calculations was acquired from the respective mineral pages on mindat.co.uk.

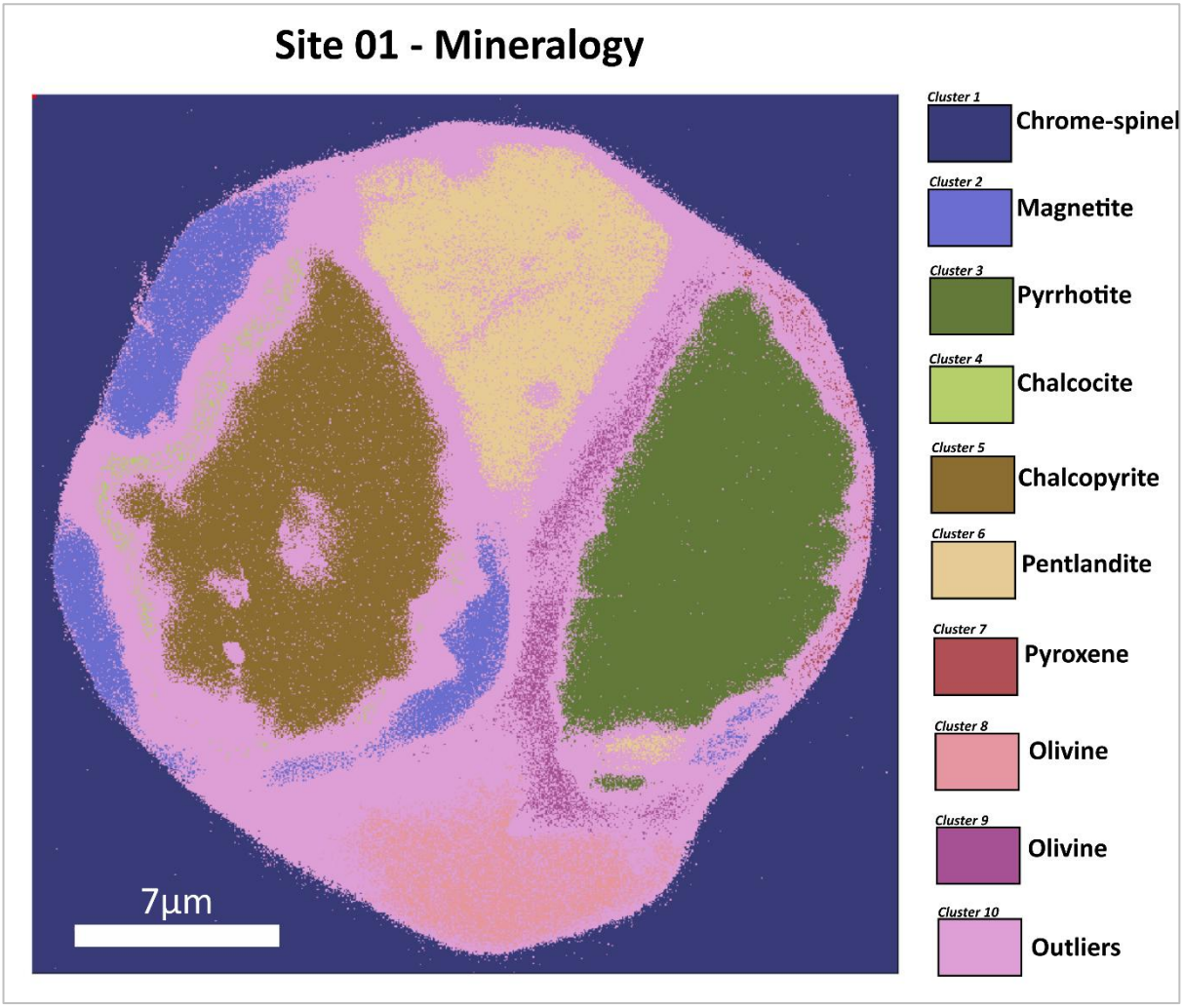

Figure 5.4.15: Figure of the mineralogy of the clusters produced from HDBSCAN - site 01. Tab20 colour scheme used.

Table 5.4.2: Mineral formulae produced from stoichiometry calculations regarding data from each cluster. Metal:sulphide ratios are also calculated for sulphide minerals.

Site 01			
	Mineralogy	Calculated formula	Metal $_{(2.d.p)}$: Sulphide ratio
Cluster 1	Chrome-spinel	$(Mg_{0.61}\ Fe^{2+}_{0.22}\ Ti^{4+}_{0.01})(Al_{1.14}\ Cr_{0.51}\ Fe^{3+}_{0.44}\ Fe^{2+}_{0.01})O_4$	/
Cluster 2	Magnetite	$Fe^{2+}_{0.66}\ Fe^{3+}_{1.33}\ O_4$	/
Cluster 3	Pyrrhotite	$Fe_{0.82}\ S_{0.77}$	1.06 : 1
Cluster 4	Chalcocite	$Cu_{1.96}\ S_{1.26}$	1.56 : 1
Cluster 5	Chalcopyrite	$Cu_{0.58}\ Fe_{0.55}\ S_{.95}$	1.20 : 1
Cluster 6	Pentlandite	$(Ni_{0.46}, Fe_{0.65})_{\Sigma 1.11}\ S_{0.96}$	1.16 : 1
Cluster 7	Pyroxene	$(Fe_{1.00}, Mg_{0.86})_{\Sigma 1.86}\ Si_{0.64}\ 0_6$	/
Cluster 8	Olivine	$(Mg_{0.77}, Fe_{0.31}, Ni_{0.18})_{\Sigma 1.26}\ Si_{1.04}\ O_4$	/
Cluster 9	Olivine	$(Mg_{0.46}, Fe_{0.81}, Ni_{0.17})_{\Sigma 1.44}\ (Si_{0.5}, Al_{0.9})_{\Sigma 1.0}\ O_4$	/
Cluster 10	Outliers	/	/

The clusters and corresponding mineralogy of site 01 is displayed in Figure 5.4.15. Calculations defined site 01 as an inclusion within chrome-spinel. The sulphide mineral is multiphase containing pyrrhotite, chalcopyrite, and pentlandite. The enriched rim, cluster 4, is a Cu rich sulphide, with a chemical formula placing it between digenite/chalcocite. The change in metal:sulphide ratio across the rim (1.20:1 vs 1.56:1) is indicative of intense sulphur loss (Table 5.4.2). The bordering iron oxide zone has also been identified as magnetite. The small fan like structure within the pyrrhotite grain is contained within cluster 6 indicating that it is pentlandite.

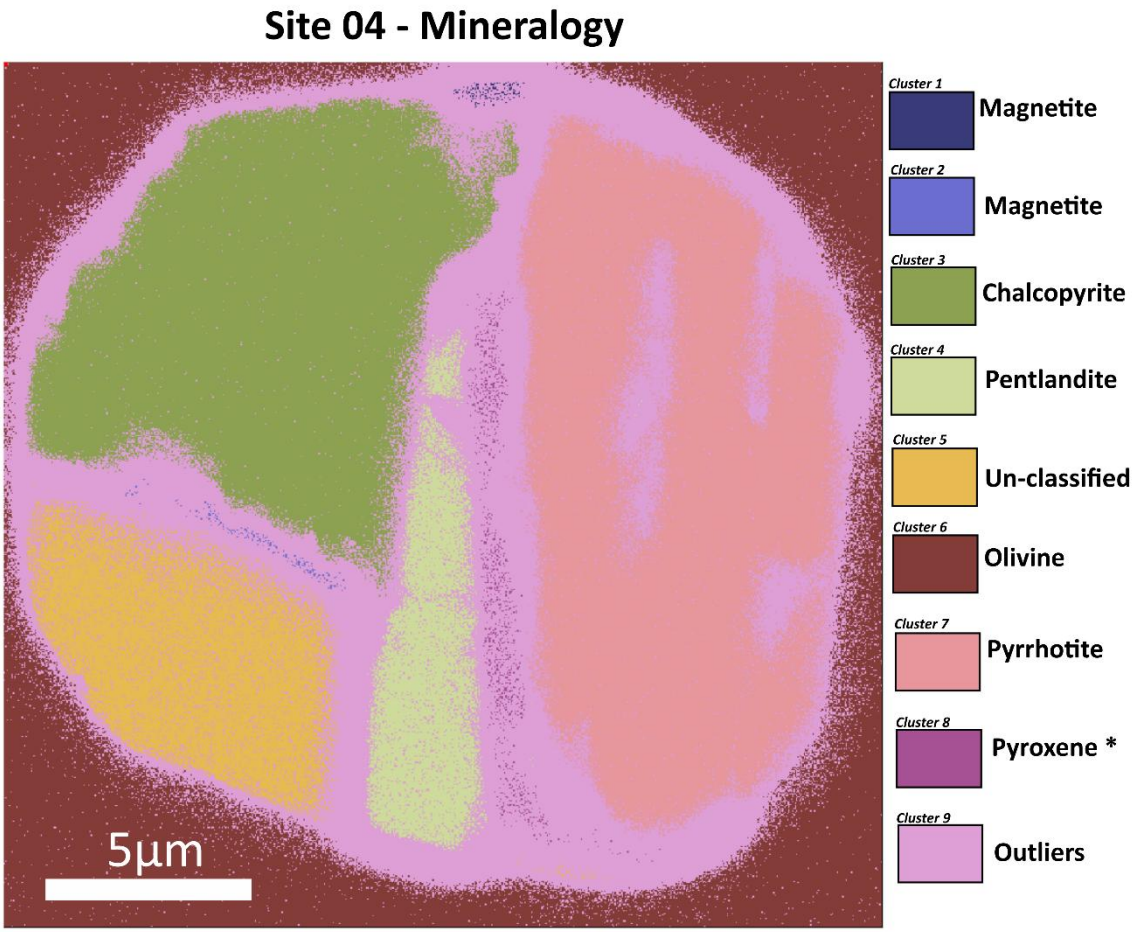

Figure 5.4.16: Figure of the mineralogy of the clusters produced from HDBSCAN - site 04. Tab20 colour scheme used.

Stoichiometry calculations of site 04 data categorises it as an inclusion within an olivine mineral, rather than a chromite mineral, highlighting the advantages of ML (Figure 5.4.16)(Table 5.4.3). Site 04 is also a multi-sulphide mineral, containing chalcopyrite, pentlandite and pyrrhotite. The enriched rim, although not picked out as a separated cluster, is located within the chalcopyrite mineral. Clusters 1 and 2 are occurrences of the iron oxide magnetite, occurring around or within proximity to the chalcopyrite mineral. Cluster 5 is unclassified, with a variety of non-compatible elements measured, however, rich in copper, iron and sulphide.

Table 5.4.3: Mineral formulae produced from stoichiometry calculations regarding data from each cluster. Metal:sulphide ratios are also calculated for sulphide minerals.

Site 04			
	Mineralogy	Calculated formula	Metal $_{(2.d.p)}$: Sulphide ratio
Cluster 1	Magnetite	$Fe^{2+}_{1.28}$ $Fe^{3+}_{1.71}$ O_4	/
Cluster 2	Magnetite	$Fe^{2+}_{1.04}$ $Fe^{3+}_{1.38}$ O_4	/
Cluster 3	Chalcopyrite	$Cu_{0.66}$ $Fe_{0.72}$ $S_{2.0}$	0.70 : 1
Cluster 4	Pentlandite	$(Ni_{1.11}, Fe_{1.22})_{2.33}$ $S_{1.68}$	1.39 : 1
Cluster 5	Un-classified	/	/
Cluster 6	Olivine	$(Mg_{0.64}, Fe_{0.60,} Ni_{0.15})$ $Si_{0.71}$ O_4	/
Cluster 7	Pyrrhotite	$Fe_{1.08}$ $S_{0.97}$	1.11 : 1
Cluster 8	Pyroxene*	$(Fe_{1.00}, Mg_{0.86})$ 1.86 $(Al_{1.19}, Si_{0.85})$ 0_6	/
Cluster 9	Outliers	/	/

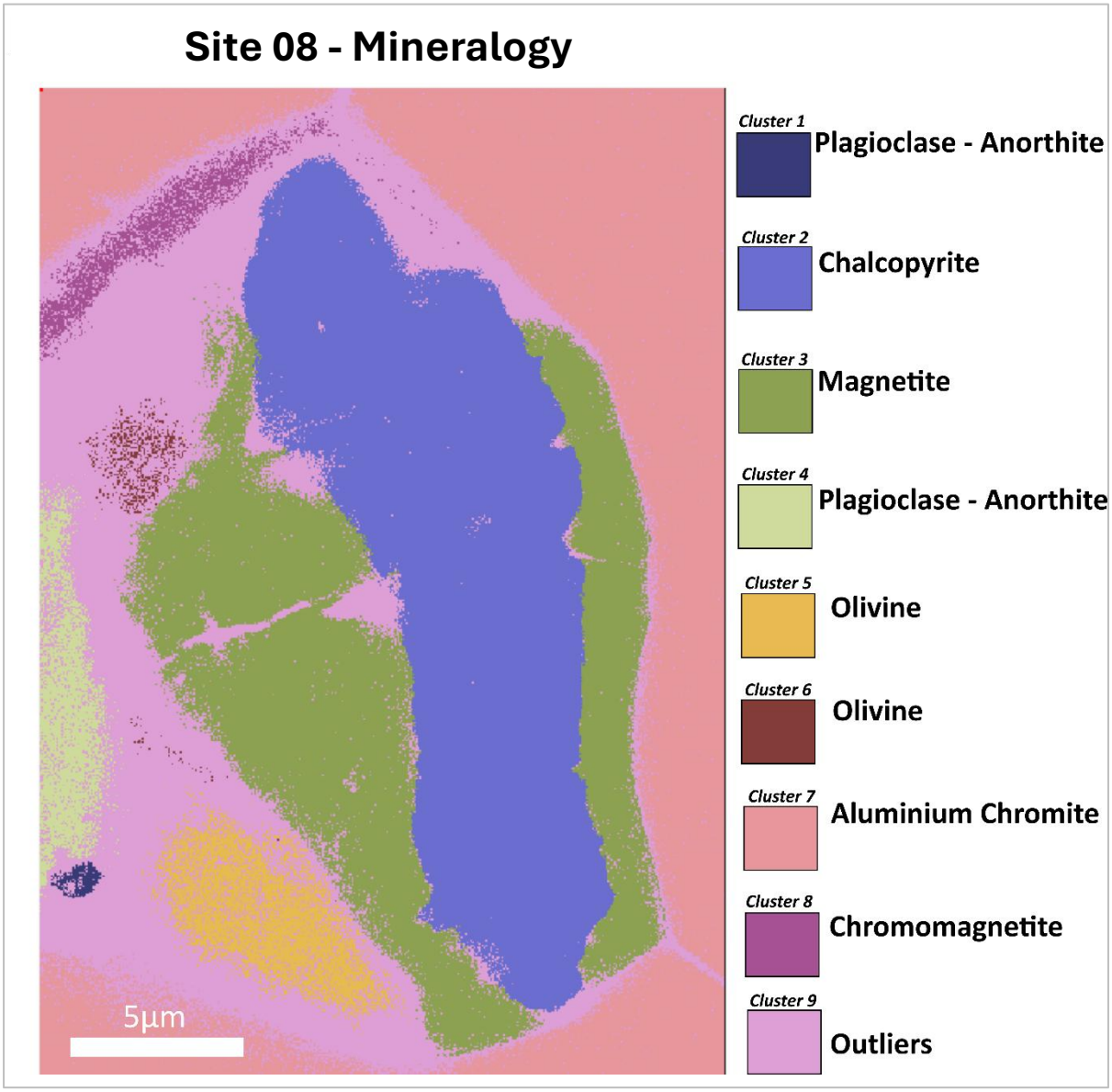

Figure 5.4.17: Navigator image of the mineralogy of the clusters produced from HDBSCAN - site 15. Tab20 colour scheme used.

Calculations defined the mineral as a monomineralic chalcopyrite grain, surrounded by a zone of magnetite (Table 5.4.4). This chalcopyrite and magnetite grain is not an inclusion, bordering mostly chromite, but also some olivine, chrome-spinel (chromo-magnetite) and anorthite (Figure 5.4.17, Table 5.4.4). The enriched rim was unfortunately not pulled out by clustering, but navigational spectral plots display a reduction in sulphur at the edge of the chalcopyrite mineral.

Table 5.4.4: Mineral formulae produced from stoichiometry calculations regarding data from each cluster. Metal:sulphide ratios are also calculated for sulphide minerals.

Site 08			
	Mineralogy	Formula	Metal $_{(2.d.p)}$: Sulphide ratio
Cluster 1	Plagioclase (Anorthite)	$Ca_{0.6}(Al_{2.55}Si_{1.50})O_8$	/
Cluster 2	Chalcopyrite	$Cu_{0.9}Fe_{0.81}S_{2.1}$	0.81 : 1
Cluster 3	Magnetite	$Fe^{2+}_{1.18}Fe^{3+}_{2.36}O_4$	/
Cluster 4	Plagioclase (Anorthite)	$Ca_{1.05}(Al_{2.08}Si_{1.87})O_8$	/
Cluster 5	Olivine	$(Mg_{0.96}Fe_{0.54})_{\Sigma 1.5}Si_{0.71}Al_{0.66}O_4$	/
Cluster 6	Olivine	$(Mg_{1.28}Fe_{1.02}Ca_{0.22})_{\Sigma 2.52}Si_{1.22}O_4$	/
Cluster 7	Aluminium chromite	$Fe^{2+}_{2.0}(Cr^{3+}_{1.01}Al_{2.25})O_4$	/
Cluster 8	Chromo-magnetite	$Fe^{2+}(Cr^{3+}_{0.98}Fe^{3+}_{0.84})O_4$	/
Cluster 9	Outliers	/	/

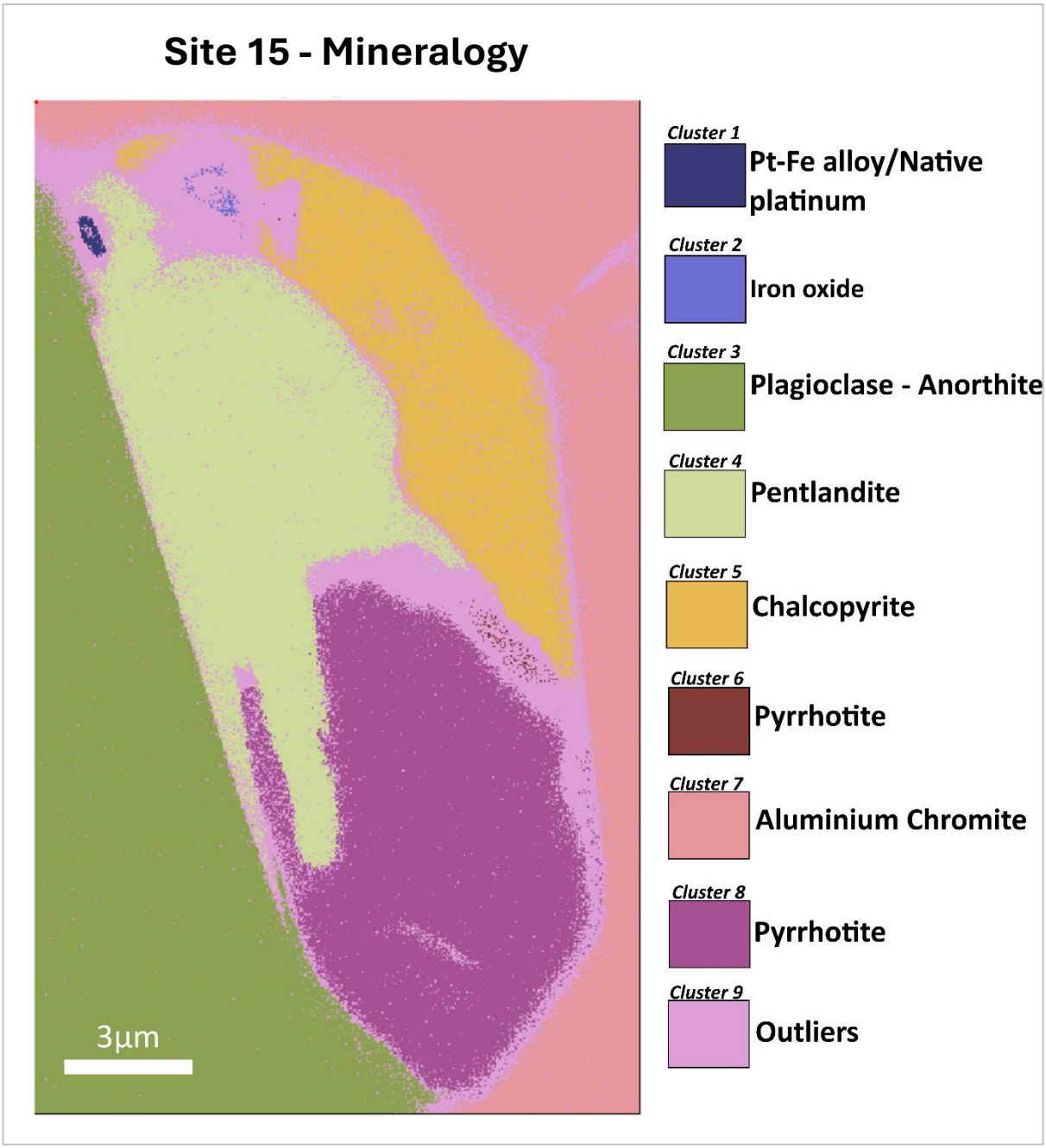

Figure 5.4.18: Navigator image of the mineralogy of the clusters produced from HDBSCAN - site 15. Tab20 colour scheme used.

Calculations classify the sulphide grain as a multiphase composite grain containing sections of pyrrhotite, pentlandite, and chalcopyrite. There is no enriched rim observed at this locality. The platinum grain is pulled out in cluster 1 and can be defined as either a Pt-Fe alloy or a native platinum grain. EDS analysis of cluster 2 indicates an area of iron oxide, however, due to the small size of the cluster leading to high contamination, identification of a specific oxide is not possible (Figure 5.4.18, Table 5.4.5).

Table 5.4.5: Mineral formulae produced from stoichiometry calculations regarding data from each cluster. Metal:sulphide ratios are also calculated for sulphide minerals

Site 15			
	Mineralogy	Formula	Metal $_{(2.d.p)}$: Sulphide ratio
Cluster 1	Pt-Fe alloy/Native platinum	/	/
Cluster 2	Iron oxide	/	/
Cluster 3	Plagioclase (Anorthite)	$Ca_{1.04}(Al_{1.93}Si_{1.94})O_8$	/
Cluster 4	Pentlandite	$(Ni_{0.5}Fe_{0.64})_{\Sigma 1.14}S_{0.85}$	1.34 : 1
Cluster 5	Chalcopyrite	$Cu_{1.16}Fe_{1.2}S_{1.7}$	1.39 : 1
Cluster 6	Pyrrhotite	$Fe_{1.06}S_{0.94}$	1.13 : 1
Cluster 7	Aluminium chromite	$Fe_{0.94}(Cr_{0.62}Al_{1.06})_{\Sigma 1.66}O_4$	/
Cluster 8	Pyrrhotite	$Fe_{1.05}S_{0.93}$	1.13 : 1
Cluster 9	Outliers	/	/

5.5 TEM analysis of selected sulphide mineral

Although two different lamellae were produced from site 04, due to time constraints within the project, only lamella 1 was analysed under the TEM. Aligned with the core aim of the project, lamella 1, located over the reaction rim within the sulphide phase, was prioritised.

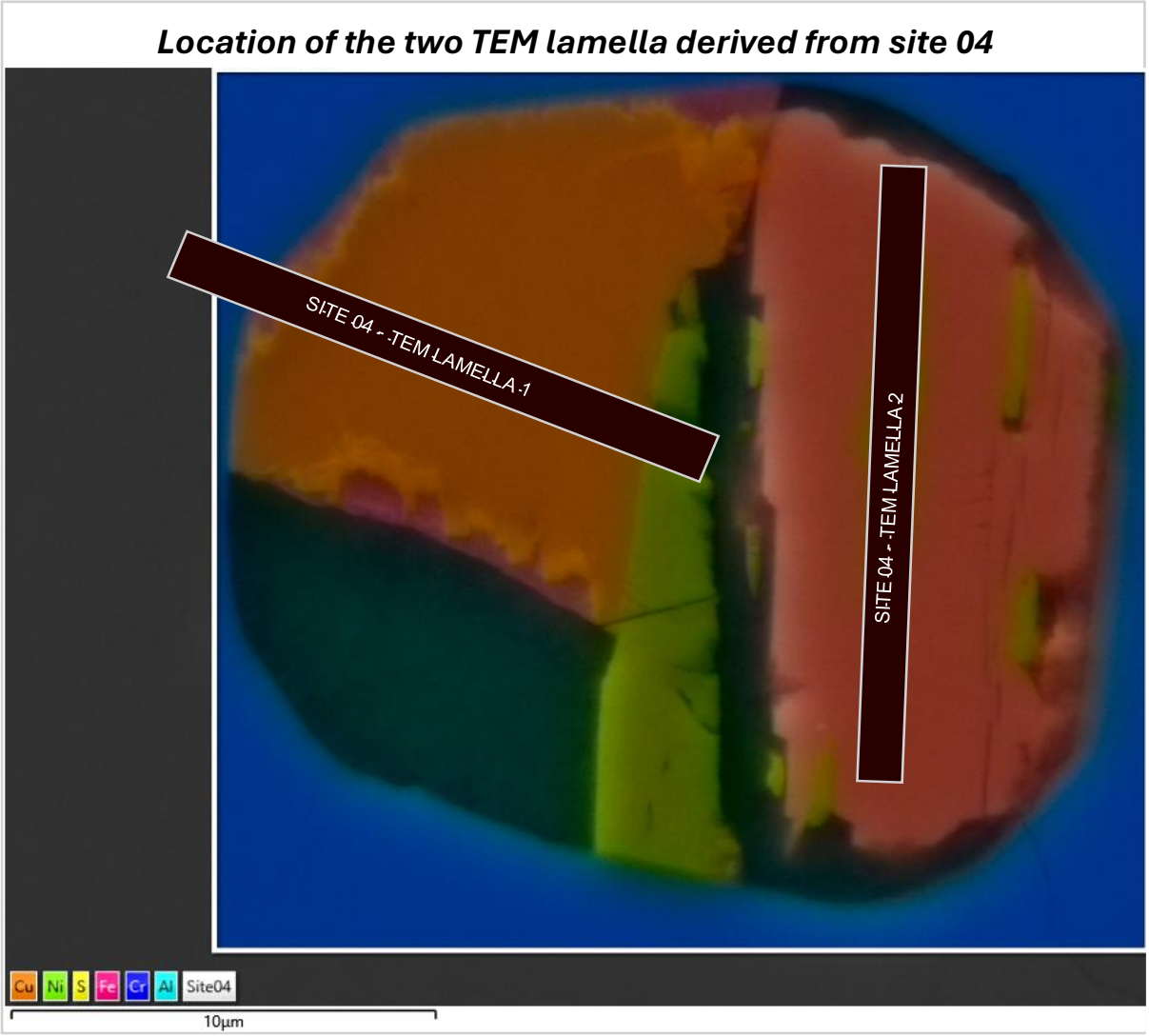

Figure 5.5.1: Figure showing the location of the two lamella extracted from site 04. Lamella 1 located over the reaction rim of the mineral. Lamella 2 located over structures within one of the sulphide phases.

The HAADF image of lamella 1 is shown in Figure 5.5.2 below, providing a cross-sectional view of the mineral grain. The sulphide grain is located on the left side, and the olivine on the right. In this image the copper and iron interaction rim is brighter in comparison to the neighbouring sulphide and chromite, and seen to be continuous downwards within the mineral

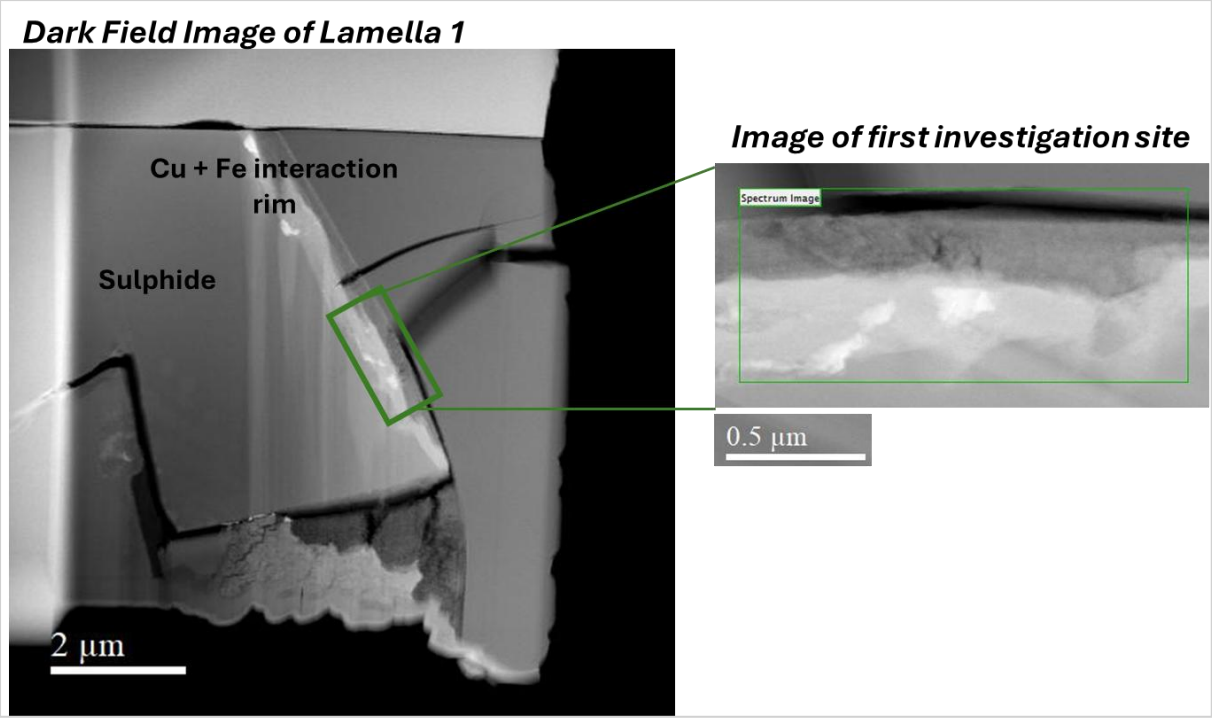

Figure 5.5.2: Figure showing the High Angle A Dark Field image (right hand side) of TEM lamella 1. The rim of interest is shown within the centre of the TEM lamella. A higher mag image of the first investigation site and its location within the lamella is shown on the left.

grain. Unexpectedly, bright nanostructures can be observed within the rim. Three locations/features within the rim were investigated using HAADF imaging and EELS.

Investigation site 1 can be seen in Figure 5.5.2 above. Bright structures within the rim can be observed well in the high mag HAADF image, ranging from 0.30um to 0.55um in length, appearing elongated in shape. The rim is well defined also, with the boarder along the top being particularly well defined.

Singular areal element density maps (Figure 5.5.3), and combined EELS maps (Figure 5.5.4), highlight elemental changes of the rim. Corresponding with previous results, the sulphide rim is seen to become enriched in copper and completely depleted in iron, before starkly transitioning into a zone enriched in iron and oxygen, but depleted in copper. However, investigations within the TEM provide new information regarding the newly observed nanostructures within the rim, some of which are observed here. Darker nanostructures in location 1 (>0.25um) are seen to be depleted in copper, absent of oxygen, and enriched in iron. Other, brighter nano-structures however are not enriched in iron and oxygen

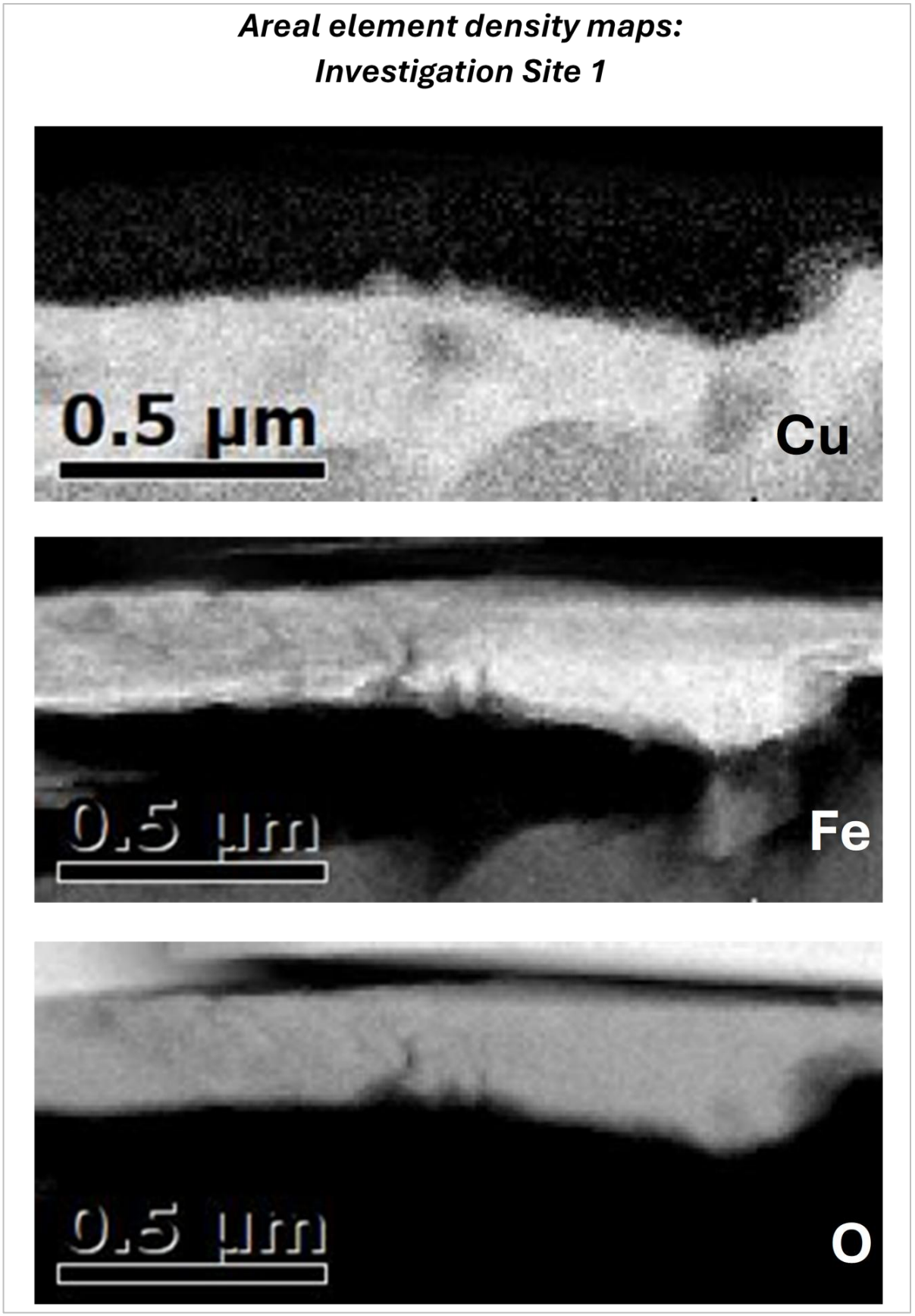

Figure 5.5.3: Individual EELS areal element density maps of location 1, including iron (Fe), copper (Cu), and oxygen (O).

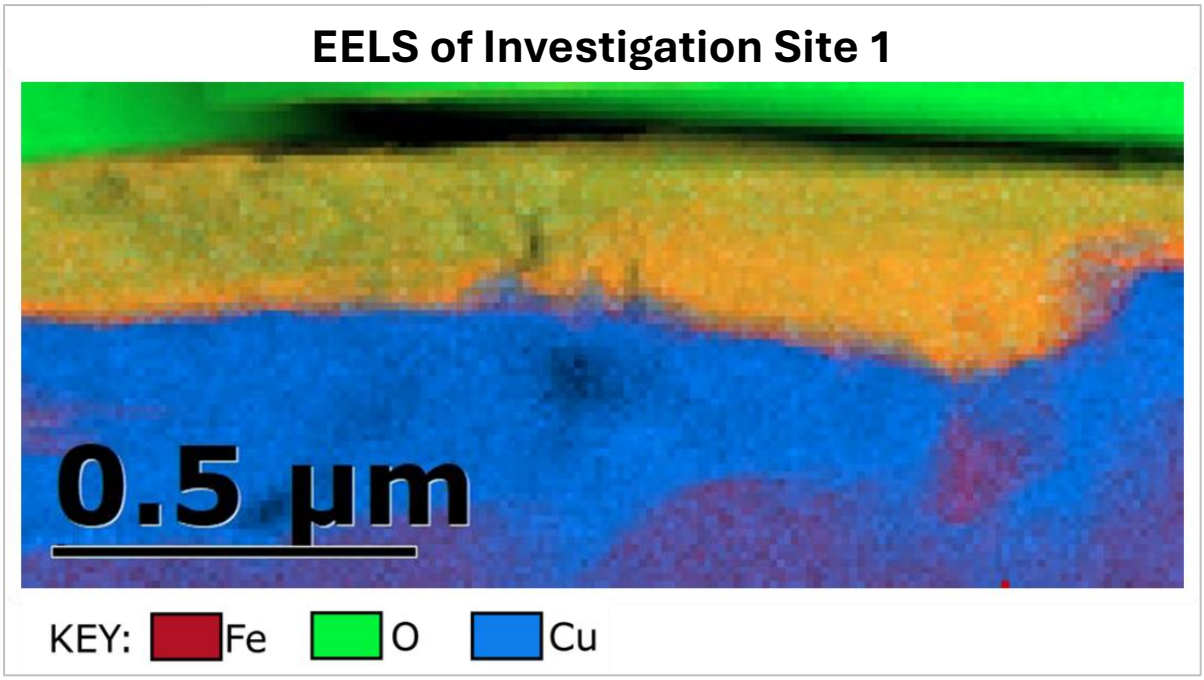

Figure 5.5.4: EELS mapping of the rim with key. Material seen to transition from iron and copper rich at base, to copper rich, to iron and oxygen rich at the top.

Location 2 investigated focuses on the brighter nanostructures within location 1 (Figure 5.5.5 *a,*). From this location, element information collected includes iron, copper and sulphur, as opposed to oxygen in the previous investigative site (Figure 5.5.5 *b, c,*).

EELS mapping highlights that the bright nanostructure (>0.2µm) is absent of iron, depleted in sulphur, and enriched in copper. Furthermore, this location further develops knowledge about the rim, displaying that the sulphide mineral at the base is composed of sulphur, copper and iron, becoming heavily enriched in copper, slightly depleted in sulphur, and completely depleted in iron within the rim, before a stark transition into an iron rich, copper, and sulphur depleted zone.

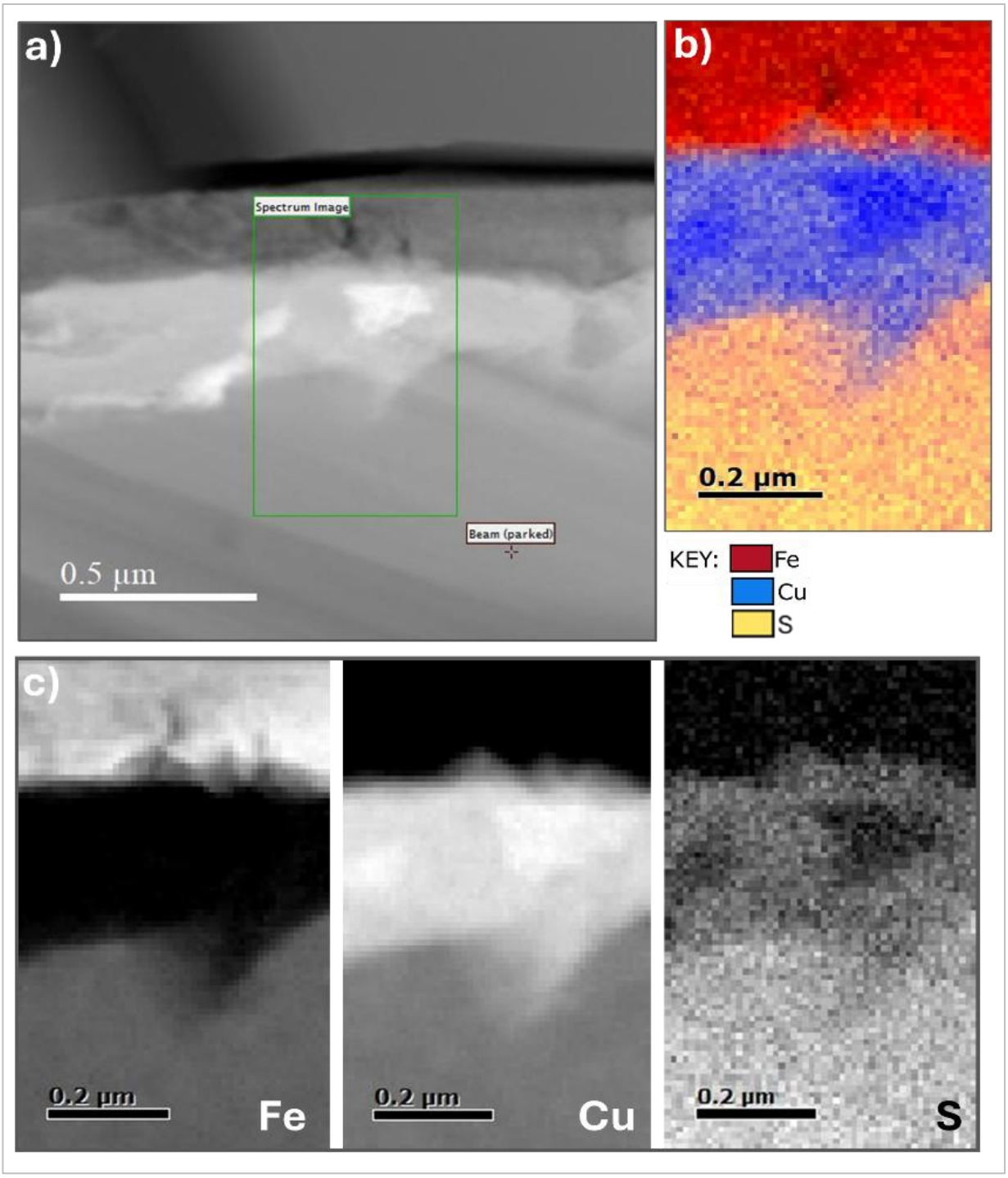

Figure 5.5.5: a) HAADF image of location 2, a bright nanostructure within the rim; b) EELS image of the nanostructure and rim of interest with corresponding key; c) EELS areal element density maps of Fe, Cu and S of the luminous nanostructure and the rim. Collected in TEM.

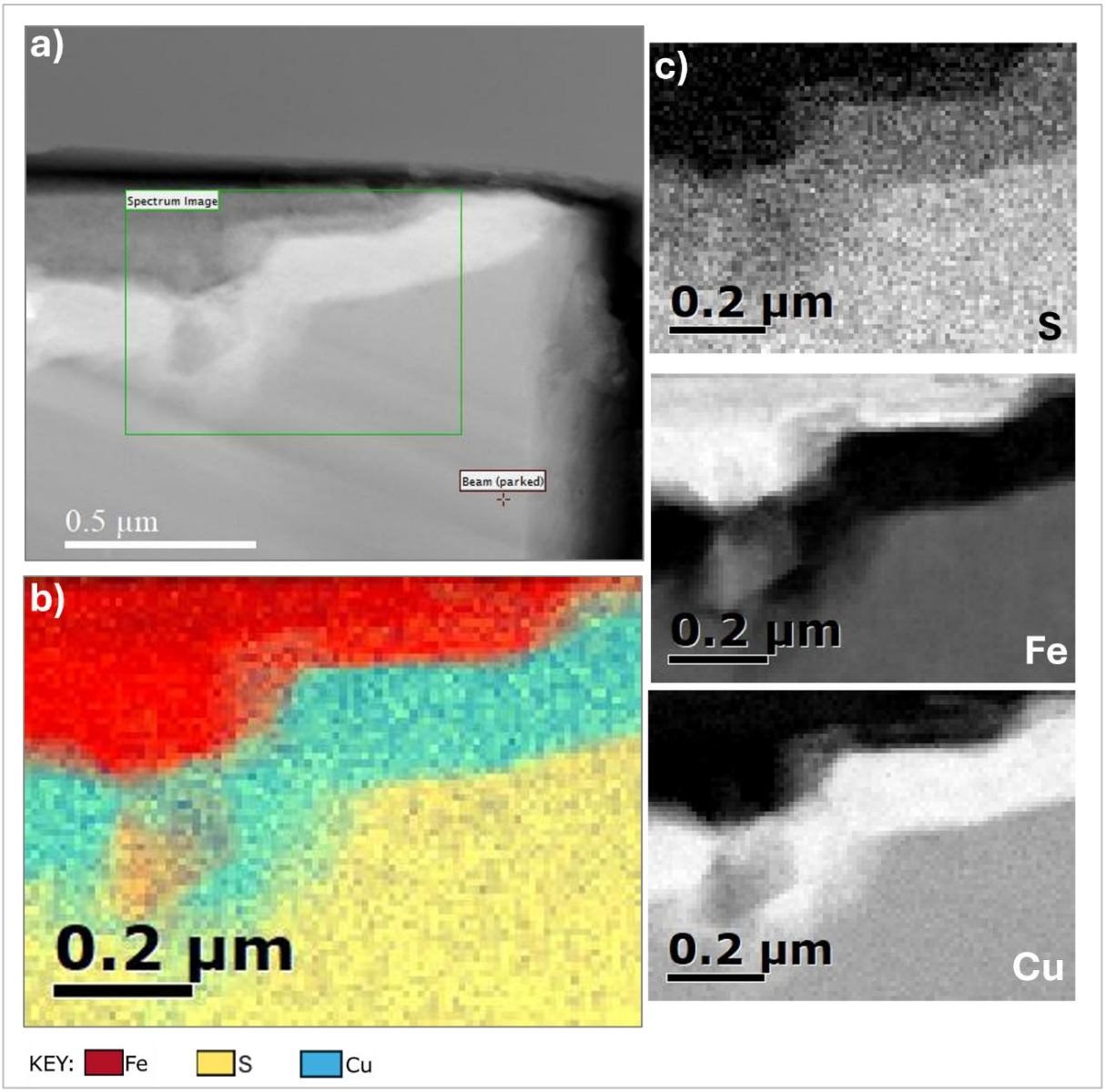

Figure 5.5.6: a) HAADF image of location 3, a dark nanostructure within the rim; b) EELS image of the nanostructure and rim of interest with corresponding key; c) EELS areal element density maps of Fe, Cu and S of the nanostructure and the rim. Collected in TEM.

The last location in which information was collected within the TEM was that towards the lower right end of the rim along the sulphide to chromite border. Here the rim zone above the rim is seen to pinch out. Nanostructures are also present here (Figure 5.5.6).

Element information produced from this site reiterates compositions within the rim (copper rich, iron depleted) and the surrounding zone (iron rich) that pinches off at this location. Sulphur intensity levels within the chalcopyrite mineral produce values of 13k whereas values within the enriched Cu rim drop to 7.5k. This near 50% reduction indicative of a significant

drop in sulphur:metal ratio within the given mineralogy. Consistent with the previous maps, iron enrichment is most intense along the contact between the copper enriched rim and iron zone. The dark nanostructure present within the rim at location 3 aligns with results from location 1, measuring >0.2um in length, whilst likely being depleted in copper and enriched in iron (Figure 5.5.6).

Overall, combined results from SEM-EDS imaging, ML clustering, and TEM analysis clearly display that the main reaction occurring across the enriched rims of the sulphide mineral is that of sulphur loss. Though the extent of alteration differs across sites, the core mineral replacement occurring is the same, being a loss of sulphur within the rim, accompanied by spatially localised iron oxide occurrence.

CHAPTER 6: DISCUSSION

6.1 What makes good quality EDS data, and, what are the advantages of using machine learning algorithms regarding this data

6.1.1 Project Aims

One of the main concerns regarding SEM-EDS analysis is the time taken for effective image acquisition, which can have a major impact on project quality by reducing the amount of sites that can be effectively analysed within a given projects time period, or, by delaying and extending projects due to the acquisition time needed. Additional concerns regard damage to the sample material caused by SEM-EDS analysis. Therefore, optimising acquisition time is essential for many projects (Duma et al., 2022).

As SEM-EDS techniques developed moving from analysis performed on individual points or a few points in a line-scan, to quantification of pixel by pixel maps, the effects of data collection parameters on the quality of data produced has become increasingly apparent (Parish & Brewer, 2010).

Machine learning algorithms performed on SEM-EDS data sets can have numerous additional advantages regarding micro-mineralogical analysis. The unsupervised workflow presented in this project can pull out more information from a data set than elemental maps alone, and, display elemental changes over a ‘smaller area’ more effectively than processing element maps in Oxford Instruments alone. Clustering and subsequent stoichiometry calculations provide accurate mineral maps accompanied by mineral formulae, a level of accuracy not obtained by SEM-EDS mapping alone. Unsupervised algorithms used in this project focus on reducing signal to noise ratio and classification of data packs, increasing the resolution of signals produced and congregating signals that are individually representable but physically linked (Kim et al., 2020; Kato et al., 2025). Exploring the extent acquisition parameters, such as average counts, have on the quality of the original data set, and, the quality of results produced by these unsupervised algorithms, will help determine an optimal baseline for acquisition which provides researchers with the most accurate results in the most efficient timeframe.

To refresh, hypothetically, increasing the average number of counts per pixel should increase the quality of the data produced. By exploring the relationship between average counts per pixel and data quality further, an optimal number of average counts per pixel was confined, providing balance to the trade-off between SEM-EDS acquisition time and data quality. This information is useful to aid streamlining all types of projects as it; (i) allows for efficient collection of good quality data, (ii) increases the amount of sites that can be analysed in a given project, (iii) protects highly sensitive sample material.

6.1.2 What makes good quality data? The effects of exposure on data quality

Results are consistent with the hypothesis and highlight that there is a positive correlation between the average number of counts and the quality of the data produced. However, not every segmented increase in counts produces an equal jump in data quality. In other words, an increase in average counts per pixel does not correlate to an exponential increase in data quality, nor is the increase a consistent rate, but rather a positive relationship which gradually slows and plateaus. The quality plateau is consistently observed from experiment 4 onwards, which contains an average of ~1200 counts per pixel. Nearly doubling average counts to ~3300 in experiment 6 produces a slight increase in image quality, however, this segmented increase is not as significant as prior increases in average counts, and therefore not significant enough to justify the extra time required to collect data sets at these parameters. It can be concluded from these results that the minimal number of average counts per pixel which should be aimed for when collecting EDS-SEM data, in which highest quality of data can be collected within the most effective period of time is ~1200 average counts per pixel.

An increase in data quality is expected when the average counts per pixel increases as it improves the signal to noise ratio (SNR) (Dahmen et al., 2016). In general SEM-EDS data sets can be affected by 7 different types of noise; shot noise, emission noise, thermal noise, quantization noise and environmental noise. The predominant source of noise in the SEM is shot noise which follows Poisson counting statistics, previously explained in the methodology section (Sim & White, 2005; Sim et al., 2025). Consequently noise observes a distribution proportional to the square root of the photon counts. For example, say the total count is X, the shot noise SNR is equivalent to $X/\sqrt{X} = \sqrt{X}$ (Smith, 1997; Takase, 2021). In other words, accumulating more counts allows the 'useful' signal to increase linearly with the number of

counts, whilst random noise increases with the square root of the number of counts. This improves the SNR and leads to a more accurate representation of the 'useful' signal (Marturi et al., 2014; Agarwal et al., 2021; Takase, 2021). This difference between the distribution patterns of noise vs total count also explains how although continuing to increase counts will continue to increase 'useful' signal and improve the SNR, the improvement is not an exponential increase, but one that eventually plateaus which has been observed and concluded from the results in this project. Using the above formula, inserting an increasing value of total counts in 200 count increments, and calculating the equivalent SNR displays how this improvement in SNR is not an exponential improvement, but one that slows over time as counts increase (Smith, 1997; Takase, 2021). It is important to bear in mind that this does not include other more minor noise additions such as partition noise, thermal noise, quantization noise, and environmental noise (Sim et al., 2025).

Table 6.1.1: Table displaying signal to noise ratio of different total counts using formulae provided by Smith, 1997 and Takase, 2021. (Accounting for shot noise only).

Signal Noise Ratio $X/\sqrt{X} = \sqrt{X}$ *X = Total counts*			
Total counts	**Respective noise calculation**	**Result *(2.d.p)***	**Equivalent SNR *(3.d.p)* Signal:Noise**
600	$600/\sqrt{600}$	24.49	1:0.040
800	$800/\sqrt{800}$	28.28	1:0.035
1000	$1000/\sqrt{1000}$	31.62	1:0.032
1200	$1200/\sqrt{1200}$	34.64	1:0.029
1400	$1400/\sqrt{1400}$	37.42	1:0.028

There are a number of notable methods implemented post-processing to improve the SNR in micro-analytical data sets such as; Poisson/Gaussian noise scaling, compressed sensing, and adaptive scanning (Dahmen et al., 2016; Agarwal et al., 2023, 2024). Although these methods do achieve an improved SNR, smaller features can still be lost or less-defined in outputted data, having a negative effect on both the quality of data produced and the quality of results and conclusions that can be made from said data. Post-processing methods also rely heavily on assumptions about the underlying image structure rather than the settings of SE emission at play,

stressing the importance of data acquisition settings in regards to producing good quality data (Agarwal et al., 2023, 2024). Making fundamental physics-based improvements, such as determining the optimal number of counts, and adjusting acquisition settings to achieve this optimum for each respective sample, will produce good quality data sets (Agarwal et al., 2024). Establishing a high quality base, and then later applying appropriate post-processing methods will produce data sets with all the more improved noise to signal ratio and therefore significantly improved resolution and quality.

6.1.3 Advantages of results produced by machine learning algorithms

Once a high quality data set has been acquired by using the optimum acquisition settings, the benefits of using post-processing machine learning algorithms on EDS-SEM data can be seen. Noise reduction and decomposition algorithms used in this workflow include Poisson Noise Reduction and FA, which are effective at distinguishing noise signals from elemental signals, and lead to their subsequent removal (Kim et al., 2020). The unsupervised classification algorithm used in this workflow is HDBSCAN, which can pull features and microstructures from the data, displaying elemental changes over a smaller more precise area (Kato et al., 2025).

A key observation made from the exposure data set outside of the core objective regarding counts is that HDBSCAN on experiment 5 which contains a higher number of average counts than its predecessor experiment 4 resulted in the production of only 8 clusters. Segmentation of minor mineralogy within the sulphide minerals does not decrease, mirroring segmentation of experiment 4, however, these minor sections are less defined. Referring back to the original table regarding the different parameters used during the production of the exposure data set (Table 3.3.1), the difference between parameters of experiment 4 and 5 is that of frames collected, time per frame, and resolution. ‘Frames’ is in regards to the number of individual scans taken the area of interest, and time per frame is a measurement of this in seconds. Resolution of experiment 5 is seen to be 512 (x) x 437 (y), less than counterparts 4 and 6 which have resolutions of 1024 (x) x 768 (y). It is likely that these parameters led to a decrease in resolution which in turn affected the clustering produced. Clustering effectiveness was not terribly adversely affected, producing similar minor-structure segmentation to experiment 4 and 6. But, a fewer number of clusters were produced. This is likely due to ‘over-sampling’ of the data provided by the increase in pixels accompanying the increase in resolution in experiments in 4 and 6. For example, each singular pixel in experiment 5 will be equivalent to around 4

pixels in experiment 4. Thus, each respective phase is being measured more often, which in turn means the clusters are pulled out better. Furthermore, due to the increased interaction volume in higher resolution data sets, over-excitation inside phases leads to improved signal detection, which is particularly useful as a tool to aid the pronunciation of signals within small features and make them stronger. Combined, these factors are incredibly useful for mineralogical analysis, particularly when trying to distinguish and analyse minor features within subjects. Emphasising the importance of resolution accompanying higher count data sets to produce accurate ML results.

6.2.4 Project strengths, weaknesses, and relevance

Conclusions drawn regarding the effect collection parameters, particularly the average counts per pixel, have on the quality of the data produced and how to produce the highest quality data sets in the shortest period of time can be useful to other projects utilising EDS-SEM analysis. This conclusion is particularly apparent to projects concerning the microanalysis of multiple sites or those with samples sensitive to radiation, as aiming for the optimal number of counts stated could help streamline projects and lead to maximising the amount of effective and quality data produced. This pre-determined number of average counts per pixel can be achieved by altering data collection parameters such as; dwell time, detector type, and magnification. Collection time will alter in each respective project as average counts per pixel can also be affected by the elemental and topographical properties of the sample material (Duma et al., 2022; Jeol, 2024).

Conclusions regarding the optimal number of average counts per pixel were later implemented whilst collecting the mineralogical data set within this project. This allowed the best quality data to be collected in the shortest possible time, which had a direct impact on the quality of research produced, increasing the number of sites analysed, allowing development from SEM work to FIB/TEM work, and, overall streamlining of the project.

The exposure data set analysed in this project had multiple points of strength which made it ideal for setting about to answer the question of what is the optimum number of counts. Firstly, there was a benefit to using the specific site chosen, as the minerals within the site are useful to identify the differences in data quality. Segmentation of micro-structures within sulphide minerals of the site are particularly useful for observation and analysis of the quality of different

data packs FA and clustering results. Secondly, choosing data packs for analysis from the exposure set based on fairly equally spaced increments (in regards to average counts per pixel), enabled efficient analysis within the timeframe of this project.

However, there were some drawbacks within this project. Although the data packs analysed where chosen in equally spaced increments, the number of packs used remains small, as well as the larger exposure data set. To improve accuracy analysis of the entire exposure data set would develop on understandings gathered from this current work. Furthermore, it would be effective to explore how the differences in FA and PCA (discussed in depth in methods) relate to average counts per pixel, and the consequence that each method has on clustering and Bruker analysis.

Analysis of the exposure experiment data set has highlighted the importance of acquisition parameters, particularly average number of counts per pixel and dimensional resolution, in producing good quality data packs. However, this study has also highlighted that further work is needed to accurately address other aspects of the exposure data set which were not fully explored.

There have been multiple other papers published spanning the last two decades which tackle ways to improve collection efficiency and reduce sample damage, whilst maintaining the signal to noise ratio, some of which address fundamental aspects not focused on within this study. For example, investigations regarding ‘total dose’, ‘dose-rate’, and ‘dose sharing multi-frame spectrum-imaging’ (MFSI). The first and second stated were coined after various studies on oxide materials presented that there is no critical total dose in which high degrees of observable damage is accumulated, however, there appears to exist a threshold of dose-rate below which damage to the sample is not observed (Jiang & Spence, 2012; Johnston-Peck et al., 2016). This is due to the fact that accumulation of observable damage is only possible when the damage rate is higher than the recovery rate, therefore, dose-rate is a significant contributing factor to sample damage (which has a subsequent effect on data quality) and could be a factor confined and optimised during acquisition, particularly when conducting research on radiation-sensitive material (Jiang & Spence, 2012). The latter is built on the premise of sampling data points randomly opposed to every single data point (Jones et al., 2018). This method was proposed to improve on drawbacks commonly faced as repercussions of attempting to improve SNR by increasing dwell-time, which can cause scanning distortions, stage-drift, focal drift, or, by

increasing beam current, which can cause rapid sample damage and carbon contamination (Egerton et al., 2004; Jones & Nellist, 2013). This dose-sharing tactic proved to be highly effective at addressing these drawbacks and more. Results displayed that MFSI decreased sample damage, increased crystallographic veracity, improved SNR, and an enlarged usable field of view (Jones et al., 2018). Use of this knowledge and various other techniques, in conjunction with the results from this project, could further confine the optimum settings and strategies during data acquisition in which good quality data sets are produced, resulting in directly improving project results.

6.2 Machine learning selection of phases and mineralogy of phases identified

6.2.1 Aims and results

The core aim of this project is to investigate the geochemical properties of observable enriched rims within the sulphide minerals of the chromite seams, confirming what elemental changes occur using SEM-EDS element maps, ML algorithms, and TEM analysis. Additionally, making observations regarding heterogeneous sulphides, inclusion/non-inclusion sulphides, possible alteration products, and proximate PGM enrichment. Building then on these observations to further understand magmatic sulphide formation, low-temperature sulphide formation/alteration processes, and possible oxidation/desulphurisation or hydrothermal processes at play within the Rum layered intrusion, and by extension other similar layered intrusions around the globe, and how these processes effect PGM enrichment.

To briefly refresh, analysis of site 01 was the most effective regarding the core aims of this project. ML analysis of site 01 was consistent with the sulphide boundaries observed in SEM-EDS element mapping, and successfully pulled out the enriched sulphide rim (cluster 4) and the bordering iron/oxygen rich material (cluster 2) (Figure 5.4.4). Cluster 4, representing this enriched sulphide rim, produced a formula of $Cu_{1.52}\ S_{0.79}$, representing a composition between chalcocite/digenite (PBZAFF). Cluster 2 can be identified magnetite, with an elemental formula of $Fe^{2+}_{0.66}\ Fe^{3+}_{1.33}\ O_4$ (Table 5.4.2). Stoichiometry calculations also confirmed the sulphide phases were that of pyrrhotite (cluster 3 - $Fe_{0.82}\ S_{0.77}$), chalcopyrite (cluster 5 - $Cu_{0.58}\ Fe_{0.55}\ S_{.95}$), and, pentlandite (cluster 6 - $(Ni_{0.46}, Fe_{0.65})_{\Sigma 1.11}\ S_{0.96}$). Similar to site 01, sites 04 and 15 are also composite sulphides, with three separate sulphides phases observed (Figure 5.4.5, 5.4.7). Consistent with results from site 01, these are pyrrhotite, chalcopyrite and pentlandite (Table 5.4.3). Site 08 is monomineralic chalcopyrite, but does contain a enriched sulphide rim (Figure 5.4.6). This rim was not pulled out from clustering, however, the same elemental changes observed in site 01 and site 04 element maps regarding enrichment of copper, and bordering material enriched in iron and oxygen, were observed (Figure 5.3.4).

6.2.2 Base metal sulphide: Features and formation

Before addressing these rims further, the origin of base-metal-sulphides and other magmatic textures observed within this project must be discussed. Textures within sulphides located in the surrounding peridotite and troctolite units suggest that the base metal sulphides crystalised within the crystal mush (O'Driscoll et al., 2025). The near-spherical shape of the sulphide inclusions of site 01 and site 04 indicate that the immiscible sulphide droplets were formed/partially formed before becoming encapsulated within the chromite/olivine hosts (Prichard and Fisher., 2004). Interstitial sites 08 and 15 are elongated, but maintain these rounded to sub-rounded boundaries. Composite sulphides containing more than one sulphide phase are likely to result from crystallisation via the MSS and ISS transitions (O'Driscoll et al., 2025). Based on experimental data detailed by Helmy et al., (2021), pentlandite phases are likely to originate from the MSS between 550º-450ºC (Etschmann et al., 2004; Helmy et al., 2021; Smith et al., 2023). Ni poor pyrrhotite is likely to form either from the MSS at around 450ºC or from decomposition of the ISS >200ºC (Helmy et al., 2021). Results from this project place pyrrhotite as Ni poor, with elemental formulae produced containing little to no Ni. For example, pyrrhotite of site 01 produced a formula of $Fe_{1.12}$ $S_{0.92}$, and pyrrhotite of site 15 produced a formula of $Fe_{1.06}$ $S_{0.94}$ (Table 5.4.2, 5.4.4). Therefore, it is likely to have formed by either of these two methods. Chalcopyrite exsolves from both the MS and ISS >450ºC (Helmy et al., 2021). However, there is no proof indicating one fractionation method over another of sulphide melt (O'Driscoll et al., 2025). Other minor features can be found within composite sulphide phases due to exsolution at lower temperatures (>250ºC), such as flames, fans or blades of pentlandite hosted within pyrrhotite (Hughes et al., 2016; Smith et al., 2023). Some of these minor features can be observed within this project. A pentlandite fan can be seen in the pyrrhotite phase in site 01, pulled out by HDBSCSAN, producing a formula of $(Ni_{0.46}, Fe_{0.65})_{\Sigma 1.11}$ $S_{0.96}$ (Table 5.4.2). Additionally, pentlandite blades can be observed within the pyrrhotite of site 04. These were not pulled out by HDBSCAN but are observable in the EDS-SEM element map (Figure 5.3.4). The presence of these features indicate that exsolution processes within some sulphides continued to temperatures >250ºC.

6.2.3 Enriched rims: Mineralogy and formation

Enriched rims are only found within chalcopyrite base-metal sulphides, and are not found at every locality sampled regardless if they are composite or monomineralic. Localised alteration

from chalcopyrite to copper rich minerals such as chalcocite, bornite etc, is a complex fluid-driven redox reaction, resulting in major sulphur and minor iron loss (Chaudhari et al., 2021; O'Driscoll et al., 2025). Metal-sulphur ratio within chalcopyrite (site 01 – cluster 5) is 1.20:1, however within the alteration rim (site 01 – cluster 4) the metal-sulphur ratio is 1.56:1 (Table 5.4.2). Supporting that one of the main reactions occurring across the rim of the mineral is that of sulphur loss. Stoichiometry calculations produced a mineral formula between chalcocite/digenite. This is consistent with recently published papers which also reported these sulphide rims within other units of the Rum suite such as unit 10 troctolite, unit 10 peridotite and a variety of peridotite plugs/dykes. On occasion, bornite rims have also been reported alongside chalcocite and digenite, with these Cu-rich S-low minerals occurring as local alteration products of chalcopyrite (Hughes et al., 2016; O'Driscoll et al., 2025). Bordering zones enriched in iron and oxygen are deposits of magnetite, an iron oxide (Table 5.4.2, 5.4.3, 5.4.4). Former projects observe that sulphides within the rum layered intrusion exhibit alteration and breakdown textures when in proximity to the chromite seams, a conclusion parallelled by this project. The extent of alteration concerning chalcopyrite rims and intergrowths of iron oxides varies in degree across the seam (Power et al., 2000; O'Driscoll et al., 2025). An observation mirrored within this project as the enriched rims within the seam differ in thickness, as site 01 are widest (2.6um), followed by site 08 (1.6um) and lastly by site 04 (1.4um) (Figure 5.3.2). Iron intergrowths are larger within the interstitial sulphide site 08, while the inclusion multi-phase sulphides site 01 and site 04 contain smaller iron intergrowths respectively (Figure 5.4.4, 5.4.5, 5.4.6). Together, these observations highlight the varying nature of alteration across sulphides of the seam. PGM enrichment, when occurring, is common at or alongside the margins of sulphide grains (site 15) (Figure 5.4.7) (Power et al., 2000; O'Driscoll et al., 2025).

Mineral replacement reactions involve the dynamic exchange of elements between a reacting fluid and mineral grain, which can be a geochemically complex development often composed of a multi-step process (Chaudhari et al., 2021). When a mineral comes into contact with a fluid, with which it is out of equilibrium, in order to reduce the free energy of the combined mineral-fluid system and re-equilibrate, reactions occur (Chaudhari et al., 2021; Chaudhari et al., 2022; Putnis, 2009). Considering the balance of free energies for solid-fluid interactions, the reduction in free energy required is achieved by considering the free energies of both the solids and fluids involved. As the composition and structure of either changes, a reaction following a method of Solid(1) + Fluid (1) → Solid (2) + Fluid (2) occurs (Putnis, 2009). The

widespread reaction involving chalcopyrite and an aqueous solution results in changes of the mineral composition and exchange of Cu and Fe ions between both the chalcopyrite and the fluid solution. This reaction is commonly regarded as a 'model' reaction for complex fluid-driven sulphide reactions involving redox and compositional changes (Chaudhari et al., 2021; Chaudhari et al., 2022). In recent years, it has become clear that many fluid induced mineral replacement reactions follow interface-coupled dissolution-reprecipitation mechanism (ICDR). ICDR mechanism involves the simultaneous union between the dissolution of the parent mineral and the precipitation of daughter minerals. This process results in preservation of the parent minerals shape to nano/micro-meter scales, as well as the crystallographic orientation and internal textures (Chaudhari et al., 2021; Chaudhari et al., 2022; Putnis., 2009; Xia et al., 2009). When the fluid comes into contact with a mineral of which it is undersaturated, the mineral begins to dissolve, and an interfacial layer can then become super saturated with a more stable product/products (Altree-Williams et al., 2015). Additionally, ICDR mechanisms typically dominate at lower temperatures, as dissolution and precipitation are fast relative to solid-state diffusion under the same conditions (Altree-Williams et al., 2015; Chaudhari et al., 2022; Putnis., 2009).

The presence of low sulphur rims within chalcopyrite, Fe-oxide minerals, and exsolutions comprising of ilmenite and Ti-rich spinel in chromite crystals where originally believed to result from moderately low temperature oxidation (<600ºC) (Power et al., 2003). Recent developments indicate that low-temperature hydrothermal processes, coupled with relatively oxidising conditions, may be the cause for observed sulphur loss (O'Driscoll et al., 2025). As previously stated, aqueous alteration of chalcopyrite commonly leads to the exchange of Cu and Fe ions (Chaudhari et al., 2021). This is consistent with petrographic observations made within this project. The enriched rims within chalcopyrite become super-saturated in Cu, forming the minerals diogenite/chalcolite, whilst preserving the shape and size of the parent chalcopyrite mineral. Fe-oxides and hydroxides then develop as intergrowths within or surrounding the altered sulphides, associated with oxidation processes and ion exchanges during alteration. Observed as magnetite within sites 01, 04, and 08 within this project. Although rare, relict sulphide can be observed within these Fe-oxides, further indicating that they are an alteration product of the sulphide (Chaudhari et al., 2021; O'Driscoll et al., 2025). Additionally, new ^{34}S isotope data displays S isotope heterogeneity over small length scales which cannot be purely accounted for by differing volumes of magma-crust interactions. The fractionating of heavier S isotope values in sulphide samples is indicative of low-temperature

alteration which has driven sulphur loss from these sulphides as aqueous sulphate, and in turn caused the original isotopic values to be partially overprinted (O'Driscoll et al., 2025). It is likely that an aqueous solution which could interact with the minerals of the Rum layered intrusion at sub-solidus temperatures (particularly <400ºC) would likely contain both So_4^{-2} and H_2S. Furthermore, dissolution of sulphur is more efficient when in contact with relatively oxidising fluids as opposed to reducing fluids (Frost, 1985; O'Driscoll et al., 2025). Sulphur loss from chalcopyrite fractionates ^{34}S strongly at low temperatures. Loss of only 5% sulphur in some chalcopyrite minerals drives heavy ^{34}S fractionation at temperatures ranging from 50ºC to 100ºC. This is an appropriate temperature range for Cu-rich S-low sulphides such as chalcolite to form (O'Driscoll et al., 2025). In addition, laboratory experiments revel that magnetite can form within this temperature range, and beyond (50-130ºC) (Kars et al., 2023).

Further conclusions can be made from petrogenic observations within the seam. As shown in this project, for example in figures 5.3.1 & 5.4.17, not all sulphides are multiphase composite minerals, highlighting the differences in sulphide droplet composition. Moreover, not all sulphides contain alteration rims and localised Fe-oxide intergrowths, with alteration features within effected sulphides differing in intensity across the seam also (e.g. site 01 altered more intensely than that of site 04). The presence of sulphides which are unaltered in proximity to sulphides containing alteration features, alongside varying degrees of alteration across the seam, is a clear indication that the alteration of magmatic sulphides by an aqueous liquid at low temperatures occurred at a low fluid-rock ratios and was extremely spatially localised. This observation echoes that of O'Driscoll et al (2025), which observed altered and unaltered sulphide minerals within <100um of each other. In the magnetite mineral of site 01 and site 08, developments of internal microstructure can be observed, particularly close to the outer rim. These microstructures parrot that of concentric banding. Concentric zoning of alteration oxide minerals, such as magnetite, suggest that growth was a stepped process occurring during alteration (O'Driscoll et al., 2025).

The final lot of petrographic observations made within this project regarding the enriched rims were made from TEM lamella 1 taken from site 04 (Figure 5.4.16). Analysis displayed the persistence of these Cu-enriched/S-depleted rims at depth within the sulphide mineral. Towards the base of the sample, highly disseminated textures can be observed, preserving evidence of chalcopyrite breakdown and Fe-oxide formation by proposed aqueous processes. This is

consistent with previous points of the discussion, corroborating that the main reaction occurring across the rim is concerning chalcopyrite loss.

Interestingly, other nano-scale structures can be observed within the rim. There appear to be two distinct nano-structure ‘blebs’ within the rim, one being lighter and the other being darker (Figure 5.5.2). EELS analysis indicates that the lighter nano-structures are likely depleted in S and enriched in Cu, within the already enriched Cu rim of likely digenite/chalcolite. The darker nano-structures are enriched in Fe, but depleted in Cu and O. The depleted S/Cu enriched structures tend to be more common, larger and elongated, ranging from 0.30-0.55um at the longest point, whereas their Fe counterparts tend to smaller and angular, around 0.25um at the longest point (Figure 5.5.3, 5.5.5, 5.5.6). The seemingly sporadic presence, shape and size of these nano-structures highlights the spatially localised nature and varying intensity of proposed alteration. Overall, the TEM sample effectively displays that the alteration rims, though minor, are more complex than a rim of pure diogenite/chalcolite.

Although no conclusive results concerning the mineralogy of these nano-structures can be made, the depletion of Cu, S, and O, within the darker ‘blebs’ is indicative of a more iron-rich mineral. Likely a product of sulphur loss and Fe ion exchange during alteration (Chaudhari et al., 2021; Chaudhari et al., 2022). Hypothetically, the product could be a Fe-enriched sulphide, in comparison to that of the chalcopyrite phase and chalcolite rim. Or, alternatively, indicative of and Fe-rich O poor spinel. Within Rum, crystallographically constrained exsolutions composed of low O, enriched Fe and Ti spinel, such as ilmenite, can be observed (Putnis & Price, 1979). These exsolutions have been observed within the unit 7-8 chromite seam, often within the mid-lower section of the seam in which site 04 is located (Figure 5.3.2), and corroborate the argument for oxidation of the seams at low temperatures (O’Driscoll et al., 2025; Power et al., 2000; Putnis & Price, 1979). Although, further work is required to fully confirm either of these possibilities.

Lastly, within the Fe-oxide (magnetite) mineral bordering the sulphide rim, minor textures can be observed. The mineral is particularly enriched in Fe along the contact boarder in all three locations analysed (Figure 5.5.3, 5.5.5, 5.5.6). In location 1, the beginning of what appears to be concentric banding can be observed consistent with prior SEM observations and other research project which identify these textures within Fe-oxide alteration minerals, and are an

indication that Fe-oxide formation was a stepped process during sulphide alteration (O'Driscoll et al., 2025).

Given the combination of petrographic observations made from the sulphides and Fe-oxides of the unit 7/8 chromite seam sampled within this project, alongside petrographic observations made in neighbouring units of the Rum layered suite by parallel projects, as well as recent sulphur isotopic and geochemical data published, it can be suggested that desulphurisation occurring under low temperature conditions (<100ºC), via aqueous alteration by an oxidising solution at low fluid to rock ratios is responsible for sulphur loss from the magmatic sulphides affected. Leading to the formation of alteration features such as enriched rims of digenite/chalcolite, and, exsolution of breakdown product minerals in close proximity such as magnetite (Hughes et al., 2016; O'Driscoll et al., 2025; Power et al., 2000).

6.2.4 Platinum group minerals: Occurrence and mineralisation

In regards to PGM mineralisation, the only site analysed containing a PGM is site 15. As established, PGMs are have high affinity to sulphides and are concentrated within the chromite seam. Previous research has recorded a large variation in which mineral species the PGMs within Rum occur, such as; Fe-Pt alloys, Pd-Cu alloys, native Pt, laurite, tellurides, bismuthides, Pd-Sb arsenide's and native Ag (Butcher et al., 1999; Power et al., 2000; Power et al., 2003). SEM analysis identified the site 15 grain as a Pt grain. EDS analysis of the cluster regarding the site 15 grain produced values high in Pt, Fe and Ni. Utilising EDS results published by Butcher., et al (1999), and comparing the most fitting results to the EDS (PBZAFF) results produced in this project, the grain presented in site 15 most consistent with either a Pt-Fe alloy or a native Pt grain (Table 6.2.1)

Table 6.2.1: Table comparing results produced by Butcher et al (1999) and results produced from site 15.

	Butcher et al., 1999	**Butcher et al., 1999**	**Site 15**
Grain size (um)	1.6 x 1.7	1.0 x 0.6	1.4 x 0.4
Enclosing phase(s)	Plagioclase	Pentlandite	Pentlandite & plagioclase
Analysis	**Pt** 85.7 **Fe** 10.4 **Ni** 1.6 **Cu** 0.5	**Pt** 57.0 **Fe** 15.8* **Ni** 12.3* **S** 14.9*	**Pt** 39.0 **Fe** 21.6 **Ni** 16.9 **Ca** 11.6* **Si** 5.6* **Al** 5.0*
Total	98.2	100.0	99.7
Classification	Pt-Fe alloy	Pt-Fe alloy or native Pt	Pt-Fe alloy or native Pt

*Contamination from surrounding minerals due to small size of the platinum grains. Low totals due to overlap with enclosing phase (Butcher et al., 1999).

Research from Power et al (2000) highlights that 71% of Rum's chromite seam PGMs are associated with sulphide minerals. A significant proportion are totally enclosed by sulphide grains (39%), with most occurring along grain boundaries sulphide-silicate (34%), sulphide-chrome-spinel-silicate (23%), and sulphide-Fe-oxide (4%) respectively (Power et al., 2000). The site 15 grain is seen to predominantly be in contact with the sulphide mineral, and partially boarders the silicate anorthite (Figure 5.4.18). This would classify the nature of its association that of sulphide-silicate, the most common of associations. Observed mineralogy for sulphide-PGM associations within the chromite seam displays that pentlandite is the most common totalling 51% of sulphide associations (Power et al., 2000). Site 15 aligns with this as the sulphide mineral in contact was identified as pentlandite (Figure 5.4.18, Table 5.4.5). Qualititive research shows that around 95% of PGM grains hosted within the chromite seam

are <6μm, with the modal size between 1-1.9μm (Power et al., 2000). The mineral grain presented in this project is elongated in shape, measuring 1.4μm along the longest section, defining it as a perfectly average PGM grain.

Interestingly, the site 15 grain is located in close proximity to an unidentified, minor, Fe-oxide mineral, likely an alteration product (Figure 5.4.18). 12% of PGMs within the chromite seam are seen to be hosted within Fe-oxide and hydroxide phases (Power et al., 2000). Research regarding PGMs within neighbouring peridotite plugs of Rum also record PGM within Fe-oxides, hydroxides, alteration rims, and thin serpentine filled fractures (Power et al., 2003). In some cases, PGMs occur as elongated grains with cleavage parallel to the cleavage within chlorite after biotite (Power et al., 2003). It is therefore clear from observations made across the board, including within this project, that PGMs are preferentially located around sulphide grain boundaries associated with or within proximity to Fe-oxide and hydroxide alteration minerals, and on occasion display cleavage alignment with altered minerals, which together is highly suggestive that late stage hydrous processes which result in the oxidation and sulphur loss of sulphides present are additionally a significant driver for PGM exsolution (O'Driscoll et al., 2025; Power et al., 2000; Power et al, 2003).

6.2.5 Key takeaways

Observations made in this project have a variety of implications, concerning previously substantiated claims and speculative considerations alike. Petrographic observations involving the wide variety of magmatic sulphides present across the seam, as either inclusions or interstitially, as either composite or monomineralic, and containing minor features or featureless, have a number of implications. The first listed observation endorses ideas concerning the nature of sulphide immiscibly and subsequent droplets, particularly in relation to the chromite seam (González-Jiménez et al., 2025). The latter two observations align with prior reports and highlight the diversity in composition of sulphide droplets produced from the immiscible sulphide liquid (Hughes et al., 2016; O'Driscoll et al., 2025). Combined with ranges of ^{34}S isotopic data which develops the understanding of crustal sulphur influence on magmatic sulphide formation, and how crustal sulphur influence may vary across the units of the Rum layered intrusion (Hughes et al., 2016; Hulbert et al., 1992; O'Driscoll et al., 2025). Confining the extent of which crustal sulphur components are present has significant implications on behalf of precious metal enrichment, as it determines that external sulphur was

indeed required to cause sulphide saturation which consequently results in PGM enrichment in the Rum intrusion (O'Driscoll et al., 2025). These latter two observations also display the variation in method in which sulphide mineralisation occurs, with composite sulphides and minor exsolution features indicating that sulphide exsolution continued within some grains to temperatures <250ºC.

Petrographic observations regarding sulphide rims and Fe-oxide formation have additional implications. Observing breakdown textures, sulphur depletion, and specific alteration products (magnetite/chalcolite) allows us to venture that these textures, features, and minerals are a consequence of a secondary process acting upon the intrusion after magmatic sulphide formation had concluded. Confirming that the core process occurring is that of desulphurisation, it can be suggested that the presence of an oxidating low temperature aqueous solution is responsible for such processes, allowing for a deeper understanding of conditions acting on the Rum intrusive suite post formation (O'Driscoll et al., 2025; Power et al., 2000; Power et al., 2003). Further observations made from TEM lamella analysis highlighting the complexity of the rims at a nano-scale display the intricacies of alteration and highlight the immensely spatialised nature of suggested alteration processes on the suite.

Lastly, observations made surrounding sulphides, alterations textures, enriched rims, and Fe-oxides have notable impacts on concerns regarding platinum group mineralisation processes within layered intrusions. PGM formation within layered intrusions is a highly important topic, with pushes for advancement in understanding mineralisation common due to both academic and industrial advantages. Developing understanding around PGMs can be utilised to indicate how similar deposits can be processed to reduce environmental risks and energy consumption, as well as help stabilise REE supply (Currie & Elliot., 2024; O'Driscoll & González-Jiménez, 2016). However, a significant proportion of work regarding PGM formation focuses on petrogenesis within magmatic environments (O'Driscoll & González-Jiménez, 2016). Observations made within this project corroborate with those made within related projects and indicate that a proportion of PGMs observed within chromite seams of the Rum layered intrusion are associated with alteration textures/products of desulphurisation processes, indicating that proposed oxidative alteration by an aqueous solution under low temperature conditions is an important driver for crystallisation of PGM (O'Driscoll et al., 2025; Power et al., 2000). Contributing to wider discussions regarding hydrothermal formation of PGMs, low-

temperature oxidation events, and aiding understandings of analogue sites such as Bushveld and Stillwater (O'Driscoll & González-Jiménez, 2016; O'Driscoll et al., 2025).

6.2.6 Project strengths and potential further work

A major strength of the data collected in this project is due to the acquisition parameters used during SEM-EDS collection, and, the ML techniques used to further dissect this data. Previous conclusions regarding optimum acquisition settings made from the exposure experiment set were utilised within this project to produce mineralogical data packs which were accurate and reliable. All data packs within this project contained an average count per pixel of over 1000 (Table 5.4.1). This enabled the ML analysis workflow applied to produce quality results, concerning both mineralogical boundaries and mineral formulae, which cannot be obtained using SEM-EDS element maps alone. Clustering of site 1 particularly greatly aided the core aim of this project by pulling out the enriched rim and producing a corresponding mineral formula, improving understanding of chemical and mineralogical changes occurring and supporting previous projects and hypothesises.

The variety of observations provided by the four sites analysed at depth provided sufficient information regarding the mineralogical aims of this project, and allowed for corroboration and development of propositions made by previous projects, or, by projects within neighbouring units of the Rum suite. However, confining the exact main sulphide mineralisation model (MSS vs ISS), the exact composition and temperature of proposed aqueous liquid alteration, and the exact means by which this hydrothermal desulphurisation may affect PGM mineralisation is beyond the scope of this project.

The study of the sulphide minerals in cross-section by TEM analysis added an additional advantage to observing chemical changes occurring within the rim, as well as uncovering interesting observations regarding nano-scale structures present. However, unfortunately, only one of the two lamellae were examined. Furthermore, due to the lack of concise elemental data from the TEM, the exact mineralogy of nano-structures cannot be determined, however, reasonable hypothesises can be made from the data available.

Future analysis is needed to study other features present within sulphide minerals at depth (e.g. pentlandite blades enclosed in lamella 2 (Figure 5.5.1). ML analysis using the workflow within

this project on data produced from TEM analysis would also reinforce interpretations made regarding the geochemistry of the grains within this project, produce precise mineral formulae of the alteration products observed, as well as possibly produce mineralogical formulae concerning nano-structures observed within the rims. Further research is also needed to establish the precise conditions of the suggested aqueous liquid acting upon the Rum layered intrusion, possibly by running a number of experimental models using methods such as ex-situ quench experiments, PXRD phase analysis, and XAS experiments, mimicking recent work produced by Chaudari et al (2021), only instead accounting for the specific geochemical composition of sulphides within Rum, and therefore providing a precise picture of the framework of the mineral replacement reaction observed within this project. Other avenues for future research include building on this work to produce an experimental model displaying how exclusion of PGMs could be driven by desulphurisation by a oxidative aqueous liquid.

CHAPTER 7: CONCLUSIONS

7.1 Exposure experiment conclusions

Conclusions are consistent with existing theory, that increasing the average number of counts per pixel will reduce noise and increase the quality of data produced by ML algorithms. However, the increase in data quality is not exponential and eventually plateaus. Results highlight the importance of obtaining over 1000 average counts per pixel, and that the optimum number of average counts, of which the most advantageous quality is achieved, lies ~ 1200 average counts per pixel.

Furthermore, results produced from both the exposure and mineralogical data set highlight the advantages of using ML algorithms, particularly with data packs containing >1000 average counts per pixel, in the interest of producing accurate mineral mapping and microanalysis. De-noising and decomposition algorithms such as Poisson-noise scaling and FA, demonstrated a significant improvement in noise reduction and data quality, aiding the production of higher quality results. In comparison to SEM-EDS maps produced by oxford elements, clusters and signal plots alone provide a lot more elemental information. Utilizing cluster packs and stoichiometry calculations provide a more concise mineralogy, achieving clarity not provided purely by SEM-EDS elemental maps.

7.2 Mineralogical conclusions

Analysis of composite BMS's and features within them (e.g. fans, blades) indicate magmatic sulphide exsolution continued to temperatures of ~ 250ºC. SEM-EDS mapping and cluster signal plots concluded that the rims are enriched in Cu, and depleted in Fe, O and partially depleted in S. Stoichiometry calculations regarding these HDBSCAN clusters confirmed that the rim is chalcocite/digenite. Adjacent minerals of Fe-oxide minerals, such as magnetite, have also been observed. These observations support the theory that a period of sulphur degassing occurred, likely due to a oxidising aqueous solution, acting within a low temperature range, leading to the formation of low-sulphur Cu sulphides, and producing Fe-oxides as an alteration product. Alteration varies across the seam, meaning that alteration occurring is highly

spatialised and occurred at low fluid-rock ratios, and, textures and S-relicts observed in Fe-oxide minerals indicated that alteration was a stepped process.

Further analysis of rims within the TEM added depth to observations. Rims are seen to be consistent at depth, but contain both light and dark nano-structures, a complexity lost in SEM data. Although more work is needed to confine the mineralogy of these nano-structures and nano-scale rim complexities, the variation and sporadic nature of nano-structures observed is consistent with highly spatialised alteration occurring at low fluid-rock ratios.

Observations regarding the PGMs are consistent with many other projects, with the Pt-alloy observed located within a sulphide-silicate contact. Interestingly, the Pt-grain is also located within proximity to an un-specified Fe-oxide, likely an alteration product. Indicating and suggesting, as other projects also have, that some PGMs are linked to hydro-thermal alteration (Power et al., 2000; O'Driscoll et al., 2025).

There are multiple avenues for potential further work developing on the information provided by this project. Enhanced analysis of the TEM lamellae produced for this project, with a focus on confining mineralogical information regarding nano-structures within the rim, could reinforce and confirm the core geochemical changes occurring. Additionally, work regarding pentlandite blade exsolutions of lamella 2 can provide insight to down-temperature magmatic sulphide formation. Building on this, composing experimental models utilising ex-situ quench experiments, PXRD phase analysis, and/or XAS experiments could provide a more precise understanding of desulphurisation reactions proposed. Extending further to produce a model proposing how low-temperature alteration by an oxidative aqueous liquid can be a driver for PGM exsolution.

APPENDIX A

Factor heat maps – up to 20 factors

Experiment 1:

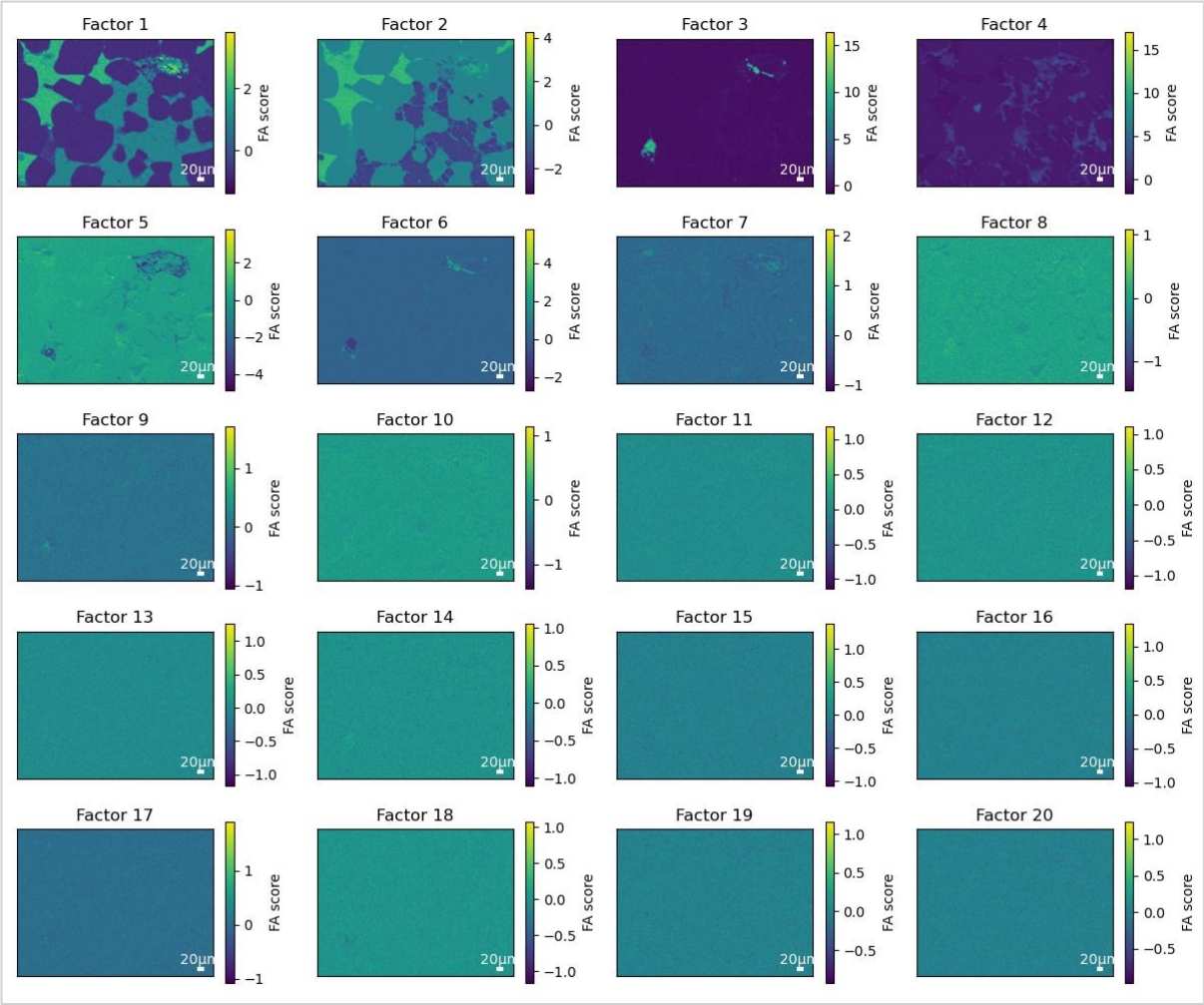

Experiment 2:

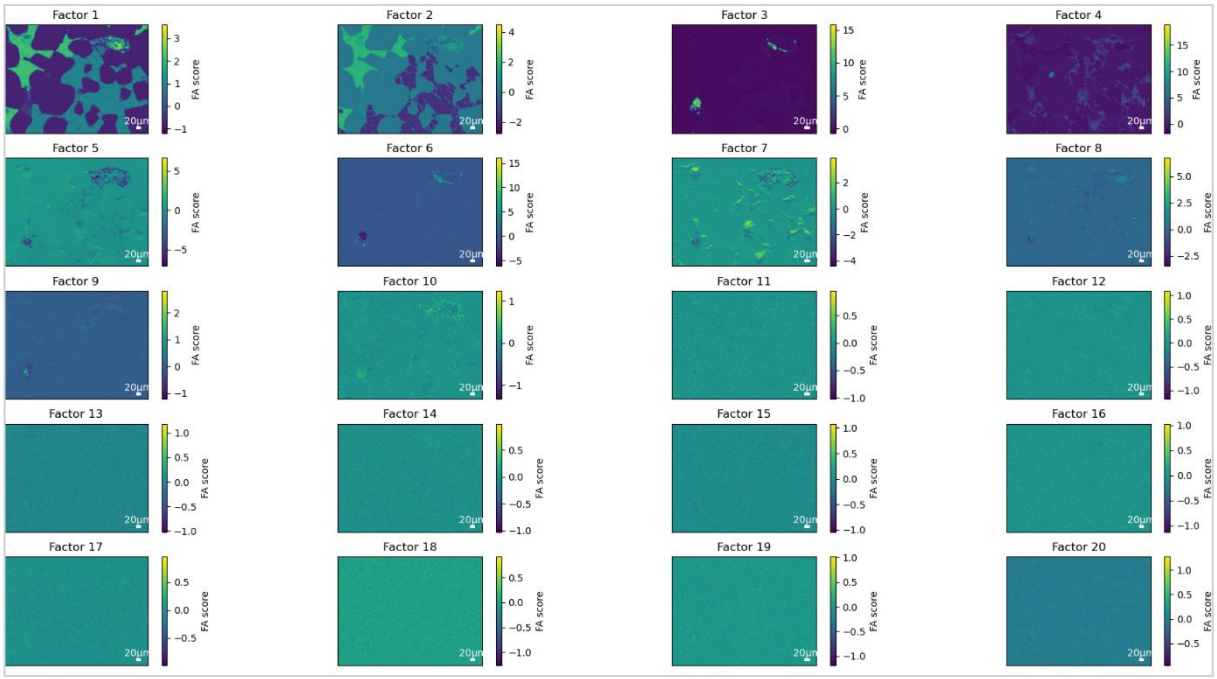

Experiment 3:

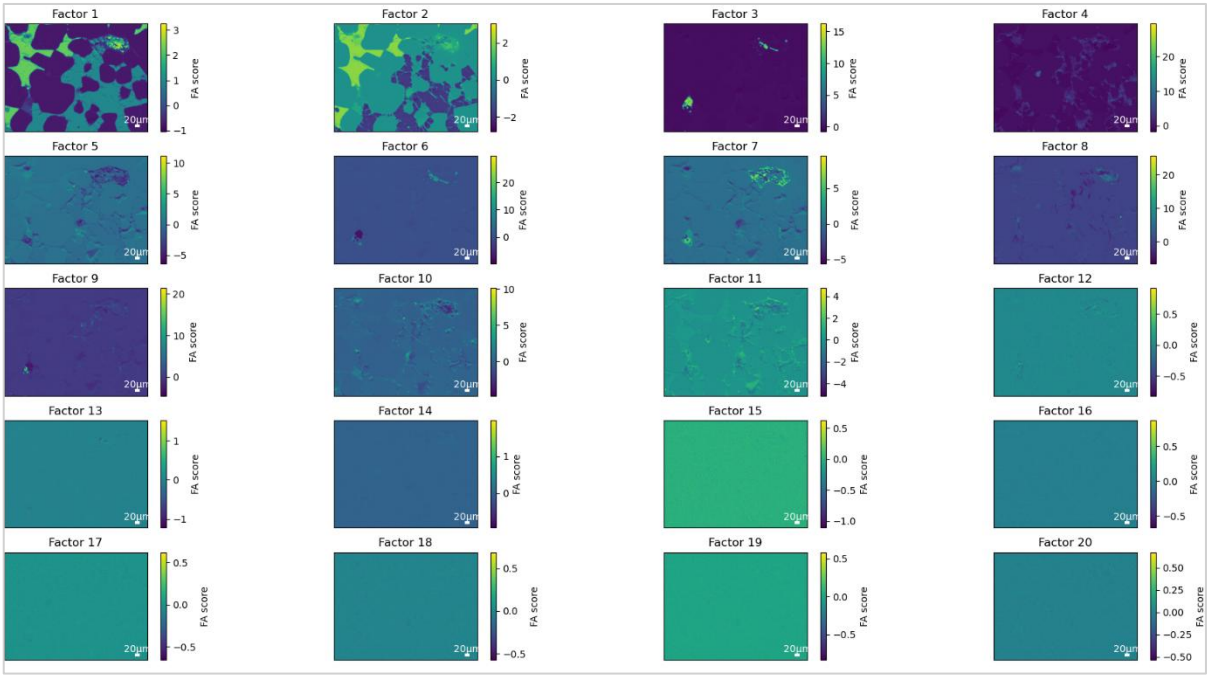

Experiment 4:

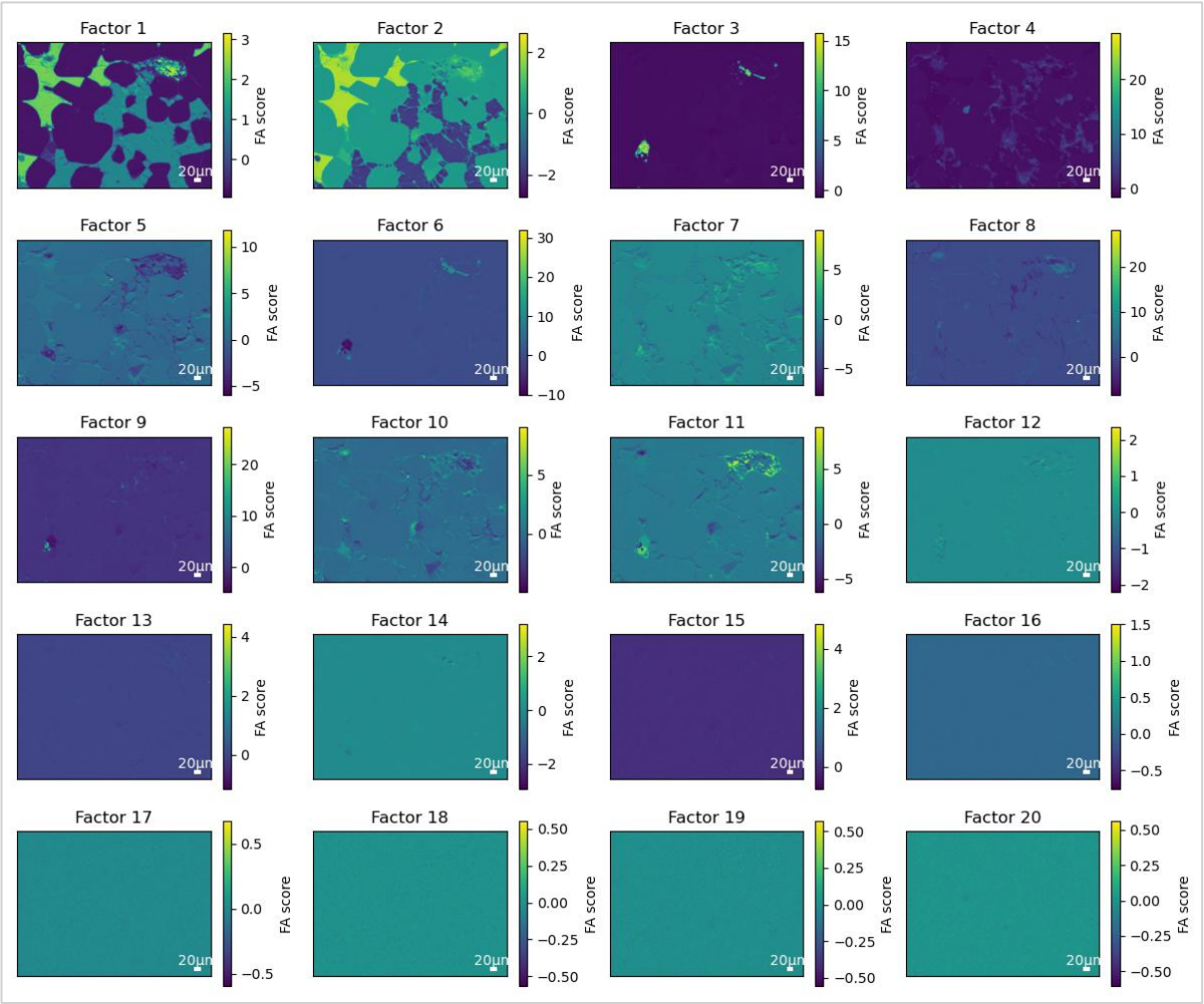

Experiment 5:

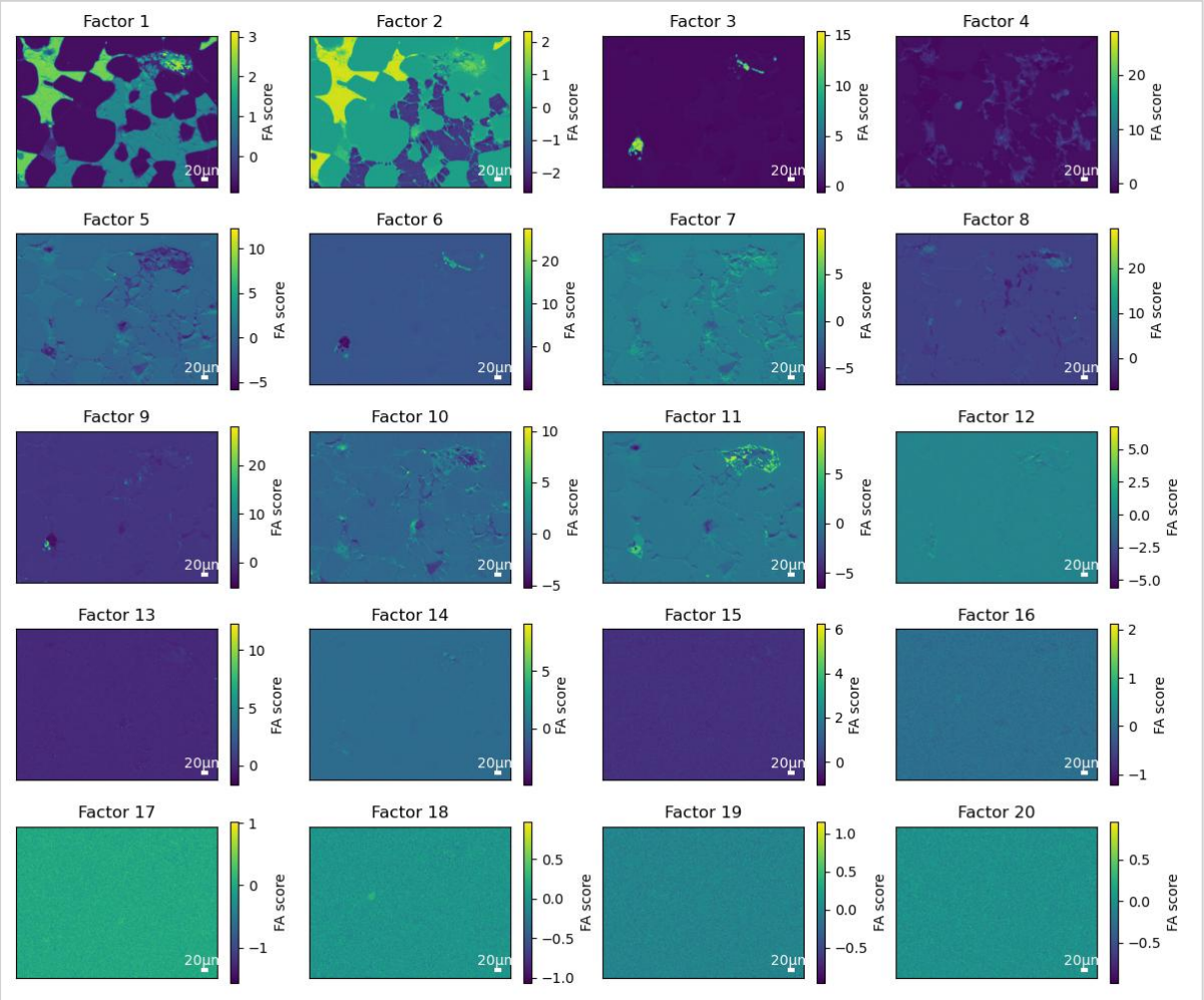

Experiment 6:

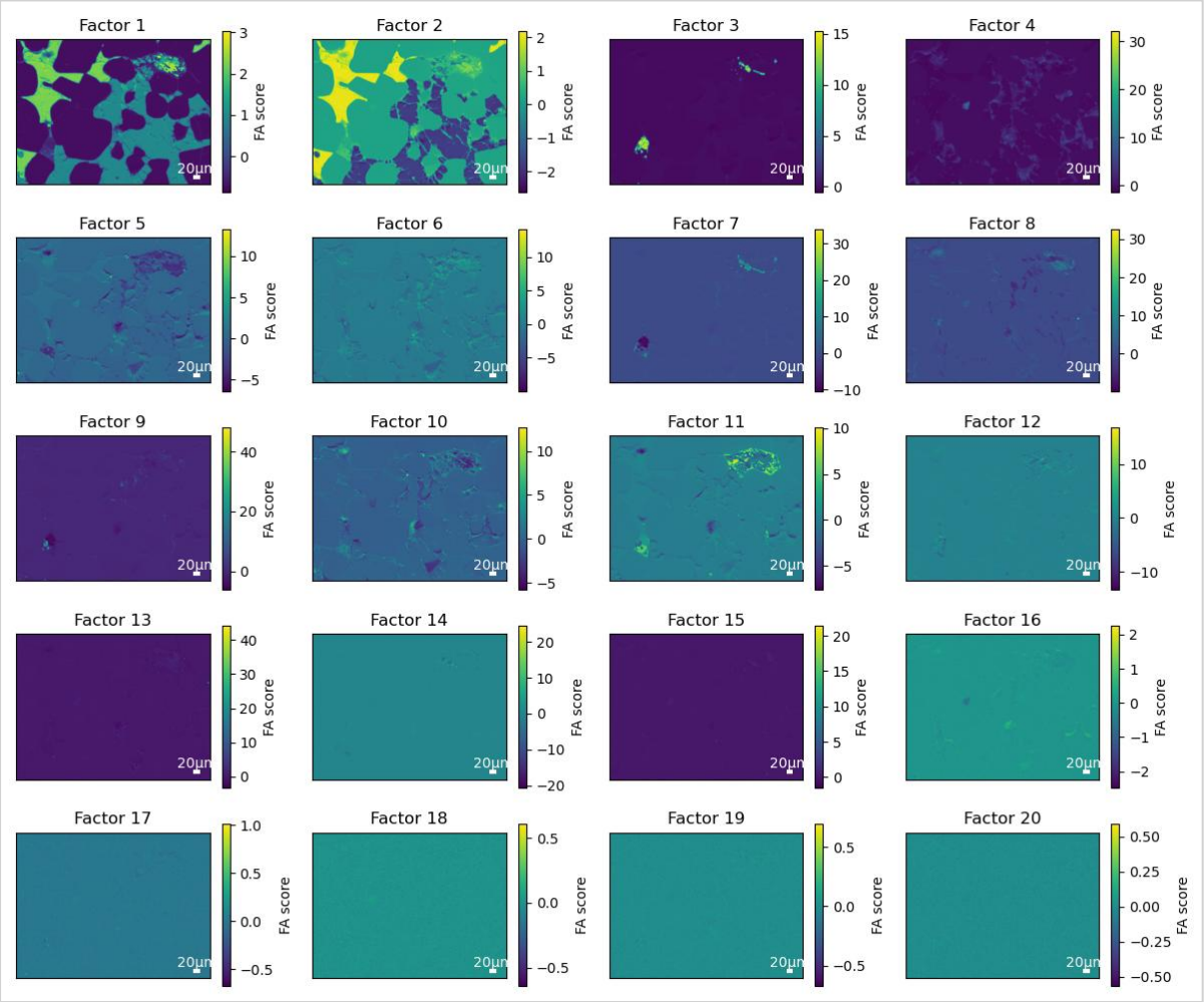

Factor & signal plots followed by scores & loadings plots for each exposure experiment.

Experiment 1:

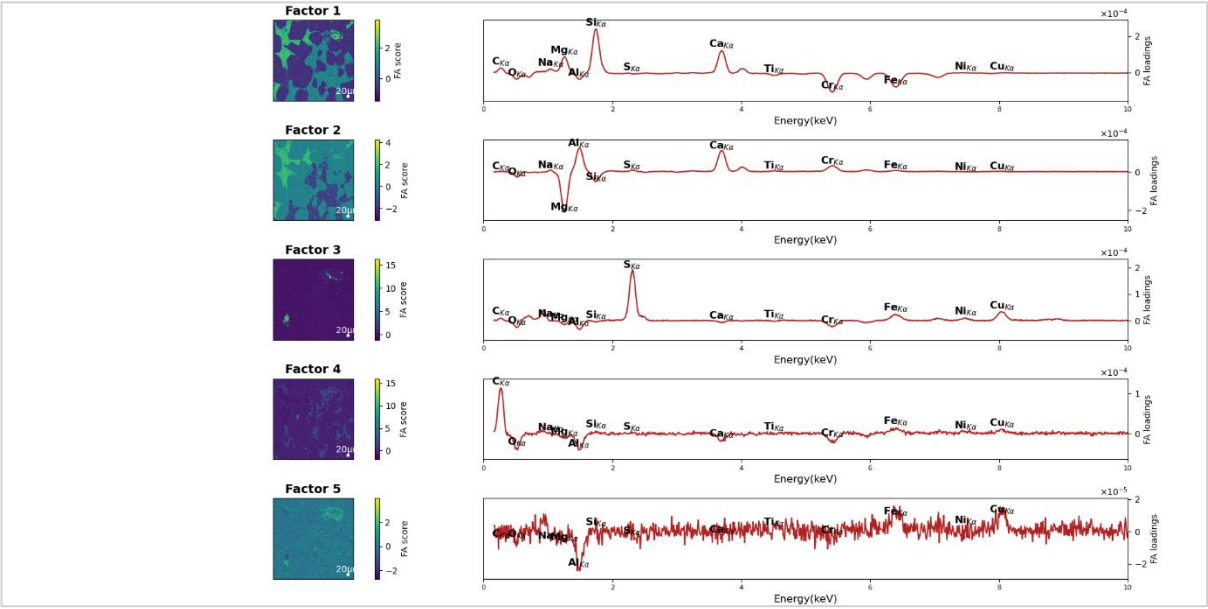

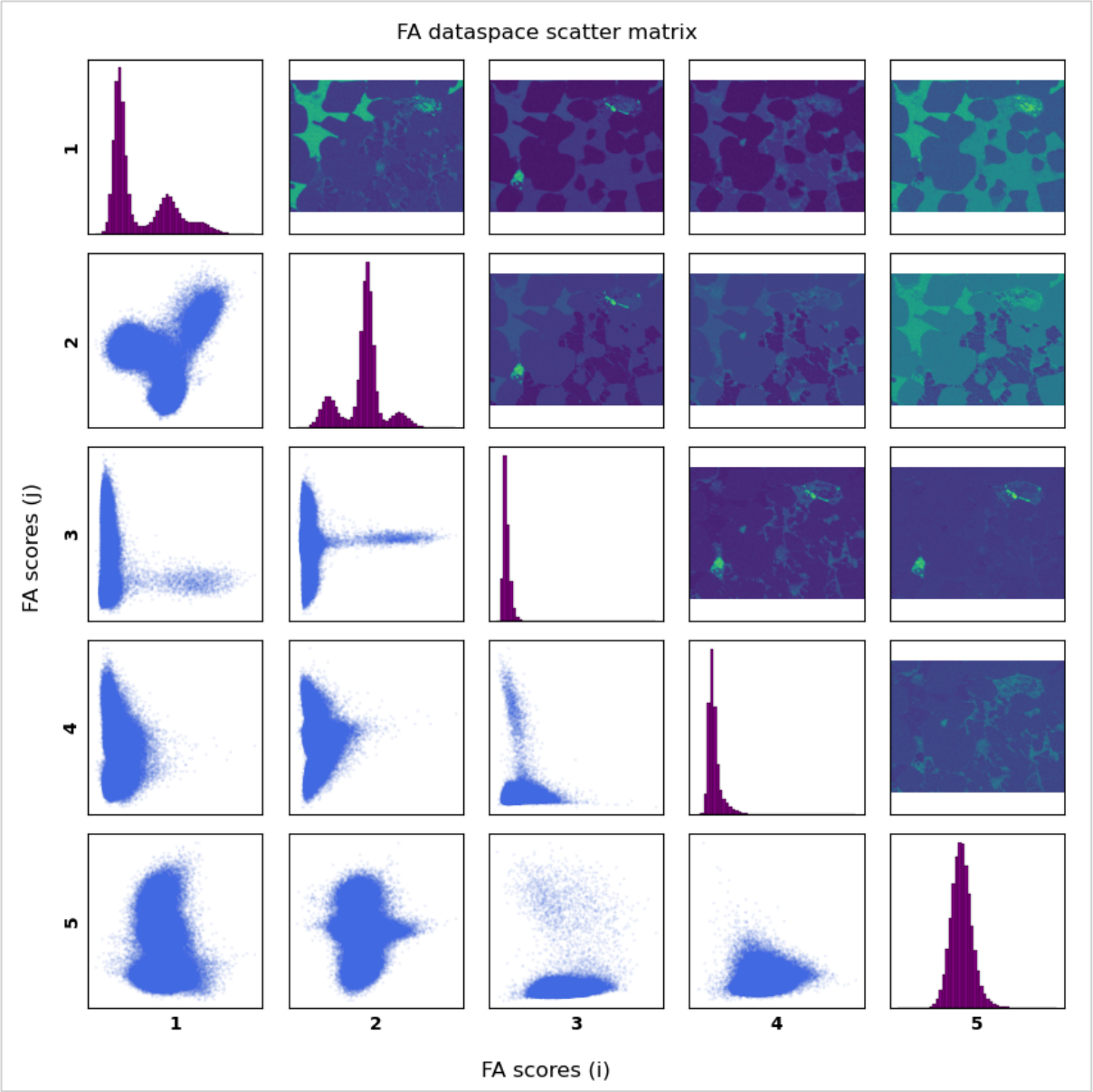
FA dataspace scatter matrix
FA scores (j)
FA scores (i)
1
2
3
4
5

Experiment 2:

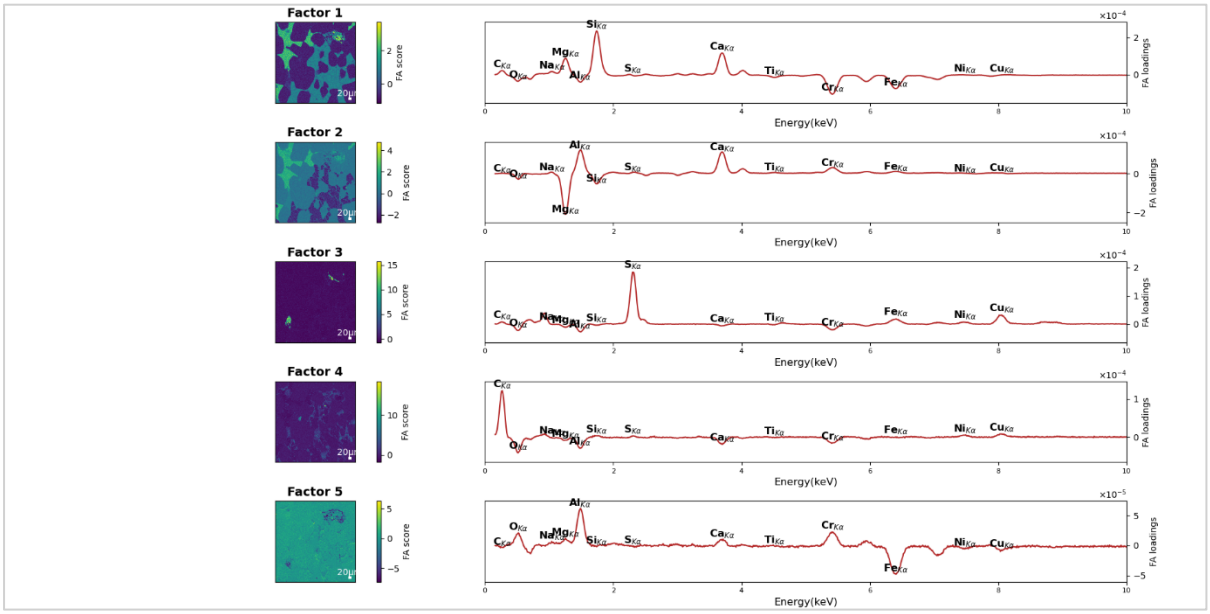

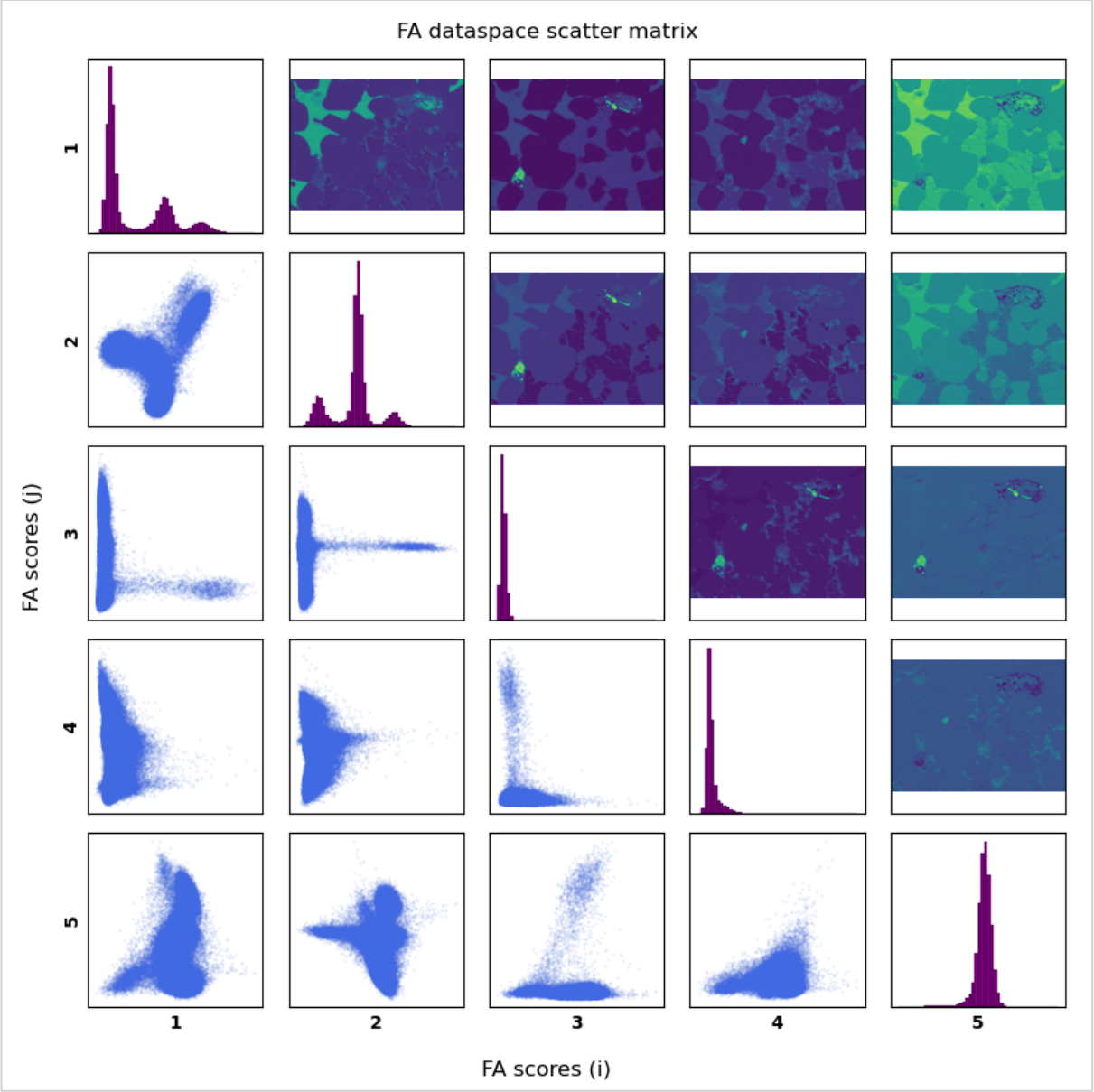
FA dataspace scatter matrix
FA scores (j)
FA scores (i)
1
2
3
4
5

Experiment 3:

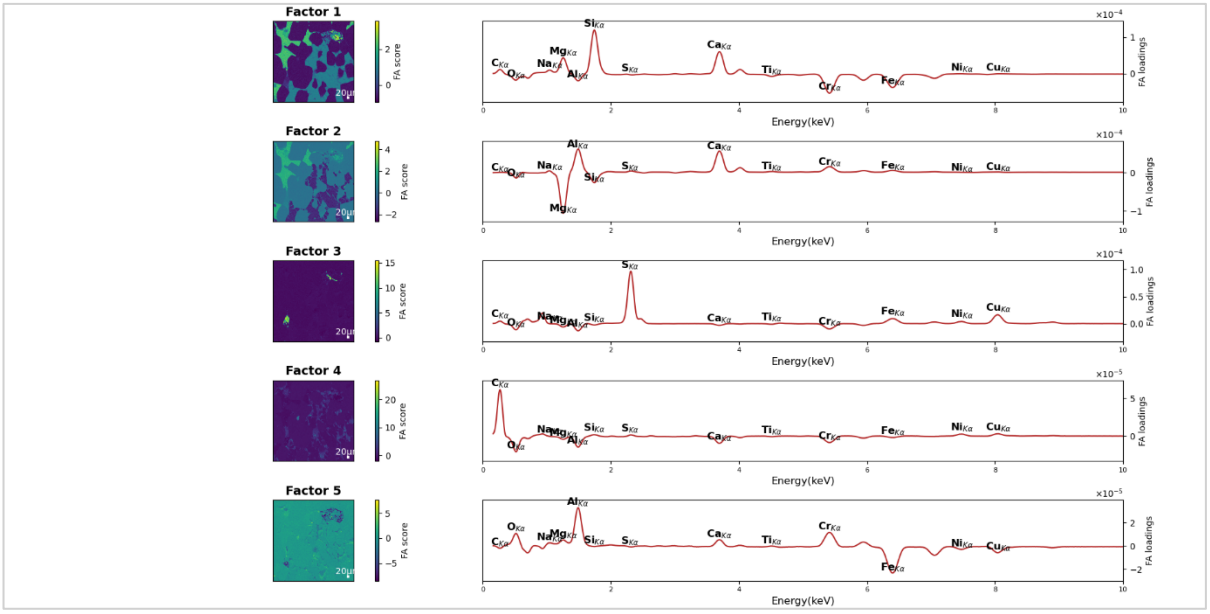

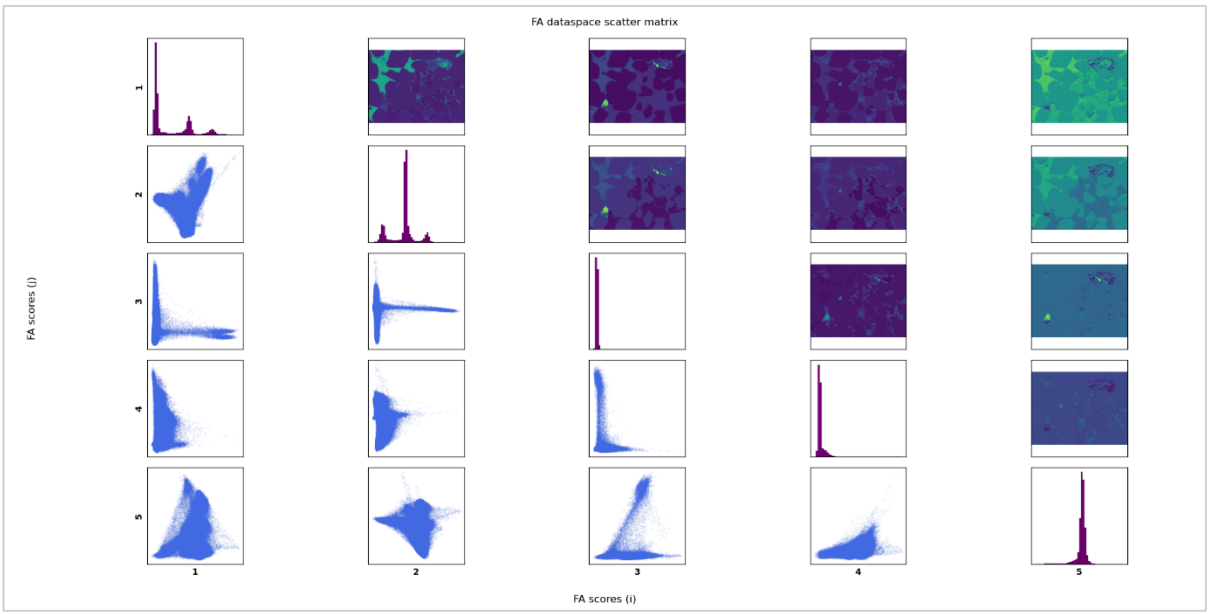

Experiment 4:

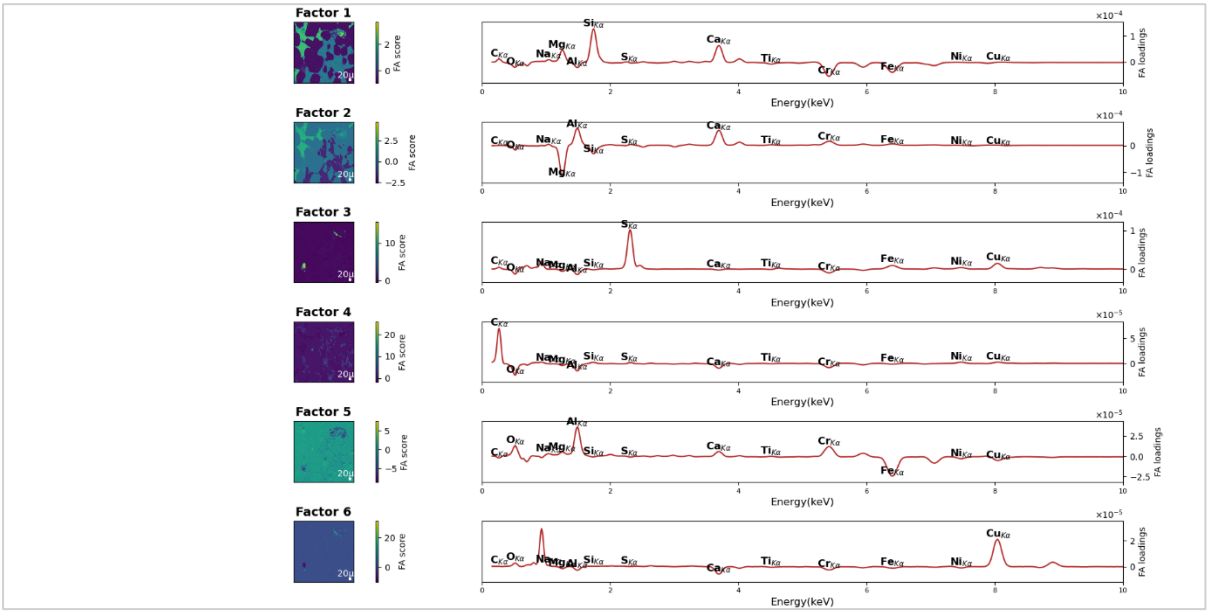

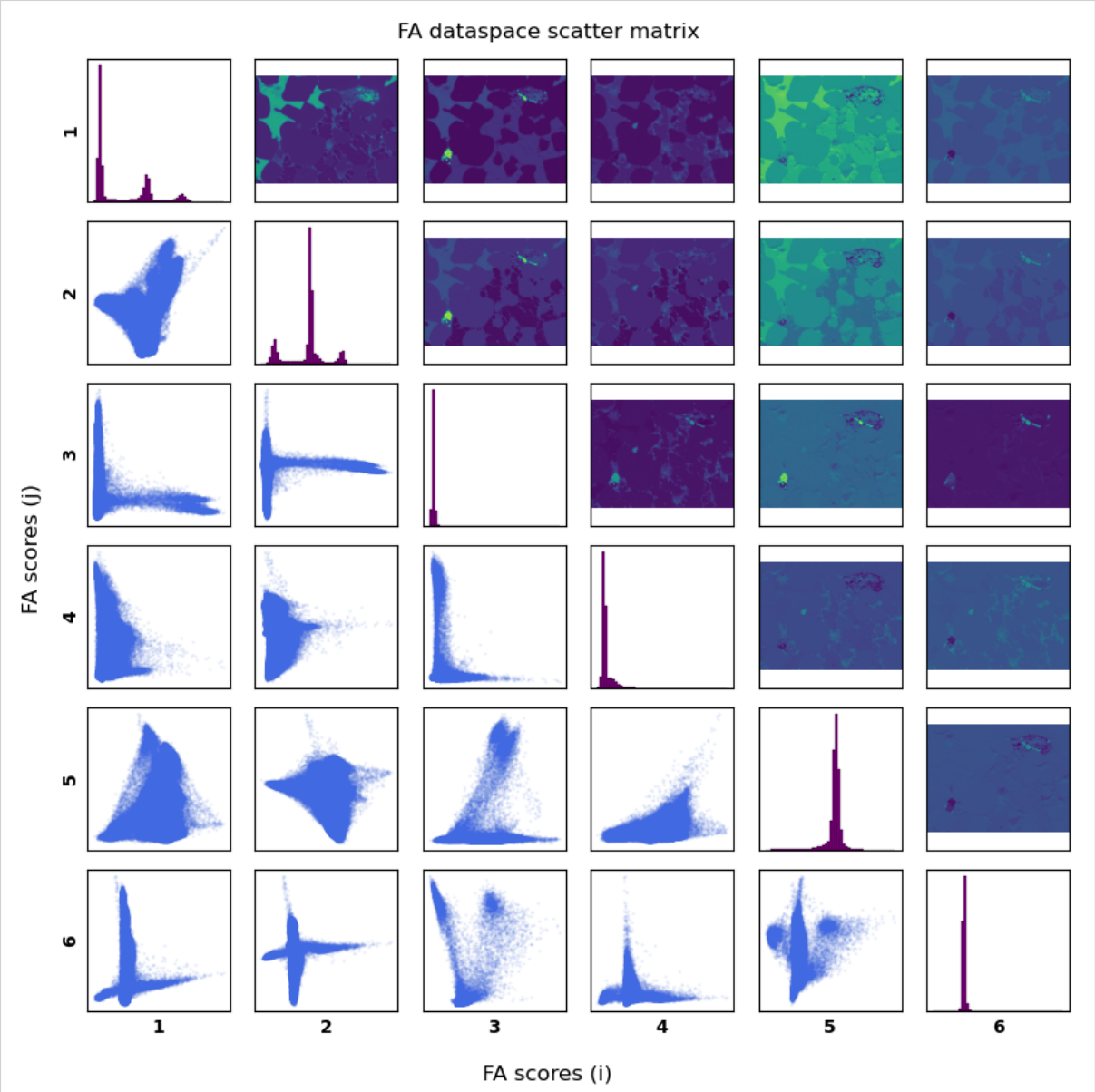
FA dataspace scatter matrix
FA scores (j)
FA scores (i)
1
2
3
4
5
6

Experiment 5

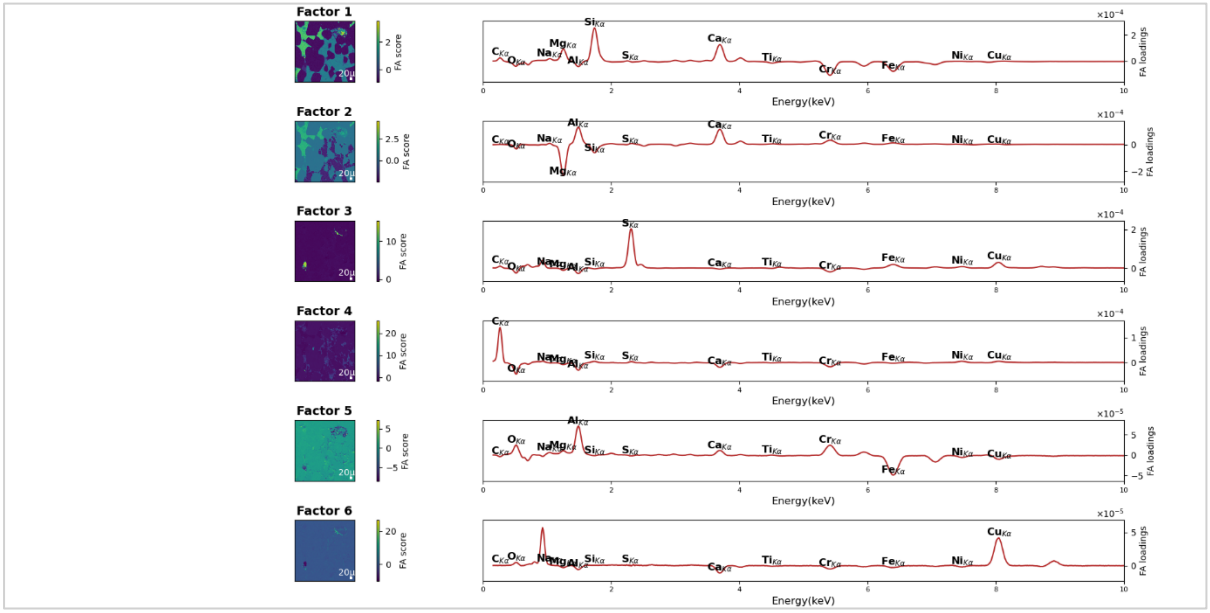

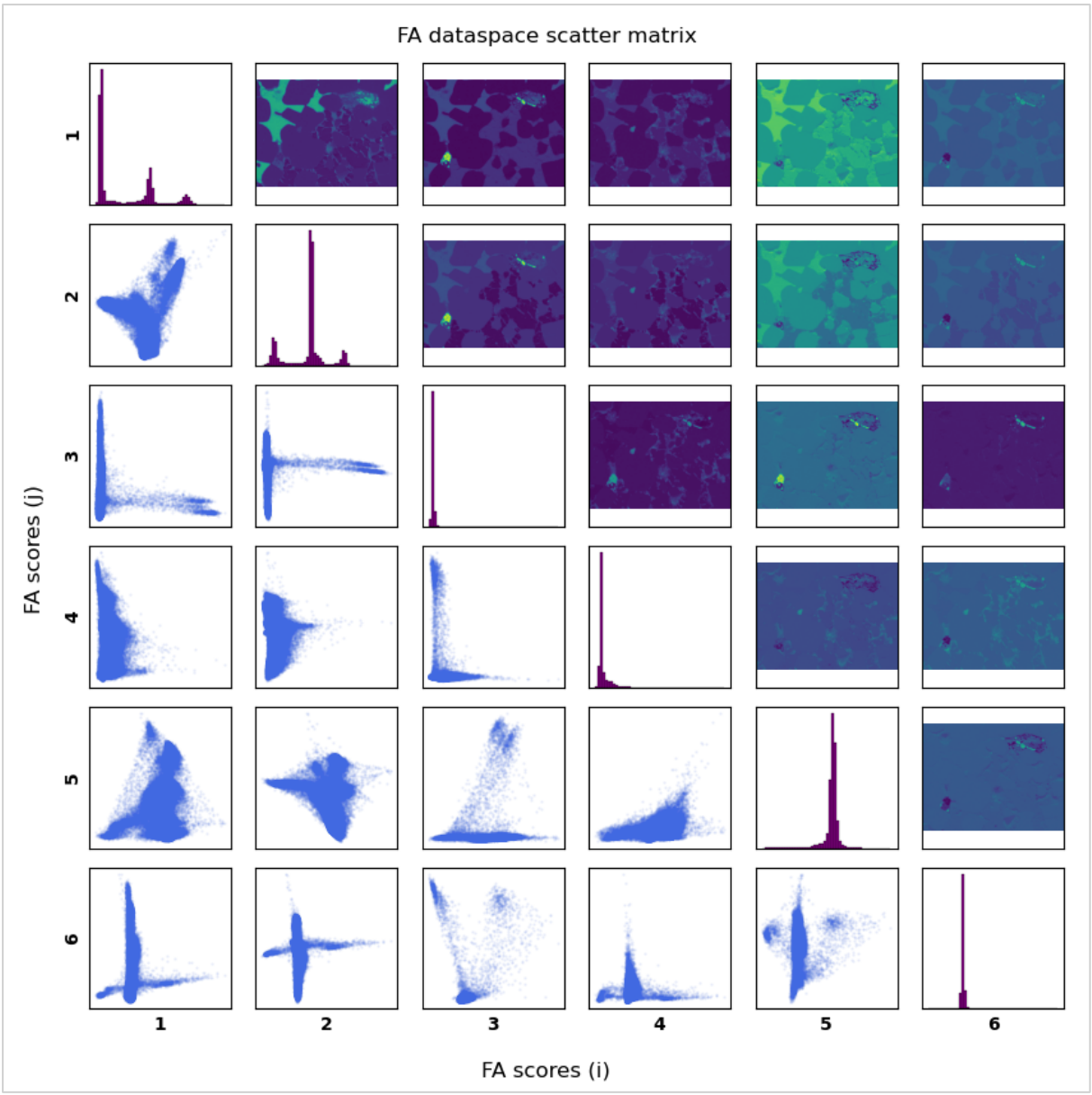
FA dataspace scatter matrix
FA scores (j)
FA scores (i)
1
2
3
4
5
6

Experiment 6

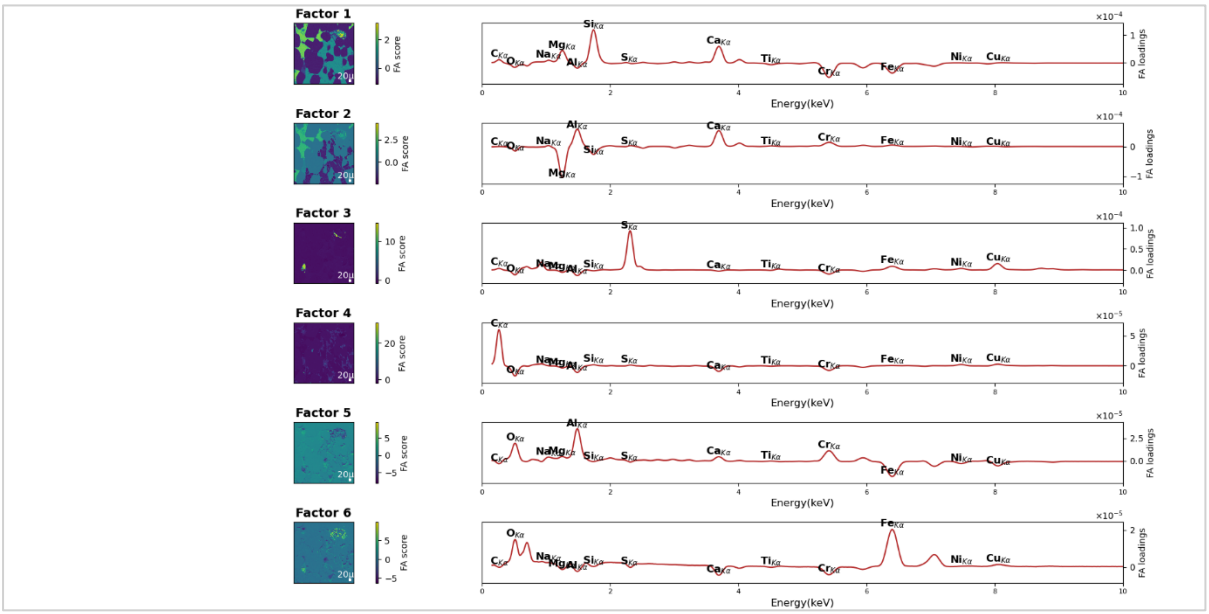

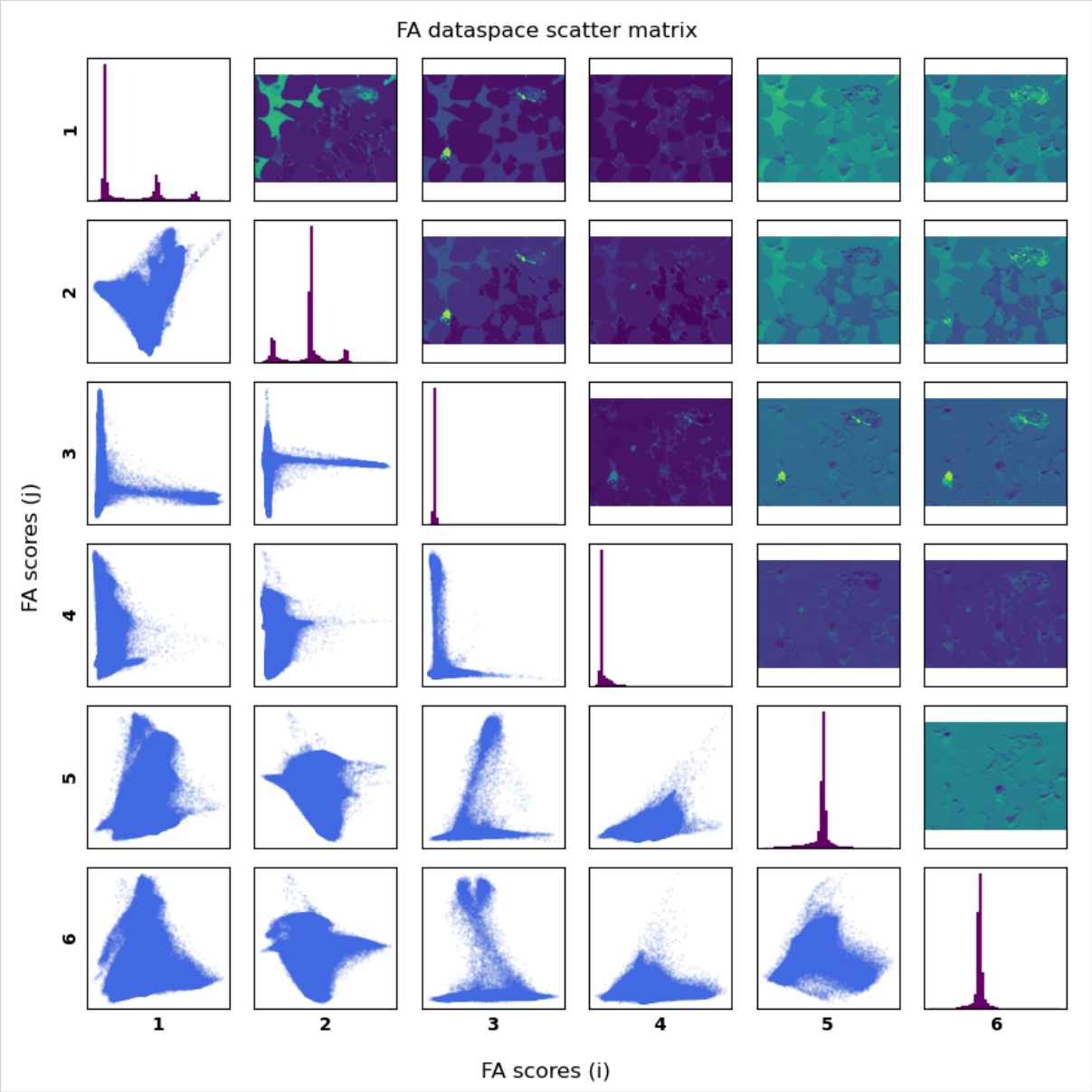
FA dataspace scatter matrix
FA scores (j)
FA scores (i)
1
2
3
4
5
6

APPENDIX B

Factor heat maps – up to 20 factors

Site 01:

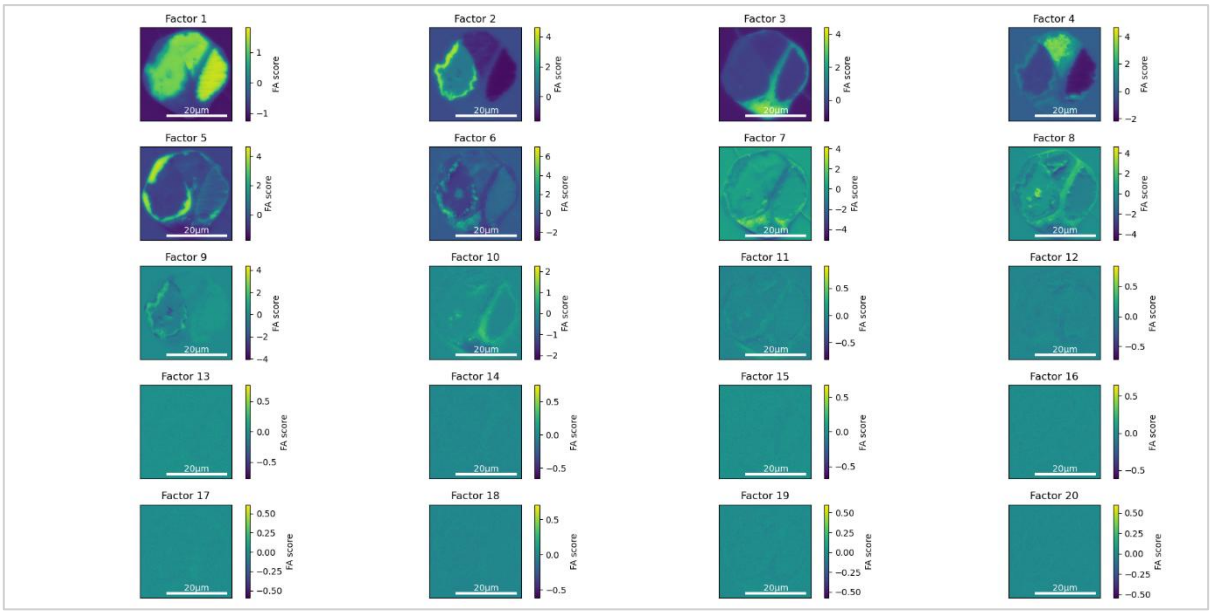

Site 04:

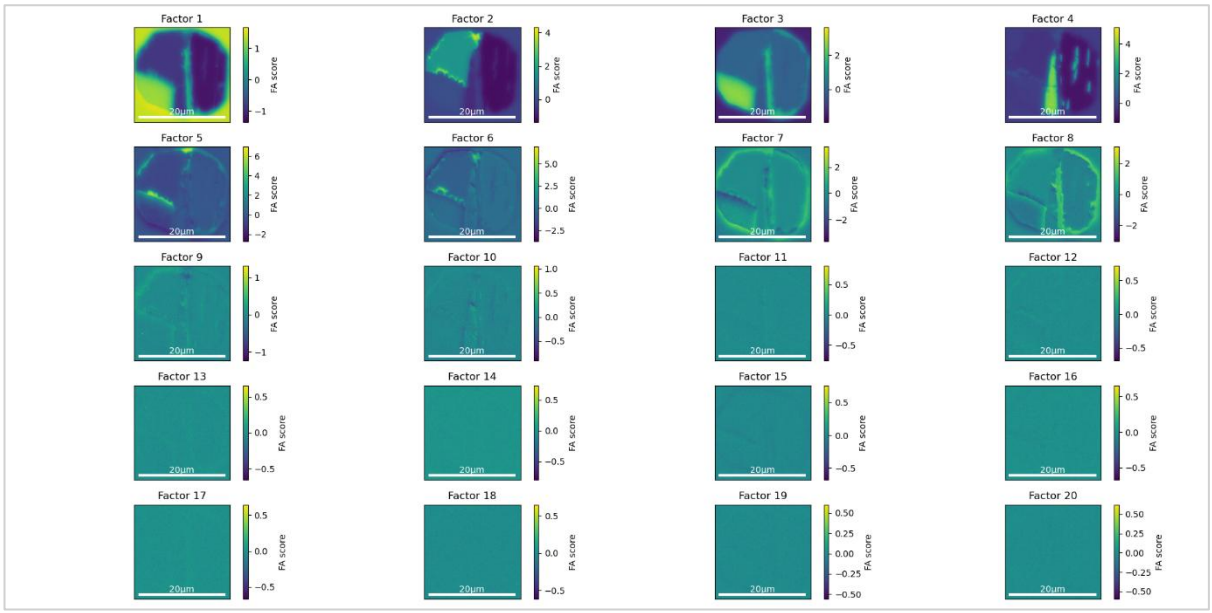

Site 08:

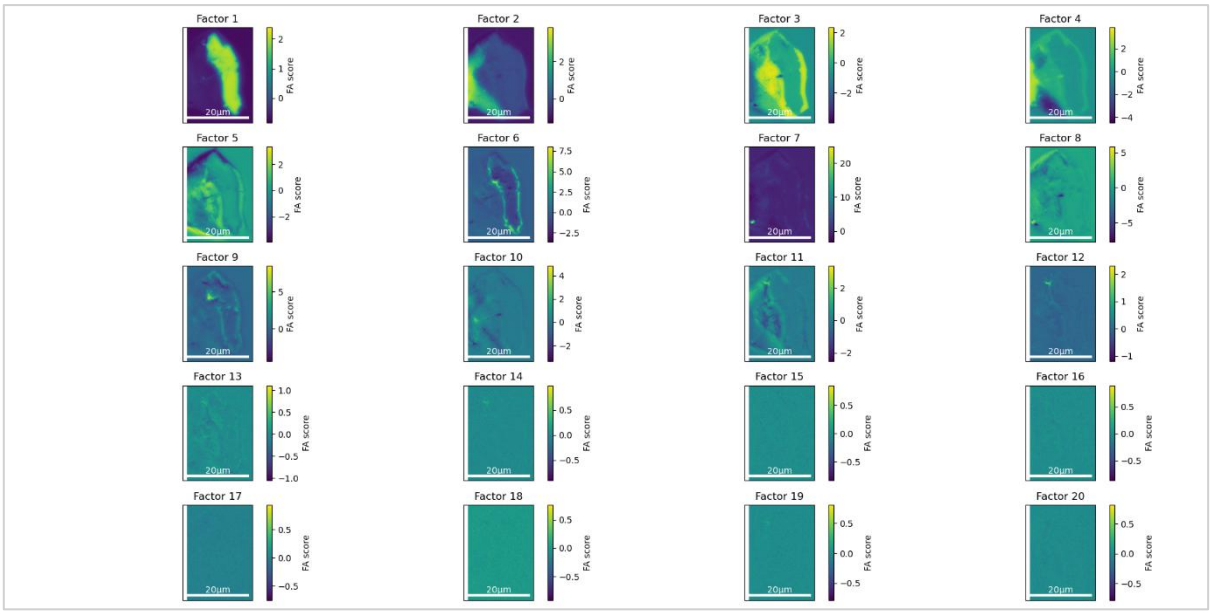

Site 15:

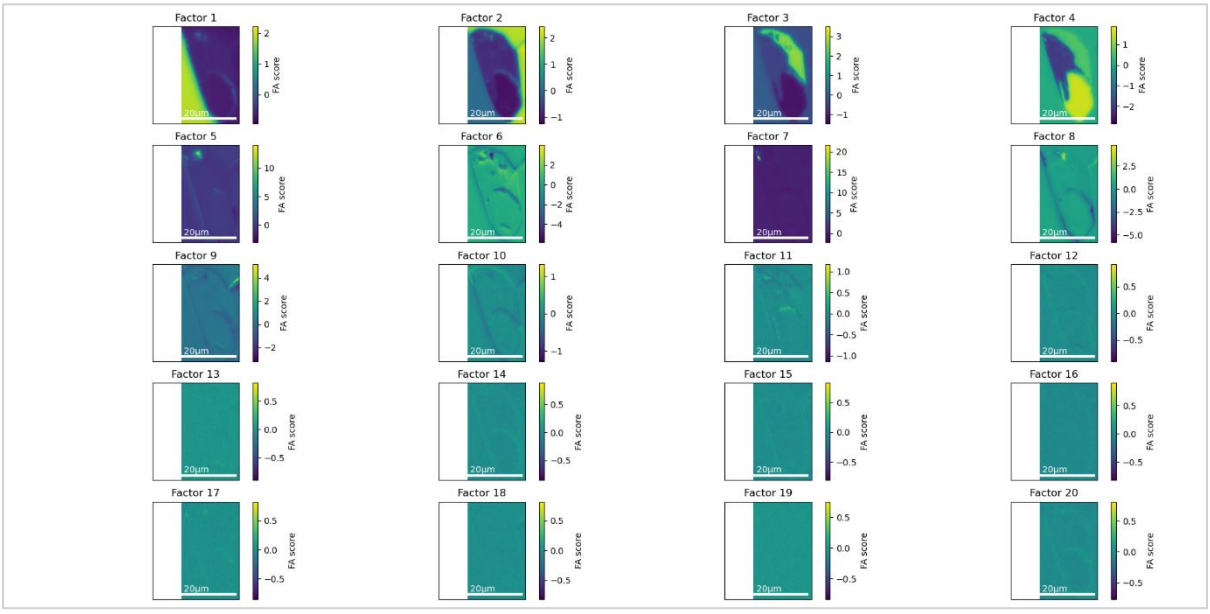

Factor & signal plots followed by scores & loadings plots for each mineralogical site.

Site 01:

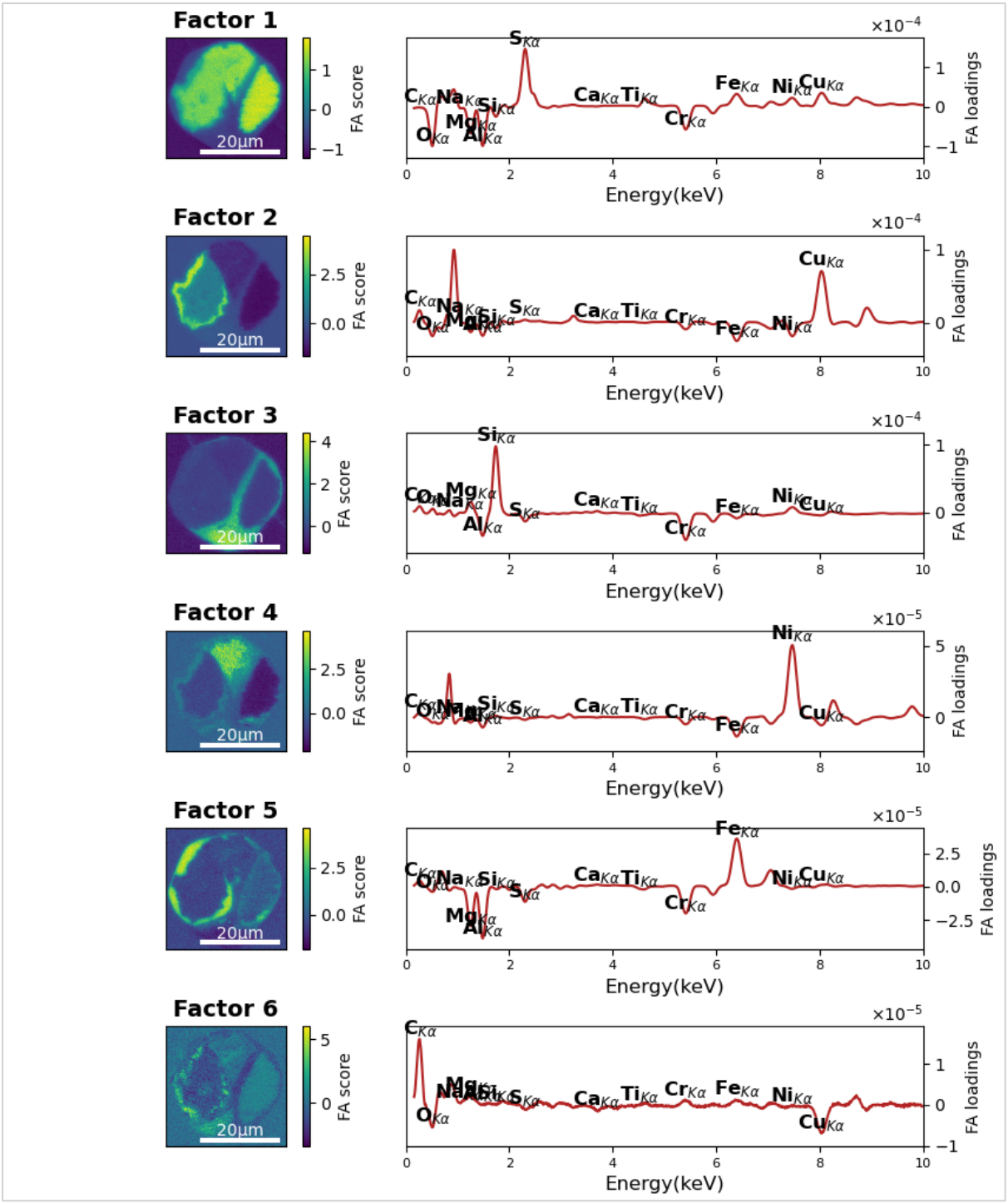

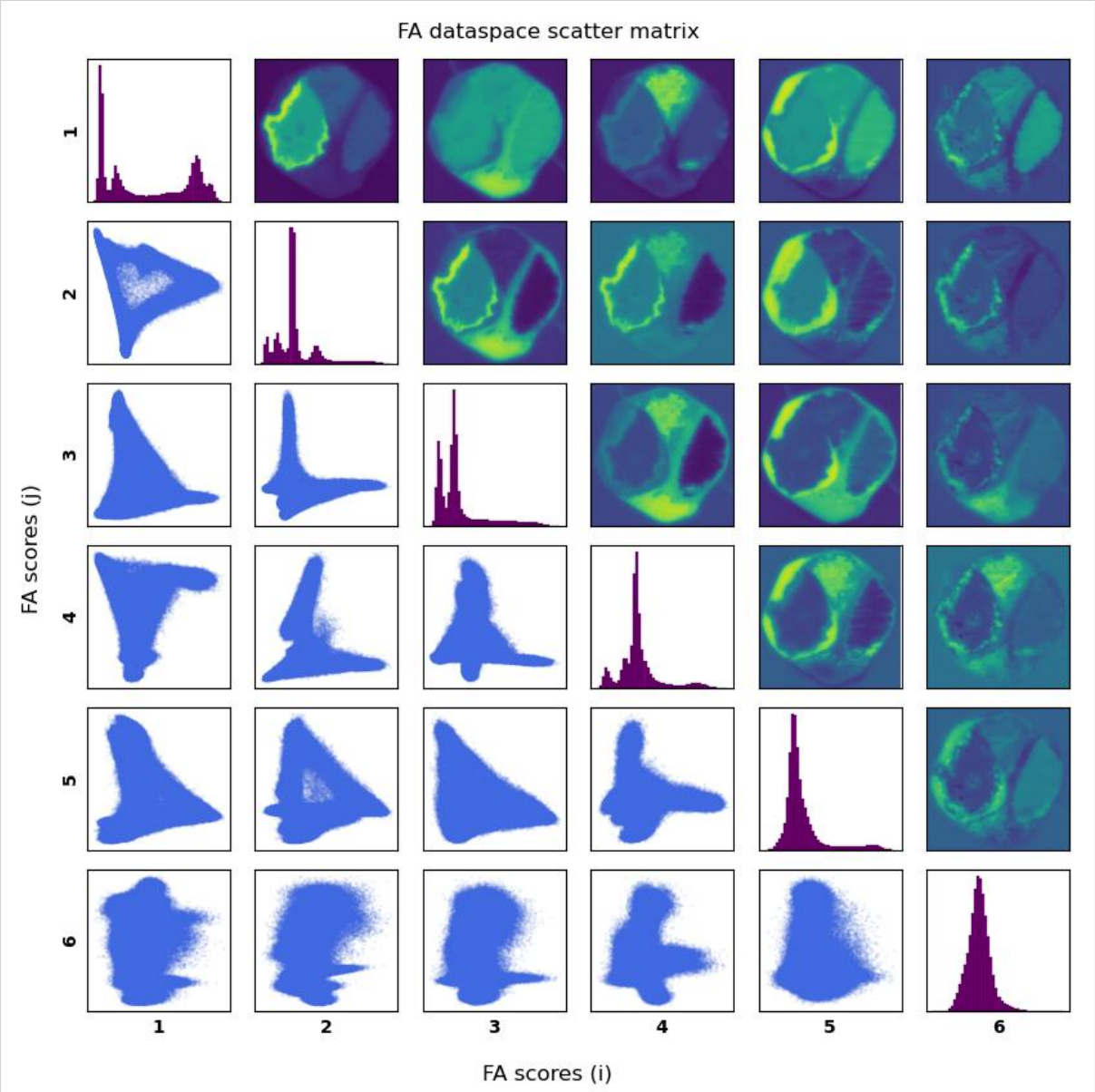
FA dataspace scatter matrix
FA scores (j)
FA scores (i)
1
2
3
4
5
6

Site 04:

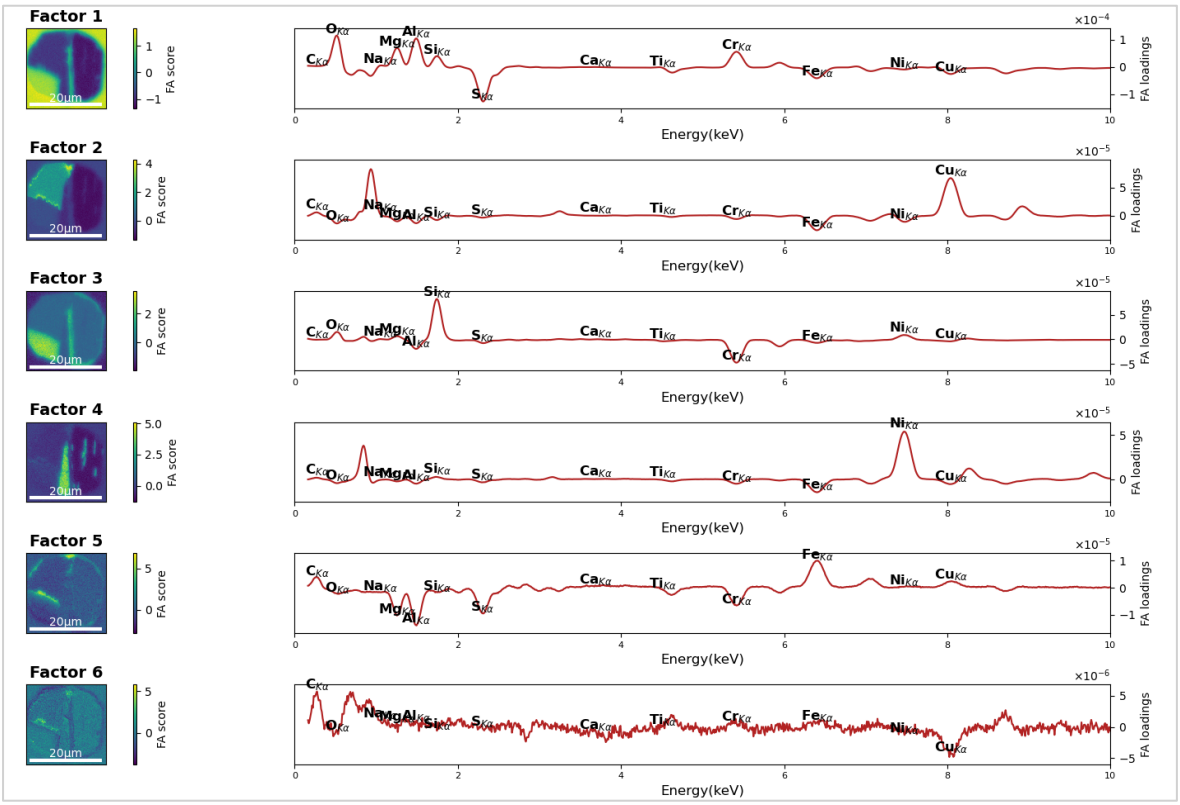
Factor 1
Factor 2
Factor 3
Factor 4
Factor 5
Factor 6
20μm
FA score
FA loadings
Energy(keV)

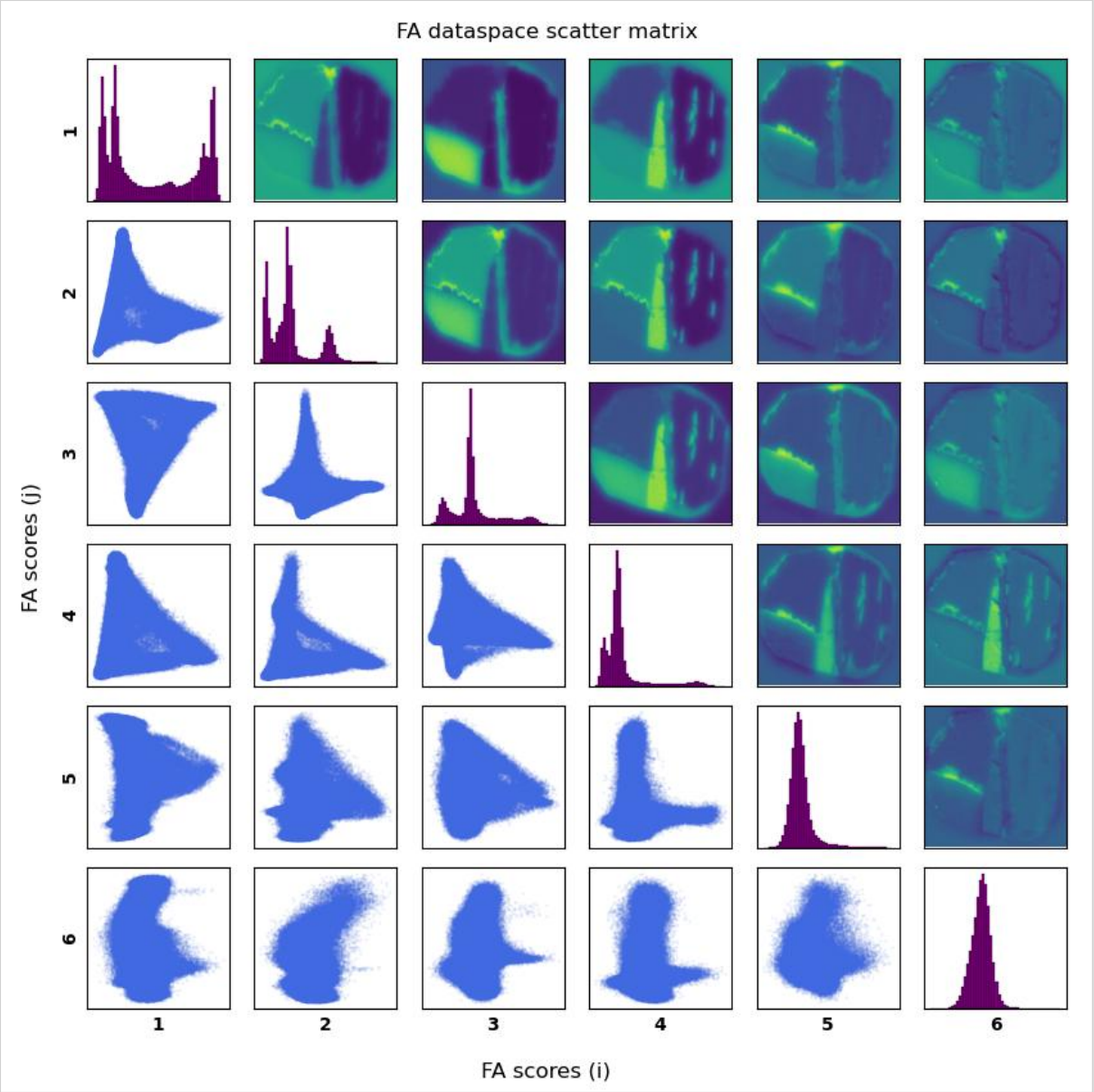
FA dataspace scatter matrix
FA scores (j)
FA scores (i)
1
2
3
4
5
6

Site 08:

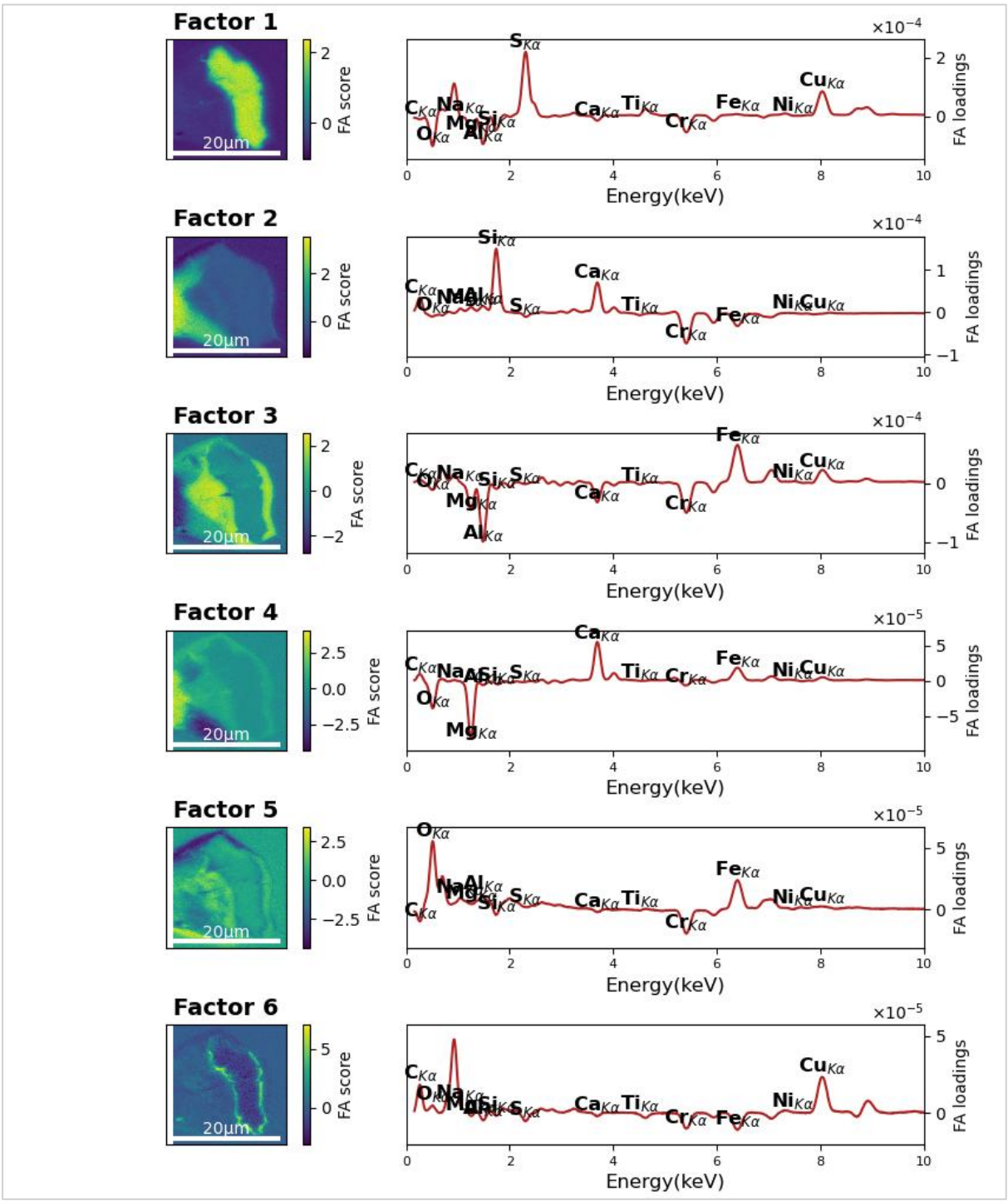
Factor 1
Factor 2
Factor 3
Factor 4
Factor 5
Factor 6
20µm
FA score
FA loadings
Energy(keV)
×10⁻⁴
×10⁻⁵

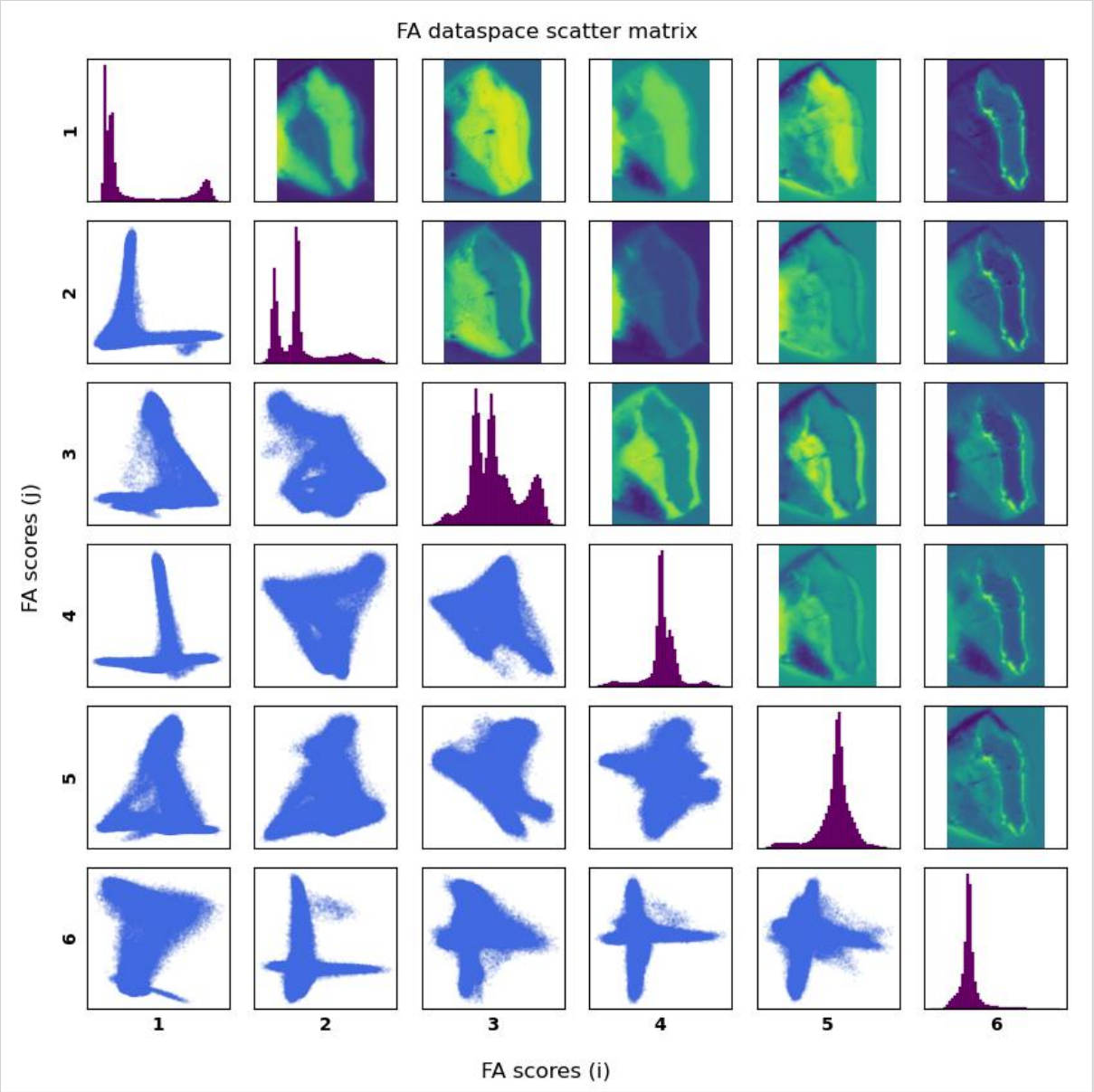
FA dataspace scatter matrix
FA scores (j)
FA scores (i)
1
2
3
4
5
6

Site 15:

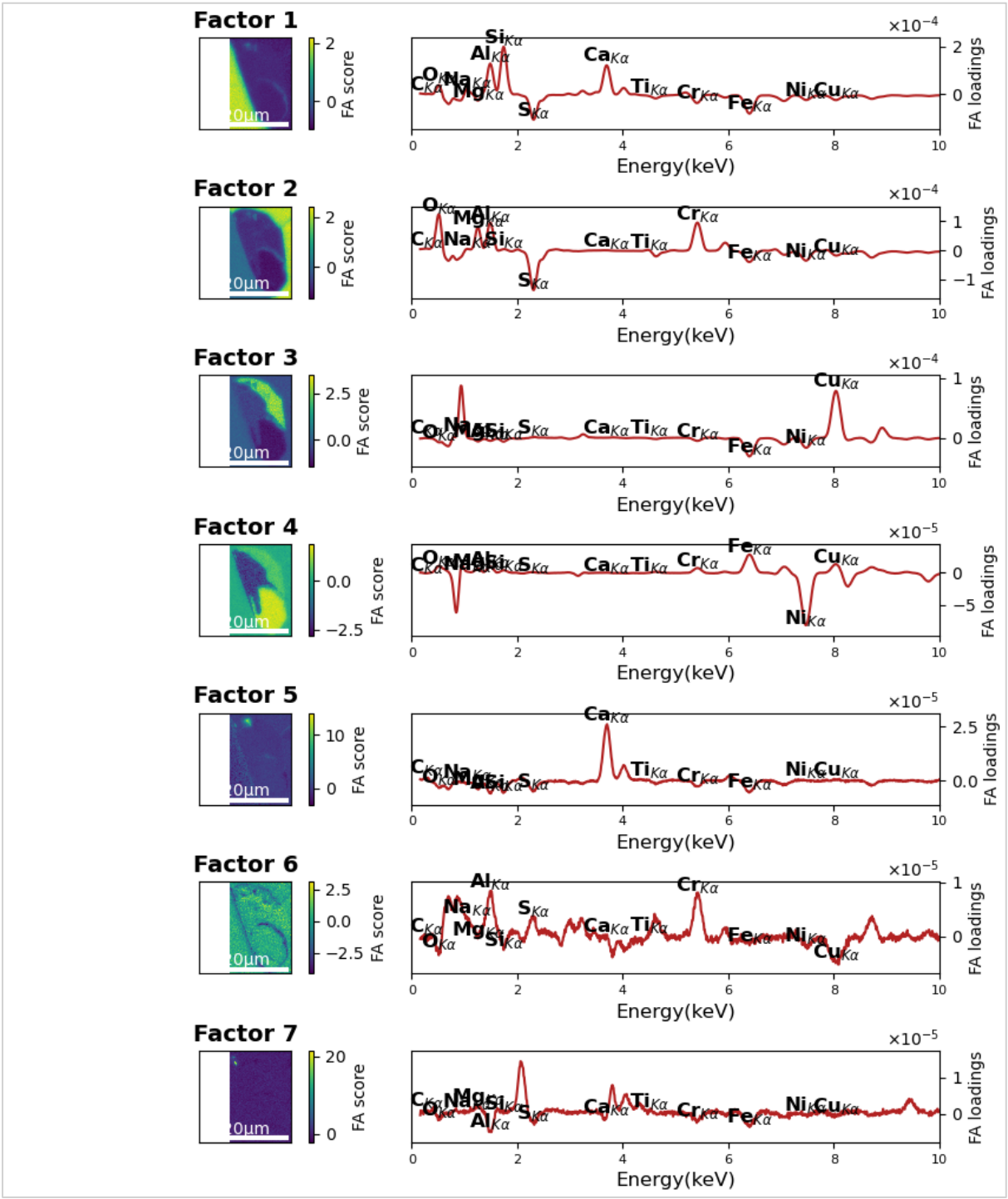
Factor 1
Factor 2
Factor 3
Factor 4
Factor 5
Factor 6
Factor 7
FA score
FA loadings
Energy(keV)
×10⁻⁴
×10⁻⁵
20μm

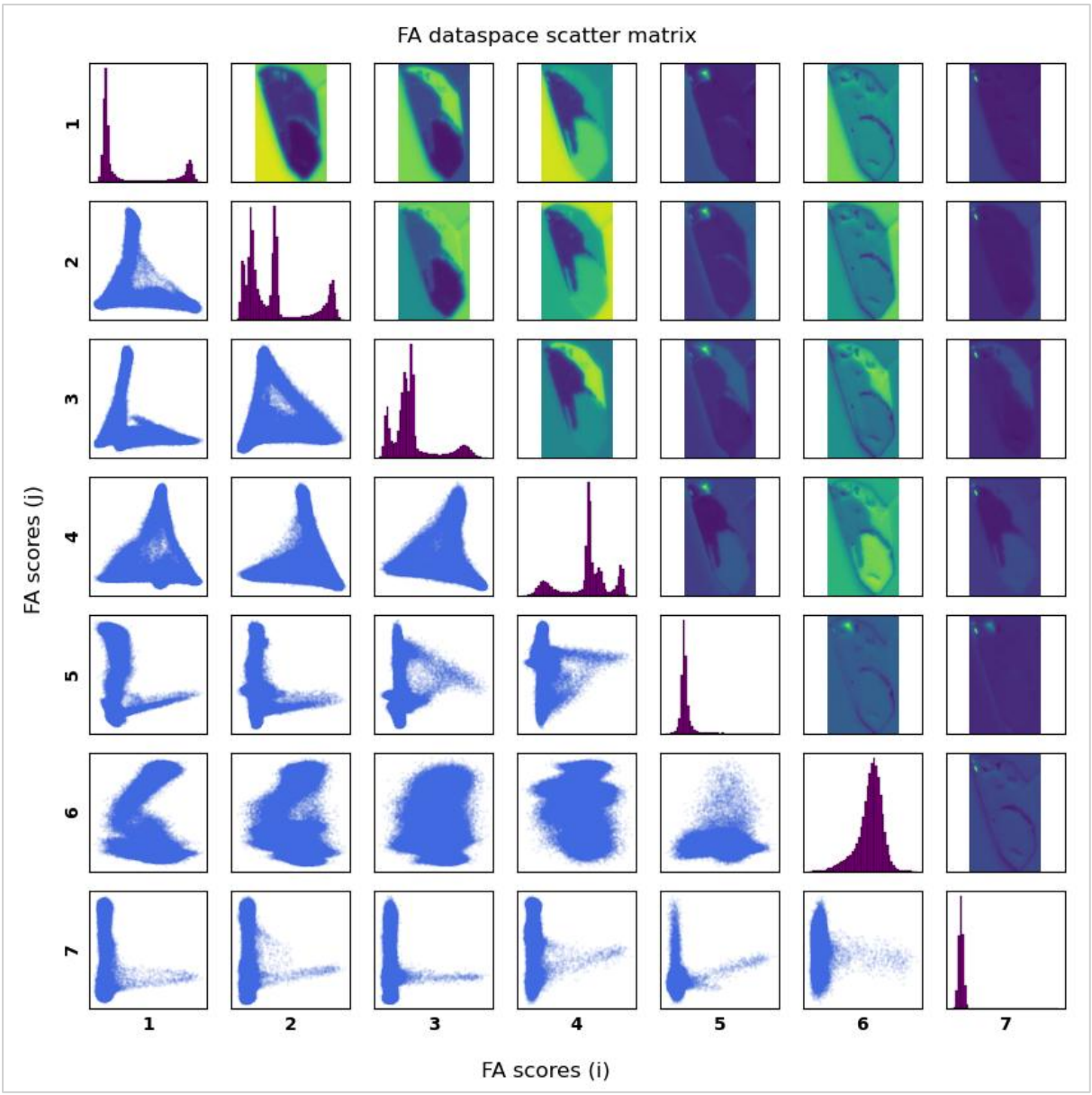
FA dataspace scatter matrix
FA scores (j)
FA scores (i)
1
2
3
4
5
6
7

Cluster signal plots

Site 01:

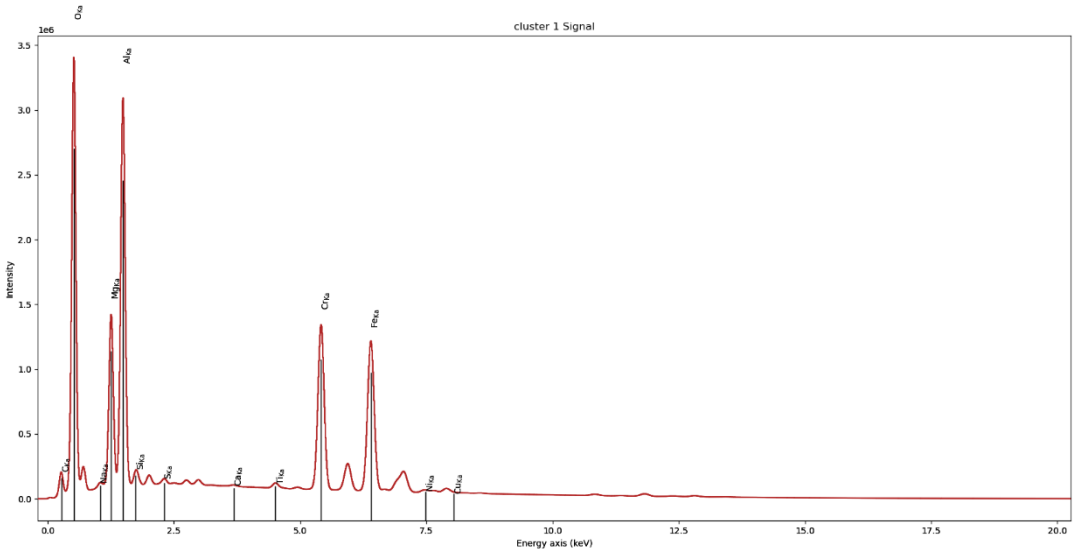

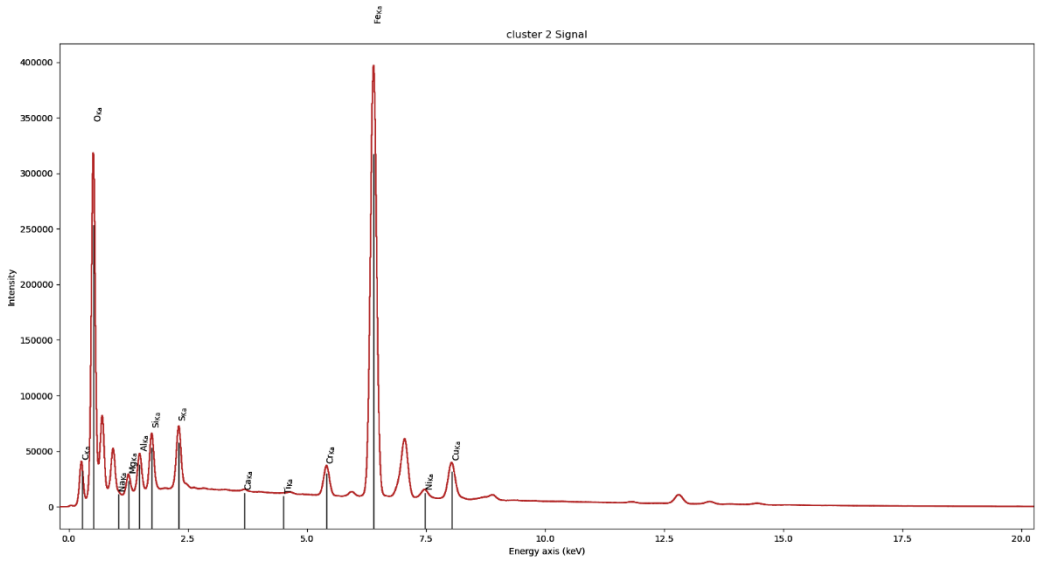

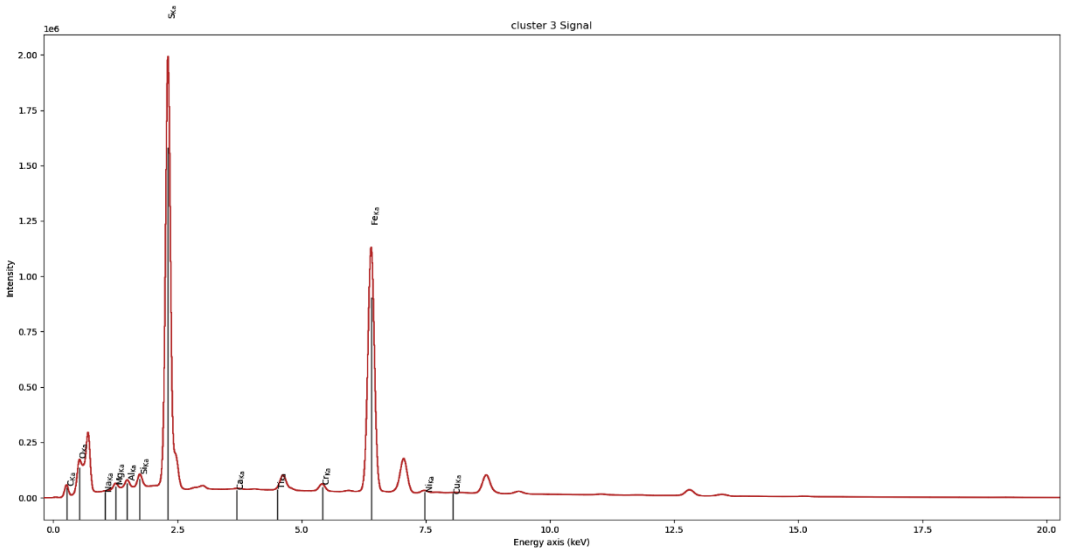
cluster 3 Signal
1e6
Intensity
Energy axis (keV)
Si Kα
Fe Kα
Cu Kα

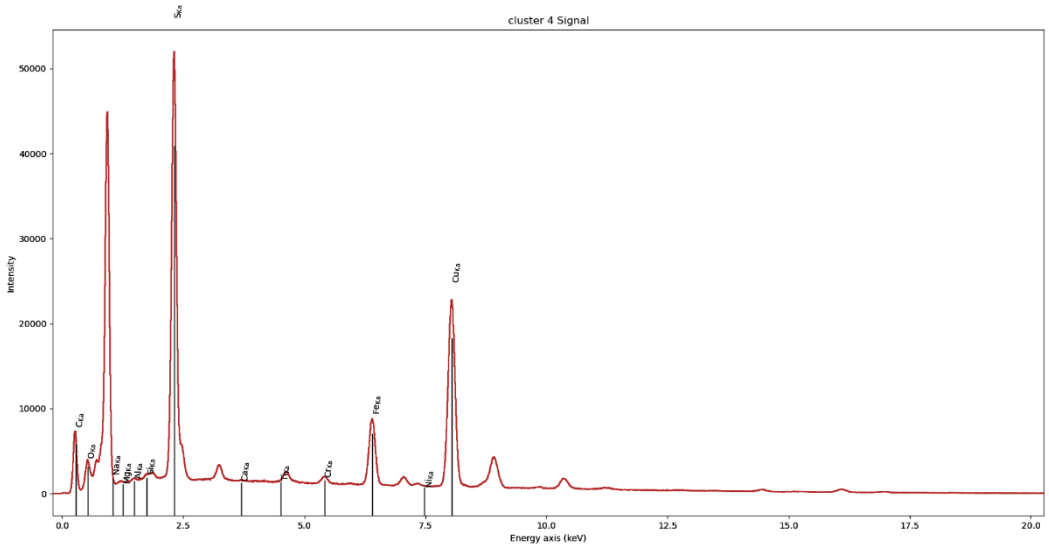
cluster 4 Signal
Intensity
Energy axis (keV)
Si Kα
C Kα
O Kα
Fe Kα
Cu Kα

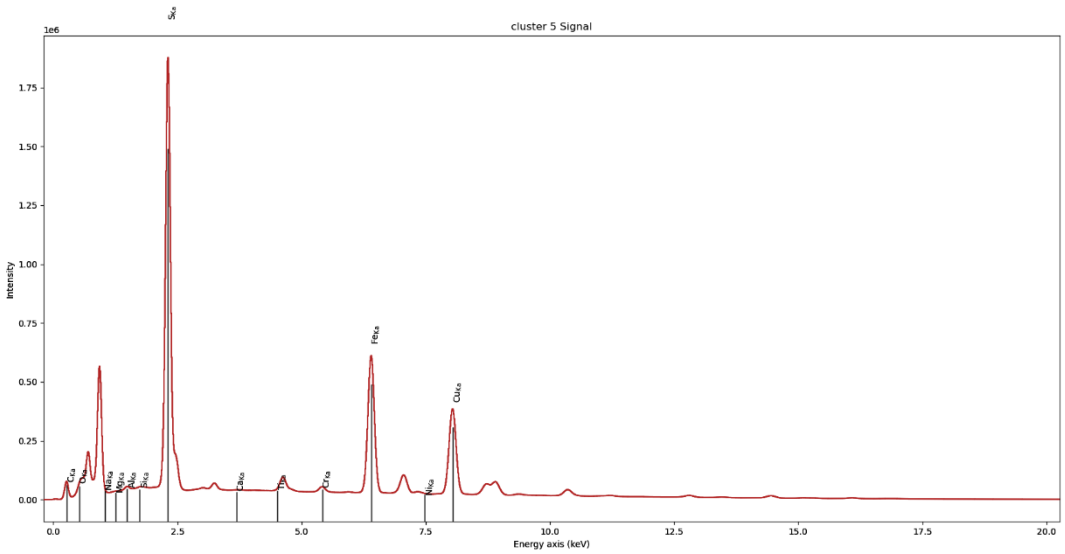
cluster 5 Signal
1e6
Intensity
Energy axis (keV)
Si Kα
Fe Kα
Cu Kα

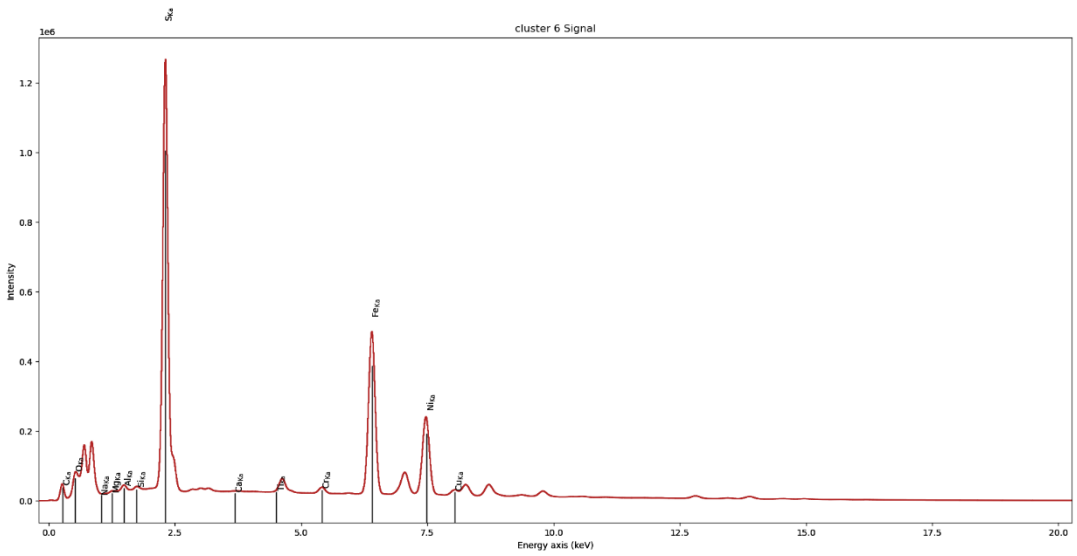
cluster 6 Signal
1e6
Intensity
Energy axis (keV)
Si Kα
Fe Kα
Ni Kα
Cr Kα
Cu Kα

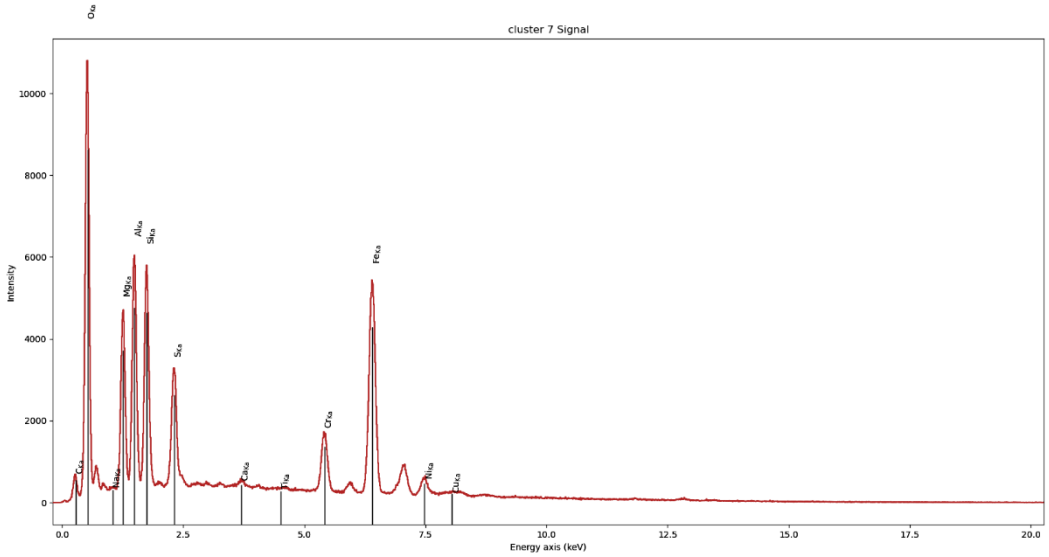
cluster 7 Signal
Intensity
Energy axis (keV)
O Kα
Al Kα
Si Kα
Mg Kα
Fe Kα
Cr Kα
Ni Kα
Cu Kα

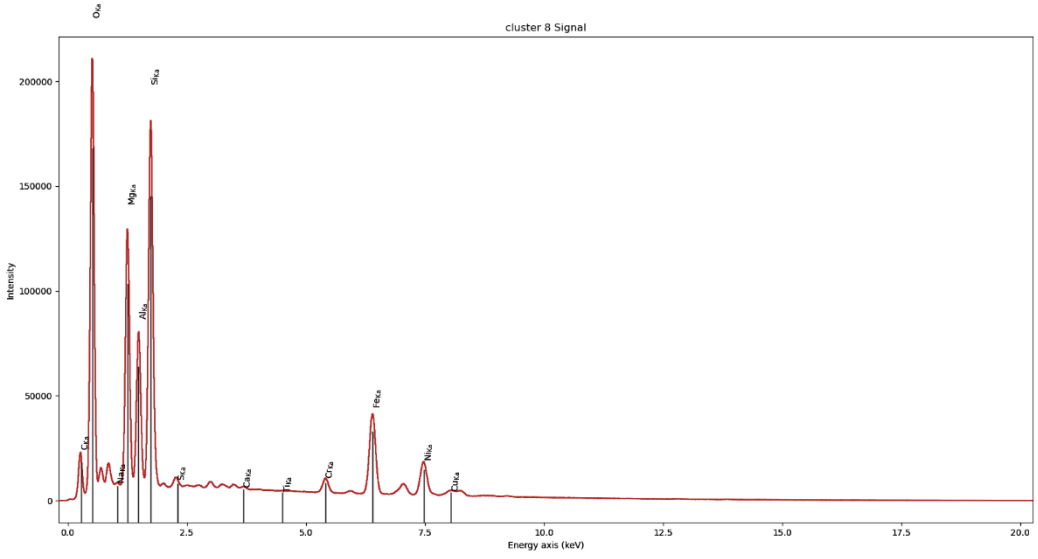
cluster 8 Signal
Intensity
Energy axis (keV)
O Kα
Si Kα
Mg Kα
Al Kα
Fe Kα
Cr Kα
Ni Kα

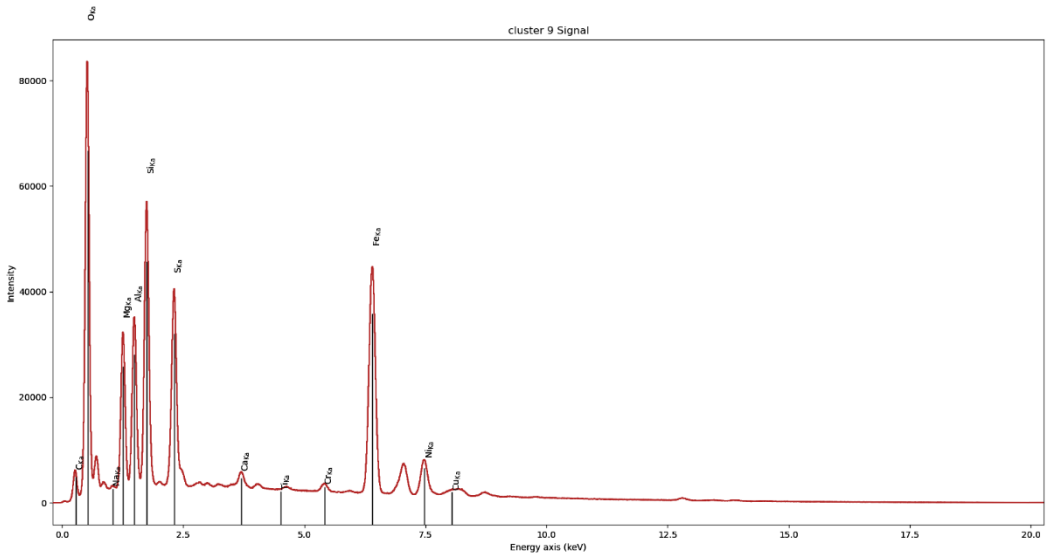
cluster 9 Signal
Intensity
Energy axis (keV)
O Kα
Si Kα
Fe Kα
Sr Kα
Mg Kα
Al Kα
Ca Kα
Cr Kα
Ni Kα
Cu Kα

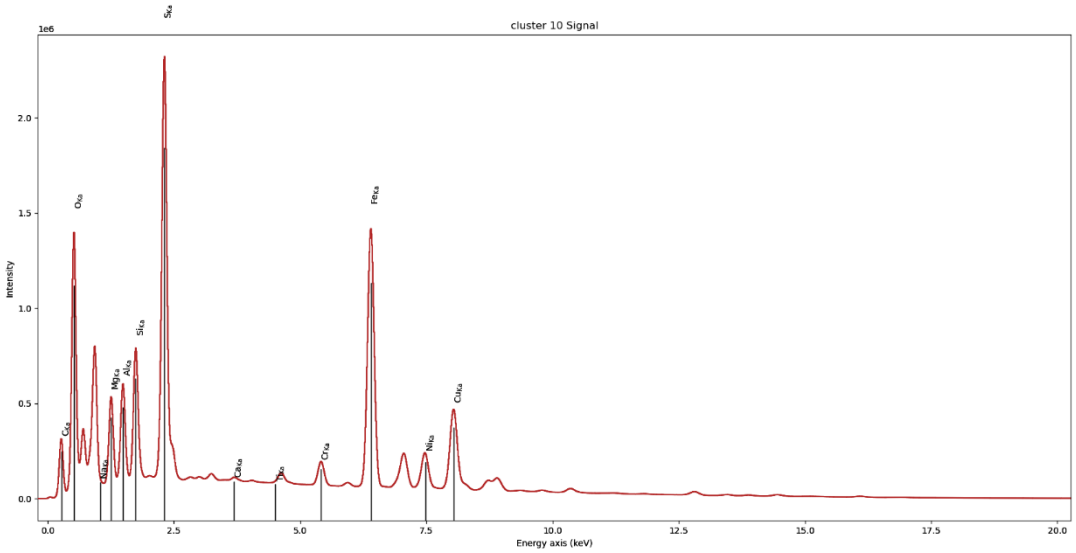
cluster 10 Signal
1e6
Intensity
Energy axis (keV)
S Kα
O Kα
Fe Kα
Si Kα
Mg Kα
Al Kα
Ca Kα
Cr Kα
Ni Kα
Cu Kα

Site 04:

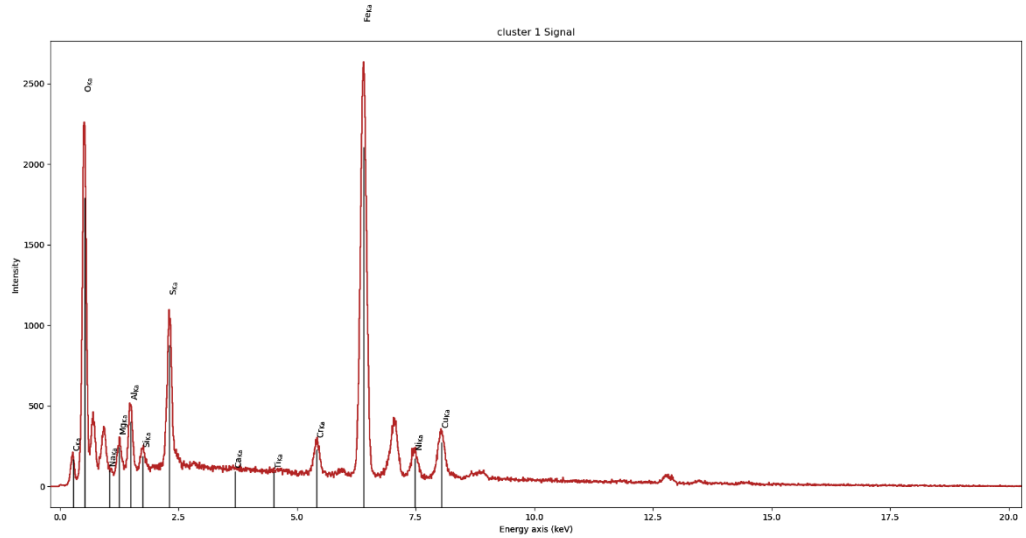
cluster 1 Signal
Intensity
Energy axis (keV)
Fe Kα
O Kα
Si Kα
Al Kα
Mg Kα
Ca Kα
Ti Kα
Cr Kα
Ni Kα
Cu Kα

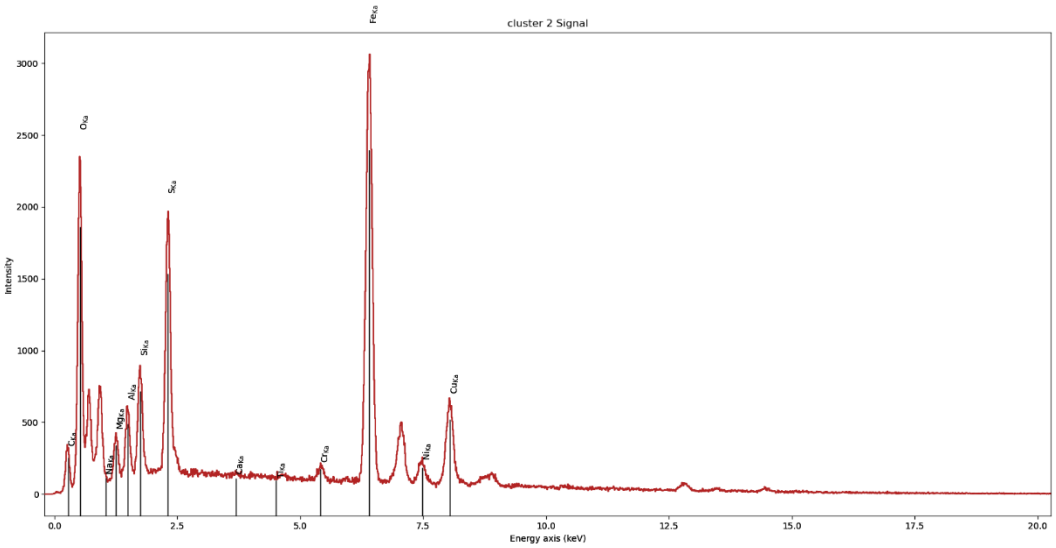
cluster 2 Signal
Intensity
Energy axis (keV)
Fe Kα
O Kα
Si Kα
Al Kα
Mg Kα
Ca Kα
Ti Kα
Cr Kα
Ni Kα
Cu Kα

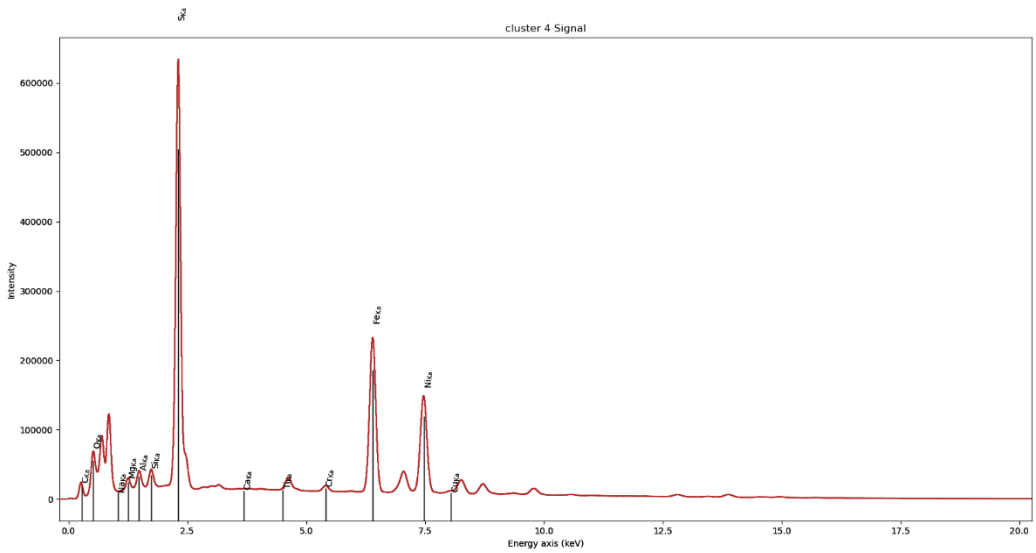
cluster 4 Signal
Intensity
Energy axis (keV)
SKa
FeKa
NiKa
OKa
CKa
MgKa
AlKa
SiKa
CaKa
TiKa
CrKa
CuKa

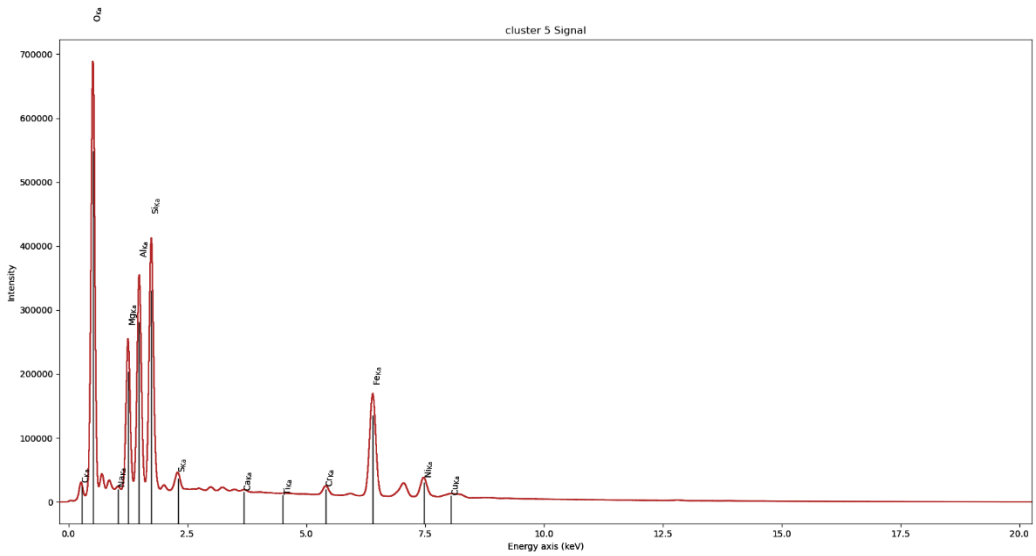
cluster 5 Signal
Intensity
Energy axis (keV)
OKa
SiKa
AlKa
MgKa
FeKa
CKa
SKa
CaKa
TiKa
CrKa
NiKa
CuKa

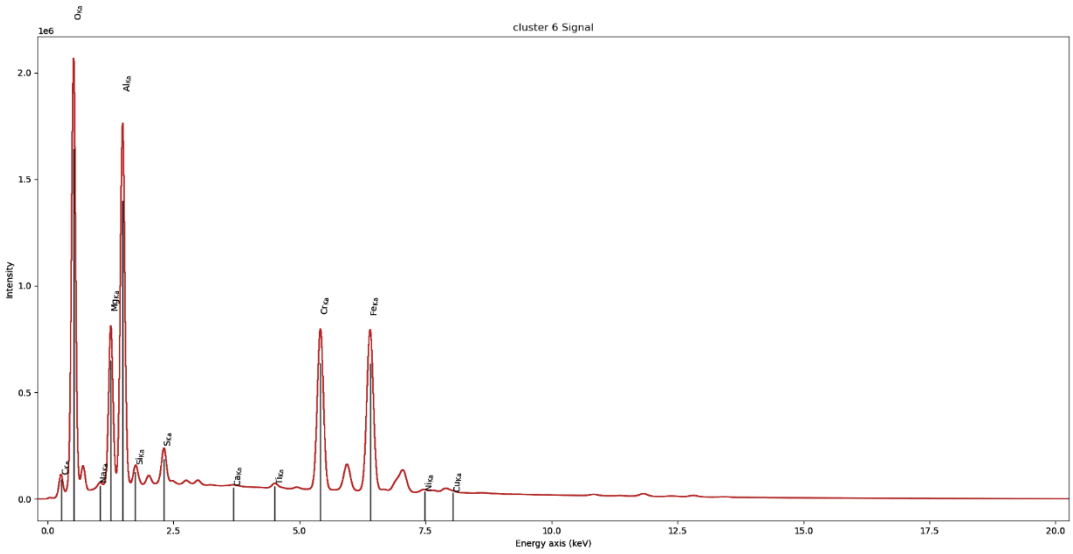
cluster 6 Signal
1e6
Intensity
Energy axis (keV)
OKa
AlKa
MgKa
CrKa
FeKa
CKa
SiKa
SKa
CaKa
TiKa
NiKa
CuKa

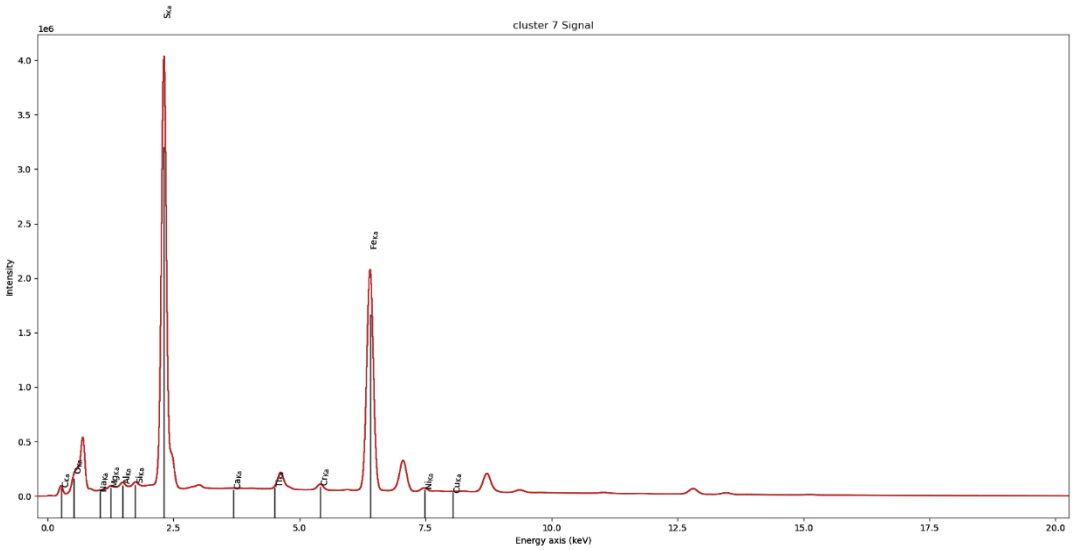
cluster 7 Signal
1e6
Intensity
Energy axis (keV)
Si Kα
Fe Kα
O Kα
Ca Kα
Cr Kα
Ni Kα
Cu Kα

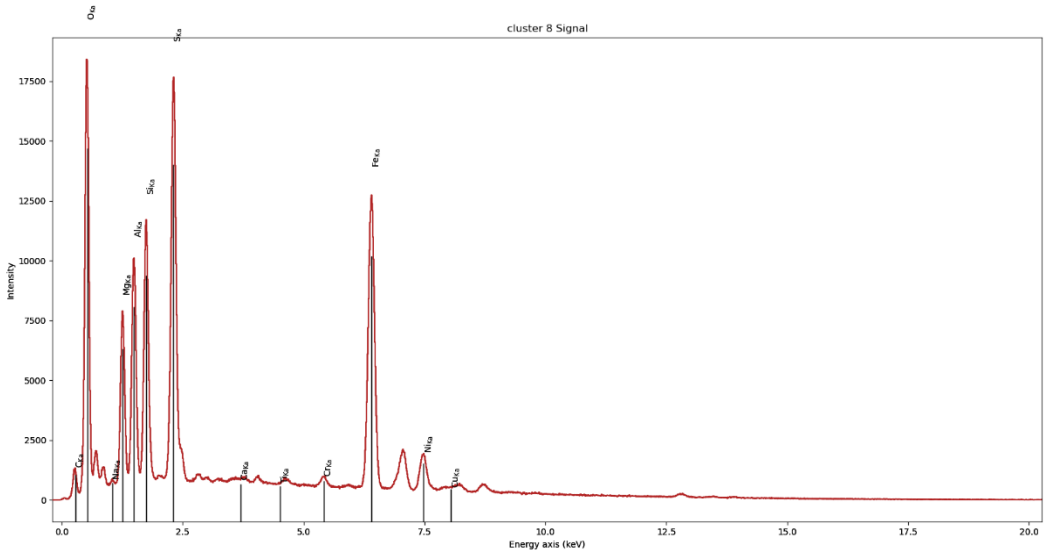
cluster 8 Signal
Intensity
Energy axis (keV)
O Kα
Si Kα
Fe Kα
Al Kα
Mg Kα
Ni Kα

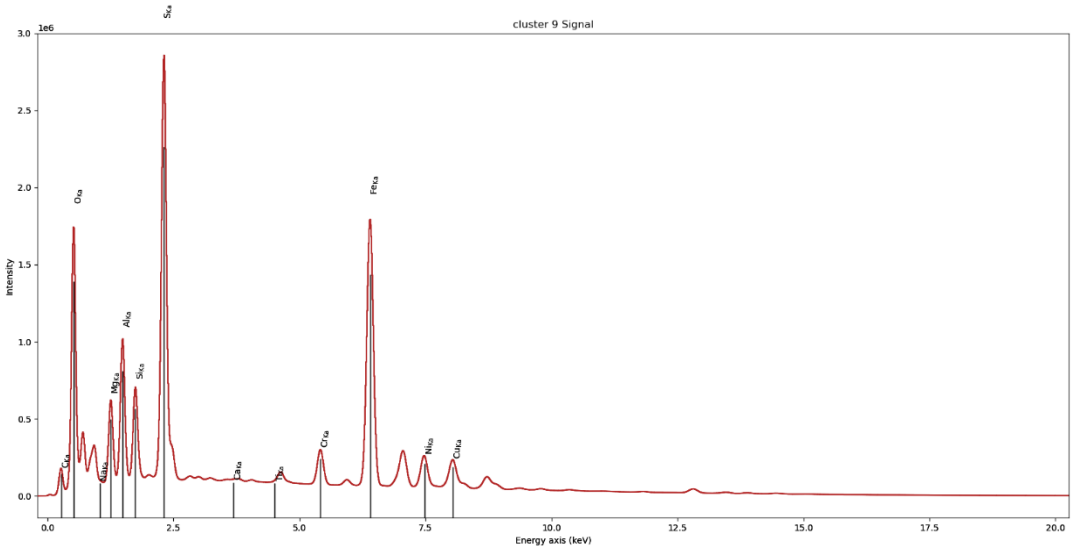
cluster 9 Signal
1e6
Intensity
Energy axis (keV)
Si Kα
O Kα
Fe Kα
Al Kα
Mg Kα
Si Kα
Ca Kα
Cr Kα
Ni Kα
Cu Kα

Site 08:

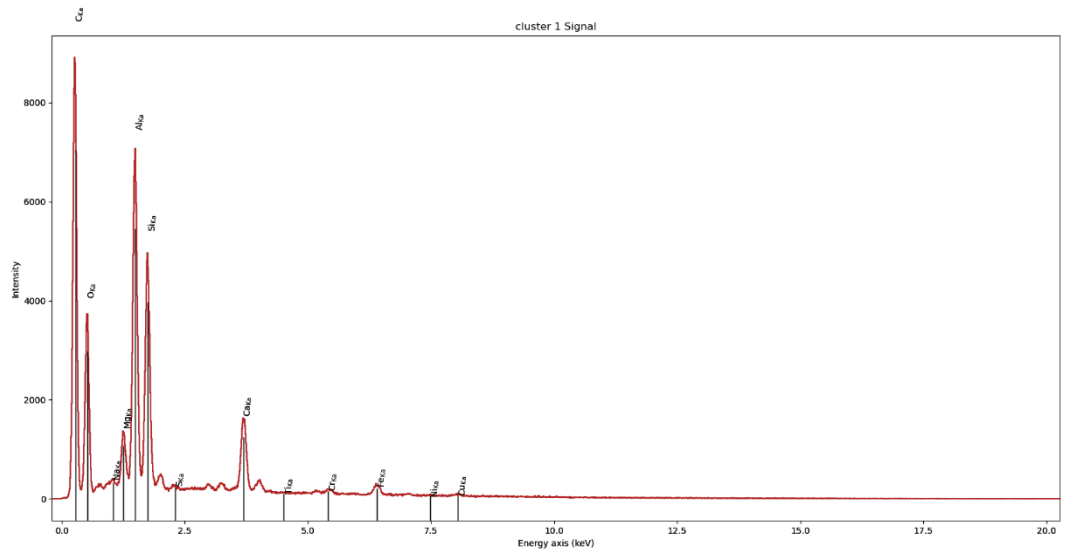
cluster 1 Signal
Intensity
Energy axis (keV)

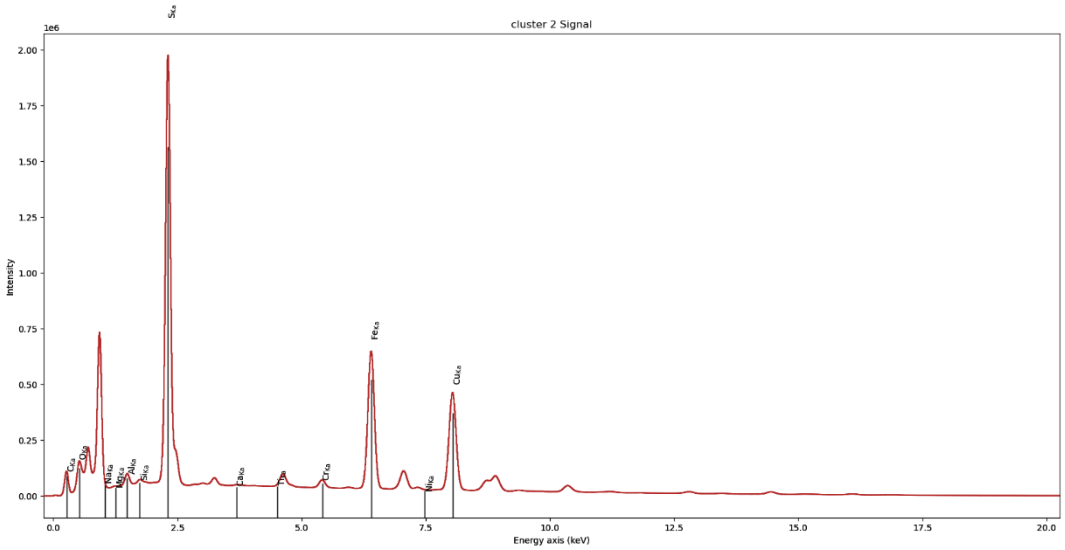
cluster 2 Signal
1e6
Intensity
Energy axis (keV)

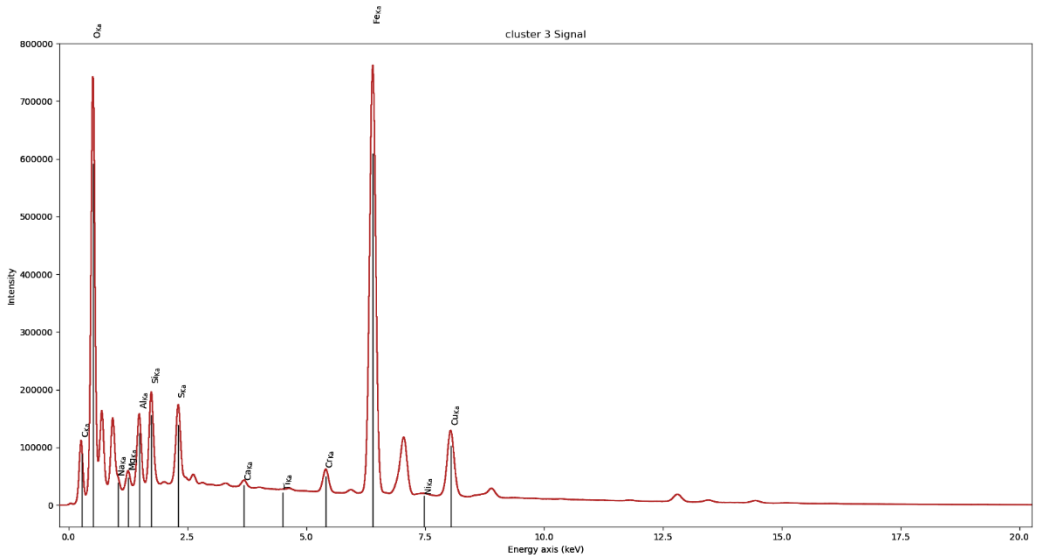
cluster 3 Signal
Intensity
Energy axis (keV)

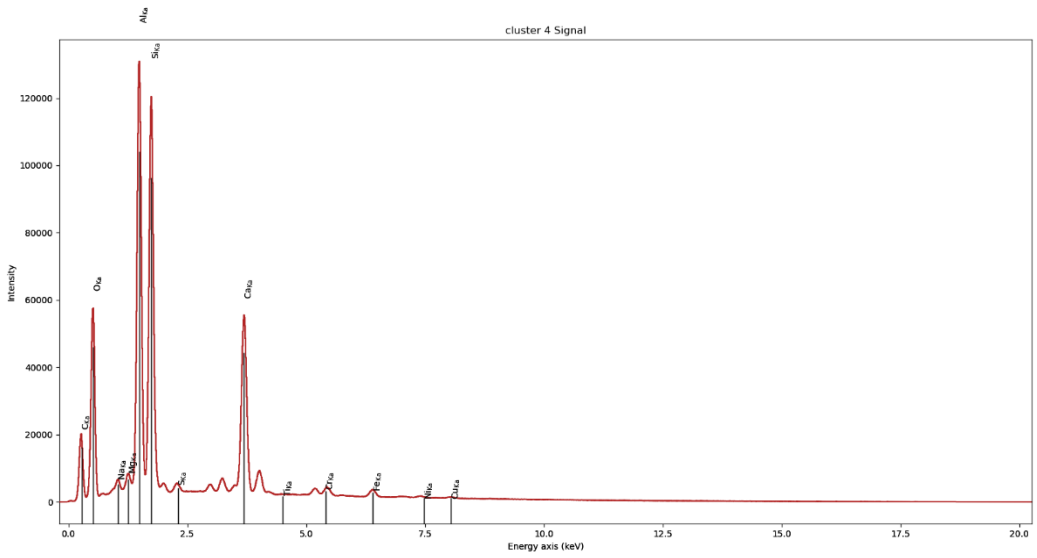
cluster 4 Signal
Intensity
Energy axis (keV)

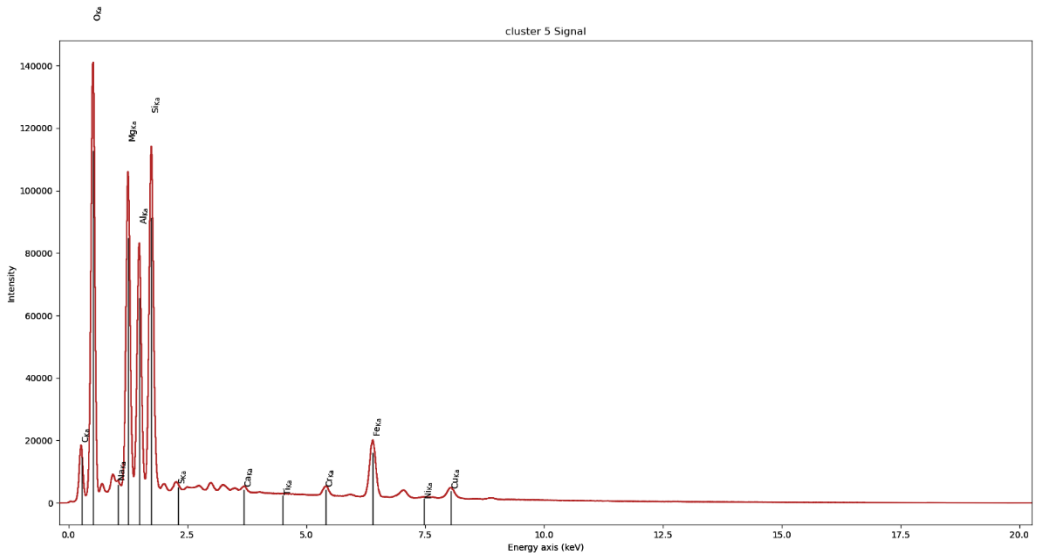
cluster 5 Signal
Intensity
Energy axis (keV)

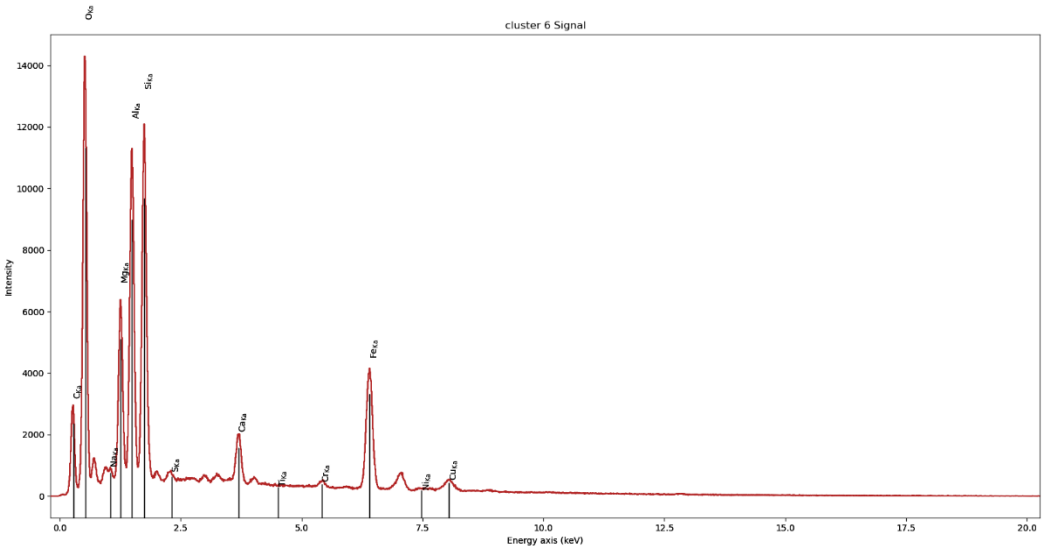
cluster 6 Signal
Intensity
Energy axis (keV)
O Kα
Si Kα
Al Kα
Mg Kα
Ca Kα
Fe Kα

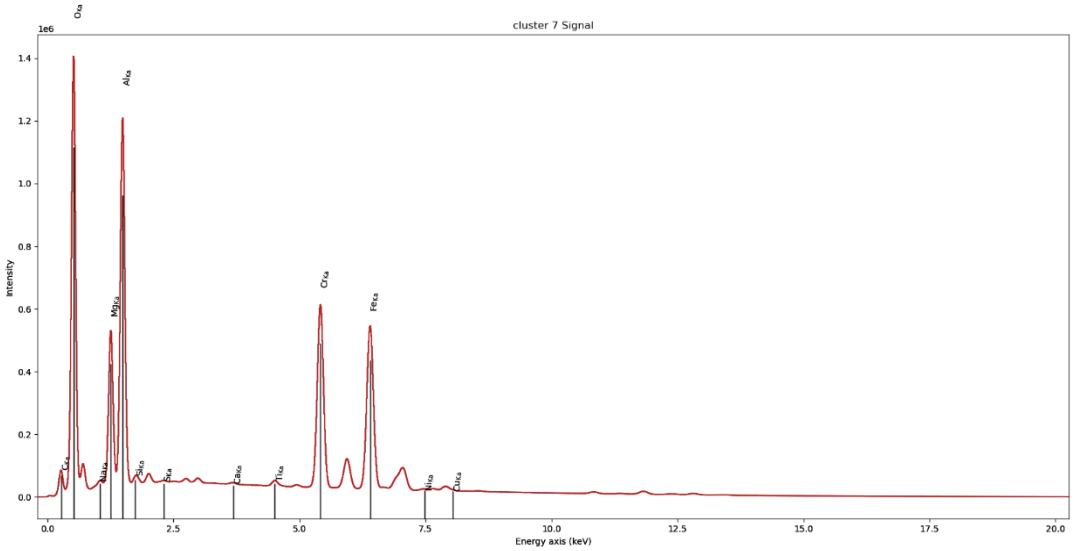
cluster 7 Signal
1e6
Intensity
Energy axis (keV)
O Kα
Al Kα
Mg Kα
Cr Kα
Fe Kα

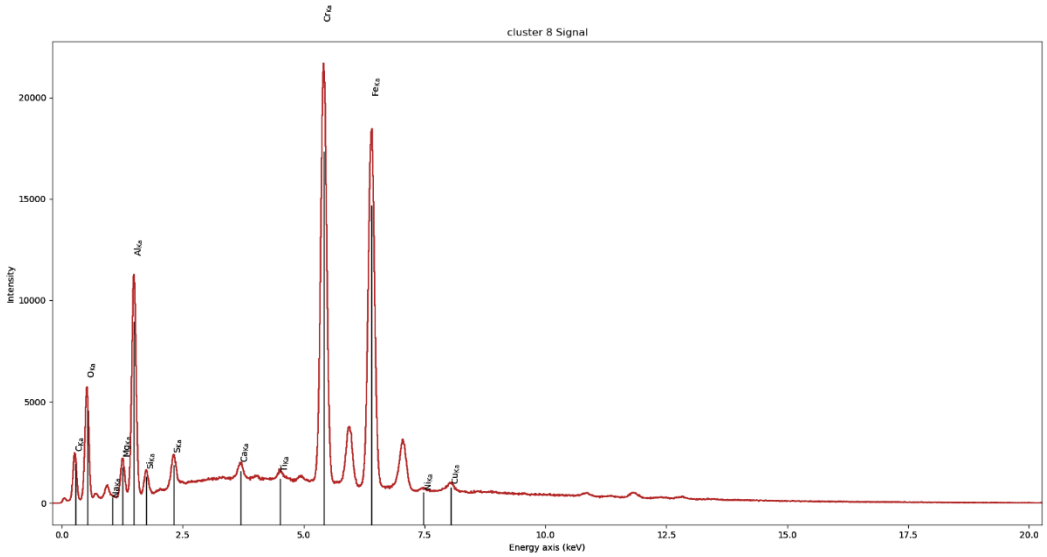
cluster 8 Signal
Intensity
Energy axis (keV)
0
5000
10000
15000
20000
0.0
2.5
5.0
7.5
10.0
12.5
15.0
17.5
20.0
Cr Kα
Fe Kα
Al Kα
O Kα
C Kα
Mg Kα
Si Kα
Ca Kα
Ti Kα
Ni Kα
Cu Kα

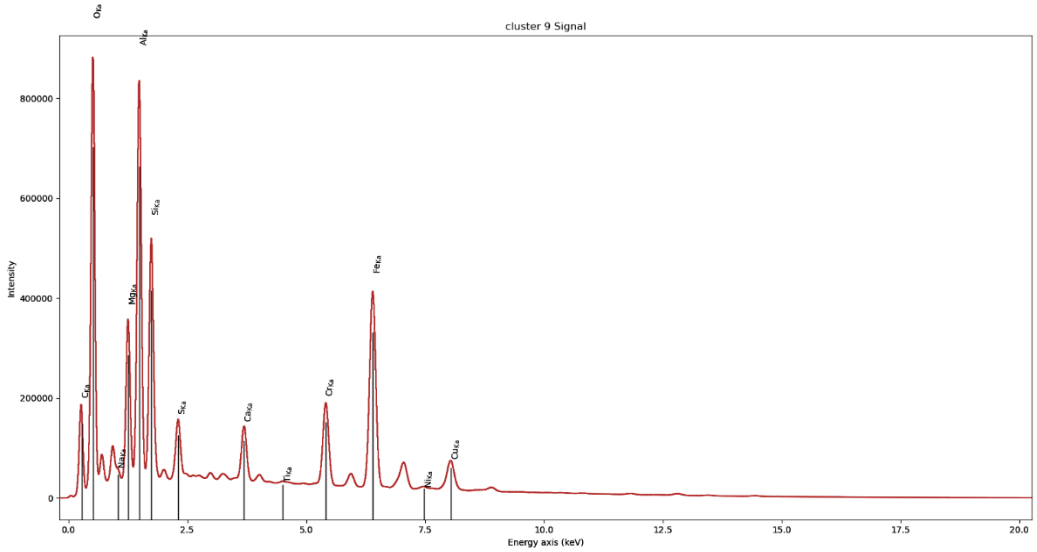
cluster 9 Signal
Intensity
Energy axis (keV)
0
200000
400000
600000
800000
0.0
2.5
5.0
7.5
10.0
12.5
15.0
17.5
20.0
O Kα
Al Kα
Si Kα
Mg Kα
C Kα
Na Kα
S Kα
Ca Kα
Ti Kα
Cr Kα
Fe Kα
Ni Kα
Cu Kα

Site 15:

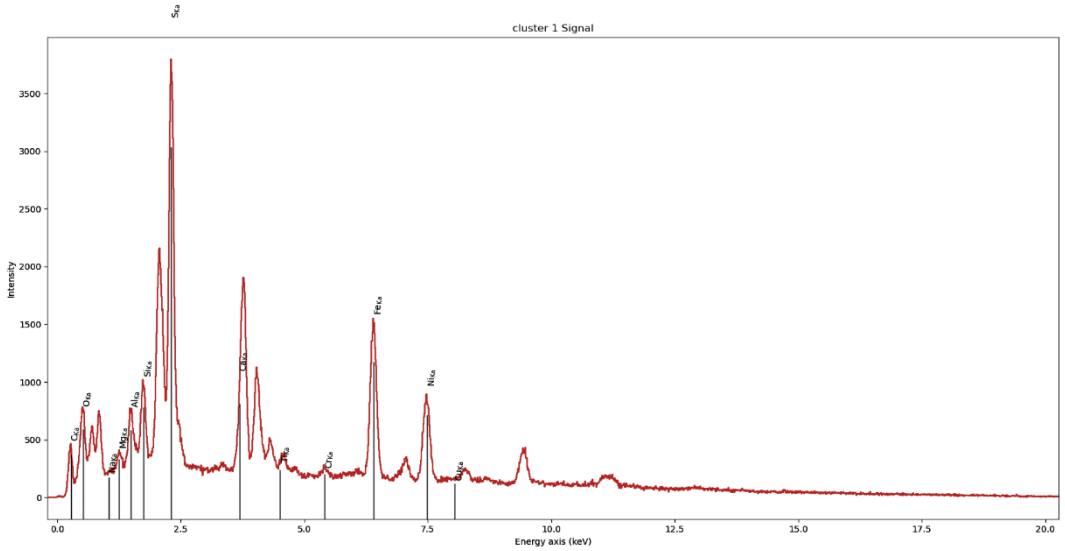
cluster 1 Signal
Intensity
Energy axis (keV)
Si Kα
Ca Kα
Fe Kα
Ni Kα
O Kα
Al Kα
C Kα
Mg Kα
Na Kα
Cl Kα
Cu Kα

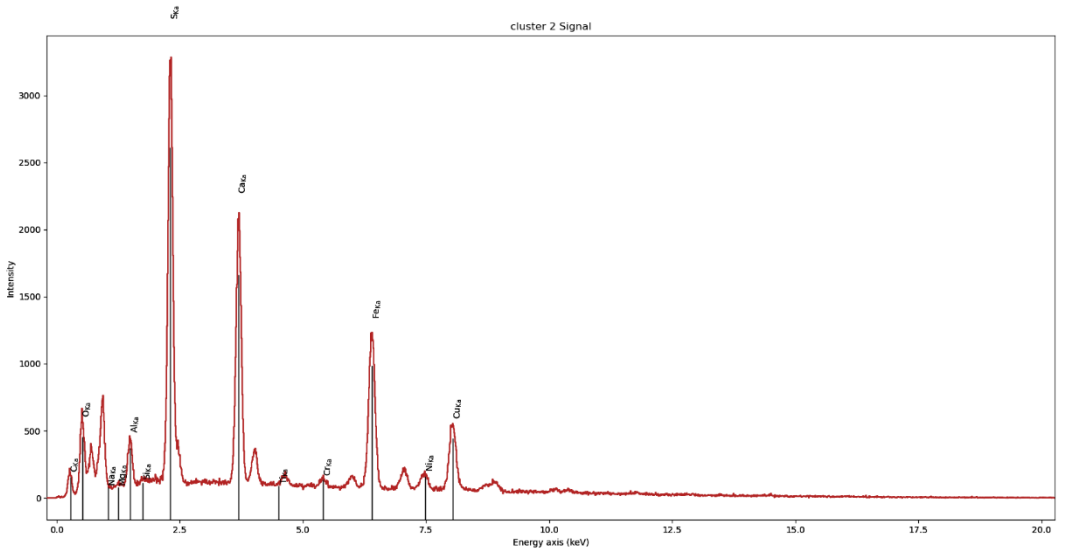
cluster 2 Signal
Intensity
Energy axis (keV)
Si Kα
Ca Kα
Fe Kα
Cu Kα
O Kα
Al Kα
C Kα
Ni Kα
Cl Kα

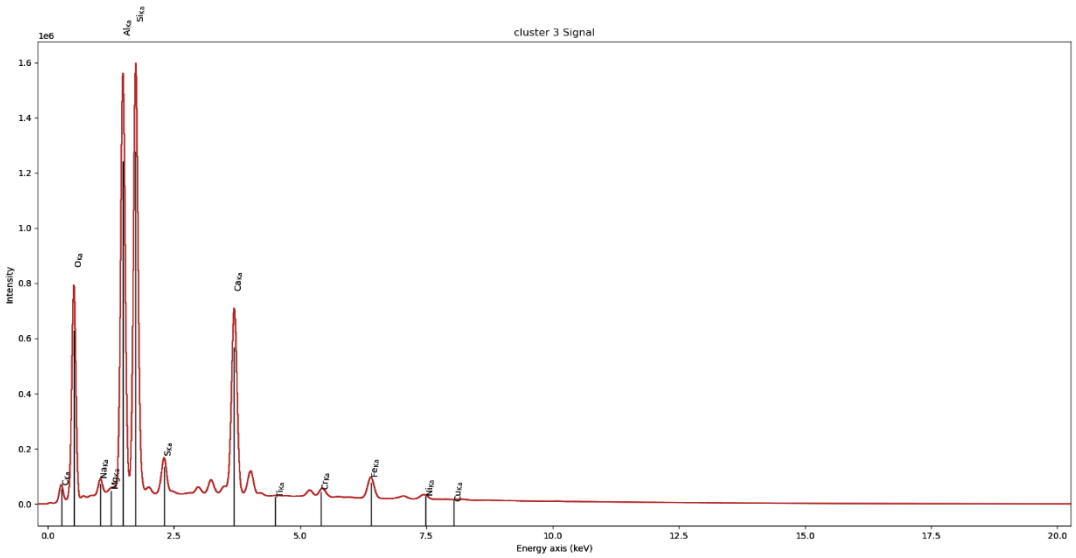
cluster 3 Signal
1e6
Intensity
Energy axis (keV)
O Kα
Al Kα
Si Kα
Ca Kα
Fe Kα
Ni Kα
Cu Kα

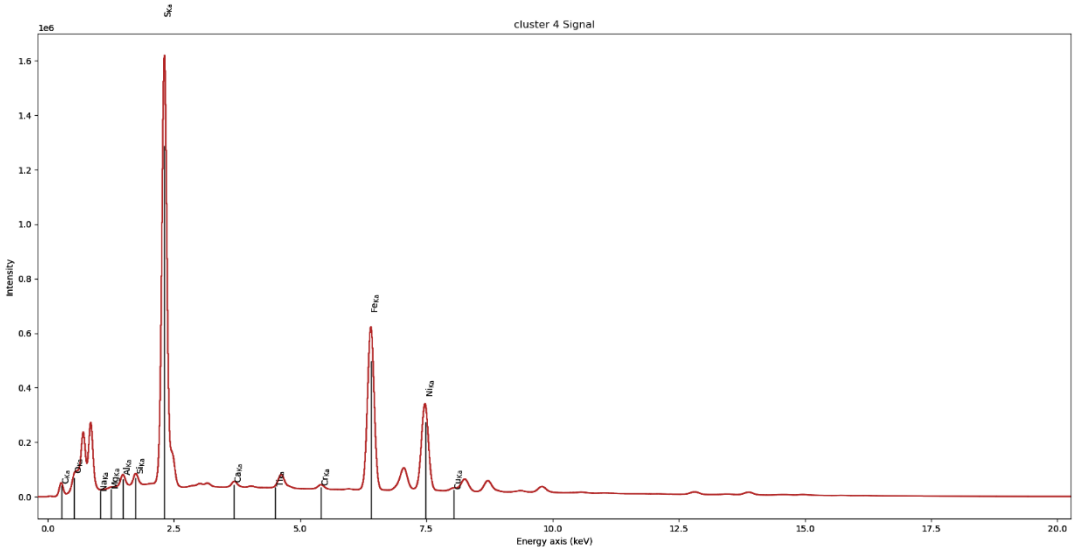
cluster 4 Signal
1e6
Intensity
Energy axis (keV)
Si Kα
Fe Kα
Ni Kα
Ca Kα
Cu Kα

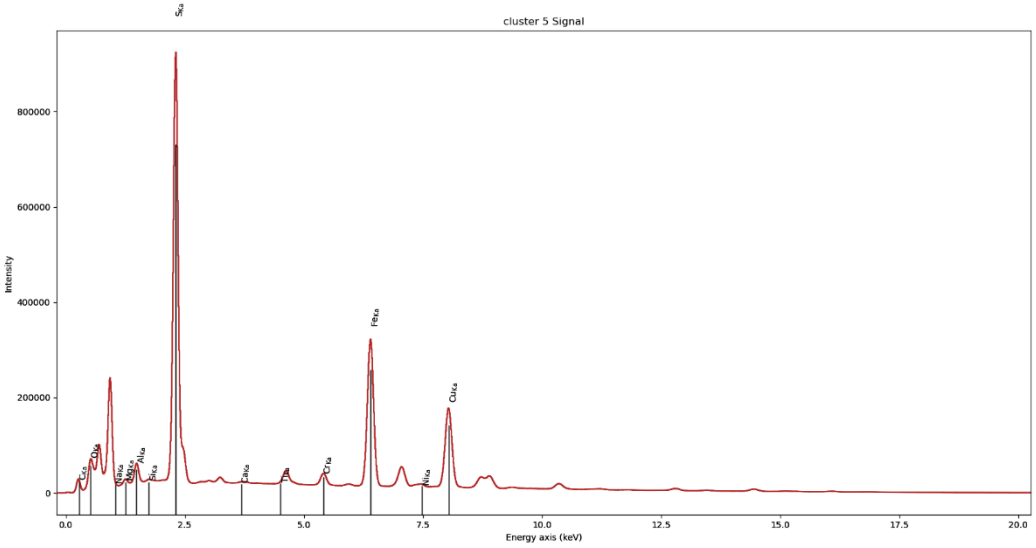
cluster 5 Signal
Intensity
Energy axis (keV)
Si Kα
Fe Kα
Ca Kα
Cu Kα

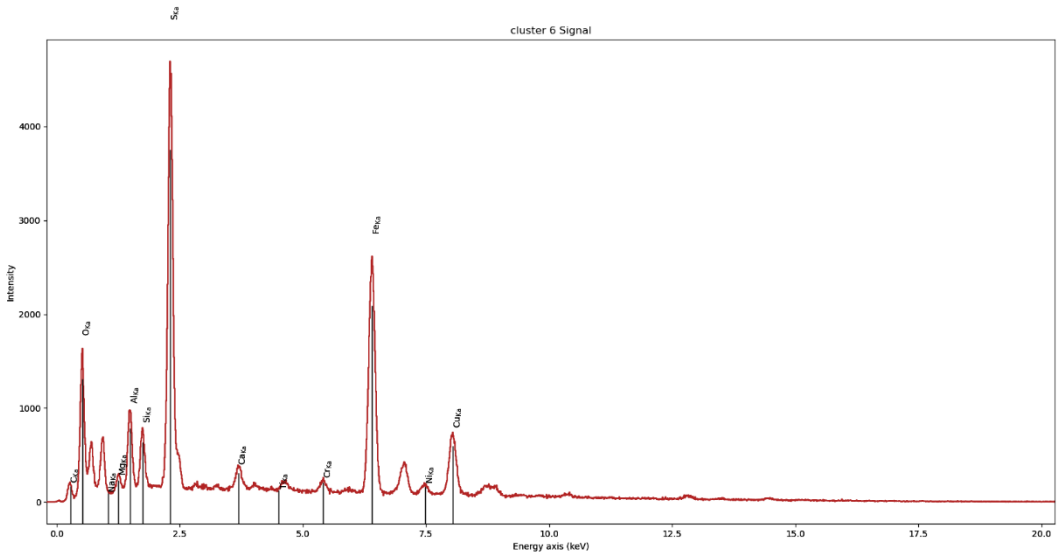
cluster 6 Signal
Intensity
Energy axis (keV)
0
1000
2000
3000
4000
0.0
2.5
5.0
7.5
10.0
12.5
15.0
17.5
20.0
Ca Kα
O Kα
Mg Kα
Al Kα
Si Kα
S Kα
Ca Kα
Ti Kα
Cr Kα
Fe Kα
Ni Kα
Cu Kα

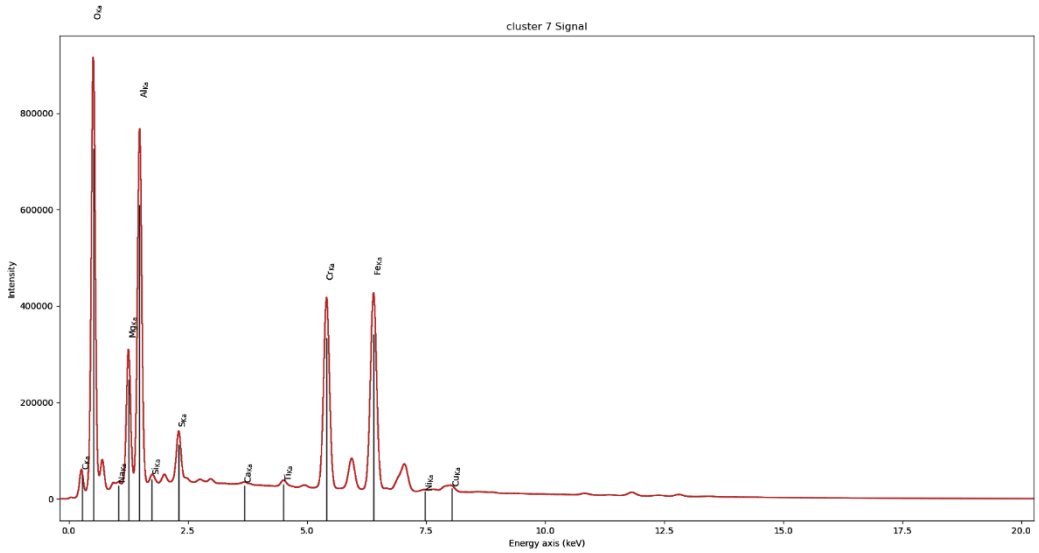
cluster 7 Signal
Intensity
Energy axis (keV)
0
200000
400000
600000
800000
0.0
2.5
5.0
7.5
10.0
12.5
15.0
17.5
20.0
O Kα
Al Kα
Mg Kα
Si Kα
S Kα
Ca Kα
Ti Kα
Cr Kα
Fe Kα
Ni Kα
Cu Kα

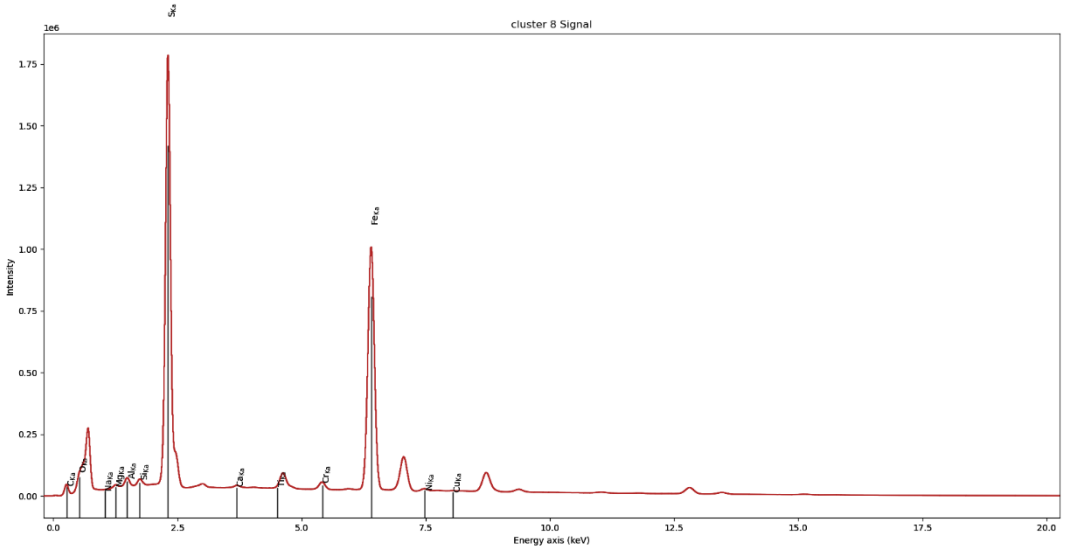
cluster 8 Signal
1e6
Intensity
Energy axis (keV)
0.00
0.25
0.50
0.75
1.00
1.25
1.50
1.75
0.0
2.5
5.0
7.5
10.0
12.5
15.0
17.5
20.0
S Kα
Ca Kα
O Kα
Mg Kα
Al Kα
Si Kα
Ca Kα
Ti Kα
Cr Kα
Fe Kα
Ni Kα
Cu Kα

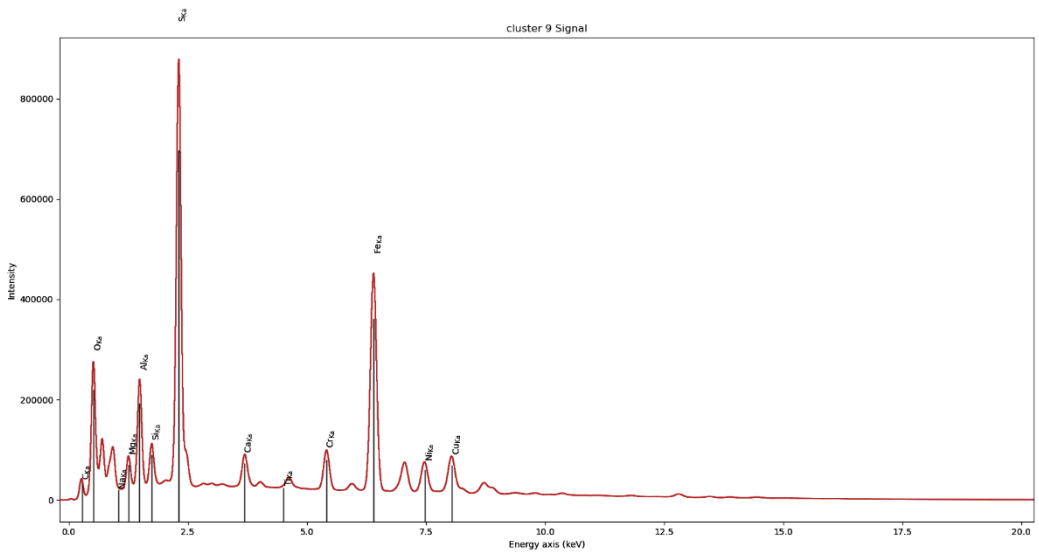
cluster 9 Signal
Intensity
Energy axis (keV)
0
200000
400000
600000
800000
0.0
2.5
5.0
7.5
10.0
12.5
15.0
17.5
20.0
CKa
OKa
MgKa
AlKa
SiKa
ScKa
CaKa
TiKa
CrKa
FeKa
NiKa
CuKa

REFERENCES

Abdi, H., (2003). Factor rotations in factor analyses. *Encyclopaedia for Research Methods for the Social Sciences. Sage: Thousand Oaks, CA*, pp.792-795.

Agarwal, A., Simonaitis, J. and Berggren, K.K. (2021) 'Image-histogram-based secondary electron counting to evaluate detective quantum efficiency in Sem', *Ultramicroscopy*, 224, p. 113238. doi:10.1016/j.ultramic.2021.113238.

Agarwal, A. *et al.* (2023) 'Secondary Electron Count Imaging in Sem', *Ultramicroscopy*, 245, p. 113662. doi:10.1016/j.ultramic.2022.113662.

Agarwal, A. *et al.* (2024) 'Shot noise-mitigated secondary electron imaging with ion count-aided microscopy', *Proceedings of the National Academy of Sciences*, 121(31). doi:10.1073/pnas.2401246121.

Altree-Williams, A. *et al.* (2015) 'Textural and compositional complexities resulting from coupled dissolution–reprecipitation reactions in geomaterials', *Earth-Science Reviews*, 150, pp. 628–651. doi:10.1016/j.earscirev.2015.08.013.

Bailey E. B. *et al.*,Tertiary and post-Tertiary geology of Mull, Loch Aline and Oban, Memoir of the Geological Survey of Great Britain, Scotland, 1924EdinburghHMSO

Ballhaus, C. and Sylvester, P. (2000) 'Noble metal enrichment processes in the Merensky Reef, bushveld complex', *Journal of Petrology*, 41(4), pp. 545–561. doi:10.1093/petrology/41.4.545.

Ballhaus C, Tredoux M, Späth A (2001) Phase relations in the Fe-Ni-Cu-PGE-S system at magmatic temperature and application to massive sulfide ores of the Sudbury Igneous Complex. J Petrol 42:1911–1926

Barnes, S.J. *et al.* (2016) 'The mineral system approach applied to magmatic Ni–Cu–PGE sulphide deposits', *Ore Geology Reviews*, 76, pp. 296–316. doi:10.1016/j.oregeorev.2015.06.012.

Barnes, S. -J. and Mungall, J. E. (2018). Up, down, or sideways: emplacement of magmatic Fe–Ni–Cu–PGE sulfide ore deposits.

Bell, B.R. (1983) 'Significance of ferrodioritic liquids in magma mixing processes', *Nature*, 306(5941), pp. 323–327. doi:10.1038/306323a0.

Bell, B.R. and Williamson, I.T. (2024) '15: Paleogene igneous activity: North Atlantic Plume-related magmatism', *The Geology of Scotland*, pp. 457–504. doi:10.1144/gos5-2021-40.

BGS Rock Classification scheme (2025) *BGS Rock Classification Scheme - Details for Anorthosite* . Available at: https://webapps.bgs.ac.uk/bgsrcs/rcs_details.cfm?code=ANO (Accessed: August 2025).

Bolle, O. *et al.* (2021) 'Central sagging of a giant mafic intrusion: The Ediacaran sept îles layered intrusion (Québec, Canada)', *Journal of the Geological Society*, 178(1). doi:10.1144/jgs2020-029.

Brown, G.M. (1956) ‘The layered ultrabasic tocks of Rhum, inner hebrides’, *Philosophical Transactions of the Royal Society of London. Series B, Biological Sciences*, 240(668), pp. 1–53. doi:10.1098/rstb.1956.0011.

Brown, D.J. and Bell, B.R. (2007) ‘How do you grade peperites?’, *Journal of Volcanology and Geothermal Research*, 159(4), pp. 409–420. doi:10.1016/j.jvolgeores.2006.08.008.

Brown, D.J., Holohan, E.P. and Bell, B.R. (2009) ‘Sedimentary and volcano-tectonic processes in the British paleocene igneous province: A Review’, *Geological Magazine*, 146(3), pp. 326–352. doi:10.1017/s0016756809006232.

Buick, I.S., Maas, R., Gibson, R., (2001). Precise U–Pb titanite age constraints on the emplacement of the Bushveld complex, South Africa. J. Geol. Soc. Lond. 158, 3–6

Bucther, A.R. *et al.* (1999) ‘Platinum-group mineralization in the Rum layered intrusion, Scottish Hebrides, UK’, *Journal of the Geological Society*, 156(2), pp. 213–216. doi:10.1144/gsjgs.156.2.0213.

Cawthorn, R.G. (1996) ‘Layered intrusions’, *Developments in Petrology* [Preprint]. doi:10.1016/s0167-2894(96)x8001-1.

Cawthorn, R.G. and Miller, J. (2018) ‘Lopolith – a 100 year-old term. is it still definitive?’, *South African Journal of Geology*, 121(3), pp. 253–260. doi:10.25131/sajg.121.0019.

Chambers, L.M. and Fitton, J.G. (2000) ‘Geochemical transitions in the ancestral iceland plume: Evidence from the Isle of Mull Tertiary Volcano, Scotland’, *Journal of the Geological Society*, 157(2), pp. 261–263. doi:10.1144/jgs.157.2.261.

Chambers, L.M., Pringle, M.S. and Parrish, R.R. (2005) ‘Rapid formation of the small isles tertiary centre constrained by precise 40ar/39ar and U–Pb Ages’, *Lithos*, 79(3–4), pp. 367–384. doi:10.1016/j.lithos.2004.09.008.

Chaudhari, A. *et al.* (2021) ‘Anatomy of a complex mineral replacement reaction: Role of aqueous redox, mineral nucleation, and ion transport properties revealed by an in-situ study of the replacement of chalcopyrite by copper sulfides’, *Chemical Geology*, 581, p. 120390. doi:10.1016/j.chemgeo.2021.120390.

Chaudhari, A. *et al.* (2022) ‘Synchronous solid-state diffusion, dissolution-reprecipitation, and recrystallization leading to isotopic resetting: Insights from chalcopyrite replacement by copper sulfides’, *Geochimica et Cosmochimica Acta*, 331, pp. 48–68. doi:10.1016/j.gca.2022.06.005.

Chistyakova, S. *et al.* (2019) ‘Merensky-type platinum deposits and a reappraisal of magma chamber paradigms’, *Scientific Reports*, 9(1). doi:10.1038/s41598-019-45288-8.

Craig, J. R., & Kullerud, G. (1969). Phase relations in the Cu-Fe-Ni-S System and their application to magmatic ore deposits. *Economic Geology Monograph*, *4*, 344-358.

Cruden, A.R., McCaffrey, K.J. and Bunger, A.P. (2018) ‘Geometric scaling of tabular igneous intrusions: Implications for emplacement and growth’, *Advances in Volcanology*, pp. 11–38. doi:10.1007/11157_2017_1000.

Currie, D. & Elliott, H (2024). ‘The potential for rare earth elements in the UK’. *British Geological. Survey*. Commissioned report. OR/24/006. 8pp

Dahmen, T. *et al.* (2016) 'Feature adaptive sampling for scanning electron microscopy', *Scientific Reports*, 6(1). doi:10.1038/srep25350.

Deer, W.A., Howie, R.A. and Zussman, J. (2013) *An introduction to the rock-forming minerals* [Preprint]. doi:10.1180/dhz.

Dickin, A.P. (1981) 'Isotope geochemistry of Tertiary Igneous Rocks from the Isle of Skye, N.W. Scotland', *Journal of Petrology*, 22(2), pp. 155–189. doi:10.1093/petrology/22.2.155.

Dickin, A.P., Exley, R.A. and Smith, B.M. (1980) 'Isotopic measurement of Sr and O exchange between meteoric-hydrothermal fluid and the coire uaigneich granophyre, isle of skye, N.W. Scotland', *Earth and Planetary Science Letters*, 51(1), pp. 58–70. doi:10.1016/0012-821x(80)90257-5.

Dilbeck, K.E. (2017) 'Factor analysis: Varimax rotation', *The SAGE Encyclopedia of Communication Research Methods* [Preprint]. doi:10.4135/9781483381411.n191.

Duma, Z.-S. *et al.* (2022) 'Optimizing energy dispersive X-ray spectroscopy (EDS) image fusion to scanning electron microscopy (SEM) images', *Micron*, 163, p. 103361. doi:10.1016/j.micron.2022.103361.

EELS Atlas (2025) *EELS.info*. Available at: https://eels.info/atlas (Accessed: August 2025).

EELS.info (2025) *EELS.info*. Available at: https://eels.info/ (Accessed: August 2025).

Egerton, R.F., Li, P. and Malac, M. (2004) 'Radiation damage in the TEM and Sem', Micron, 35(6), pp. 399–409. doi:10.1016/j.micron.2004.02.003.

Eldholm, O. and Grue, K. (1994) 'North Atlantic volcanic margins: Dimensions and production rates', *Journal of Geophysical Research: Solid Earth*, 99(B2), pp. 2955–2968. doi:10.1029/93jb02879.

Emeleus, C.H. *et al.* (1996) 'The rum layered suite', *Developments in Petrology*, pp. 403–439. doi:10.1016/s0167-2894(96)80014-5.

Emeleus, C.H., 1997. *Geology of Rum and the adjacent islands: Memoir for 1:50 000 Geological Sheet 60 (Scotland).* London: The Stationery Office for the British Geological Survey. ISBN 0118845179

Emeleus C.H. Bell B.R. (2005) 'British Regional Geology: the Palaeogene volcanic districts of Scotland' (Fourth Edition). *British Geological Survey,* Keyworth, Nottingham, UK.

Emeleus, C.H. and Troll, V.R. (2011) 'Recent research developments on the Isle of Rum, NW Scotland', *Geology Today*, 27(5), pp. 184–193. doi:10.1111/j.1365-2451.2011.00808.x.

Emeleus, C.H. and Troll, V.R. (2014) 'The Rum Igneous Centre, Scotland', *Mineralogical Magazine*, 78(4), pp. 805–839. doi:10.1180/minmag.2014.078.4.04.

Etschmann, B. *et al.* (2004) 'A kinetic study of the exsolution of pentlandite (ni, fe) from the monosulfide solid solution (Fe, ni)s', *American Mineralogist*, 89(1), pp. 39–50. doi:10.2138/am-2004-0106.

Evans, K.A., O'Neill, H.St. and Mavrogenes, J.A. (2008) 'Sulphur solubility and sulphide immiscibility in silicate melts as a function of the concentration of manganese, nickel, tungsten

and copper at 1 atm and 1400 °C', *Chemical Geology*, 255(1–2), pp. 236–249. doi:10.1016/j.chemgeo.2008.06.042.

Fonseca, R.O.C. *et al.* (2009) 'Solubility of PT in sulphide mattes: Implications for the genesis of PGE-rich horizons in layered intrusions', *Geochimica et Cosmochimica Acta*, 73(19), pp. 5764–5777. doi:10.1016/j.gca.2009.06.038.

Foose, M. and Nicholson, S. (1990) *Sulfide inclusions within the B chromitite, Stillwater Complex, Montana*. doi:10.3133/b1674d.

Francis, D. (2011) 'Columbia Hills — an exhumed layered igneous intrusion on Mars?', *Earth and Planetary Science Letters*, 310(1–2), pp. 59–64. doi:10.1016/j.epsl.2011.08.003.

Frost, B. R. (1985). On the stability of sulfides, oxides and native metals in serpentinite. Journal of Petrology 26(1), 31–63.

Gatan (no date) *DigitalMicrograph software*. Available at: https://www.gatan.com/products/tem-analysis/digitalmicrograph-software (Accessed: 22 August 2025).

Godel, B. (2015) 'Platinum-group element deposits in layered intrusions: Recent advances in the understanding of the ore forming processes', *Springer Geology*, pp. 379–432. doi:10.1007/978-94-017-9652-1_9.

Godel, B., Barnes, S.-J. and Maier, W.D. (2007) 'Platinum-group elements in sulphide minerals, platinum-group minerals, and whole-rocks of the Merensky Reef (bushveld complex, South Africa): Implications for the formation of the reef', *Journal of Petrology*, 48(8), pp. 1569–1604. doi:10.1093/petrology/egm030.

González-Jiménez, J.M. *et al.* (2025) 'Micron-to-nanoscale investigation of cu-fe-ni sulfide inclusions within laurite (ru, Os)S2 from Chromitites', *Mineralium Deposita*, 60(2–3), pp. 581–604. doi:10.1007/s00126-024-01285-0.

Gordon, J.E. and Stone, P. (2021) 'Scotland: Geological Foundations and landscape evolution', *World Geomorphological Landscapes*, pp. 15–40. doi:10.1007/978-3-030-71246-4_2.

Harker, A. 1908. The geology of the Small Isles of Inverness-shire. *Memoirs of the Geological Survey: Scotland,* Sheet 60.

Hamilton, M.A. *et al.* (1998) 'Rapid eruption of Skye lavas inferred from precise U–pb and ar–ar dating of the rum and Cuillin plutonic complexes', *Nature*, 394(6690), pp. 260–263. doi:10.1038/28361.

Hasinoff, S.W. (2016) 'Photon, Poisson noise', *Computer Vision*, pp. 980–982. doi:10.1007/978-3-030-63416-2_482.

Helmy, H.M. *et al.* (2021) 'Evolution of magmatic sulfide liquids: How and when base metal sulfides crystallize?', *Contributions to Mineralogy and Petrology*, 176(12). doi:10.1007/s00410-021-01868-4.

Helmy, H.M. *et al.* (2023) 'How pt and PD are hosted in magmatic sulfides, substitutions and/or inclusions?', *Contributions to Mineralogy and Petrology*, 178(7). doi:10.1007/s00410-023-02018-8.

Hepworth, L.N. *et al.* (2018) 'Linking in situ crystallization and magma replenishment via sill intrusion in the Rum Western layered intrusion, NW Scotland', *Journal of Petrology*, 59(8), pp. 1605–1642. doi:10.1093/petrology/egy073.

Hepworth, L.N. *et al.* (2020) 'Braided peridotite sills and metasomatism in the Rum layered suite, Scotland', *Contributions to Mineralogy and Petrology*, 175(2). doi:10.1007/s00410-019-1652-9.

Hole, M.J. and Natland, J.H. (2020) 'Magmatism in the North Atlantic Igneous Province; mantle temperatures, rifting and geodynamics', *Earth-Science Reviews*, 206, p. 102794. doi:10.1016/j.earscirev.2019.02.011.

Holness, M.B. *et al.* (2020) 'Insights into magma chamber processes from the relationship between fabric and grain shape in troctolitic cumulates', *Frontiers in Earth Science*, 8. doi:10.3389/feart.2020.00352.

Holwell, D.A. and Blanks, D.E. (2020) 'Emplacement of magmatic Cu-Au-te(-ni-pge) sulfide blebs in alkaline mafic rocks of the Mordor complex, Northern Territory, Australia', *Mineralium Deposita*, 56(4), pp. 789–803. doi:10.1007/s00126-020-01015-2.

Hughes, H.S. *et al.* (2016) 'Sulphide sinking in magma conduits: Evidence from mafic–ultramafic plugs on rum and the wider North Atlantic Igneous Province', *Journal of Petrology*, 57(2), pp. 383–416. doi:10.1093/petrology/egw010.

Hughes, L. (2021) *Optimising data acquisition for Biological Sem*, *Oxford Instruments*. Available at: https://www.oxinst.com/blogs/optimising-data-acquisition-for-biological-sem (Accessed: 06 June 2025).

Hughes, A.E. *et al.* (2021) 'Platinum group metals: A review of resources, production and usage with a focus on catalysts', *Resources*, 10(9), p. 93. doi:10.3390/resources10090093.

L.J. Hulbert et al. (1992) 'Sedimentary nickel, zinc, and platinum-group-element mineralization in Devonian black shales at the Nick property, Yukon, Canada: A new deposit type'. *Explore. Min. Geology*

Jeol (2024) *Jeol USA : How to decipher an SEM-eds spectrum*, *JEOL USA, Inc.* Available at: https://www.jeolusa.com/NEWS-EVENTS/Blog/how-to-decipher-an-sem-eds-spectrum#:~:text=The%20quality%20of%20SEM%2DEDS,to%20ensure%20accurate%20chemical%20analysis.

Jerram, D.A., Goodenough, K.M. and Troll, V.R. (2009) 'Introduction: From the British tertiary into the future – modern perspectives on the British palaeogene and North Atlantic Igneous Provinces', *Geological Magazine*, 146(3), pp. 305–308. doi:10.1017/s001675680900627x.

Jiang, N. and Spence, J.C.H. (2012) 'On the dose-rate threshold of beam damage in Tem', Ultramicroscopy, 113, pp. 77–82. doi:10.1016/j.ultramic.2011.11.016.

Jin, W., Kim, J. and Kim, S., 2020. *Factor Analysis*. In: Paul Atkinson, ed., Sage Research Methods Foundations. London: SAGE Publications Ltd. Available at: https://doi.org/10.4135/9781526421036943172dw

Johnston-Peck, A.C. et al. (2016) 'Dose-rate-dependent damage of cerium dioxide in the scanning transmission electron microscope', Ultramicroscopy, 170, pp. 1–9. doi:10.1016/j.ultramic.2016.07.002.

Jolliffe, I.T. (2002) *Principal component analysis*. New York: Springer.

Joliffe, I. and Morgan, B. (1992) 'Principal component analysis and exploratory factor analysis', *Statistical Methods in Medical Research*, 1(1), pp. 69–95. doi:10.1177/096228029200100105.

Jones, L. and Nellist, P.D. (2013) 'Identifying and correcting scan noise and drift in the scanning transmission electron microscope', Microscopy and Microanalysis, 19(4), pp. 1050–1060. doi:10.1017/s1431927613001402.

Jones, L. et al. (2018) 'Managing dose-, damage- and data-rates in multi-frame spectrum-imaging', Microscopy, 67(suppl_1), pp. i98–i113. doi:10.1093/jmicro/dfx125.

Joy, D.C. (2008) 'Noise and its effects on the low-voltage sem', *Biological Low-Voltage Scanning Electron Microscopy*, pp. 129–144. doi:10.1007/978-0-387-72972-5_4.

Judd, J. W. (1889) 'The Tertiary volcanoes of the Western Isles of Scotland' *Quarterly Journal of the Geological Society of London* 45, 187–219.

Kars, M., Aubourg, C. and Pozzi, J.-P. (2023) 'Impact of temperature increase on the formation of magnetic minerals in shales. the example of Tournemire, France', *Physics of the Earth and Planetary Interiors*, 338, p. 107021. doi:10.1016/j.pepi.2023.107021.

Kato, T. *et al.* (2025) 'A comprehensive and quantitative SEM–EDS analytical process applied to lithium-ion battery electrodes', *Scientific Reports*, 15(1). doi:10.1038/s41598-025-89362-w.

Kaufmann, F.E., O'Driscoll, B. and Hecht, L. (2020) 'Lateral variations in the unit 7–8 boundary zone of the rum eastern layered intrusion, NW Scotland: Implications for the origin and timing of CR-Spinel Seam Formation', *Contributions to Mineralogy and Petrology*, 175(9). doi:10.1007/s00410-020-01732-x.

Keenan, M.R. and Kotula, P.G. (2004) 'Accounting for poisson noise in the multivariate analysis of TOF-Sims Spectrum Images', *Surface and Interface Analysis*, 36(3), pp. 203–212. doi:10.1002/sia.1657.

Kent, R.W. and Fitton, J.G. (2000) 'Mantle sources and melting dynamics in the British palaeogene igneous province', *Journal of Petrology*, 41(7), pp. 1023–1040. doi:10.1093/petrology/41.7.1023.

Kerans, C. (1983) 'Timing of emplacement of the muskox intrusion: Constraints from Coppermine homocline cover strata', *Canadian Journal of Earth Sciences*, 20(5), pp. 673–683. doi:10.1139/e83-061.

Kerr, A.C. (1995) 'The geochemistry of the mull-morvern tertiary lava succession, NW Scotland: An assessment of mantle sources during plume-related volcanism', *Chemical Geology*, 122(1–4), pp. 43–58. doi:10.1016/0009-2541(95)00009-b.

Kerr, A.C. *et al.* (1999) 'Geochemical evolution of the tertiary mull volcano, western Scotland', *Journal of Petrology*, 40(6), pp. 873–908. doi:10.1093/petroj/40.6.873.

Kotula, P.G. and Keenan, M.R. (2006) 'Application of multivariate statistical analysis to stem X-ray spectral images: Interfacial analysis in Microelectronics', *Microscopy and Microanalysis*, 12(6), pp. 538–544. doi:10.1017/s1431927606060636.

Khudhur, F.W. *et al.* (2024) 'Interrogation of ecotoxic elements distribution in slag and precipitated calcite through a machine learning-based approach aided by mass spectrometry', *Advanced Sustainable Systems*, 8(7). doi:10.1002/adsu.202300559.

Kim, H.-K. *et al.* (2020) 'Nanoscale light element identification using machine learning aided STEM-eds', *Scientific Reports*, 10(1). doi:10.1038/s41598-020-70674-y.

Koek, M. *et al.* (2010) 'A review of the PGM industry, deposit models and exploration practices: Implications for Australia's PGM Potential', *Resources Policy*, 35(1), pp. 20–35. doi:10.1016/j.resourpol.2009.08.001.

Kostryzhev, A. and Murphy, T. (2024) 'Phase characterisation in minerals and metals using an SEM-eds based automated mineralogy system', *Methods in Microscopy*, 1(2), pp. 163–175. doi:10.1515/mim-2024-0015.

Larsen, L.M. *et al.* (2015) 'Age of Tertiary volcanic rocks on the West Greenland continental margin: Volcanic evolution and event correlation to other parts of the North Atlantic Igneous Province', *Geological Magazine*, 153(3), pp. 487–511. doi:10.1017/s0016756815000515.

Latypov, R. *et al.* (2014) 'Field evidence for the *in situ* crystallization of the Merensky Reef', *Journal of Petrology*, 56(12), pp. 2341–2372. doi:10.1093/petrology/egv023.

Latypov, R., Chistyakova, S. and Mukherjee, R. (2017) 'A novel hypothesis for origin of Massive Chromitites in the bushveld igneous complex', *Journal of Petrology*, 58(10), pp. 1899–1940. doi:10.1093/petrology/egx077.

Latypov, R. *et al.* (2022) 'A 5-km-thick reservoir with > 380,000 km3 of magma within the ancient Earth's crust', *Scientific Reports*, 12(1). doi:10.1038/s41598-022-19915-w.

Latypov, R.M. *et al.* (2024) 'Layered intrusions: Fundamentals, novel observations and concepts, and controversial issues', *Earth-Science Reviews*, 249, p. 104653. doi:10.1016/j.earscirev.2023.104653.

Lauri, L.S., Mikkola, P., Karinen, T., (2012). Early Paleoproterozoic felsic and mafic magmatism in the Karelian province of the Fennoscandian shield. Lithos 151, 74–82

Lee, M.R. (2010) 'Transmission Electron Microscopy (TEM) of Earth and planetary materials: A Review', *Mineralogical Magazine*, 74(1), pp. 1–27. doi:10.1180/minmag.2010.074.1.1.

Le Vaillant, M. *et al.* (2020) 'Multidisciplinary study of a complex magmatic system: The Savannah Ni-Cu-Co Camp, Western Australia', *Ore Geology Reviews*, 117, p. 103292. doi:10.1016/j.oregeorev.2019.103292.

Lewis, W., (1753). 'Experimental examination of a white metallic substance said to be found in the goldmines of the Spanish West Indies, and is there known by the appellations of platina, platina di Pinto, Juan Blanca'. *Philosophical Transactions of the Royal Society*, 48, 638–689.

Lewis, W., (1757). 'Experimental examination of platina'. *Philosophical Transactions of the Royal Society*, 50, 156–166.

Li, P. *et al.* (2023) 'Mapping global platinum supply chain and assessing potential supply risks', *Frontiers in Energy Research*, 11. doi:10.3389/fenrg.2023.1033220.

Liu, J. *et al.* (2020) 'Effect of ion irradiation introduced by focused ion-beam milling on the mechanical behaviour of sub-micron-sized samples', *Scientific Reports*, 10(1). doi:10.1038/s41598-020-66564-y.

Maier, W.D. (2005) 'Platinum-group element (PGE) deposits and occurrences: Mineralization styles, genetic concepts, and exploration criteria', *Journal of African Earth Sciences*, 41(3), pp. 165–191. doi:10.1016/j.jafrearsci.2005.03.004.

Maier, W.D., Barnes, S.-J. and Groves, D.I. (2013) 'The Bushveld Complex, South Africa: Formation of Platinum–Palladium, chrome- and vanadium-rich layers via hydrodynamic sorting of a mobilized cumulate slurry in a large, relatively slowly cooling, subsiding magma chamber', *Mineralium Deposita*, 48(1), pp. 1–56. doi:10.1007/s00126-012-0436-1.

Marturi, N., Dembélé, S. and Piat, N. (2014) 'Scanning electron microscope image signal-to-noise ratio monitoring for micro-nanomanipulation', *Scanning*, 36(4), pp. 419–429. doi:10.1002/sca.21137.

Mathez, E.A. and Kinzler, R.J. (2017) 'Metasomatic chromitite seams in the Bushveld and rum layered intrusions', *Elements*, 13(6), pp. 397–402. doi:10.2138/gselements.13.6.397.

McInnes, L., Healy, J. and Astels, S. (2016) *How HDBSCAN works*, *How HDBSCAN Works - hdbscan 0.8.1 documentation*. Available at: https://hdbscan.readthedocs.io/en/latest/how_hdbscan_works.html (Accessed: 23 February 2025).

Meyer, R. *et al.* (2009) 'Trace element and isotope constraints on crustal anatexis by upwelling mantle melts in the North Atlantic Igneous Province: An example from the Isle of Rum, NW Scotland', *Geological Magazine*, 146(3), pp. 382–399. doi:10.1017/s0016756809006244.

Michaud, Alexander B; Laufer, Katja; Findlay, Alyssa; Pellerin, Andre; Antler, Gilad; Turchyn, Alexandra V; Røy, Hans; Wehrmann, Laura Mariana; Jørgensen, Bo Barker (2019): Svalbard summer 2016 fjord sediment sulfide oxidation and iron reactivity study [dataset publication series].

Millett, J.M. *et al.* (2024) 'High-precision u pb zircon dating of explosive volcanism in an early bi-modal volcano-sedimentary sequence from the Isle of Mull, North Atlantic igneous province', *Lithos*, 482–483, p. 107729. doi:10.1016/j.lithos.2024.107729.

Mina, A. and Anenburg, M. (2024) 'Finding and identifying platinum group elements in the Eastman layered mafic intrusion', *Australian Journal of Earth Sciences*, 71(8), pp. 1170–1182. doi:10.1080/08120099.2024.2375063.

Mindat.org (2025). Available at: https://www.mindat.org/searchmenu.php (Accessed: 30 August 2025).

Mondal, S.K. and Mathez, E.A. (2006) 'Origin of the ug2 chromitite layer, bushveld complex', *Journal of Petrology*, 48(3), pp. 495–510. doi:10.1093/petrology/egl069.

Morse, S.A., (1988). Motion of crystals, solute, and heat in layered intrusions. Can. Mineral. 26, 209–224.

Mudd, G.M., Jowitt, S.M. and Werner, T.T. (2018) 'Global Platinum Group Element Resources, reserves and mining – a critical assessment', *Science of The Total Environment*, 622–623, pp. 614–625. doi:10.1016/j.scitotenv.2017.11.350.

Mungall, J.E. (2007) 'Crystallization of magmatic sulfides: An empirical model and application to Sudbury Ores', *Geochimica et Cosmochimica Acta*, 71(11), pp. 2809–2819. doi:10.1016/j.gca.2007.03.026.

Mungall, J.E. *et al.* (2005) 'Partitioning of cu, ni, au, and platinum-group elements between monosulfide solid solution and sulfide melt under controlled oxygen and sulfur fugacities', *Geochimica et Cosmochimica Acta*, 69(17), pp. 4349–4360. doi:10.1016/j.gca.2004.11.025.

MyScope Training, (2025) EDS spectral resolution. [online] Available at: <https://myscope.training/EDS_EDS_spectral_resolution> [Accessed. 2025].

Naldrett, A.J. (2004). Platinum group element (PGE) deposits. In: Magmatic Sulfide Deposits. Springer, Berlin, Heidelberg. https://doi.org/10.1007/978-3-662-08444-1_9

Naldrett, A.J. and Duke, J.M. (1980) 'Platinum metals magmatic sulfide ores', *Science*, 208(4451), pp. 1417–1424. doi:10.1126/science.208.4451.1417.

Namur, O. *et al.* (2015) 'Igneous layering in basaltic magma chambers', *Springer Geology*, pp. 75–152. doi:10.1007/978-94-017-9652-1_2.

National Trust for Scotland (2018) *Staffa shines with new archaeological discoveries*, *National Trust for Scotland*. Available at: https://www.nts.org.uk/stories/staffa-shines-with-new-archaeologic-discoveries#:~:text=Staffa%20and%20its%20best%2Dknown,as%20an%20early%20tourist%20destination.

Oldroyd, D.R. and Hamilton , B.M. (2002) 'Themes in the early history of Scottish geology', *The Geology of Scotland*, pp. 27–43. doi:10.1144/gos4p.2.

Ozawa, K. (2023) 'Noise reduction of low-count stem-EDX data by low-rank regularized spectral smoothing', *Microscopy and Microanalysis*, 29(2), pp. 606–615. doi:10.1093/micmic/ozad008.

O'Driscoll, B. *et al.* (2009) 'The roles of melt infiltration and cumulate assimilation in the formation of anorthosite and a CR-spinel seam in the rum eastern layered intrusion, NW Scotland', *Lithos*, 111(1–2), pp. 6–20. doi:10.1016/j.lithos.2008.11.011.

O'Driscoll, B. *et al.* (2010) 'CR-spinel seam petrogenesis in the Rum layered suite, NW Scotland: Cumulate assimilation and in situ crystallization in a deforming Crystal Mush', *Journal of Petrology*, 51(6), pp. 1171–1201. doi:10.1093/petrology/egq013.

O'Driscoll, B. and González-Jiménez, J.M. (2016) 'Petrogenesis of the platinum-group minerals', *Reviews in Mineralogy and Geochemistry*, 81(1), pp. 489–578. doi:10.2138/rmg.2016.81.09.

O'Driscoll, B., Parker, A.P. and Day, J.M. (2025) 'Origin of sulfur isotope heterogeneity in platinum-group element mineralized rocks of the rum layered suite, NW Scotland', *Journal of Petrology*, 66(6). doi:10.1093/petrology/egaf037.

O'Driscoll, B. and VanTongeren, J.A. (2017) 'Layered intrusions: From petrological paradigms to Precious Metal Repositories', *Elements*, 13(6), pp. 383–389. doi:10.2138/gselements.13.6.383.

Parish, C.M. and Brewer, L.N. (2010) 'Multivariate statistics applications in phase analysis of STEM-eds spectrum images', *Ultramicroscopy*, 110(2), pp. 134–143. doi:10.1016/j.ultramic.2009.10.011.

Phillips, J.C. *et al.* (2013) 'The formation of columnar joints produced by cooling in basalt at Staffa, Scotland', *Bulletin of Volcanology*, 75(6). doi:10.1007/s00445-013-0715-4.

Power, M.R., Pirre, D. and Andersen, J.C. (2003) 'Diversity of platinum-group element mineralization styles in the North Atlantic Igneous Province: New evidence from rum, UK', *Geological Magazine*, 140(5), pp. 499–512. doi:10.1017/s0016756803008045.

Power, M.R. *et al.* (2000) 'Stratigraphical distribution of platinum-group minerals in the eastern layered series, rum, Scotland', *Mineralium Deposita*, 35(8), pp. 762–775. doi:10.1007/s001260050278.

Puchtel, I.S. (2018) 'Platinum group elements', *Encyclopedia of Earth Sciences Series*, pp. 1–5. doi:10.1007/978-3-319-39193-9_274-1.

Putnis, A. (2009) '3. mineral replacement reactions', *Thermodynamics and Kinetics of Water-Rock Interaction*, pp. 87–124. doi:10.1515/9781501508462-005.

Putnis, A. & Price, G. D. (1979). The nature and significance of exsolved phases in some chrome spinels from the Rhum layered intrusion. Mineralogical Magazine 43, 519–526.

Rasmussen, K.D. *et al.* (2019) 'Platinum demand and potential bottlenecks in the global green transition: A dynamic material flow analysis', *Environmental Science & Technology*, 53(19), pp. 11541–11551. doi:10.1021/acs.est.9b01912.

Renne, P.R. *et al.* (1998) 'Intercalibration of standards, absolute ages and uncertainties in 40ar/39ar dating', *Chemical Geology*, 145(1–2), pp. 117–152. doi:10.1016/s0009-2541(97)00159-9.

Ruan, B. *et al.* (2020) 'Sulfide segregation mechanism of magmatic ni mineralization in Western Beishan region, Xinjiang, NW china: Case study of the hongshishan mafic–ultramafic complex', *Ore Geology Reviews*, 122, p. 103503. doi:10.1016/j.oregeorev.2020.103503.

Saunders, A.D. *et al.* (2013) 'The North Atlantic Igneous Province', *Geophysical Monograph Series*, pp. 45–93. doi:10.1029/gm100p0045.

Saunders, A.D. (2015) 'Two lips and two Earth-system crises: The impact of the North Atlantic Igneous Province and the siberian traps on the Earth-surface carbon cycle', *Geological Magazine*, 153(2), pp. 201–222. doi:10.1017/s0016756815000175.

Schulz, B., Sandmann, D. and Gilbricht, S. (2020) 'SEM-based automated mineralogy and its application in geo- and Material Sciences', *Minerals*, 10(11), p. 1004. doi:10.3390/min10111004.

Scoates, J.S. and Wall, C.J. (2015) 'Geochronology of layered intrusions', *Springer Geology*, pp. 3–74. doi:10.1007/978-94-017-9652-1_1.

She, Y.-W. *et al.* (2025) 'Platinum-group element geochemistry of the Heigutian Fe ti oxide-bearing layered intrusion, Emeishan Large Igneous Province, SW china', *Lithos*, 514–515, p. 108209. doi:10.1016/j.lithos.2025.108209.

Sim, K.S. *et al.* (2025) 'Signal-to-noise ratio in scanning electron microscopy: A comprehensive review', *IEEE Access*, 13, pp. 154395–154421. doi:10.1109/access.2025.3603013.

Sim, K.S. and White, J.D. (2005) 'New technique for in-situ measurement of backscattered and secondary electron yields for the calculation of signal-to-noise ratio in a Sem', Journal of Microscopy, 217(3), pp. 235–240. doi:10.1111/j.1365-2818.2005.01448.x.

Smith, J. *et al.* (2023) 'Crystallographic controlled exsolution and metal partitioning in magmatic sulfide deposits', *Geochemistry*, 83(2), p. 125954. doi:10.1016/j.chemer.2023.125954.

Smith, M., Strachan, R. and Leslie, A.G. (2024) 'Scotland's geology: Evolution, crustal structure and societal relevance', *The Geology of Scotland*, pp. 1–31. doi:10.1144/gos5-2023-1.

Smith, S. (1997) 'Chapter 25: Special Imaging Techniques', in *The Scientist and Engineer's Guide to Digital Signal Processing*. California Technical Publishing.

Smith, W.D. and Maier, W.D. (2021) 'The geotectonic setting, age and mineral deposit inventory of global layered intrusions', *Earth-Science Reviews*, 220, p. 103736. doi:10.1016/j.earscirev.2021.103736.

Spandler, C., Mavrogenes, J. and Arculus, R. (2005) 'Origin of chromitites in layered intrusions: Evidence from chromite-hosted melt inclusions from the Stillwater complex', *Geology*, 33(11), p. 893. doi:10.1130/g21912.1.

Stone, P. *et al.* (2012) 'British Regional Geology: South of Scotland (4th edn)British Regional Geology: South of Scotland (4th edn) 2012. British Geological Survey, Nottingham. 247 pp. ISBN 978-085272-694-5 ', *Scottish Journal of Geology*, 50(1), pp. 93–94. doi:10.1144/sjg2014-003.

Suhr, D.D. (2005) 'Principal component analysis and exploratory factor analysis', *Statistical Methods in Medical Research*, 1(1). doi: http://www2.sas.com/proceedings/sugi30/203-30.

Takase, A. (2021) 'How to Improve the Signal-to-noise Ratio of X-ray CT Images', *Rigaku*. https://rigaku.com/products/imaging-ndt/x-ray-ct/learning/blog/how-improve-signal-noise-ration-xray-ct-images

Tennant, S., (1804). 'On two metals, found in the black powder remaining after the solution of platina'. *Philosophical Transactions of the Royal Society of London*, 94, 411–418.

Tenger, C. *et* al (1999). Assimilation of crustal xenoliths in a basaltic magma chamber: Sr and Nd isotopic constraints from the Hasvik Layered Intrusion, Norway. J. Petrol. 40, 363–380.

Thompson, W.J. (2001) 'Poisson distributions', *Computing in Science & Engineering*, 3(3), pp. 78–82. doi:10.1109/5992.919271.

Thompson, A., Vaughan, D., (2001) 'X-Ray Data Booklet', *Lawrence Berkeley National Laboratory.*

Tominaga, M. *et al.* (2021) 'Tracking subsurface active weathering processes in serpentinite', *Geophysical Research Letters*, 48(6). doi:10.1029/2020gl088472.

Troll, V.R., Emeleus, C.H. and Donaldson, C.H. (2000) 'Caldera formation in the Rum Central Igneous Complex, Scotland', *Bulletin of Volcanology*, 62(4–5), pp. 301–317. doi:10.1007/s004450000099.

Troll, V.R. *et al.* (2008) 'Dating the onset of volcanism at the Rum Igneous Centre, NW Scotland', *Journal of the Geological Society*, 165(3), pp. 651–659. doi:10.1144/0016-76492006-190.

Troll, V.R. *et al.* (2020) 'Fault-controlled magma ascent recorded in the central series of the Rum layered intrusion, NW Scotland', *Journal of Petrology*, 61(10). doi:10.1093/petrology/egaa093.

Upton, B.G.J. *et al.* (2023) 'The central series of the Rum Igneous Complex, nw scotland: The rises and falls of magma in a large mafic-ultramafic volcano', *Geology Today*, 39(4), pp. 130–143. doi:10.1111/gto.12441.

Vesseur, E.J. (2022) *Why is microanalysis so slow?*, *Advancing Materials*. Available at: https://www.thermofisher.com/blog/materials/why-is-microanalysis-so-slow/ (Accessed: June 2025).

Vukmanovic, Z. *et al.* (2019) 'The creation and evolution of Crystal Mush in the upper zone of the Rustenburg layered suite, Bushveld complex, South Africa', *Journal of Petrology*, 60(8), pp. 1523–1542. doi:10.1093/petrology/egz038.

Woan, G., *Quick Facts #3: Poisson Noise*. [pdf] University of Glasgow. Available at: https://radio.astro.gla.ac.uk/old_OA_course/pw/qf3.pdf

Wollaston, W. H., (1805). 'On the discovery of palladium; with observations on other substances found with platina'. *Philosophical Transactions of the Royal Society of London*, 95, 316–330.

Williams. P., (2001) 'X-Ray Data Booklet', *Lawrence Berkeley National Laboratory.*

Williamson, I.T. and Bell, B.R. (2012) 'The Staffa Lava Formation: Graben-related volcanism, associated sedimentation and landscape character during the early development of the Palaeogene Mull Lava Field, NW Scotland', *Scottish Journal of Geology*, 48(1), pp. 1–46. doi:10.1144/0036-9276/01-439.

Wilkinson, C.M. *et al.* (2016) 'Compilation and appraisal of geochronological data from the North Atlantic Igneous Province (NAIP)', *Geological Society, London, Special Publications*, 447(1), pp. 69–103. doi:10.1144/sp447.10.

Wilkinson, A.J. *et al.* (2019) 'Applications of multivariate statistical methods and simulation libraries to analysis of electron backscatter diffraction and transmission Kikuchi Diffraction Datasets', *Ultramicroscopy*, 196, pp. 88–98. doi:10.1016/j.ultramic.2018.09.011.

Xia, F. *et al.* (2009) 'Three-dimensional ordered arrays of zeolite nanocrystals with uniform size and orientation by a pseudomorphic coupled dissolution−reprecipitation replacement route', *Crystal Growth & Design*, 9(11), pp. 4902–4906. doi:10.1021/cg900691a.

Yale West Campus Materials Characterization Core, 2023. *TEM sample manual preparation procedure*. Version 1.10. [online] Yale University. Available at: https://ywcmatsci.yale.edu/sites/default/files/files/FIB%20manual%20TEM%20sample%20preparation%20SOP%20v1_1_0.pdf [Accessed 16 February 2025].

Zientek, M.L. (2012) 'Magmatic ore deposits in layered intrusions - descriptive model for reef-type PGE and contact-type Cu-Ni-pge deposits', *Open-File Report* [Preprint]. doi:10.3133/ofr20121010.